SOLID STATE SPECTROSCOPY:

THE ELECTRON PARAMAGNETIC RESONANCE SPECTRA OF GADOLINIUM AND ERBIUM IONS IN HYDROGENATED ALKALINE EARTH FLUORIDE CRYSTALS

A thesis submitted in partial fulfilment
of the requirements for the Degree of
Doctor of Philosophy in Physics
in the University of Canterbury

by

A. Edgar

University of Canterbury

1974

ABSTRACT

The Electron Paramagnetic Resonance technique has been used to study alkaline earth fluoride crystals doped with both hydride and gadolinium (or erbium) ions, and the spin Hamiltonian parameters have been determined for the various kinds of charge-compensated rare earth ion site which occur. In particular, two sites of tetragonal symmetry with the structures RE^{3+}-F_I^-, RE^{3+}-H_I^- have been examined, and small shifts in the EPR spectra of the latter site have been measured when a deuteride or tritiide ion replaces the hydride ion. A crystal lattice model of point charges and point dipoles at distorted lattice sites predicts a value of the crystal field parameter B_0^2 for the tetragonal sites which is only one half of that estimated from the observed spectra, but the model successfully accounts for the larger value of B_0^2 for the RE^{3+}-H_I^- site compared with the RE^{3+}-F_I^- site on the basis of the larger polarisability of the H^- ion. Isotope shifts are interpreted by the electron phonon interaction between the 4f electrons of the rare earth ion and the localised mode of vibration of the light anion. The magnitudes of the shifts, calculated on a point charge/point dipole model, are in good agreement with experiment.

The reorientation of the tetragonal Gd^{3+}-H_I^- sites has been examined by EPR line broadening and dielectric loss techniques. No distinct dielectric loss peak corresponding to this site was observed, and it is proposed that it cannot be distinguished from that for Gd^{3+}-F_I^- sites. An

interstitialcy model for the reorientation has been investigated and is found to be consistent with this explanation and with the observation of a metastable Gd^{3+}-H_S^--F_I^- site in u.v. irradiated calcium fluoride.

CONTENTS

LIST OF FIGURES

LIST OF TABLES

ACKNOWLEDGEMENTS

Many people have been of great assistance to me in the preparation and presentation of this thesis. In particular, I would like to thank my supervisor, Dr G.D. Jones, for his enthusiastic guidance and interest in this project, and Dr K. Zdansky for many valuable discussions on the results obtained here. I would also like to thank Dr J.A. Campbell, Professor A.G. McLellan and Professor B.G. Wybourne for their encouragement and for their interest in my progress during the past four years. The tribulations of experimental work were eased by the valued advice and assistance of B. Bradshaw, R.A. Ritchie and D. Greig of the Physics Department technical staff, and by many discussions of techniques and results with my fellow students, Murray Presland, Tim McMahon and Carey Freeth.

Dr R.F.C. Claridge of the Chemistry Department, and Dr S. Dryden, Mr H.R. Welsh and Mr R. Heyden of the CSIRO, Sydney, have all generously made their equipment available for parts of this work.

The Royal Society of New Zealand kindly awarded a travel grant for the journey to Sydney, and the University Grants Committee provided a Post Graduate Scholarship.

Finally I should like to thank my parents and my long suffering wife for their moral support and encouragement.

CHAPTER I

INTRODUCTION

This thesis will present the results of an experimental and theoretical investigation into alkaline earth fluoride crystals doped with both rare earth ions and hydride ions. The object of this chapter is to give a short review of the background to this field of research, and to discuss the incentive for performing the experiments described herein.

I. GENERAL INTRODUCTION

A crystal doped with several different impurities is a physical problem which is too complex to be capable of a direct solution. However, many quantum mechanical systems can be solved by subdividing the system into two or more subsystems, in such a way that each subsystem is almost independent of the others, and is itself capable of solution. The interaction effects between them can then be included by means of perturbation theory. This approach is only useful if the energy of interaction is small compared with the internal energy of each subsystem; otherwise the properties of the whole system bear little relation to those of its component parts, and the subdivision neither aids physical insight nor mathematical solution. The system of interest in this thesis can be broken up into the following parts: i) the rare earth ion considered as an electronic system which is influenced by the static crystal field produced by the other ions in the crystal when located at their equilibrium positions, ii) the

neighbouring hydride ion considered as a single particle vibrational system (a localised phonon mode), and iii) the remaining regular lattice ions, considered as a many-particle vibrational system (a phonon bath). The Hamiltonian of these three basic subsystems can be considered separately before the terms representing electron-phonon and phonon-phonon interactions are included. The electron-phonon interaction between the rare earth ion and the localised mode of vibration of the hydride ion will be of particular interest here.

Previous research on alkaline earth fluoride crystals which is of direct relevance to this work can be classified according to whether the crystals were doped with rare earth ions, or hydride ions, or both. Such studies have yielded much information on the subsystems (i), (ii) and (iii) discussed above, and on their interactions, so brief reviews of the important results obtained for the three types of doping will now be given.

II. RARE EARTH DOPED ALKALINE EARTH FLUORIDE CRYSTALS

The properties of rare earth ions introduced as impurities into MeF_2 crystals (Me = Ca, Sr, Ba) have been extensively investigated in recent years[1]. It is now well established that the rare earth ion in either the divalent or trivalent state substitutionally occupies an Me^{2+} site. If the rare earth ion is in the trivalent state, some form of charge compensation is required to preserve the electrical neutrality of the crystal. A common site in calcium and strontium fluoride crystals doped with the rare earth fluoride involves an F^- interstitial occupying the empty cube of

regular lattice F^- ions adjacent to that occupied by the rare earth ion, as shown in Figure 1. This tegragonal site, and some others of different symmetry, have been investigated for most of the rare earth ions in MeF_2 crystals by means of optical spectroscopy, using $4f^n \rightarrow 4f^n$, $4f^n \rightarrow 4f^{n-1}5d$ transitions, and by E.P.R. in the ground states. A feature of the low temperature optical spectra for interconfiguration transitions is the appearance of phonon sidebands alongside the purely electronic ('no-phonon') lines. This manifestation of the ion-lattice interaction is due to simultaneous electronic and vibrational transitions. Peaks in the sidebands correspond to peaks in the phonon density of states or to localised modes centred near the rare earth ion.

Ion-lattice interaction effects are not so apparent in the EPR spectra, although spin-lattice relaxation does result in the EPR lines being strongly broadened above 30^oK for most of the rare earth ions. The Jahn-Teller effect is one interesting consequence of ion lattice coupling which is most easily investigated by the EPR technique. However, Jahn-Teller energies are expected to be very small for rare earth ions in $4f^n$ configurations due to their relatively weak interactions with the lattice[2].

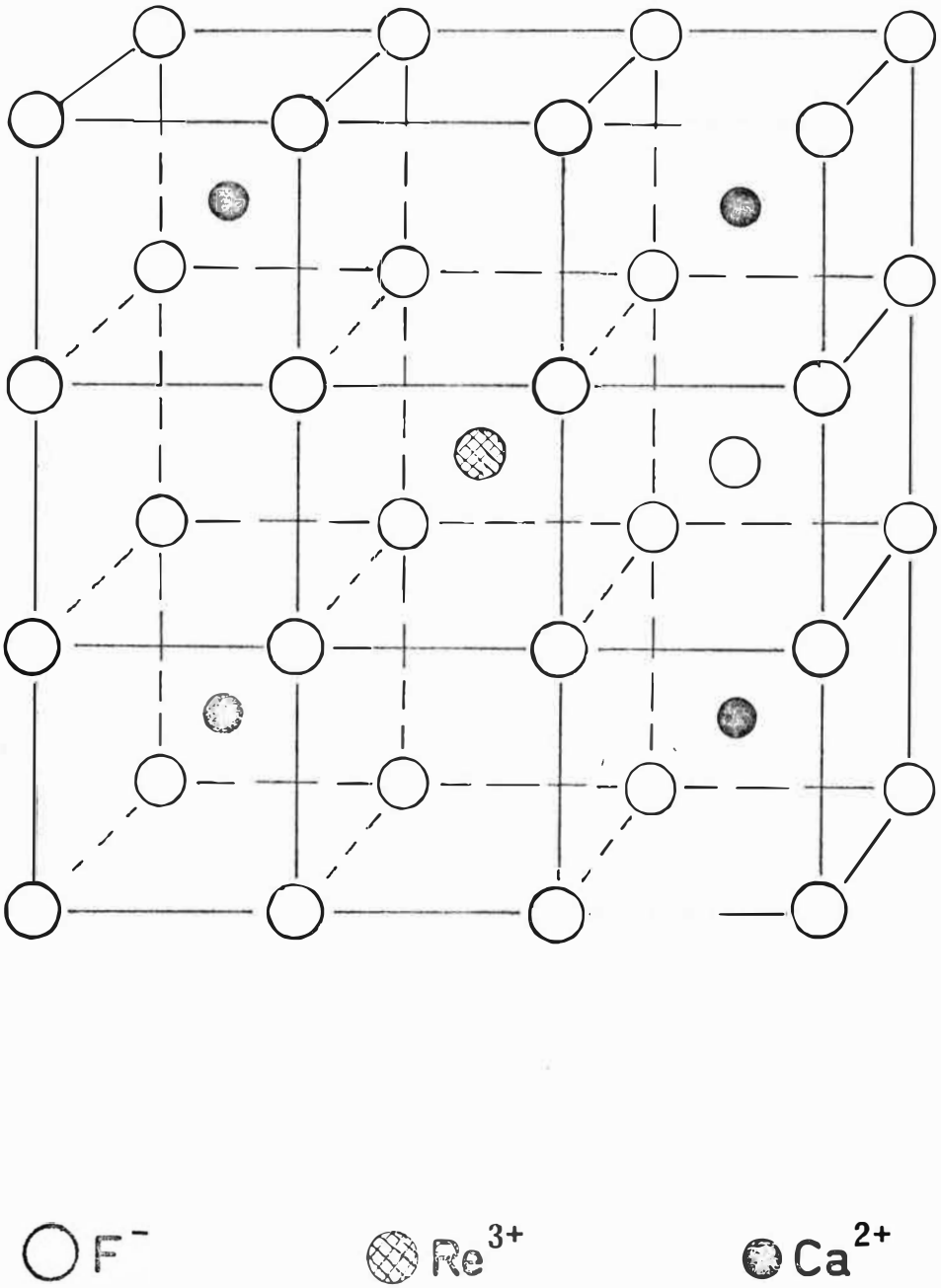

Fig 1: The tetragonal $RE^{3+} - F_I^-$ site in alkaline earth fluoride crystals.

III. HYDROGENATED ALKALINE EARTH FLUORIDE CRYSTALS

Hall and Schumacher[3] have shown that it is possible to introduce hydrogen (or its isotopes deuterium and tritium) into MeF_2 lattices by a chemical process. The hydrogen enters the lattice as hydride (H^-) ions and substitutes for fluoride ions at some of the regular F^- lattice sties. The hydride ion is subject to similar force constants to the fluoride ion which it replaces, but has a very much smaller mass. This results in an H^- vibrational frequency which is higher than the vibrational pass bands of the crystals. Thus any excitation of the hydride ion cannot propagate through the crystal and a strongly localised mode of vibration ensues. In fact it can be shown that to a very good approximation the hydride ion can be considered to vibrate almost independently of the rest of the crystal lattice, and that it is accurately described by the theory of a perturbed harmonic oscillator[4,5]. Transitions from the ground state (principal quantum number $N = 0$) to the $N = 1$, 2, or 3 excited states can be detected as sharp absorption lines in the 500-3000 cm^{-1} (infrared) region.[5] The coupling between the hydride ion local mode and the lattice results in the presence of small sidebands on either side of the main absorption lines[5]. These are due to simultaneous lattice mode and local mode phonon transitions.

IV. ALKALINE EARTH FLUORIDE CRYSTALS DOPED WITH BOTH RARE EARTH AND HYDRIDE IONS

MeF_2 crystals which have been doped with rare earth ions can also be hydrogenated. Jones et al.[6] have investigated such crystals and have found that new lines appear in both the optical spectra of the rare earth ion and the infrared spectra of the hydride ion. These authors showed that their observations were consistent with the formation of a tetragonal RE^{3+}-H_I^- site analogous to the RE^{3+}-F_I^- site described previously. This new RE^{3+}-H_I^- site provides an excellent experimental situation for investigating the electron phonon interaction for several reasons. The RE^{3+} ion is an electronic system whose general structure is now well understood; in particular there have been several theoretical investigations[7,8,9] of the tetragonal RE^{3+}-F_I^- site. The hydride ion oscillating in its potential well is a good approximation to the ideal case of a single particle vibrational system and so may be described by the comparitively straightforward Simple Harmonic Oscillator Formalism. The amplitude of the oscillation varies when deuterium or tritium is substituted for hydrogen since the amplitude is inversely proportional to the particle mass. Finally, the interaction between the two systems is not so great that a perturbation approach is inapplicable, but not so small that interaction effects cannot be observed. The appearance of such interaction effects in the spectra of the rare earth and hydride ions will now be discussed.

Jones and his coworkers[6] have observed the infrared spectrum of the tetragonal H_I^- sites for all of the rare earth series ions. In most cases they found two absorption line fundamentals, corresponding to the longitudinal and (doubly degenerate) transverse modes of motion. Erbium was anomalous in having two sets of fundamental lines separated by a few wavenumbers. It has been suggested[4] that this spectrum can be explained by an electron-phonon interaction if there is an excited electronic state of the erbium ion within a few wavenumbers of the ground state. This suggestion has recently been substantiated by Presland[10], who has found a first excited state 4.5 cm^{-1} above the ground state.

A different but related interaction effect has been observed for Ce^{3+}-H_I^- and Pr^{3+}-H_I^- sites by Jacobs et al.[11]. They observed that the first harmonic transverse lines, when examined at helium temperatures and under high resolution, were in fact split into two component lines for the Ce^{3+}-H_I^- site and three for the Pr^{3+}-H_I^- site. They proved that this "xy splitting" could in principle be produced by an electron-phonon interaction, and that simple electrostatic models predicted the size of the splittings to within an order of magnitude.

Jones et al.[6] and Jacobs et al.[11] have also investigated the optical spectrum of the rare earth-hydride ion site. The new spectrum reveals the presence of an electron-phonon interaction in two ways. Firstly, there is a small shift in the positions of the absorption or fluorescence lines when deuterium or tritium is substituted for hydrogen in the crystal. Secondly a local mode vibronic sideband structure

appears, consisting of two sharp lines on either the high frequency or low frequency sides of the main no-phonon line, depending on whether absorption or fluorescence is being observed. These two lines correspond to the creation of a longitudinal or transverse H_I^- local mode phonon in conjunction with an electronic transition of the rare earth ion. Jacobs et al.[11] attempted to explain the isotope shift of the no-phonon lines by means of simple electrostatic models but obtained theoretical isotope shifts which were only one quarter the magnitude and of opposite sign to the experimental values.

The RE^{3+}-H_I^- pairs have also been investigated for calcium fluoride doped with Ce^{3+}, Sm^{3+} and Nd^{3+} by means of Electron Paramagnetic Resonance[12]. Rare earth ions with odd numbers of electrons in the $4f^n$ shell usually have a Kramers doublet ground state, whose effective g values may be accurately measured by E.P.R. The electron-phonon interaction results in a small isotope shift in the g values when deuterium or tritium is substituted for hydrogen. No theoretical calculation of these g value isotope shifts has yet been attempted.

V. THE PRESENT APPLICATION OF EPR SPECTROSCOPY TO $MeF_2:RE^{3+}:H^-$ CRYSTALS

The major incentive for performing the EPR work described herein was to complement the optical and infrared measurements on $MeF_2:RE^{3+}:H^-$ crystals of Jones et al.[6], Jacobs et al.[11], Presland[10], and other workers. The previous EPR measurements discussed above were made before the results of investigations

using other spectroscopic techniques were known, and the paucity of data discouraged theoretical interpretation of the g values and their isotope shifts. Of the three rare earth ions (Ce^{3+}, Nd^{3+}, Sm^{3+}) which were investigated, only the Ce^{3+}-H_I^- site has since been examined optically[11], and this problem is currently being investigated by P.T. McMahon[118]. However the optical and infrared spectra of CaF_2:Gd^{3+}:H^- crystals have been measured by Jones et al.[6], and Presland[10] has recently analysed the optical spectrum of CaF_2:Er^{3+}:H^-. Both sets of results relate primarily to the tetragonal RE^{3+}-H_I^- site and so there is an established pool of spectroscopic data for the Gd^{3+}-H_I^- and Er^{3+}-H_I^- sites, although no EPR measurements have yet been made. For these reasons the Er^{3+} and Gd^{3+} ions were chosen for the current work, with the assurance that a theoretical interpretation of the corresponding RE^{3+}-H_I^- sites would not be unduly limited by lack of data. Most of the results reported here are for Gd^{3+} ions because at the beginning of this work no cryogenic facilities were available for the EPR spectrometer.

A secondary aim in this research was to extend the knowledge of charge compensation mechanisms in both hydrogenated and untreated MeF_2:RE^{3+} crystals. This chapter has concentrated on the simple tetragonal RE^{3+}-F_I^-/H_I^- site because most of the previous research relates to this site and also because it is structurally the simplest site. However, many other charge compensation arrangements involving, for example, O_s^{2-}, Na^+ and H_s^- ions are possible, and the EPR technique is a particularly useful tool for investigating these centres because the site symmetry can be directly

identified. This important physical characteristic of a RE^{3+} site cannot be unambiguously determined by optical or infrared spectroscopy and some form of magnetic field spectroscopy, e.g. Optical Zeeman, EPR, or ENDOR, is required. EPR does not furnish as much information as ENDOR, but it is technically and analytically simpler, whilst EPR is much more accurate than optical Zeeman measurements.

The EPR spectra of the various charge compensated Er^{3+} and Gd^{3+} sites in untreated MeF_2 crystals have largely been dealt with by other workers, although some revisions and extensions are included here. However, no EPR work has yet been done for hydrogenated crystals containing these ions, and such measurements are desirable both to confirm the tetragonal symmetry of the Gd^{3+}-H_I^- and Er^{3+}-H_I^- sites discussed previously and, more importantly, to examine the symmetry of other hydrogenic RE^{3+} sites. For example, Jones et al.[6] suggested that u.v. irradiation converts the tetragonal Gd^{3+}-H_I^- centre into a similar Gd^{3+}-H_I^0 site. It is possible with EPR to test this hypothesis directly by examining the symmetry and structure of the spectrum; other unreported sites can be similarly investigated.

VI. THE STRUCTURE OF THIS WORK

Chapter II of this thesis will give a brief review of the basic theories used in subsequent chapters. Experimental techniques and instrumentation will be discussed in Chapter III. The EPR spectra of Gd^{3+} in unhydrogenated MeF_2 crystals have been measured by previous workers. Unfortunately some of

these measurements are either incomplete or incorrect. These measurements are revised and extended in Chapter IV, and new results for Gd^{3+} charge compensated by monovalent cations are also presented. Chapter V will give the experimental results for hydrogenated CaF_2, SrF_2 crystals containing Gd^{3+}; a comparison with theoretical predictions of the isotope shifts will be made in Chapter VI. During this research the Physics Department acquired a liquid helium "Janis" dewar which made possible measurements on rare earths other than Gd^{3+}. Chapter VII will present and discuss results obtained for Er^{3+}-H_I^-/D_I^- in calcium fluoride.

Chapter VIII will be concerned with a different facet of the behaviour of RE^{3+}-H_I^- pairs in MeF_2 crystals. It is apparent from Figure 1 that there is a six-fold orientational degeneracy of the RE^{3+}-F_I^- axis, corresponding to the six equivalent interstices that the F_I^- can occupy. The thermally-activated reorientation of the axis gives rise to lifetime broadening of the RE^{3+} EPR lines, and also to dielectric loss since the RE^{3+}-F_I^- site has a net dipole moment. Chapter VIII will present the results of EPR linewidth and dielectric loss measurements on tetragonal Gd^{3+}-F_I^-, Gd^{3+}-H_I^- and Gd^{3+}-D_I^- sites in calcium fluoride.

CHAPTER II

A REVIEW OF THE BASIC THEORIES

This chapter will review those particular aspects and theories of solid state physics which provide a common foundation for the discussion presented in Chapters IV, V, VI and VII. The theory of dipole reorientation is of importance in Chapter VIII only, and so a discussion of this subject will be presented there.

I. THE PERTURBED HARMONIC OSCILLATOR

Elliott et al.[5] have shown that the vibrational properties of low mass impurity atoms or ions in crystals can be adequately represented by the static well approximation. In this theory the neighbouring atoms are considered to be essentially stationary at their equilibrium positions, and the impurity atom vibrates in the potential well generated by its interaction with the neighbouring atoms and the rest of the crystal lattice. Under these assumptions the Greens Functions method of analysis[13] is unnecessary and the defect motion can be described by the simple theory of a single particle oscillating in an anharmonic, anisotropic potential well. The potential well must be invariant under the operations of the point group of the particular defect site and hence must transform according to the Γ^1 (totally symmetric) representation of that group. For the tetragonal RE^{3+}-H_I^- ion pairs of interest here, the potential energy of the H^- ion has C_{4v} symmetry. Taking into account this symmetry restraint, the expansion of the potential in a Taylor series about the

equilibrium point of the H_I^- ion yields

$$V(xyz) = a(x^2+y^2) + bz^2 + cz^3 + dz(x^2+y^2) + f(x^4+y^4) + gz^4 + hz^2(x^2+y^2) + kx^2y^2 + \text{higher order terms} \quad (2\text{-}1)$$

where x,y,z are the displacements from the equilibrium position of the H_I^- ion. The first two terms in this expansion are dominant and constitute a harmonic oscillator potential. The remaining terms are relatively small and may be treated as a perturbation of this potential. Figure 2 shows the resulting energy level scheme and the possible transitions. Jones et al.[6] have observed the first harmonic transitions for Gd^{3+}-H_I^-/D_I^- and Er^{3+}-H_I^- in CaF_2, and second harmonics for Gd^{3+}-H_I^- in calcium fluoride. These results will be of use later in this thesis and so are summarised in table 1.

Newman[4] has given an extensive review of theoretical and experimental results for perturbed harmonic oscillators of C_{4v} and other symmetries.

II. ELECTRONIC PROPERTIES OF TRIVALENT LANTHANIDE IONS IN MeF_2 CRYSTALS

The electronic structure of neutral lanthanide ions consists of a common xenon structure, two or three outer electrons ($6s^2$ or $5d6s^2$), and a $4f^N$ (N = 1,14) shell which is progressively filled through the series. Ionization proceeds by successive removal of the outer electrons (and sometimes one of the 4f electrons) until in the +3 oxidation state only the xenon core and $4f^N$ shell remain. The spectroscopic properties of the trivalent lanthanides are due to the $4f^N$

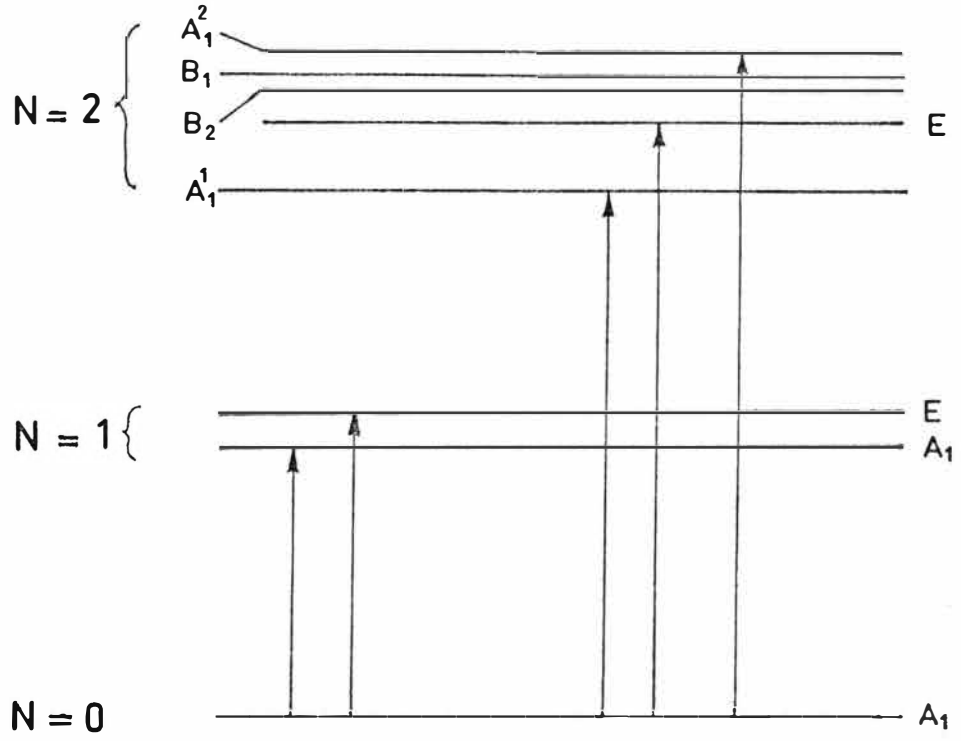

Fig 2: The splittings of the N=0,1,2 levels of a simple harmonic oscillator by a perturbation of C_{4v} symmetry.

TRANSITION	FUNDAMENTALS		2nd HARMONICS		
ION PAIR	x,y	z	x,y	x+z	z
Gd^{3+}-H_I^-	1017.0	1104.2	2029.2	2108.5	2189
Er^{3+}-H_I^-(I)	1036.2	1086.6	-	-	-
Er^{3+}-H^-(II)	1037.6	1081.2	-	-	-

TABLE 1 Frequencies of observed infrared absorption lines (in cm^{-1}) for Gd^{3+}-H_I^- sites in calcium fluoride at $20^{o}K$ (from reference 6)

shell ground configuration and to the excited configurations ($4f^{N-1}6p$ etc.). The 4f electrons are drawn into the interior of the common xenon core due to their imperfect mutual shielding, and behave as an inner shell[14]. This phenomenon, known as the lanthanide contraction, and the consequent shielding furnished by the $5s^2$ and $5p^6$ outer xenon core shells results in the 4f electrons having a rather weak electrostatic interaction with any external environment. Thus the lanthanide series ions show much weaker crystal field splittings than the transition metal ions.

The Hamiltonian for a rare earth ion in a crystal field may be written as

$$H = \left[-\frac{h^2}{2m_e} \sum_{i=1}^{N} \nabla_i^2 - \sum_{i=1}^{N} \frac{Ze^2}{r_i} + \sum_{i<j}^{N} \frac{e^2}{r_{ij}} + \sum_i \xi(\underline{r})\,\underline{\ell}_i \cdot \underline{s}_i \right] + \sum_{i=1}^{N} \sum_{k,q} B_q^k C_q^k \quad , \tag{2-2}$$

where the symbols have their usual meanings[14]. The free-ion terms in the bracket are the kinetic energy, electron-nuclear potential energy, electron-electron potential energy, and electron spin-orbit energy respectively. The first three of these terms commute with both the total orbital angular momentum operator L and the total spin angular momentum operator S. Thus the eigenfunctions of this part of the Hamiltonian may be labelled by their S and L values to give a <u>term</u> ^{2S+1}L of degeneracy $(2L+1)\times(2S+1)$. The spin-orbit interaction only commutes with the total angular momentum operator J = L+S and so splits the terms into levels characterised by different values of J.

If the magnitude of the spin orbit interaction is relatively small, the new eigenvalues are commonly calculated by the SL coupling approximation in which only the diagonal matrix elements are considered. The splitting patterns of the various terms are then given by the well known Landé interval rule, and the eigenfunctions may still be labelled by the values of L and S. However, for the lanthanide ions the spin orbit coupling is of moderate magnitude and so its off-diagonal matrix elements cannot be neglected. This case is known as intermediate coupling and the intermediate coupling eigenfunctions are linear combinations of the terms. The dominant term in the combination is usually used as a label; hence an eigenfunction is designated as $^{2S+1}L_J$ even though S and L are no longer constants of motion.

The crystal field term splits the intermediate coupling free ion levels further, although two-fold Kramers degeneracy must remain for ions with odd numbers of electrons. If the crystal field is invariant under the operations of a point group G, the eigenfunctions may be labelled according to their transformation properties by the appropriate irreducible representation Γ_h of G. Although the previous labels such as S, L and J are no longer good quantum numbers in the strict sense, they are still useful indicators of the parentage of an eigenfunction and so are often included in the labelling scheme.

The crystal field can be expanded as a linear combination of spherical harmonics Y_ℓ^m or spherical tensors C_ℓ^m; these quantities are defined by

$$Y_\ell^m(\theta,\phi) = (-1)^m \left[\frac{(2\ell+1)(\ell-|m|)!}{4\pi(\ell+|m|)!}\right]^{\frac{1}{2}} P_\ell^m(\cos\theta)\, e^{im\phi} \tag{2-3}$$

$$C_\ell^m = \left(\frac{4\pi}{2\ell+1}\right)^{\frac{1}{2}} Y_\ell^m \tag{2-4}$$

where (r,θ,ϕ) are spherical coordinates and P_ℓ^m is an associated Legendre polynomial. Wybourne's book[14] gives detailed formulae by which the matrix elements of these operators may be calculated.

Figure 3 shows the lowest energy levels of the Er^{3+} and Gd^{3+} ions in environments of decreasing symmetry. The Gd^{3+} ion ($4f^7$) has very weak crystal field splittings due to the special properties of half-filled shells. In particular, no crystal field splitting of first order is possible between pure LS states and so higher order perturbations have to be invoked to explain the splittings.

III. THE ELECTRON-PHONON INTERACTION

The electron-phonon interaction arises from the modulation of the crystal field at the rare earth ion site due to the thermal motion of the lattice, and is thus defined by

$$V_{ev} = V_c - V_c^o, \tag{2-5}$$

where V_c is the instantaneous crystal field at the rare earth ion site and V_c^o is the static crystal field produced by the lattice ions at their equilibrium positions. The general form of the interaction, in the adiabatic approximation, can be written[15] as

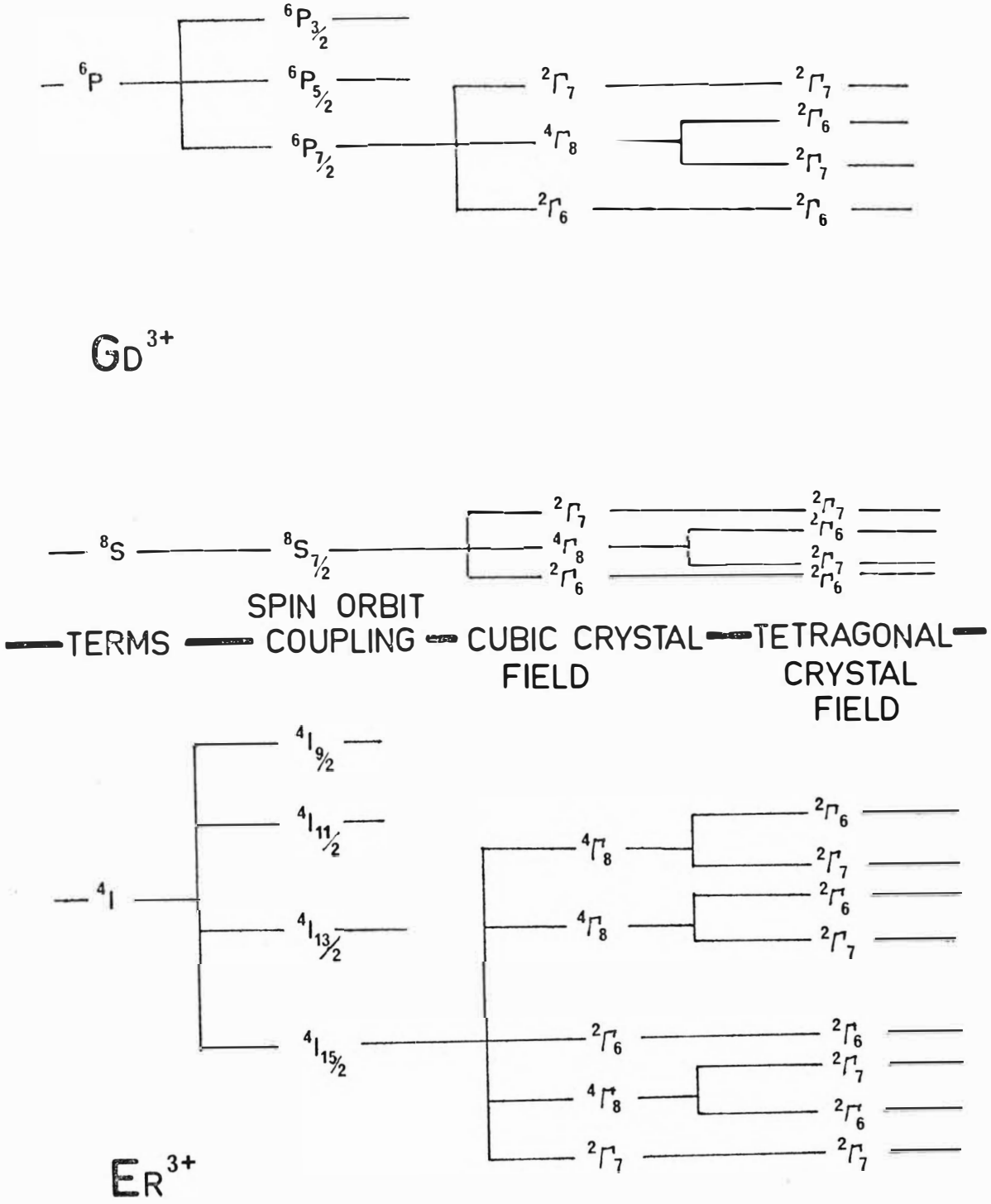

Fig 3: Schematic energy level diagram for Er^{3+} and Gd^{3+} ions in environments of diminishing symmetry.

$$V_{ev} = \sum_{\substack{i \\ \alpha}} f_i{}^{\alpha} Q_i{}^{\alpha} + \sum_{\substack{i,j \\ \alpha,\beta}} g_{ij}{}^{\alpha\beta} Q_i{}^{\alpha} Q_j{}^{\beta} + \cdots , \qquad (2\text{-}6)$$

where the $Q_i{}^{\alpha}$ are the phonon normal coordinates which transform according to the α^{th} irreducible representation Γ^{α} of the point group of the rare earth ion site. The $f_i{}^{\alpha}$ and $g_{ij}{}^{\alpha\beta}$ are functions of the coordinates of the rare earth ions' electrons and must transform according to the representations $(\Gamma^{\alpha})^*$, $(\Gamma^{\alpha}\times\Gamma^{\beta})^*$ respectively since V_{ev} is invariant under the point group operations.

Both the regular lattice modes and the H^- ion localised mode will produce a shift in the electronic energy levels of the rare earth through the interaction V_{ev}. However, for the purposes of electronic level isotope shift calculations, the regular lattice modes may be omitted from equation (2-6) since their contribution is expected to be the same for both hydrogenated and deuterated crystals. The H^- ion localised mode normal coordinates are just X,Y,Z, the displacements of the ion from its equilibrium position, and so equation (2-6) reduces to

$$V_{ev} = f_z Z + f_x X + f_y Y + g_{zz} Z^2 + \tfrac{1}{2}(g_{xx}+g_{yy})(X^2+Y^2)$$
$$+ \tfrac{1}{2}(g_{xx}-g_{yy})(X^2-Y^2) + g_{xz} XZ + g_{xy} XY + g_{yz} YZ + \cdots \qquad (2\text{-}7)$$

This interaction, involving the rare earth and hydride ion only, must be invariant under the operations of the $C_{\infty v}$ group, and so the displacement coordinate terms in (2-6) have been grouped, where necessary, in (2-7) so that they form basis functions for the irreducible representations of $C_{\infty v}$[16]. The

associated electronic functions f and g must transform as the complex conjugate representations and so their most general form is;

$$
\begin{aligned}
f_z &= \sum_{n=0}^{\infty} \alpha_0{}^n C_0{}^n & g_{zz} &= \sum_{n=0}^{\infty} \beta_0{}^n C_0{}^n \\
& & g_{xx}-g_{yy} &= \sum_{n=0}^{\infty} \beta_2{}^n (C_2{}^n + C_{-2}{}^n) \\
f_x &= \sum_{n=0}^{\infty} \alpha_1{}^n (C_1{}^n + C_{-1}{}^n) & g_{xx}+g_{yy} &= \sum_{n=0}^{\infty} \gamma_0{}^n C_0{}^n \\
& & g_{yz} &= \sum_{n=0}^{\infty} -i\beta_1{}^n (C_1{}^n - C_{-1}{}^n) \\
f_y &= \sum_{n=0}^{\infty} -i\alpha_1{}^n (C_1{}^n - C_{-1}{}^n) & g_{xz} &= \sum_{n=0}^{\infty} \beta_1{}^n (C_1{}^n + C_{-1}{}^n) \\
& & g_{xy} &= \sum_{n=0}^{\infty} -i\gamma_2{}^n (C_2{}^n - C_{-2}{}^n) .
\end{aligned}
\qquad (2\text{-}8)
$$

The equations (2-8) may be readily derived from point group tables and a straightforward application of Van Vleck's "basis function generating machine" procedure applied to the Racah spherical tensors $C_m{}^\ell$. The expansion coefficients α,β,γ depend upon the particular model chosen to represent the interaction. They are most easily evaluated by utilising the solid harmonics $T_{\ell x}{}^m$, $T_{\ell y}{}^m$ discussed in Appendix I.

For the simple electrostatic models to be considered in this thesis, the coefficients α,β,γ may be determined by expanding that part of the crystal field at the rare earth ion site which is due to the point charge and point dipole of the hydride ion, in a Taylors series:

$$V = V)_{XYZ=0} + \sum_i \frac{\partial V}{\partial X_i}\Big)_{XYZ=0} \Delta X_i + \tfrac{1}{2} \sum_{ij} \frac{\partial^2 V}{\partial X_i \partial X_j}\Big)_{XYZ=0} \Delta X_i \Delta X_j \qquad (2\text{-}9)$$

The inclusion of the dipole moment of the hydride ion is important because of the very large polarisability of this ion. Experimental and theoretical investigations[17] have shown that the free hydride ion has a polarisability of approximately 30 $\mathring{A}^3$, which is an order of magnitude greater than that of heavier anions such as F^-, Cl^- etc. The derivatives in equation (2-9) may be found by utilising the expansion of the Coulombic interaction in terms of solid harmonics and the formulae given by Zdansky[11] for the derivatives of solid harmonics. In this way Jacobs et al.[11] evaluated the coefficients α,β,γ for both the point charge and point dipole model. These coefficients and the formulae of Zdansky are summarised, with some corrections, in Appendix I.

IV. THE SPIN HAMILTONIAN FORMALISM

The detailed theory of paramagnetic ions in crystals aims at predicting the energies and effective g values of all of the eigenstates which are experimentally accessible. However, because of the Boltzmann thermal population factor, EPR is usually only observed in Zeeman-split states which are within about 30 cm^{-1} of the ground state. The task of the experimentalist is to summarise the observed properties of these lowest states in as concise a fashion as possible. Fitting the parameters of the full Hamiltonian to the experimental EPR spectrum is extremely unwieldy since all of the unobserved states are also involved. An alternative

method, called the spin Hamiltonian formulation, aims at reproducing the properties of only the (2S+1) lowest states, by means of an empirical Hamiltonian acting within a basis set of (2S+1) spin angular momenta eigenkets $|S\rangle\ |S-1\rangle \cdots |-S\rangle$. No direct relationship of the spin S to the true spin of the ion is necessarily implied; the only requirement is that the spin Hamiltonian has the same symmetries and eigenvalues as the full Hamiltonian.

The original perturbation theory derivation of spin Hamiltonians (S.H.'s) by Pryce[18,19] has been found to be unsatisfactory in some respects, and has now been replaced by group theoretical[20] and tensor decomposition methods[21,22,23,24]. These latter techniques are basically equivalent, and utilize the symmetries of the problem to establish the sorts of terms which can appear in the S.H., without prejudging their relative magnitudes. The new techniques are now well established but some debate on details and methods has appeared in recent literature[25,26,27,28].

As a specific example, which will be required later in this thesis, the S.H. of the $^8S_{7/2}$ ground state of Gd^{3+} in a cubic crystal field will be derived. The first excited state ($^6P_{7/2}$) is some 30,000 cm^{-1} above the ground state[6] so magnetic field mixing of this and higher states into the $^8S_{7/2}$ state may be safely ignored. Also nuclear hyperfine structure is usually unresolved in Gd^{3+} EPR spectra, and so a S.H. basis set of dimension 2S+1 = 8 may be used. The S.H. must be expressible as some polynomial in the field H and the spin S, or equivalently in terms of products of tensor operators $T_L^M(S)$, $T_L^M(H)$. Expanding in field tensors of increasing rank, the S.H. is

$$\mathcal{H} = \sum_{L_S,M_S} a_{L_S}^{M_S} T_{L_S}^{M_S}(S) + \sum_{L_S,M_S,M_H} b_{L_S}^{M_S} T_{L_S}^{M_S}(S)\, T_1^{M_H}(H)$$

$$+ \sum_{L_S,M_S H} c_{L_S}^{M_S} T_{L_S}^{M_S}(S)\, T_2^{M_H}(H) \qquad (2\text{-}10)$$

The terms in this equation may be rewritten in terms of the tensor products $T_L^M(S,H)$ defined by[29]

$$T_L^M = T_L^M(S,H) = (2L+1)^{\frac{1}{2}} \sum_{M_S M_H} (-1)^{-L_S+L_H-M} \begin{pmatrix} L_S & L_H & L \\ M_S & M_H & -M \end{pmatrix} \times T_{L_S}^{M_S}(S)\, T_{L_H}^{M_H}(H) \qquad (2\text{-}11)$$

to obtain

$$\mathcal{H} = \sum_{L,M} {}^0A_L^M\, T_L^M + {}^1A_L^M\, T_L^M + {}^2A_L^M\, T_L^M + \cdots \qquad (2\text{-}12)$$

where the prefix denotes the field tensor rank parentage. There are three conditions which impose constraints on the values of the coefficients ${}^nA_L^M$ in the above equations:

1) The S.H. must be Hermitian, so that[21]

$$(A_L^M\, T_L^M)^\dagger = (-1)^M (A_L^M)^*\, T_L^{-M} \qquad (2\text{-}13)$$

implies

$$A_L^{-M} = (-1)^M (A_L^M)^* \qquad (2\text{-}14)$$

2) The S.H. must have the same symmetry properties as the full Hamiltonian.

a) Under time reversal, represented by the Kramers operator K, we must have

$$KHK^{-1} = H \qquad (2\text{-}15)$$

and it can be shown that[21]

$$K(A_L{}^M T_L{}^M + (-1)^M A_L{}^{M^*-M} T_L{}^{M^*-M})K^{-1} = (-1)^L (A_L{}^M T_L{}^M + (-1)^M A_L{}^{M^*-M} T_L{}^{M^*-M}), \tag{2-16}$$

so odd L terms are excluded.

b) The S.H. must be invariant under the operations of the cubic group. The linear combination of the $T_L{}^M$ which satisfies this and the previous conditions is

$$A_0{}^0 T_0{}^0 + A_4 (T_4{}^0 + (\tfrac{5}{14})^{\frac{1}{2}} (T_4{}^4 + T_4{}^{-4})) + A_6 (T_6{}^0 - (\tfrac{7}{2})^{\frac{1}{2}} (T_6{}^4 + T_6{}^{-4})) \tag{2-17}$$

Since the field tensors of a given rank transform amongst themselves only, each term in equation (2-12) must be of the above form. The tensor product terms may now be decomposed by equation (2-11) into the products of the component field and spin tensors subject to the following conditions:

(i) The triangle rule on the 3J symbol requires that:

$$M_S + M_H = M \quad \text{and} \quad |L-n| \leqslant L_S \leqslant |L+n|.$$

(ii) Odd parity products do not satisfy time reversal invariance, i.e. $n + L_S$ must be even.

(iii) Matrix Elements of spin tensors of rank greater than 7 vanish due to the triangle rule.

(iv) Usually only linear terms in the field are required, i.e. $n \leqslant 1$.

The decomposition of the n = 0 terms and the $T_0{}^0(H,S)$ term for n = 1 is given in Appendix II. Decomposing the tensors $T_L{}^M$ for n = 1 but L > 0 gives rise to the so-called

Bleaney-Koster terms of the form HS^3, HS^5, etc.; these will be omitted in this analysis in the interests of simplicity since they are generally found to be very small. (The form of these terms for a spin Hamiltonian of tetragonal symmetry is derived in Appendix II since they will be required later in this thesis.) The tensor operators $T_L^M(S)$ have been tabulated by Buckmaster et al.[29]. Using their tables, the spin Hamiltonian may finally be written as

$$\mathcal{H} = g\beta(H_xS_x + H_yS_y + H_zS_z) + A_4(T_4^0(S) + \sqrt{\frac{5}{14}}(T_4^4 + T_4^{-4}) + A_6(T_6^0(S) - (\frac{7}{2})^{\frac{1}{2}}(T_6^4 + T_6^{-4}) \quad (2\text{-}18)$$

Unfortunately EPR literature does not yet use the tensor operators $T_L^M(S)$ but the related operators

$$\bar{O}_L^M(S) = N(T_L^M(S) + (-1)^M T_L^{-M}(S)) \quad (2\text{-}19)$$

where N is a normalisation constant. In terms of these operators the S.H. becomes

$$\mathcal{H} = g\beta\underline{H}\cdot\underline{S} + B_4(\bar{O}_4^0(S) + 5\bar{O}_4^4(S)) + B_6(\bar{O}_6^0(S) - 21\bar{O}_6^4(S)).$$

CHAPTER III

EXPERIMENTAL TECHNIQUES

I. CRYSTAL GROWTH AND TREATMENT

Crystals of rare earth doped MeF_2 (Me = Ca, Sr, Ba) were grown by Mr Ross Ritchie using the Bridgeman-Stockbarger technique and an A.D. Little R.F. induction furnace. The melt, consisting of crystal fragments of pure MeF_2, an appropriate quantity of rare earth fluoride, and 2% by weight of lead fluoride oxygen scavenger, was placed in a graphite crucible and slowly drawn through the furnace. The amount of rare earth fluoride added to the melt was usually chosen to give a nominal RE^{3+} concentration in the crystal of .05%. This figure was the best compromise between the conflicting requirements of narrow linewidth but adequate intensity of the EPR lines, and also was low enough to ensure that only inappreciable quantity of complex RE^{3+}-H^- clusters[6] was formed.

Hydrogen or deuterium was introduced into the crystals by the standard method of Hall and Schumacher[3], which involves heating the samples at 800^{o}C in contact with molten aluminium and in a hydrogen or deuterium atmosphere. In order to enhance the concentration of the simple tetragonal rare earth-hydride ion sites, the crystals were quenched to 77^{o}K directly after the treatment by immersing the quartz hydrogenation tube in liquid nitrogen. The concentration of the tetragonal hydride ion sites so produced was up to one third of the corresponding fluoride ion site for calcium fluoride, and typically one twentieth for strontium fluoride.

Tritium was obtained in capsules containing 2 cm^3 of the gas so special precautions were taken to restrict the volume of the hydrogenation chamber. Initial attempts at tritiation using a graphite crucible yielded crystals which contained a greater quantity of hydrogen than tritium, possibly because of the presence of water vapour, which may have been trapped in the graphite. Later tritiations used an alumina crucible, which reduced the hydrogen content to one third that of tritium.

For EPR measurements the crystals were usually mounted with the (110) axis parallel to the sample holder axis. This mounting was achieved on an optical goniometer by using reflections from the (111) cleavage planes, which intersect along a (110) type direction. With the sample holder axis in a vertical direction, the $(1\bar{1}0)$ plane, containing the important (001), (111) and (110) directions, may be conveniently studied. The (100) plane is accessible with the sample holder axis horizontal.

II. INFRA-RED MEASUREMENTS

Measurements were made with a Beckmann IR-12 double beam infra-red spectrophotometer. This instrument uses a grating and rotating filter system to produce the necessary dispersion, and has a maximum resolution of .3 cm^{-1} in the region of 1000 cm^{-1} where most of the measurements were taken. A conduction-type dewar with cesium bromide windows was used for low temperature work. The crystal is clamped to a block of high purity copper, using indium foil to maximise the heat transfer, and the block is in turn clamped to the base of the liquid helium reservoir.

III. OPTICAL SPECTROSCOPY

Fluorescence spectra of Gd^{3+} were recorded photoelectrically with a 3/4 meter Czerny-Turner spectrometer manufactured by Spex Industries Inc. Appropriate Corning glass filters were used to eliminate background radiation from the Phillips 500 watt high pressure mercury lamp which was used to excite the fluorescence. Low temperature spectra were again obtained by means of a cold-finger dewar.

IV. ELECTRON PARAMAGNETIC RESONANCE MEASUREMENTS

Three EPR spectrometers were used in this work, two operating in the X band (9 GHz) and the other in the Q band (35 GHz). The bulk of the measurements were made on the 35 GHz spectrometer, which was constructed in the department, and consequently a detailed description will be given of this equipment only. The 35 GHz spectrometer was favoured over those operating at 9 GHz for the work on Gd^{3+} ions because of the large zero field splittings which were observed for the sites reported in this thesis. The X-band spectra of such sites is difficult to interpret because of the strong magnetic field mixing of the crystal field states which occurs for low field strengths. It was also used for the Er^{3+} measurements because of the availability of a liquid helium dewar to fit this machine, and because of the greater resolution available at Q band.

(1) The X Band Spectrometers

Room temperature spectra were recorded on an X-band machine constructed by Dr T.J. Seed. The static magnetic field (0-11 Kg) is provided by a Varian 12" electromagnet and is stable and homogeneous (over the sample volume) to within 2 ppm. The field is measured by an NMR probe to within ±1 gauss, and the microwave frequency by a frequency converter/counter to 1 part in 10^6. The microwave circuit employs a circulator rather than a magic tee but is otherwise of conventional design. The TE_{102} cavity described by Hutton and Seed[30] was used in this work since it features the convenience of two orthogonal axes of sample rotation. A Teflon tuning screw was added to provide for frequency adjustment.

The reorientation experiments described in Chapter VIII required measurements ranging from -200°C to +200°C which were not possible on the spectrometer described above. Instead, the Varian E-12 spectrometer of the Chemistry Department was used. This machine was equipped with the Varian V-4257 variable temperature accessory, which had a thermal stability of ±1°K. The calibration of this accessory was unsatisfactory and so a Copper-Constantan thermocouple was glued to the sample with epoxy resin.

(2) The Q Band Spectrometer

The Q band spectrometer was originally constructed by Dr D.R. Hutton and was inherited by the author and his fellow student Mr P.T. McMahon. A block diagram of the spectrometer is given in Figure 4. The following improvements have been made to the machine during this thesis work. The original

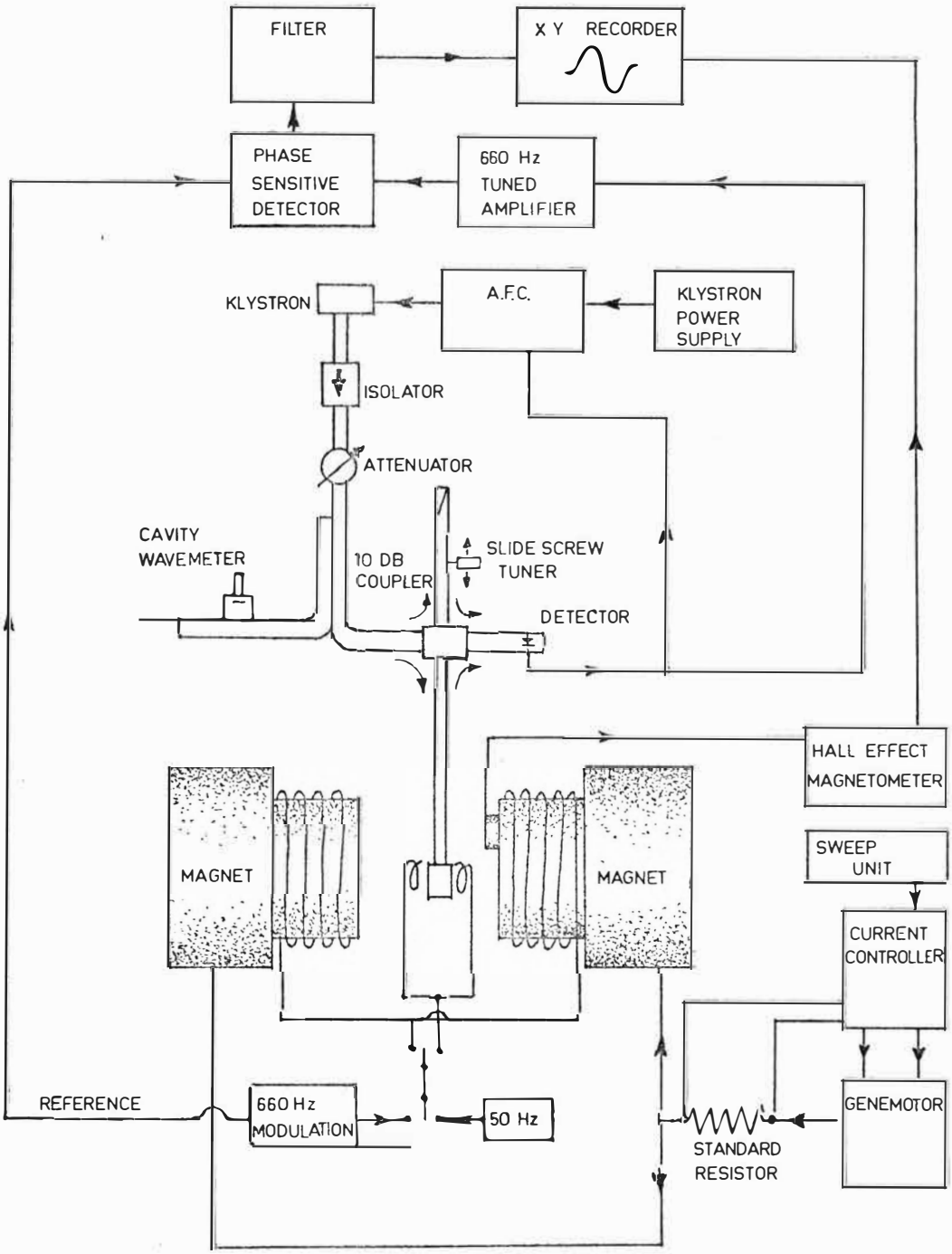

Fig 4: Block diagram of the 35 GHz E.P.R. spectrometer.

magnetic field system could only cover the range 3-15 Kg in three manually switched ranges. This has been replaced by a current regulated genemoter system which can provide .2 Kg to 20.6 Kg in a single continuously variable range. The original field sweeping unit, based on motor driven potentiometers, has also been replaced with an electronic ramp generator of variable output voltage and time constant. The maximum and minimum field sweep rates with the new unit are 10 kg/min and 5 g/min, the latter being a significant improvement over the original system. A new transistorised automatic frequency controller (AFC) was installed, replacing the old valve design which was found to lack sufficient gain for low Q cavities, and to be unreliable in operation. Provision was made in the new AFC for sweeping the klystron (EMI type R5146) through its oscillation mode so as to facilitate tuning to the resonant frequency of the cavity.

The block diagram of the machine (Fig. 4) in its present form shows that it is of conventional homodyne design. Most of the cavities are of fixed iris design and so the slide screw tuner is used to bias the detector crystal (type SIM8) to its linear response region. Two magnetic field modulation frequencies are employed; 50 Hz for visual presentation of the EPR signal on an oscilloscope, which is useful for sample alignment adjustments, and 660 Hz for greater sensitivity using a tuned phase sensitive detection system and an XY recorder. The sensitivity of the equipment is estimated at 10^{15} spins, which may be compared with the figure of 10^{11} spins quoted for the X band Varian machine discussed previously. One method of improving the signal to

noise ratio, and hence the sensitivity, is to increase the modulation frequency since the noise generated by the crystal detector is inversely proportional to that frequency. Equipment for 110 kHz modulation is currently under construction.

The features of the machine which affect measurements are:

(a) Magnetic Field Homogeneity and Stability. At low fields ($\tilde{}$ 5 kg) the field is well behaved with an inhomogeneity of about ±1 gauss over 1 cm^3 of the central region between the pole pieces, and an instability of ±1.5 gauss over a few minutes. However, the field homogeneity falls off rapidly with increasing distance from the axis of the 8" diameter coned pole-pieces. At high fields (15-20 kg) the inhomogeneity rises to ±5 gauss in the central region, and the short term stability similarly diminishes to about ±5 gauss for periods of a few minutes.

(b) Magnetic Field Measurement. NMR measurements of field strength using glycerine as a sample were used wherever possible. The NMR probe coil was placed coaxially with the ESR cavity to minimise field inhomogeneity effects. Five probes built by the author covered the range 2-20 kg in overlapping steps when used with the marginal oscillator circuit of Troup and Hutton[31]. A Varian FH-20 Hall effect magnetometer was used for fields less than 2 kg. This device was also used to measure fields from 0-20 kg when the Janis dewar was in position, since the dewar tail filled the entire central magnet region. The field outside this region was generally too inhomogeneous to enable NMR measurements to be performed. The FH-20 magnetometer was always calibrated immediately after a low

temperature experiment by the NMR magnetometer with the dewar removed. The estimated uncertainty of measurement was ±2 gauss with the NMR probe and ±4 gauss with the FH-20 magnetometer.

(c) Microwave Frequency. This was measured by cementing a small speck of di phenyl picryl hydrazyl (DPPH) to the sample. The resonance condition and the g value (2.0036) of this substance can be used to determine the microwave frequency.

(d) Resonant Cavity Design. TE_{011} cylindrical cavities were used since they have a high Q value which is relatively insensitive to lossy material placed along the cylinder axis. The cavities were electroformed from copper and side coupled to various wave guide feed arrangements so that their axes could be either vertical or horizontal. Samples were glued to the Teflon sample holders by epoxy resin, and both components were inserted along the cylinder axis. Cavities with horizontal axes were equipped with worm and pinion or string drive mechanisms to rotate the sample holder about this axis. The worm and pinion technique was used for all cavities intended for low temperature usage.

(e) Cryogenic Techniques. A Janis liquid helium dewar with a variable temperature exchange gas accessory was acquired during the period of this research. A cavity which fits the small space available in the dewar tail but which still retains the attributes of orthogonal rotation axes, variable frequency, and vertical RF field, was designed by the author. This cavity is illustrated in Figure 5.

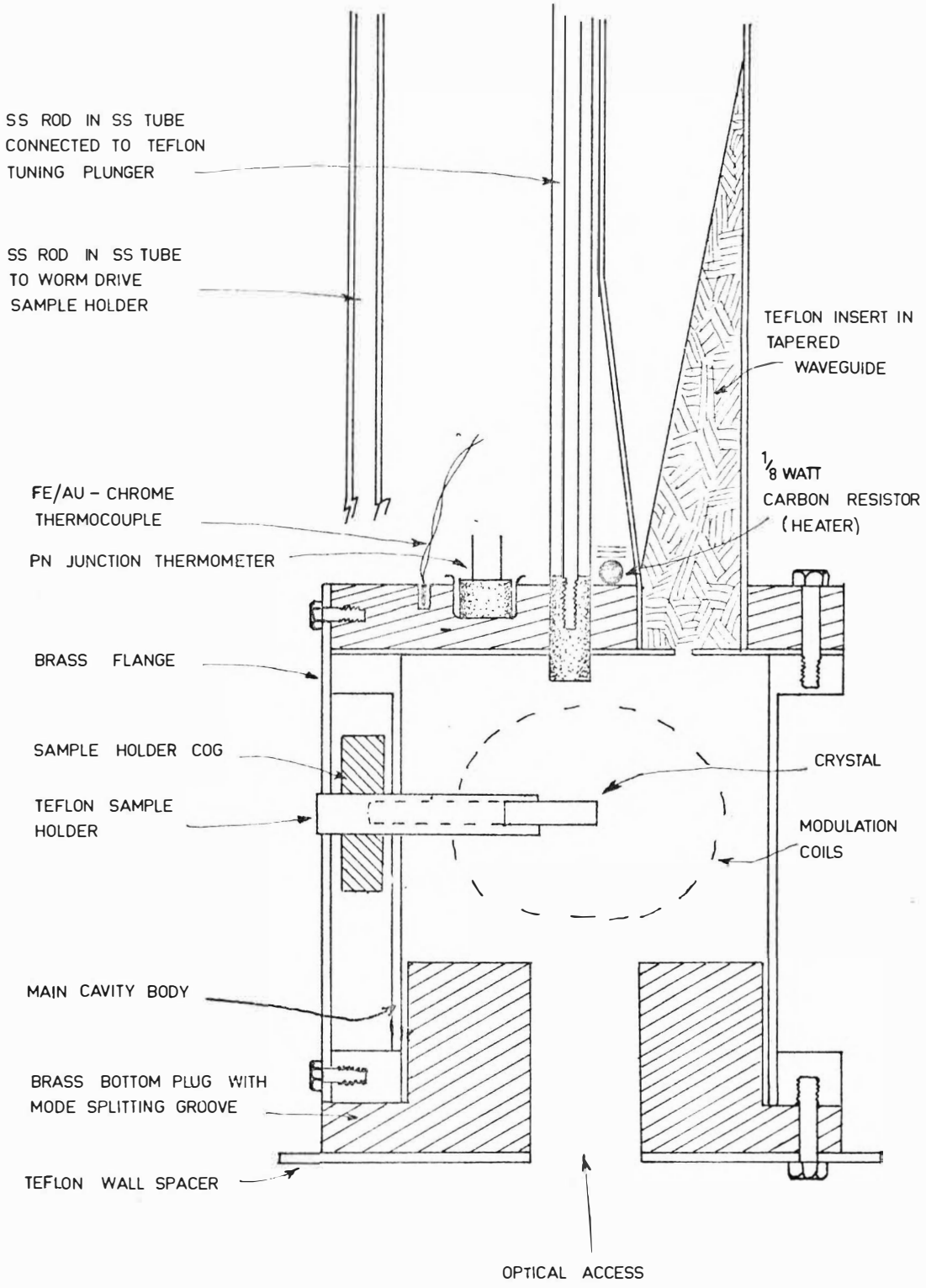

Fig 5: The Q-band(35 GHz) resonant cavity used for measurements at liquid helium temperatures.

It was found that at low temperatures the 660 Hz modulation field from the pole-piece modulation coils did not penetrate through the inner copper tail of the dewar because the skin depth of copper under these conditions is comparable with the tail thickness. The possibility of producing the required modulation within the cavity itself was investigated by inserting two taut copper wires of .008" diameter along the length of cavity, i.e. parallel to the RF magnetic field. This arrangement satisfactorily produced modulation fields of up to one gauss, but in a magnetic field the wires vibrated due to the $i\underline{\ell}\times\underline{B}$ force and modulated the cavity resonance. The resulting 660 Hz signal was larger than typical EPR signals for fields above about 4 kg. Using larger diameter wires reduced the vibrational amplitude but also reduced the cavity Q, and so this approach was abandoned. Instead, coils of 1 cm diameter comprising 50 turns of copper wire were attached to the outside of the brass cavity. This method was generally satisfactory, but for fields above 15 kg some vibrational effects, presumably of the cavity walls, were observed.

The copper dewar tail also caused some problems with the 50 Hz modulation from the pole piece coils because of joule heating produced by the induced eddy currents. The cavity temperature typically rose from $6^{o}K$ to $20^{o}K$ after several minutes if the exchange space contained only helium gas. Condensing some liquid helium in the exchange space cured this problem but appreciable boil off from the liquid helium reservoir still occurred. It was not possible to apply the 50 Hz modulation to the cavity coils because of the high amperages involved.

The cavity temperature could be varied between $6^{o}K$ and $40^{o}K$ by adjusting the exchange gas pressure and the current passing through the heater. A semiconductor diode (the base-collector junction of transistor type 2N3646) was used as a temperature sensor by measuring the voltage drop across it under conditions of constant forward current (20 μA). This device was convenient because the voltage-temperature relationship was almost linear from $300^{o}K$ to $60^{o}K$, with $\Delta V/\Delta T \simeq 2$ mV/^{o}K. At lower temperatures the relationship was non-linear but the sensitivity increased. However, the output voltage below about $20^{o}K$ was found to be strongly dependent on the magnetic field strength and so a chromel-gold/iron thermocouple was added for use in this region. The gold/iron alloy (.03% Fe) has the advantage of a high thermopower at low temperatures.

Electronic automatic temperature control units were used with both types of sensor to stabilize the cavity temperature to within $.5^{o}K$ by controlling the heater current. For measurements at $4.2^{o}K$ a cold finger plug was attached to the base of the cavity in place of the optical access plug, and a small quantity of liquid helium was condensed in the bottom of the exchange space by overpressurising the helium gas.

Two modifications to the original cavity design were found to be necessary after tests. Inserting the teflon sample holder into the empty cavity considerably reduced the Q factor due to dielectric losses in the teflon close to the cavity walls where the RF electric field is at a maximum. This problem was reduced by hollowing out the sample holder. The

cavity was originally attached to 80 cm of thin walled stainless steel waveguide to provide thermal insulation, but it was found that the heavy microwave attenuation resulted in very little microwave power reaching the detector. Brass waveguide was therefore used from the cavity to within 20 cm of the exit from the dewar. The remaining section of stainless steel provided adequate thermal insulation without producing excessive microwave attenuation.

IV. DIELECTRIC LOSS MEASUREMENTS

The reorientation of Gd^{3+}-anion dipoles in calcium fluoride was studied by the dielectric loss technique using the instrumentation facilities of the CSIRO Division of Applied Physics, Sydney, Australia. The dielectric loss spectrum of samples was examined from 100 kHz to 10 MHz with a substitution bridge described by Dryden and Weir[32]. These authors also describe the sample cells and electrodes used in this work. Measurements from 1.6 Hz to 160 kHz were made on a direct reading audio bridge which is a modified version of that described by Thompson[33].

The crystal samples were ground approximately plane parallel, but it was still necessary to correct the results for the small air gap between the wedge-shaped sample and the top electrode. If $\varepsilon_m"$ is the measured complex part of the permittivity and $\varepsilon"$ the corrected value then

$$\varepsilon" = \left(\frac{\varepsilon'}{\varepsilon_{app}}\right)^2 \varepsilon_m",$$

where ε', ε_{app}' are the true and apparent real parts of the

permittivity. This result follows from simple circuit theory by considering the air gap to be a series capacitor.

Sample temperatures between $300^{o}K$ and $200^{o}K$ were obtained by immersing the sample cell in an alcohol bath. The large thermal mass of the bath ensured that the sample temperature did not fluctuate by more than $.5^{o}K$ during a measurement. For measurements below $200^{o}K$ a different cell was used in which the electrodes and sample were cooled by a (variable) flow of cold nitrogen gas or liquid. The temperature stability over the measurement period for this cell was no better than $\pm 5^{o}K$ because of fluctuations in the flow rate of refrigerant through the cooling coils.

CHAPTER IV

ELECTRON PARAMAGNETIC RESONANCE SPECTRA OF ALKALINE EARTH FLUORIDE CRYSTALS CONTAINING TRIVALENT GADOLINIUM

The Electron Paramagnetic Resonance (EPR) spectra of hydrogenated alkaline earth fluoride crystals containing trivalent rare earth ions shows a large number of absorption lines; typically 100 for gadolinium. Most of these lines also occur in the crystals before hydrogenation and so must be due to rare earth ions in sites not associated with hydrogen. Several of these lines have been reported in the literature and assigned to specific sites. However, in many cases the published data is incomplete or in error and so a re-evaluation of the previous work seemed warranted.

This chapter reports briefly on the observed spectra and in more detail on the technique used to re-evaluate the spin Hamiltonian parameters. In addition, the possible inclusion of the Bleaney-Koster terms in the spin Hamiltonian is discussed. New results are reported for calcium fluoride crystals doped with both gadolinium and alkali metal ions.

I. EPR SPECTRA OF GADOLINIUM IONS IN THE ALKALINE EARTH FLUORIDES

(1) Gadolinium Ions in Calcium Fluoride

Calcium fluoride crystals containing .05% GdF_3 showed a strong tetragonal EPR spectrum from three magnetically inequivalent sites, and also a cubic spectrum at about one tenth the intensity. The tetragonal spectrum has been ascribed

to a Gd^{3+} ion charge compensated by an F^- interstitial at either the (±1,0,0), (0,±1,0) or (0,0,±1) positions in the lattice[34,35]. The cubic site is due to Gd^{3+} ions with the charge compensating ion at least three lattice spacings away. The EPR spectra for H parallel to the (001) crystal axis at X and Q bands are shown in figures 6 and 7 respectively.

Crystals of CaF_2 doped with Gd_2O_3, or those doped with GdF_3 which have been heated in an oxygen atmosphere, show only a strong trigonal T2 spectrum from four magnetically inequivalent sites. Crystals doped with GdF_3 which are heated in a wet hydrogen atmosphere show in addition another trigonal spectrum (T1). Both sites have the three-fold axis along the (111) direction. Reddy et al.[36] have established the models $RE^{3+}O_4^{2-}F^-$ and $RE^{3+}O^{2-}F_7^-$ for two similar sites which form in Yb^{3+} doped calcium fluoride on the basis of their ENDOR measurements; both of these site structures are illustrated in figure 8.

It is reasonable that the two Gd^{3+} sites have the same structures, and it is proposed here that the T1 spectra arises from a $Gd^{3+}(O^{2-})_4F^-$ site and the T2 spectra from a $Gd^{3+}F_7^-O^{2-}$ site. This association of the Yb^{3+} and Gd^{3+} sites is based on (a) a comparison of the crystal growth conditions used here with those reported for the Yb^{3+} sites by McLaughlan and Neumann[77], (b) on the argument that there are insufficient O^{2-} ions in oxide doped calcium fluoride for <u>all</u> the Gd^{3+} sites to have the $Gd^{3+}(O^{2-})_4F^-$ structure, and (c) on the observation of Kitts[78] of dielectric relaxation in crystals which showed the T1 EPR spectrum. The significance of (c) is that although both structures carry a net electric dipole moment, only in

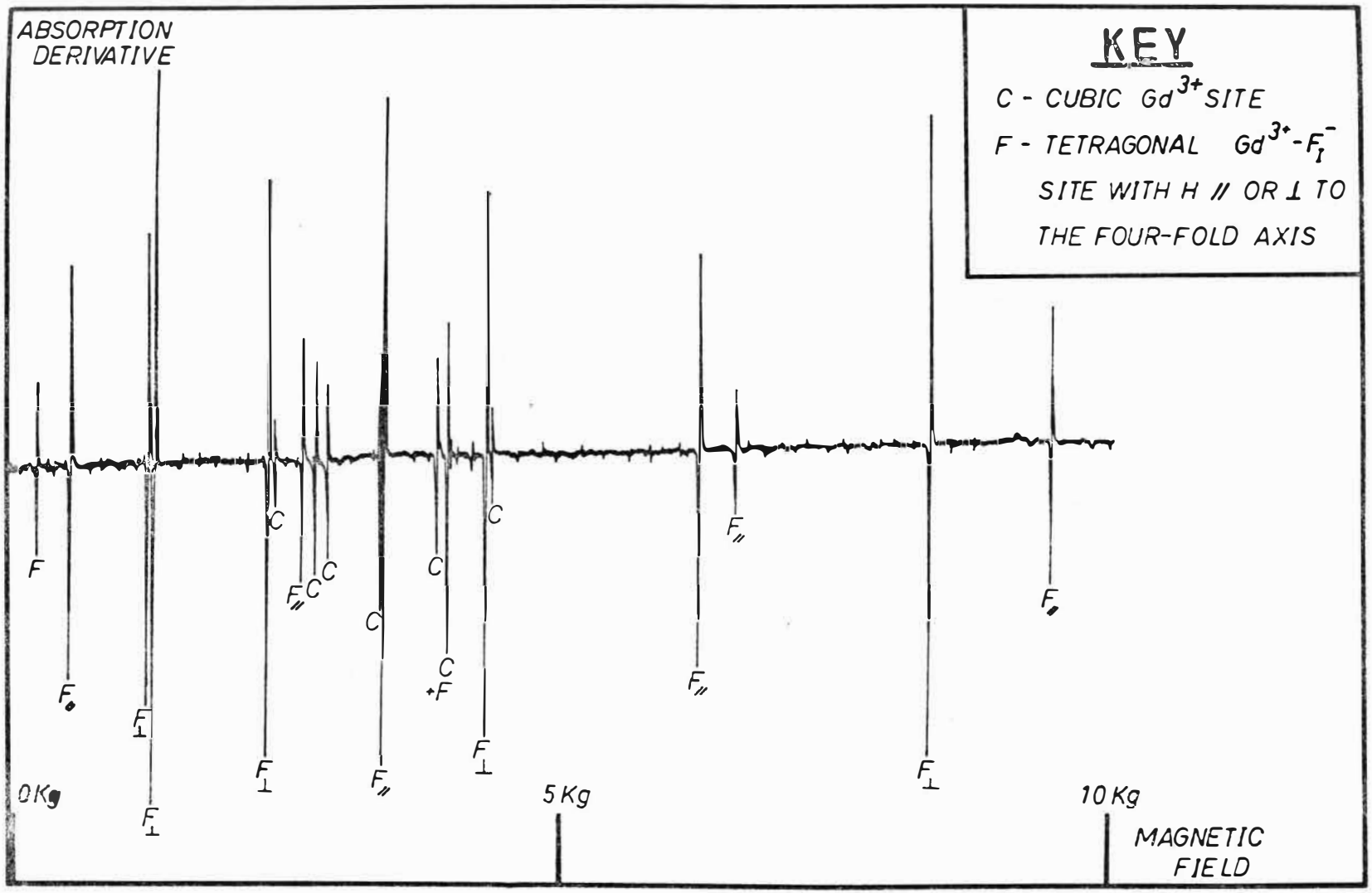

Fig 6: X-Band (9.55 GHz) E.P.R. spectrum of calcium fluoride doped with .05% GdF_3 for H // to the (001) axis

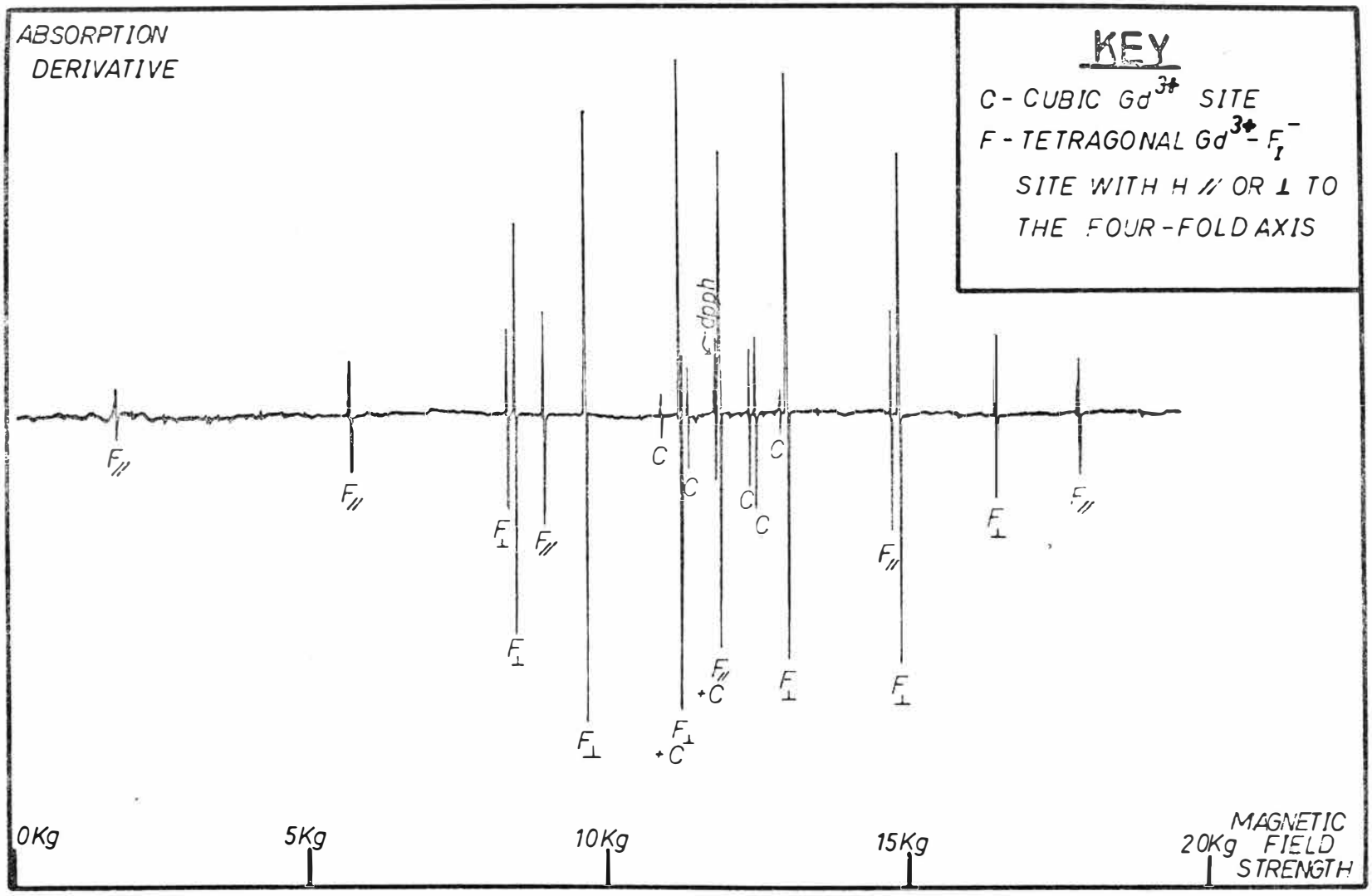

Fig 7: Q-Band (33.7GHz) E.P.R. spectrum of calcium fluoride doped with .05% GdF_3 for H // to the (001) axis

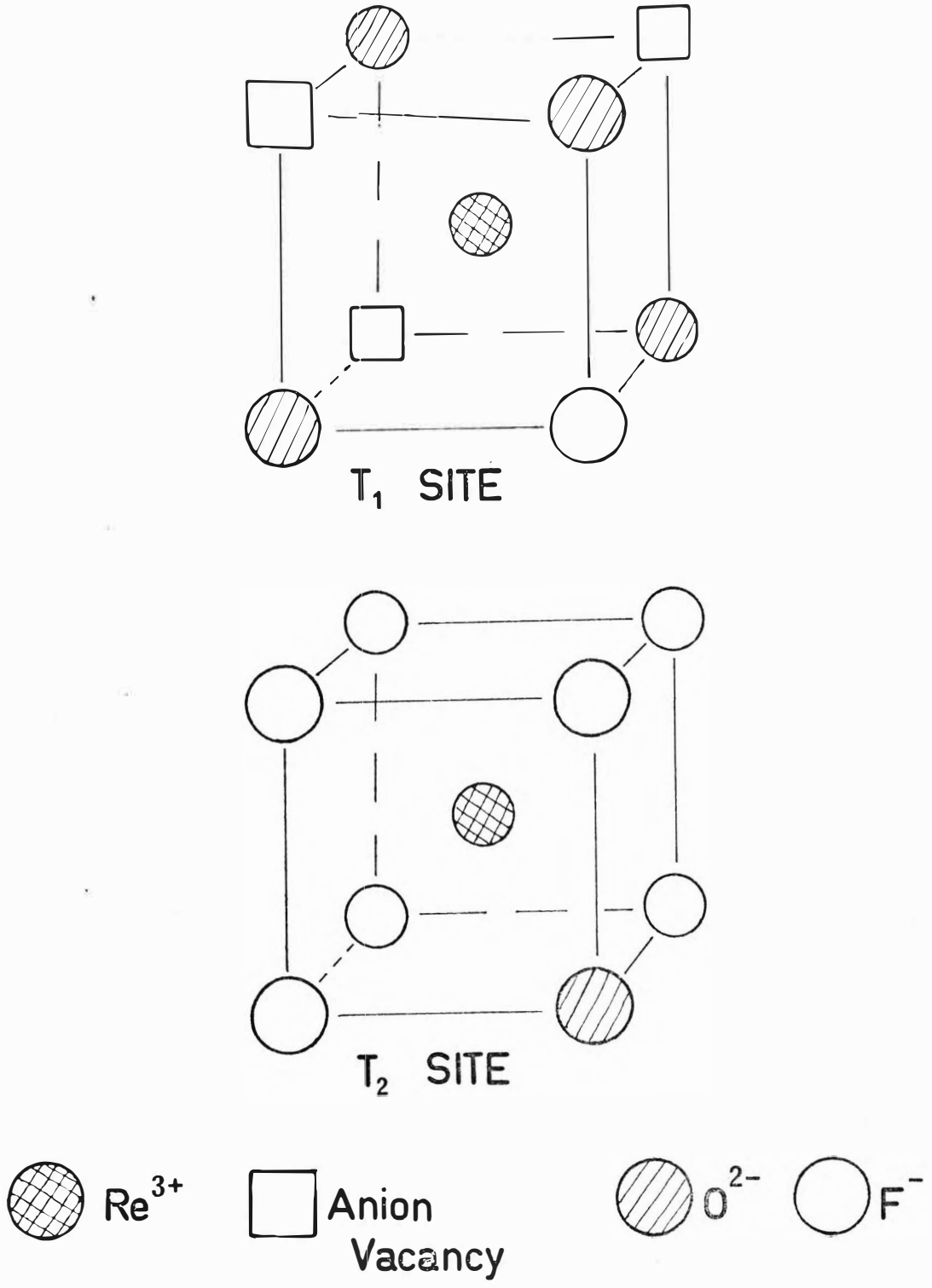

Fig 8: The trigonal T1 and T2 sites in oxygenated calcium fluoride.

the $RE^{3+}-(O^{2-})_4-F^-$ case can the dipole axis be realigned (by an F^--vacancy interchange) and so give rise to an I.T.C. peak.

The Q band T1 and T2 spectra for H parallel to the (111) axis are shown in figure 9. For both spectra only six strong triplet lines are observed when seven are expected. Using the parameters in table 3 the position of the seventh line was predicted and a weak, broad line was observed within 5 gauss of the predicted position.

(2) Gadolinium Ions in Strontium Fluoride

Strontium fluoride crystals doped with .05% GdF_3 showed a strong tetragonal spectrum similar to that in calcium fluoride, and also a weaker trigonal spectrum (T4). No cubic spectrum was observed. The trigonal spectrum has not yet been definitely identified, but a proposed model has an interstitial F^- ion at the nearest empty cube along the (111) direction[37]. This would produce a weak trigonal perturbation on the cubic crystal field as is apparent in the T4 spectrum.

Heating such crystals in an oxygen atmosphere converts both of the above sites into another trigonal site analogous to the T2 site in CaF_2. No analogue of the T1 site was observed.

(3) Gadolinium Ions in Barium Fluoride

Barium fluoride crystals doped with .05% GdF_3 showed a cubic spectrum and a strong trigonal T4 spectrum. These spectra were not examined in detail since accurate spin Hamiltonian parameters have been evaluated by Boatner et al.[38], and also by Antipin and Kurkin[53]. The latter authors comment unfavourably on the previous results of Sierro[43] for these

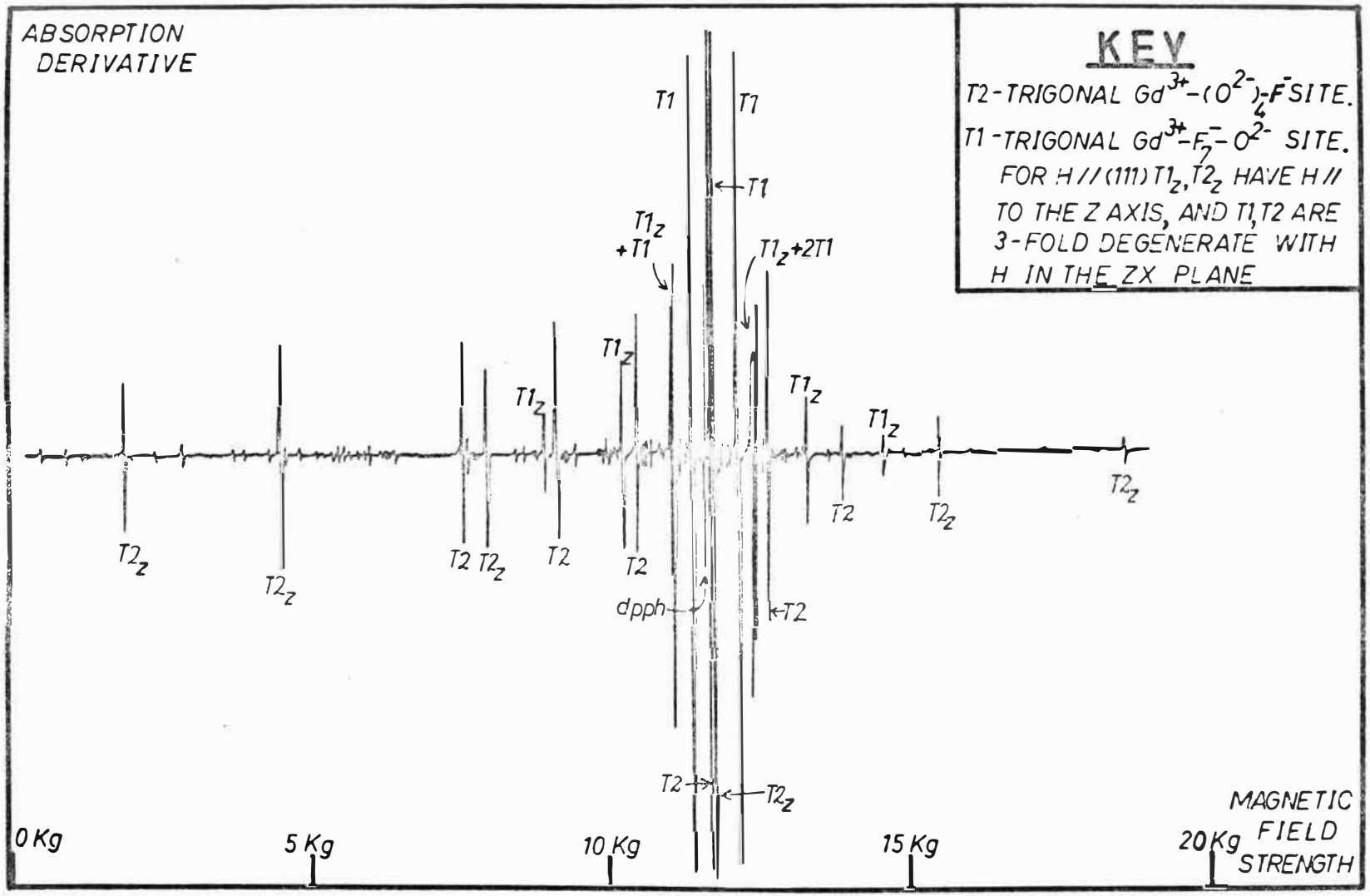

Fig 9: Q-Band (34.21 GHz) EPR spectrum of hydrolysed calcium fluoride doped with .05% GdF_3 for H // to the (111) axis.

sites. An intensive search failed to find a tetragonal spectrum analogous to that observed in calcium and strontium fluorides.

Crystals which were subjected to the hydrogenation treatment showed a weak trigonal T2 spectrum which has not been previously observed. This spectrum appeared to be caused by water vapour contamination in the hydrogen gas.

(4) Summary of Charge Compensation Mechanisms for Gadolinium Ions in the Alkaline Earth Fluorides

These results show that the relative stability of the various charge compensation arrangements for untreated crystals doped with rare earth fluoride depends markedly on the particular host lattice. For calcium fluoride the tetragonal interstitial fluoride ion site is predominant, for strontium fluoride both the tetragonal interstitial fluoride ion and the trigonal (T4) sites are stable, while for barium fluoride only the trigonal symmetry site is observed.

It is difficult to predict whether a similar trend would be expected for Gd^{3+} sites associated with hydride ions in hydrogenated crystals. The situation is complicated by the possibility of sites involving substitutional hydride ions in addition to an F_I^- or H_I^- compensator. Also the ionic radii of the F^- and H^- ions are significantly different, 1.33Å and 1.54Å respectively. However, if a simple tetragonal Gd^{3+}-H_I^- site does exist then it is reasonable that its stability will diminish from calcium to strontium fluoride.

II. EVALUATION OF SPIN HAMILTONIAN PARAMETERS FOR Gd^{3+}

(1) Numerical Technique

The spin Hamiltonians for the ground state of $Gd^{3+}({}^8S_{7/2})$ in sites of cubic, tetragonal and trigonal symmetry are:

$$\mathcal{H}_C = g\beta\underline{H}\cdot\underline{S} + B_4(O_4^0 + 5\bar{O}_4^4) + B_6(O_6^0 - 21\bar{O}_6^4), \qquad (4.1)$$

$$\mathcal{H}_{TET} = \beta(g_{//} H_z S_z + g_{\perp}(H_x S_x + H_y S_y)) + B_2^0 O_2^0 + B_4^0 O_4^0 + B_4^4 \bar{O}_4^4 + B_6^0 O_6^0 + B_6^4 \bar{O}_6^4,$$

$$\mathcal{H}_{TRIG} = \beta(g_{//} H_z S_z + g_{\perp}(H_x S_x + H_y S_y)) + B_2^0 O_2^0 + B_4^0 O_4^0 + B_4^3 \bar{O}_4^3 + B_6^0 O_6^0 + B_6^3 \bar{O}_6^3 + B_6^6 \bar{O}_6^6.$$

The nuclear spin I has been omitted since hyperfine structure is not usually resolved in Gd^{3+} EPR spectra. The operators O_n^m, and their matrix elements, are given by Hutchings[39]. The operators O_n^0 and S_z have only diagonal elements whilst the operators $\bar{O}_n^m (m \neq 0)$ and S_x, S_y have only off-diagonal elements. The diagonal terms are usually greater in magnitude than the off-diagonal for H//z and so their values may be simply obtained by a first order perturbation calculation. The off-diagonal terms only affect the eigenvalues in second order perturbation for H//z and so they are best evaluated from the spectrum for some other direction. In general they cannot be obtained by a simple perturbation theory type calculation of the sort described above.

In order to accurately evaluate all the S.H. parameters it is necessary to resort to numerical diagonalisation of the S.H. matrix on an electronic computer. A program was written (by the author) which provides a least squares fit of the parameters to the observed spectrum in the sense that the mean square deviation (M.S.D) given by

$$\text{M.S.D.} = \frac{1}{N} \sum_{i=1}^{N} (h\nu - \Delta E_i)^2,$$

is a minimum. Here ν is the microwave frequency and ΔE_i is the energy difference of two levels at a field value of H_i. The program proceeds by diagonalising the S.H. for estimated values of the parameters for each H_i, and selecting the initial and final states (ϕ_i and ψ_i) involved in the i^{th} transition. This selection is made by comparing $(E_{\phi_i} - E_{\psi_i})$ with $h\nu$, and by comparing the calculated and theoretical transition probabilities. The parameters are then refined by solving the usual least-squares normal equations. The derivatives required in setting up the normal equations may be calculated in first order from the eigenvectors:

$$\frac{\partial \Delta E_i}{\partial B_n^m} = \langle \phi_i | O_n^m | \phi_i \rangle - \langle \psi_i | O_n^m | \psi_i \rangle$$

where the ϕ_i, ψ_i are eigenvectors of the spin Hamiltonian. Repeated iterations of the procedure are performed until the reduction in the M.S.D. is negligible. The problem of complex matrices which arises for non-zero H_y can be overcome by the usual supermatrix technique[40].

Buckmaster et al.[41] have recently published an alternative procedure for performing the same least squares fitting. Their fitting proceeds by testing the parameters $B_n^m + p\Delta B_n^m$ (p = -5,-4,···,4,5) to determine the value of p which gives the minimum M.S.D. The spread factor ΔB_n^m is then reduced ten fold and the process repeated. This procedure is inefficient since it requires many diagonalisations. Another unsatisfactory aspect is that transitions are considered to occur only between states which are adjacent in order of energy magnitude. This assumption does not appear to have any physical justification.

Since any parameter-evaluation routine fits parameters to energy differences, only the relative signs of the parameters may be determined. The overall sign must be determined by observing the relative intensities of the lines at very low temperatures. Here the overall signs found in the previous work[46] were assumed to be correct .

(2) Spin Hamiltonian Parameters for Gd^{3+} in Calcium and Strontium Fluorides

The S.H. parameters evaluated by this author for various sites of Gd^{3+} in calcium, strontium and barium fluoride crystals are given in tables 2, 3 and 4. These parameters b_n^m are related to the B_n^m in equation (4.1) by,

$$b_2^m = 3B_2^m, \qquad b_4^m = 60B_4^m, \qquad b_6^m = 1260B_6^m.$$

The accuracy of fit is indicated by the standard deviation of the observed and predicted transition frequencies, and also by the standard deviation of the observed and predicted field strengths. Sierro[42,43] and Vinokurov et al.[44,45,46] have measured the S.H. parameters for some of the

TABLE 2

Spin Hamiltonian parameters for tetragonal Gd^{3+} sites in CaF_2 and SrF_2

Site	No. of Lines Meas.	Field Orient.	$g_{//}$	$g_{\perp}$	b_2^0	b_4^0	b_6^0	b_4^4	b_6^4	S.D. field (gauss)	S.D. frequency (cm^{-1})	Frequency	Author
Gd^{3+}-F_I^- SrF_2	14	(100)	1.9924(5)*	1.9923(5)	±.11262(6)	±.00204(4)	±.00006(2)	±.01406(16)	∓.00036(30)	2.3	2.1×10^{-4}	Q	Edgar
"	-	-	1.992(3)	-	±.1123(7)	±.0020(3)	±.00006(36)	±.0057(20)	±.00070(410)	-	-	X	Sierro[42]
Gd^{3+}-F_I^- CaF_2	13	(100)	1.9920(5)	1.9920(5)	-.14878(7)	-.00231(4)	-.00007(2)	-.01476(16)	+.00051(30)	.6	$.9 \times 10^{-4}$	Q	Edgar
"	-	-	1.9920(10)	-	-.14840(30)	-.00230(7)	-.00007(3)	-.01458(17)	.0	-	-	Q X	Vinokurov et al.[45]
"	-	-	1.9930(10)	-	-.14882(47)	-.00229(16)	-.00006(12)	-.01517(66)	.000(7)	-	-	X	Sierro[42]
"	11	(100)	1.9924(5)	1.9920(5)	-.14841(7)	-.00229(4)	-.00007(2)	-.01463(17)	+.00062(30)	.9	$.8 \times 10^{-4}$	X	Franklin & Marzullo[49]†
"	5 x 13	(100)	1.9920(3)	1.9920(3)	-.14874(4)	-.00231(3)	-.00007(2)	-.01477(12)	+.00052(22)	2.3	2×10^{-4}	Q	Edgar
"	12	(100)	1.9918(5)	1.9923(5)	-.14868(7)	-.00230(4)	-.00009(2)	-.01473(17)	+.00047(30)	.9	1.4×10^{-4}	X	Edgar

NOTE: All values of b_n^m in cm^{-1}

*The bracket encloses the uncertainty expressed in units of the last significant digit.

†Field strength data analysed by Edgar.

TABLE 3

Spin Hamiltonian Parameters of Trigonal Sites in CaF_2 and SrF_2

Host Xtal	Site	No. of Lines meas.	Field Orient.	$g_{\parallel}$	$g_{\perp}$	b_2^0	b_4^0	b_6^0	b_4^3	b_6^3	b_6^6	S.D. Field	S.D. Frequency (cm^{-1})	Author
CaF_2	T2	11	(111)	1.9918(5)	1.9918(5)	-.16692(7)	+.00263(4)	-.00001(2)	-.07037(15)	+.00050(20)	-.00023(20)	2 g	1.9×10^{-4}	Edgar
CaF_2	T2	-	-	1.9900(30)	-	-.16664(15)	+.00262(8)	-.00018(12)	-.003100(70)	-.00000(18)	-.00093(186)	-	-	Sierro[42]
CaF_2	T2	-	-	1.9920(10)	-	-.16678(33)	+.00260(7)	-.0000(4)	-.07072(17)	-.00167(17)	.0	-	-	Vinokurov et al.[45]
BaF_2	T2	10	(111)	1.9925(8)	1.9925(8)	∓.17044(11)	±.00201(8)	∓.00001(2)	∓.04788(20)	∓.00145(40)	∓.00097(4)	2.5 g	2.4×10^{-4}	Edgar
CaF_2	T1	-	-	1.9900(20)	-	±.04073(8)	±.00141(4)	±0.00000(4)	±.00119(23)	±.00007(18)	±.00093(93)	-	-	Sierro[42]
CaF_2	T1	13	(111)	1.9910(5)	1.9914(5)	±.04092(7)	±.00138(4)	±0.00000(2)	∓.02326(15)	±.00010(20)	±.00049(20)	1.2 g	1.1×10^{-4}	Edgar
SrF_2	T4	-	-	1.992		±.01380(80)	±.00408(4)	-	-	-	-	-	-	Sierro[43]
SrF_2	T4	18	(100) (111)	1.9920(5)	1.9918(5)	±.01356(6)	±.00278(4)	±.00002(2)	±.07849(15)	∓.00040(20)	±.00048(20)	1.4 g	1.3×10^{-4}	Edgar
SrF_2	T2	-	-	1.9920(30)	-	±.18162(8)	∓.00201(4)	±.00030(6)	±.00138(12)	±.00000(4)	±.00000(900)	-	-	Sierro[42]
SrF_2	T2	11	(111)	1.9928(5)	1.9920(5)	±.18151(7)	∓.00228(4)	±.00001(2)	±.05583(15)	±.00032(20)	∓.00054(20)	1.2 g	1.1×10^{-4}	Edgar

Gd^{3+} sites listed, and so their results are also tabulated for comparison. It can be seen that the results here for g, b_n^0 compare favourably with those of the other workers, but that there is some disagreement for the parameter b_n^m with $m \neq 0$. Some of Sierro's values for these parameters appear to be in error because they differ markedly from both those of Vinokurov et al. and the results reported here. The two latter sets of results differ for the parameters b_n^m ($m \neq 0$). Vinokurov et al. determined these parameters by transforming the S.H. so that the Zeeman term was diagonal with the field at an angle to the axis of symmetry. Weiler and Wylie[47], and Buckmaster et al.[48] have recently published transformation formulae for operators O_n^m and T_n^m respectively. Using these results, it appears that there are several errors in Vinokurov et al's transformed spin Hamiltonians for both C_{3v} and C_{4v} symmetries. Hence their values of b_n^m ($m \neq 0$) may not be reliable.

In conclusion, the least squares fitting procedure discussed in this section appears to perform satisfactorily and yields results slightly superior to those of previously used procedures. Consequently it has been used throughout the later chapters to analyse new Gd^{3+} spectra.

(3) The Bleaney-Koster Terms

It was shown in Chapter II that additional terms linear in the magnetic field (the "Bleaney-Koster terms") were permitted in the $^8S_{7/2}$ spin Hamiltonian for C_{4v} symmetry. It would be expected that a difference between the usual S.H. parameters derived from Q band (high field) and X band (low field) spectra would be detected if the coefficients of these

extra terms were non-zero and they were omitted from the S.H.

A small difference (Δb_2^0) in the values of b_2^0 for Gd^{3+}-F^-/CaF_2 derived by the author from his Q band data and that derived by Vinokurov et al. from their X band data was noticed (Table 2). The author's analysis of the published X band magnetic field data of Franklin and Marzullo[49] gave similar results. (The data of Sierro is insufficiently precise.) To reduce experimental uncertainties, the Q band parameters were rederived from five separate measurements, but practically the same value of b_2^0 was obtained. The value of Δb_2^0 cannot therefore be explained by inaccuracy in the Q band parameters, since it is five times larger than the experimental uncertainty in b_2^0.

Fitting both X and Q band data with an S.H. augmented by all nine extra B-K terms (derived in Appendix 2) was considered impractical due to the large number of parameters involved. An attempt to fit the spectra with the addition of the $T_3^0(S)$ term only, resulted in a negligible decrease in the goodness of fit. Consequently the X band spectra was remeasured by the author; the value of b_2^0 thereby obtained agreed to within .00005 cm^{-1} of the Q band value. The reason for the difference between this authors X band value of b_2^0 and that of the other workers is unknown; possibly a slightly different measurement temperature may be the cause.

It is concluded that the Bleaney-Koster terms are unnecessary for the experimental accuracy presently available, and they will be omitted in subsequent discussions of the gadolinium EPR spectra.

III. EPR SPECTRA OF CALCIUM FLUORIDE DOPED WITH BOTH SODIUM AND GADOLINIUM IONS

Gilfanov et al.[50] have investigated the optical spectrum of Gd^{3+} ions in calcium fluoride co-doped with GdF_3 and MeF (Me = Na, K, Ag). They proposed that the Gd^{3+} ion can be charge compensated by a monovalent cation substituting for the divalent calcium at the (110) position, to give the site of C_{2v} symmetry shown in Figure 10. It should be interesting to study the electron-phonon interaction for a Gd^{3+}-Li^{+} site of this type since lithium is a low mass atom with two readily available isotopes Li^6 and Li^7.

Attempts to produce such a site by adding up to 3% (atomic) LiF to the melt were unsuccessful, probably due to the large mismatch between the Li^{+} and Ca^{2+} ionic radii (0.68Å and 0.99Å respectively). The EPR spectrum revealed a strong tetragonal Gd^{3+}-F_I^{-} spectrum, a weak Gd^{3+} cubic spectrum, and an unidentified line near g = 2.0. The spectrum of crystals grown with up to 3% K^{+} (ionic radius = 1.33Å) was very similar, although Gilfanov et al.[50] managed, with some difficulty, to observe the Gd^{3+}-K^{+} rhombic site optically. However, crystals doped with Na^{+} (ionic radius = .97Å) showed a distinctive rhombic spectrum (Fig. 11) whose intensity depended upon the amount of NaF added to the melt. A correlation between the optical spectrum observed by Gilfanov et al., and the EPR spectrum was attempted to confirm that they originated from the same Gd^{3+} site. Since absolute intensity measurements are very difficult to perform in EPR, the intensity of the rhombic site was in each case measured

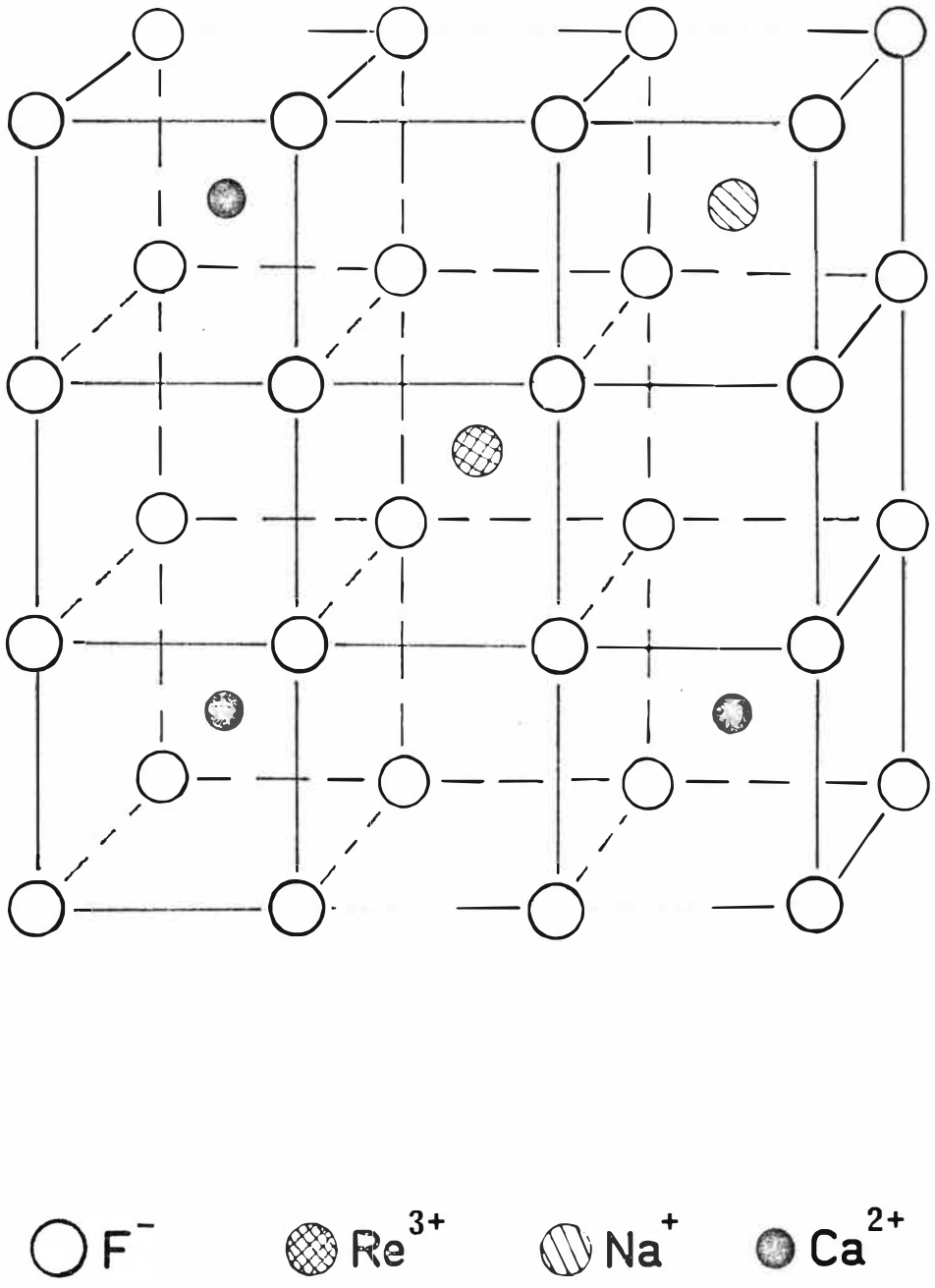

Fig 10: the rhombic Gd^{3+}-Na^{+} site in calcium fluoride.

TABLE 4

Spin Hamiltonian parameters for the cubic site of Gd^{3+} in CaF_2

No. of Lines Meas.	Field Orient.	g	b_4	b_6	S.D. field	S.D. frequency	Frequency	Author
14	(100) (111)	1.9922(5)	-.00467(5)	-.00001(1)	.6 g	.5 x 10^{-4}	X	Edgar
-	-	1.9918(10)	-.00466(3)	-.00001(4)	-	-	X	Ryter[51]

TABLE 5

Intensity Ratios for Optical and EPR Spectra of Gd^{3+} cubic sites and Gd^{3+}-Na^{+} rhombic sites in calcium fluoride

Nominal Gd^{3+} at %	Nominal Na^{+} at %	EPR Intensity Ratio†	Optical Intensity Ratio†	Tetragonal F^{-} site observed EPR	Optical
.05	.75	1	1	X	X
.05	.25	.68 ± 10%	.71 ± 15%	✓	✓
.05	1.5	.32 ± 10%	.38 ± 15%	X	X

†The ratio is the (normalised) cubic/rhombic intensity ratio.

TABLE 6

Spin Hamiltonian parameters for the Gd^{3+}-Na^{+} rhombic site in CaF_2

No. of Lines Meas.	Field Orient.	g	b_2^0	b_2^2	b_4^0	b_4^2	b_4^4	b_6^0	b_6^2	b_6^4	b_6^6	S.D. field	S.D. frequ. (cm^{-1})	Comments
12	(100)	1.9920(10)	.00442(20)	.00495(20)	.00090(20)	-.02310(25)	-.01642(25)	.00014(20)	.00074(30)	.00007(30)	.00158(30)	.4 g	$.4\times10^{-4}$	
		1.9922			.00117(1)	-.02335(25)	-.01751(16)	.00002(2)	.00007(7)	-.00014(14)+.00015(15)		-	-	Cubic Parameters expressed for z//(110)

relative to the cubic site. In the EPR spectrum the lowest field lines of the rhombic and cubic sites were chosen, and in the optical spectra the rhombic line at 32062.1Å and the cubic line at 32092.6Å. These lines best fitted the criteria of high resolution and minimal overlap; their intensities were found by integrating with a mechanical planimeter. The intensity ratios (normalised) are given in Table 5.

The table shows that there is a satisfactory correlation between the optical and EPR spectra. It is also evident that the ratio of cubic to rhombic sites depends markedly on small changes in the crystal growth conditions and not just on the nominal Na^+ concentration. The disappearance of the tetragonal Gd^{3+}-F_I^- site with increasing Na^+ concentration is expected since the addition of NaF creates F^- ion vacancies which can be filled by interstitial F^- ions.

The EPR spectrum of the rhombic site was very similar to that observed by Smith and Cole[52] for Gd^{3+}-Na^+ pairs in CdF_2. For arbitrary directions of the field six distinct spectra are observed since there are a total of twelve possible sites for the Na^+ ion relative to the Gd^{3+} ion, and inversion related pairs of sites are magnetically equivalent. If the principal axes (x,y,z) for one site are defined as $(1\bar{1}0)$, (001), (110) then the C_{2v} spin Hamiltonian has the form:

$$\mathcal{H} = \beta(g_x H_x S_x + g_y H_y S_y + g_z H_z S_z) + \sum_{n=1}^{3} \sum_{m=0}^{n} B_{2n}^{2m} \bar{O}_{2n}^{2m}. \qquad (4.2)$$

The accurate evaluation of all 12 parameters in equation (4.2) would require the spectrum to be measured at several different field orientations. This is difficult because the large number

of inequivalent rhombic sites, and the Gd^{3+} cubic spectrum, result in a complex spectrum of many overlapping lines for arbitrary field orientations. Consequently the rhombic spectrum was only measured for H along the (100) direction where one set of four-fold degenerate, and one set of two-fold degenerate lines were observed. The number of parameters in equation (4.2) can be reduced to 10 by the observation that the g value of Gd^{3+} is usually almost isotropic. Fitting these 10 parameters to the 12 identified lines for H along 100 resulted in the values shown in Table 6. For comparison the cubic parameters have been expressed in the (xyz) axis system and tabulated below the rhombic values. It can be seen that the rhombic crystal field is a moderately weak perturbation on the cubic crystal field, as would be expected for a screened compensator such as the Na^{+} ion in a next nearest neighbour site.

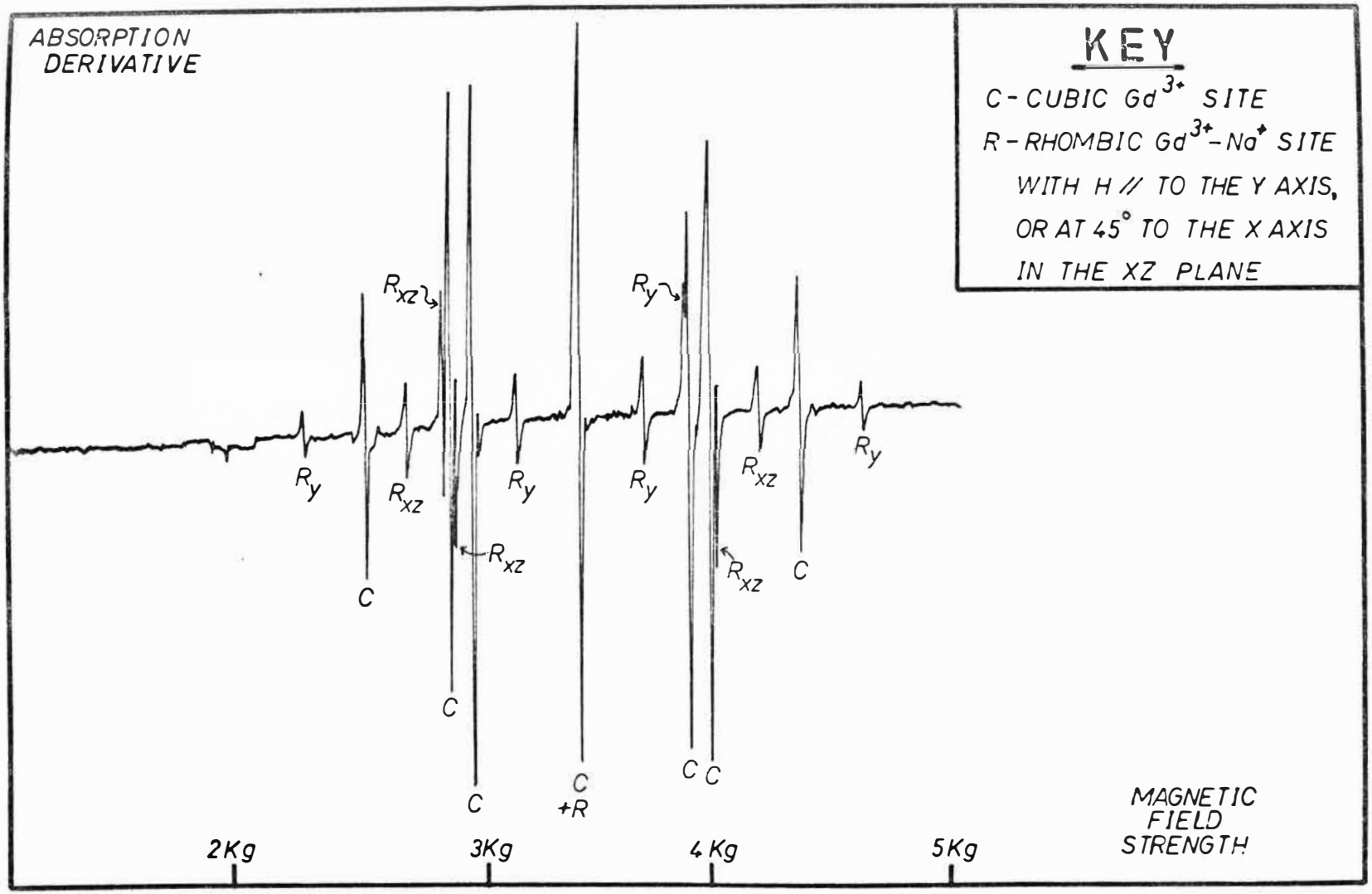

Fig 11 : X-Band (9.56GHz) EPR spectrum of calcium fluoride doped with 1.5% NaF and .05% GdF_3 for H // to the (001) axis

CHAPTER V

THE EPR SPECTRA OF HYDROGENATED ALKALINE EARTH FLUORIDE CRYSTALS CONTAINING GADOLINIUM IONS

I. THE EPR SPECTRUM OF HYDROGENATED CRYSTALS OF GADOLINIUM-DOPED CALCIUM FLUORIDE

Crystals of calcium fluoride doped with .05% gadolinium fluoride which have been hydrogenated show EPR spectra characteristic of three different Gd^{3+} sites. The two dominant sets of lines are due to the cubic Gd^{3+} site and the tetragonal Gd^{3+}-F_I^- site, as may be seen by comparing the spectrum of the hydrogenated crystals (Fig. 12) with that of the untreated crystals (Fig. 7). The absorption lines of the third set form a satellite structure around the spectrum of the tetragonal Gd^{3+}-F_I^- site, and the lines are typically one-third as intense as those of the latter site. The EPR spectrum of this new Gd^{3+} site also has tetragonal symmetry about the 001 axis. When a crystal is treated in a mixed hydrogen-deuterium atmosphere, all the lines of the new site appear as doublets. Thus the new site may be identified as the hydride ion analogue of the tetragonal Gd^{3+}-F_I^- site shown in Fig. 1 . The spin Hamiltonian parameters for this new Gd^{3+}-H_I^- site for all three isotopes of hydrogen are listed in table 7. Each Gd^{3+}-$(_1H^n)^-$ (n = 1,2 or 3) site is characterised by a distinct value of b_2^0, but the other parameters are identical to within the experimental uncertainty.

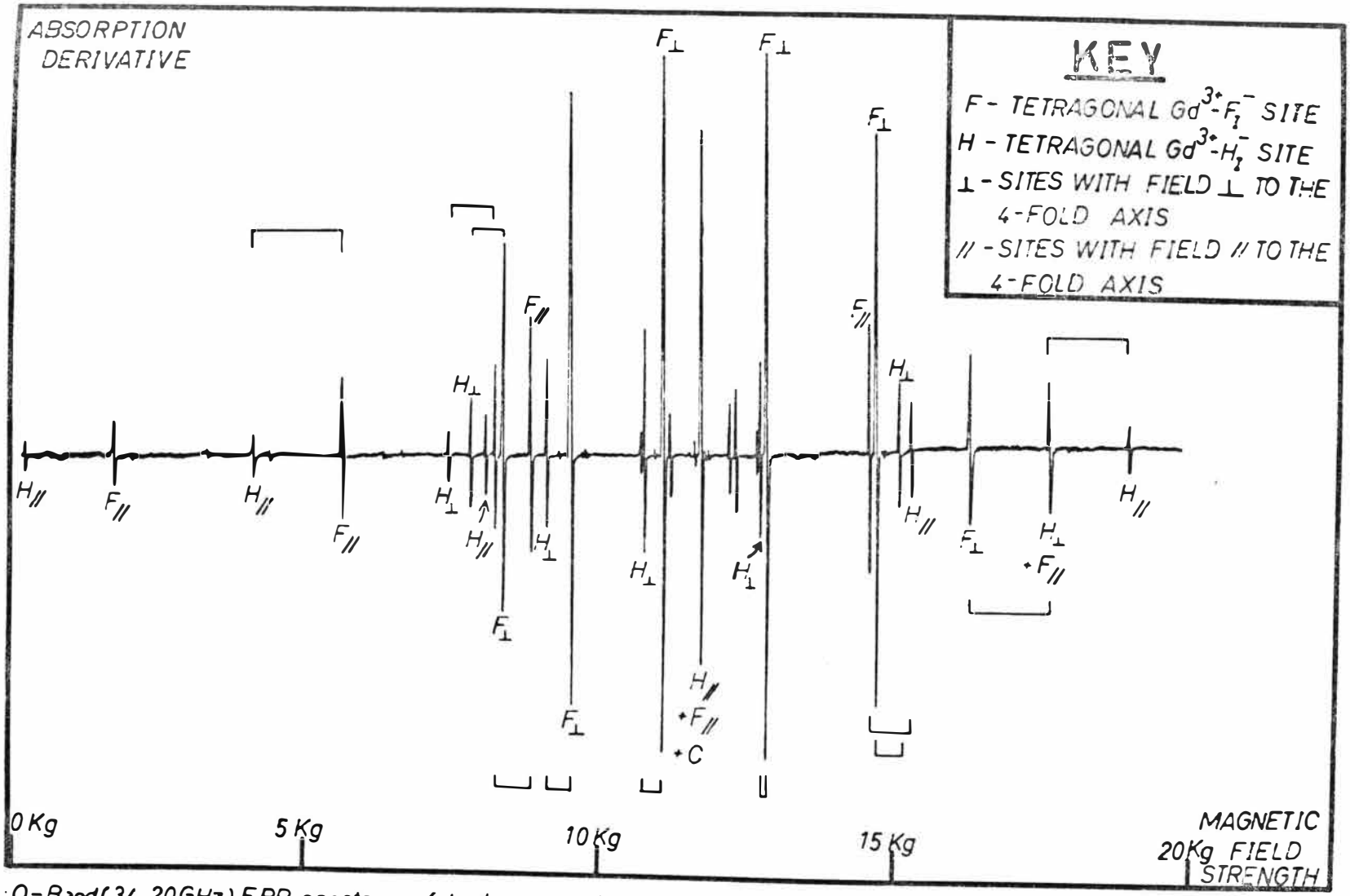

Fig 12: O-Band (34.20 GHz) EPR spectrum of hydrogenated calcium fluoride doped with .05% GdF_3 for H // to the (001) axis. The brackets indicate equivalent transitions for the two tetragonal sites.

TABLE 7

Spin Hamiltonian parameters of tetragonal Gd^{3+}-$H^-/D^-/T^-$ sites in calcium and strontium fluorides

Ion Pair	Host Xtal	$g_{//}$	$g_{\perp}$	b_2^0	b_4^0	b_6^0	b_4^4	b_6^4	No. of Lines Meas.	S.D. Field (gauss)	S.D. Frequency (cm^{-1})
Gd^{3+}-H_I^-	CaF_2	1.9921(5)	1.9920(5)	-.18414(5)	-.00239(5)	-.00009(3)	-.01148(15)	+.00075(30)	12	.4	$.4 \times 10^{-4}$
	77°K	1.9938(10)	1.9911(10)	-.19232(10)	-.00254(10)	-.00005(6)	-.01138(30)	+.00088(60)	8	1.3	1.2×10^{-4}
Gd^{3+}-D_I^-	CaF_2	1.9923(5)	1.9924(5)	-.18600(5)	-.00232(5)	-.00008(3)	-.01136(15)	+.00053(30)	12	1.6	1.5×10^{-4}
	77°K	1.9938(10)	1.9914(10)	-.19465(10)	-.00252(10)	-.00005(6)	-.01130(30)	+.00064(60)	8	3.0	2.7×10^{-4}
Gd^{3+}-T_I^-	CaF_2	1.9916(8)	1.9924(8)	-.18683(8)	-.00236(8)	-.00007(5)	-.01131(20)	+.00034(45)	10	4.1	3.7×10^{-4}
Gd^{3+}-H_I^-	SrF_2	1.9916(6)	1.9916(6)	-.13985(6)	-.00204(6)	-.00006(3)	-.01134(20)	+.00062(40)	10 + 8	2.7	2.5×10^{-4}
Gd^{3+}-D_I^-	SrF_2	1.99.3(6)	1.9923(6)	-.14211(6)	-.00203(6)	-.00005(3)	-.01103(20)	+.00084(40)	10 + 8	2.9	2.7×10^{-4}
Gd^{3+}-T_I^-	SrF_2	1.9927*6)	1.9921(6)	-.14323(6)	-.00201(6)	-.00005(3)	-.01147(20)	-.00008(40)	10	2.4	2.2×10^{-4}

NOTE: Units are cm^{-1}, the brackets enclose the uncertainty expressed in units of the last significant digit.

A useful quantity in discussing the influence of the various hydrogen isotopes is the zero field splitting isotope shift (Z.F.S.I.S.). This is defined as the difference between the overall zero-field splitting of the $^8S_{7/2}$ ground state for the Gd^{3+}-H_I^- site and that for Gd^{3+}-D_I^- or Gd^{3+}-T_I^-. To a good approximation,

$$ZFSIS = 12(b_2^0(_1H^1) - b_2^0(_1H^n)), \quad n = 2,3$$

and numerical values are listed in table 8.

II. SPECTRA OF HYDROGENATED CALCIUM FLUORIDE CRYSTALS CONTAINING GADOLINIUM AFTER IRRADIATION WITH ULTRA VIOLET LIGHT

Jones et al.[6] have reported that the optical fluorescence spectrum associated with the Gd^{3+}-H_I^- site decays after irradiating hydrogenated CaF_2:Gd^{3+} crystals with ultra-violet (u.v.) light at 77°K, and that the lines of a new Gd^{3+} site appear. They suggested that the new site may have the structure Gd^{3+}-H^0. This type of site would be interesting to examine by the EPR technique since both the Gd^{3+} ion and the neutral hydrogen atom are paramagnetic. An EPR investigation of u.v. irradiated crystals was therefore undertaken.

Preliminary experiments, using cold-finger and exchange gas dewars, indicated that u.v. irradiation did not change the EPR spectra of CaF_2:Gd^{3+}:H^- at all. The optical and infrared experiments of Jones et al.[6] were therefore repeated to confirm the presence of the new irradiation-induced site reported by these workers.

TABLE 8

ZERO FIELD SPLITTING ISOTOPE SHIFTS FOR TETRAGONAL GD^{3+}-$H^-/D^-/T^-$ SITES IN CALCIUM AND STRONTIUM FLUORIDES

Host Crystal		Ion Pair	Isotope Shift (cm^{-1})
CaF_2	Room	Gd^{3+}-D_I^-	-.0223(12)
	77^oK	"	-.0280(24)
CaF_2	Room	Gd^{3+}-T_I^-	-.0323(16)
SrF_2	Room	Gd^{3+}-D_I^-	-.0271(13)
	77^oK		-.0342(24)
SrF_2	Room	Gd^{3+}-T_I^-	-.0406(13)

(1) Optical Spectroscopy of the New Site

It was found that u.v. irradiation did in fact reduce the intensity of the tetragonal Gd^{3+}-H_I^- optical spectrum and cause a corresponding growth in the spectrum of a new Gd^{3+} site. These experiments largely reproduced the detailed results of Jones et al.[6] which will be briefly summarised below for the purposes of later discussion. The three main features of the new site spectrum are that: (a) The splitting pattern of the $^6P_{7/2}$ multiplet of the new site is very similar to that of the tetragonal Gd^{3+}-F_I^- and Gd^{3+}-H_I^- sites and the magnitude of the splitting is intermediate in value between them; (b) The hydrogen/deuterium isotope shift of the electronic fluorescence lines is only one third the magnitude of that for the Gd^{3+}-H_I^-/D_I^- tetragonal sites, and is of opposite sign; (c) A single set of vibronic transitions are observed which are separated from the parent electronic lines by 767 cm^{-1} (H_I^-) or 565 cm^{-1} (D_I^-).

Jones et al.[6] state that the new site is unaffected by short term heating above 100°K, but this author's experiments indicate that it becomes thermally unstable at temperatures in the vicinity of 90°K. A two hour u.v. irradiation of a crystal held at 77°K by direct immersion in liquid N_2 resulted in a 90% site conversion, though a similar period of irradiation for a crystal at 85°K clamped to a cold-finger produced only 30% conversion. In both cases the new site rapidly degenerated back to the tetragonal Gd^{3+}-H_I^- centre when the temperature was raised to 100°K. It is thought that the apparent stability of the new site above 100°K observed by Jones et al.[6] may be due to regeneration of the site by the u.v. lamp used to excite the fluorescence. The author found

that the heat filter commonly used in Gd^{3+} fluorescence work (Corning 7-54, passband 240-400 nm) reduced the rate of site conversion but did not prevent it.

A search for any vibronics other than that at 767 cm^{-1} reported by Jones et al.[6] was unsuccessful.

(2) Infrared Spectroscopy of the New Site

No new infrared absorption spectrum was observed after a $CaF_2:Gd^{3+}:H^-$ crystal clamped to a cold finger at 77°K was subjected to intense u.v. irradiation for several hours; in accordance with the similar null result of Jones et al.[6]. It was considered possible, in the light of the results of the previous section, that the sample temperature (unmonitored) was being elevated above the stability regime of the new site. Consequently, the crystal was weakly irradiated for periods of up to ten hours. In this case the two absorption lines characteristic of the Gd^{3+}-H_I^- tetragonal site diminished and two new lines appeared, as shown in Fig. 13. The sharp line at 768.5 cm^{-1} is in excellent agreement with the vibronic separation in the optical spectrum. The second line is broad (linewidth $\simeq$ 15 cm^{-1}) and occurs at 1326 cm^{-1}. Both lines disappeared when the crystal was raised to room temperature for a few minutes and recooled.

Ashburner and Newman[55] have recently performed similar irradiation experiments and have observed two new absorption lines at 984.3 cm^{-1} and 997.6 cm^{-1} which did not appear in this author's experiments. It is possible that the particular site produced by u.v. irradiation depends critically on the sample temperature.

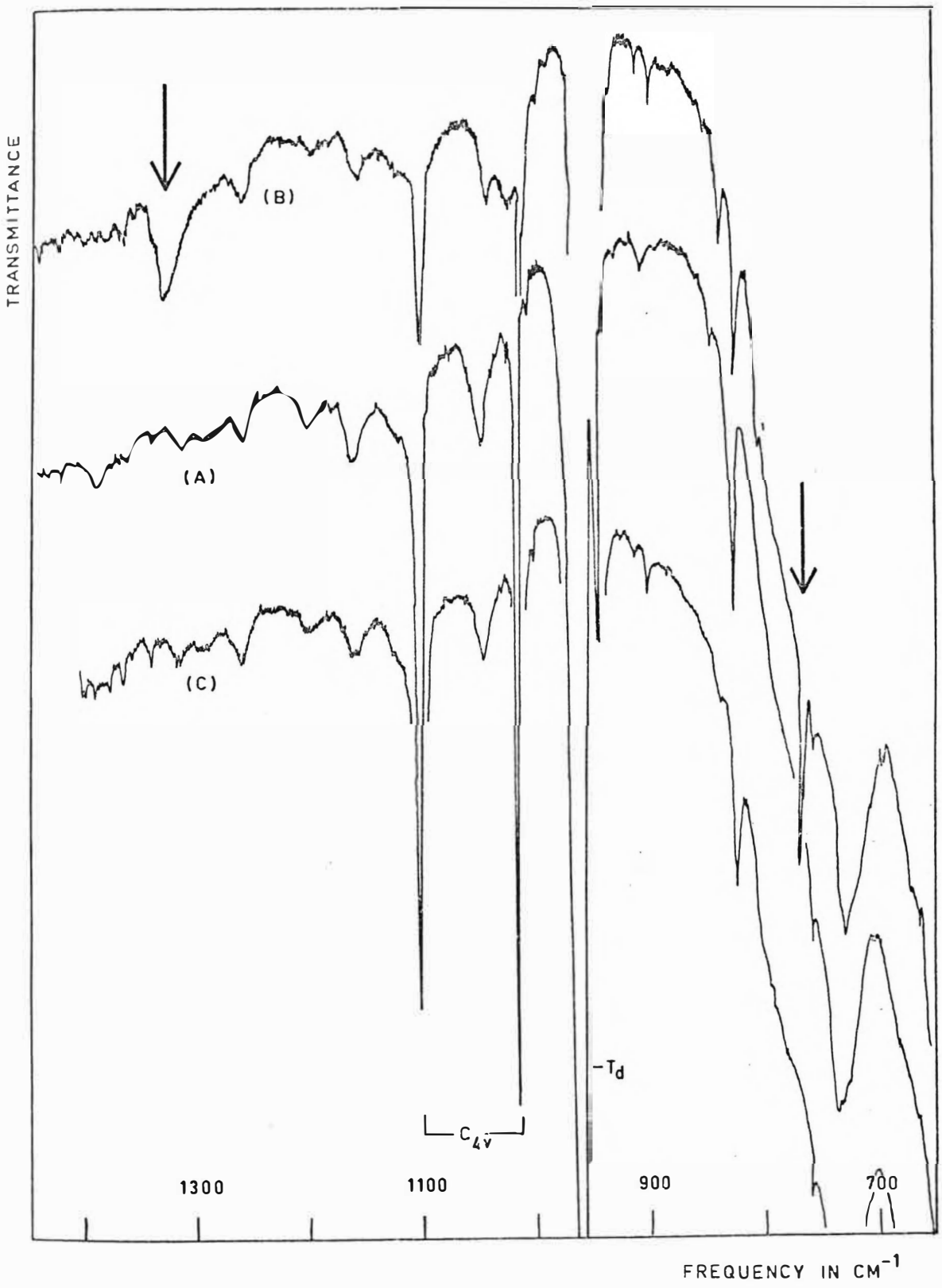

FIG. 13: Infrared spectrum of hydrogenated CaF_2 doped with ·05% GdF_3, (A) at 77°K, (B) after 12 hours UV irradiation at 77°K, and (C) after subsequently warming to room temperature and recooling. Arrows mark the position of new absorption lines.

(3) EPR Spectroscopy of the New Site

The u.v.-induced site conversion was difficult to monitor by EPR because of the conflicting requirements of the irradiation and EPR techniques. A suitable arrangement was finally devised using a cylindrical cavity with quartz windows placed inside a quartz tipped glass dewar, as shown in Fig. 14. A fine capillary tube was soldered to the bottom of the cavity. During irradiation the waveguide above the cavity was evacuated resulting in liquid nitrogen being drawn through the capillary and sprayed over the crystal. For EPR measurements the waveguide was pressurised with N_2 gas and the liquid driven out of the cavity through the capillary. In this way the crystal was held at $77^{o}K$ throughout the irradiation period ensuring adequate site conversion.

The spectrum of the pre-irradiated $CaF_2:Gd^{3+}:H^-$ crystal at $77^{o}K$ showed many weak lines, especially over the 0-10 kg region, which were not present in the room temperature spectrum. These lines were not investigated in detail. After two hours of u.v. irradiation at $77^{o}K$ the EPR lines of the tetragonal Gd^{3+}-H_I^- site had diminished to about one-tenth their former intensity and a new spectrum had appeared, as shown in Fig. 15. The site associated with this new spectrum will henceforth be labelled "R3" by analogy with a similar site observed in $SrF_2:Gd^{3+}:H^-$ which is discussed later in this chapter.

The large number of magnetically inequivalent R3 sites and the low intensity of the R3 spectrum precludes a full study of the angular variation of the spectrum, and so the symmetry of the site must be determined by less direct techniques. The pattern of the R3 spectrum of H//001 bears a

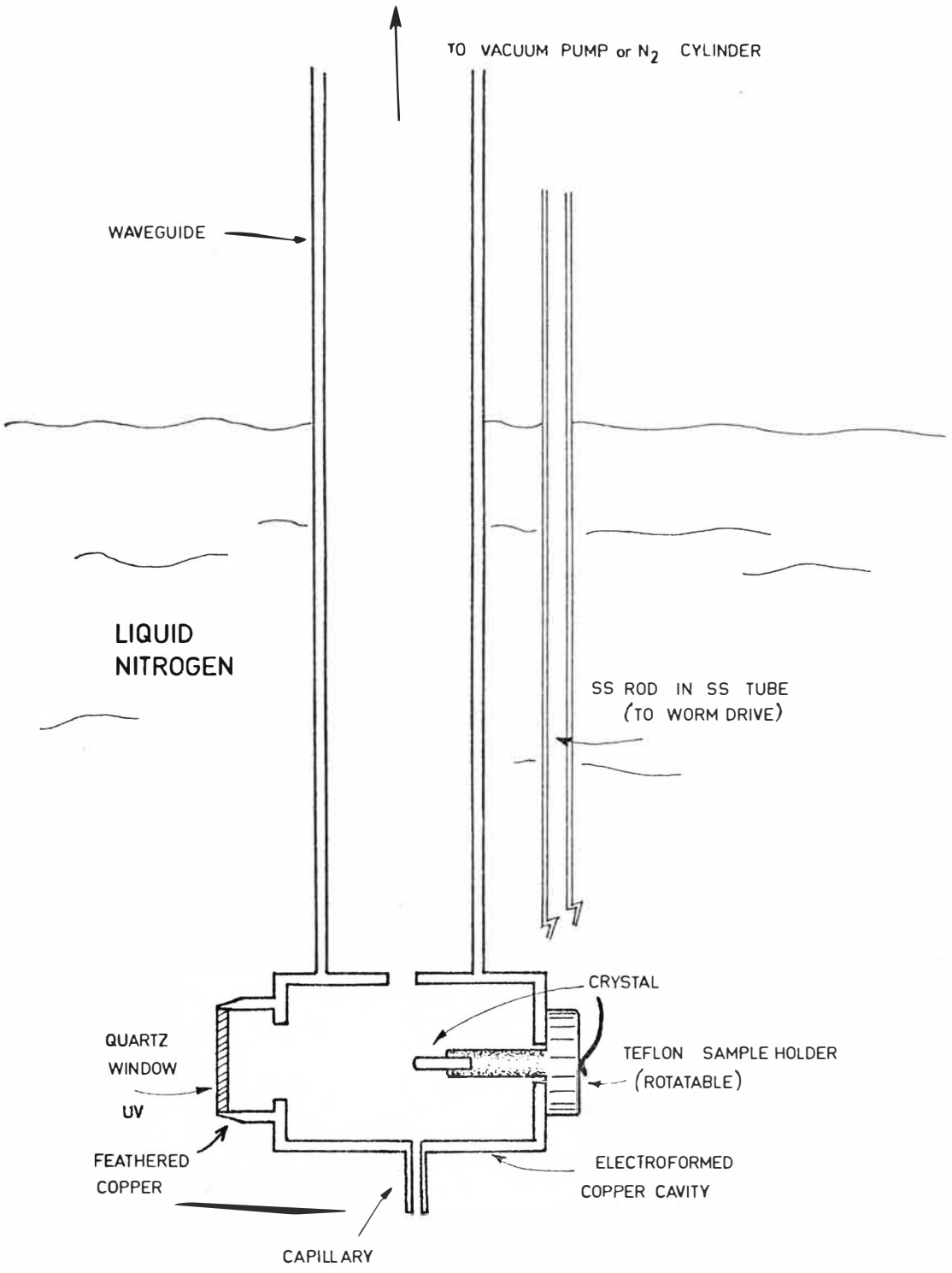

Fig 14: The resonant cavity used for u.v. irradiation experiments.

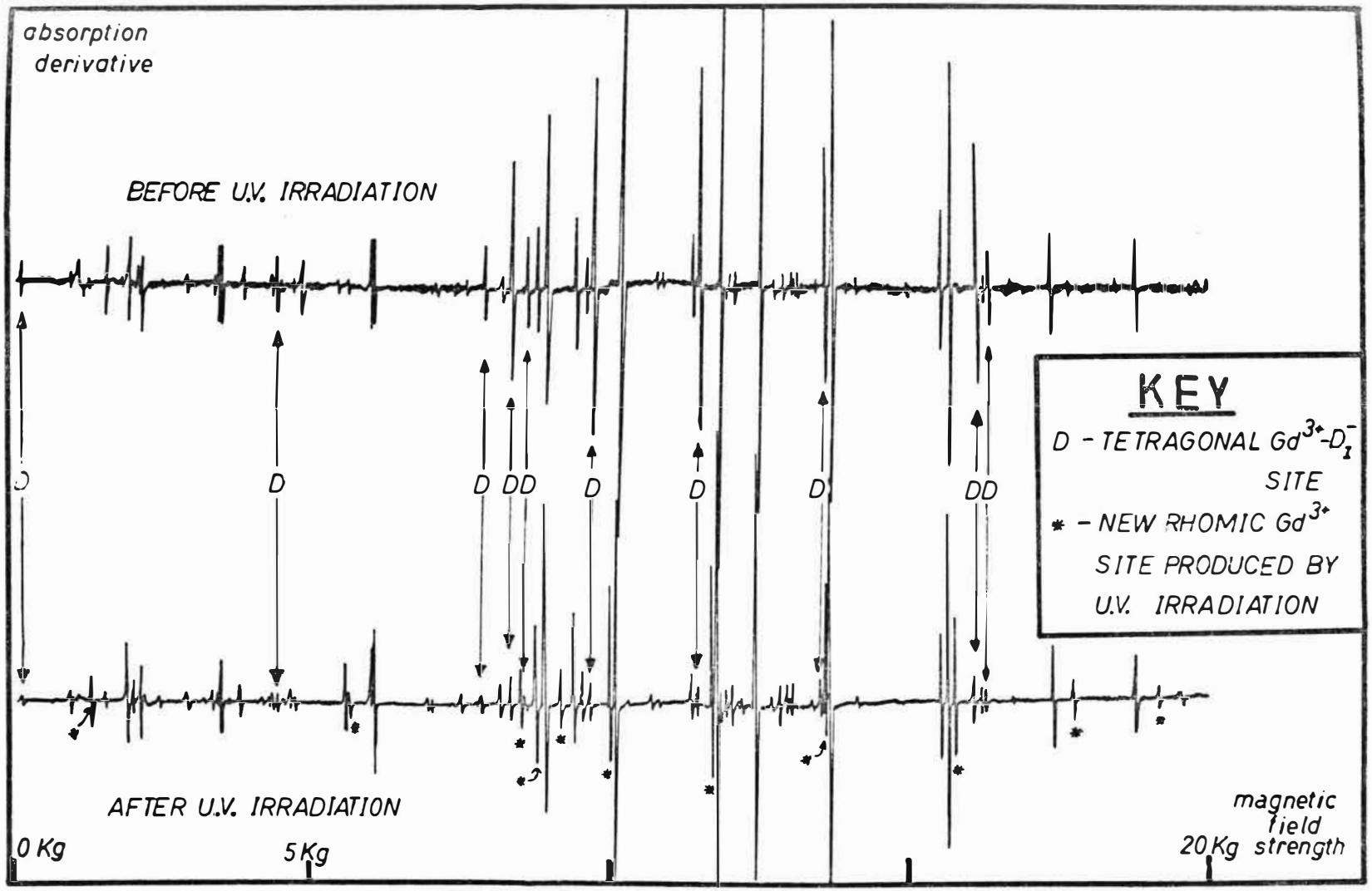

Fig 15: Q-Band (36.1 GHz) EPR spectrum of deuterated calcium fluoride doped with .05% GdF_3 for H // to the (001) axis and at 77°K, before and after 2 hours u.v. irradiadiation at 77°K.

strong resemblance to that of the tetragonal Gd^{3+}-H_I^-/F_I^- sites. There are three magnetically inequivalent sites for the Gd^{3+}-F_I^- (or Gd^{3+}-H_I^-) species, so for H//001 the spectrum consists of seven singlets (H//z) and seven degenerate doublets (H//x and H//y). The positions of the lines are determined mainly by the dominant second degree field, and so the two tetragonal spectra are similar in pattern, although the overall splitting of Gd^{3+}-H_I^- is 25% larger due to the larger value of b_2^0 for this site. The R3 site also fits into this pattern, indicating that it too is dominated by the second degree field. However, the H//001 spectrum consists of seven degenerate quadruplets and seven degenerate octets. When the field is rotated away from the (001) axis in the 110 plane the quartets split into two singlets and a doublet; a least squares fitting revealed that the overall splitting reached a maximum at a tilt angle of 3.2^{o} from the (001) axis. When the field was rotated away from (001) in the 100 plane, each quartet split into two doublets. The R3 spectrum was also examined with the magnetic field along a 111 direction. In this case the degenerate triplets which would be expected for a strictly tetragonal site are replaced by sets of lines consisting of two triplets and a hextet. All of these features are consistent with 12 magnetically inequivalent sites of rhombic (C_s) symmetry, the only symmetry element for each site being a reflection in a (110) type plane.

If the x-z plane is chosen as the plane of reflection symmetry the spin Hamiltonian involves only real parameters:

$$\mathcal{H} = \beta(g_x H_x S_x + g_y H_y S_y + g_z H_z S_z) + \sum_{n=1}^{3} \sum_{m=0}^{2n} B_{2n}^{m} O_{2n}^{m}. \qquad (5.2)$$

To a very good approximation the g value of Gd^{3+} may be assumed to be isotropic. In this case the x axis may be chosen to lie anywhere in the $\bar{1}10$ plane, and so for convenience the axis system has therefore been chosen as x,y,z: $110,\bar{1}10,001$. The experimental data is inadequate for the determination of all the 18 parameters in the full spin Hamiltonian (5.2). It is evident from the spectra that the crystal field at the Gd^{3+} position contains a dominant component of tetragonal symmetry about the 001 axis, together with a weaker rhombic perturbation. The spin Hamiltonian may therefore be approximated by:

$$= g\beta\underline{H}\cdot\underline{S} + (B_2^0O_2^0 + B_4^0O_4^0 + B_4^4\bar{O}_4^4 + B_6^0O_6^0 + B_6^4\bar{O}_6^4) + B_2^1\bar{O}_2^1 + B_2^2\bar{O}_2^2 \qquad (5\text{-}3)$$

The EPR spectrum of the R3 site for H//111 shows a definite and well resolved isotope shift between hydrogenated and deuterated crystals, although a shift could not be observed with the field parallel to the 001 direction. Thus the R3 site definitely involves hydride ions. The parameters which provide the best least squares fit of the R3 (H^-) and R3 (D^-) spectra for H//(001), (010) and (111) to the spin Hamiltonian 5-3 are presented in table 9. The fit is not as good as in the case of the tetragonal sites, probably because of the omission of the higher order rhombic terms.

(4) Proposed Model for the New Site

Jones et al.[6] suggested that u.v. irradiation of the tetragonal Gd^{3+}-H_I^- centre ionized the hydride ion without displacement to give a new tetragonal Gd^{3+}-H_I^0 site. The evidence presented in the previous section suggests that this

TABLE 9

Spin Hamiltonian parameters for rhombic Gd^{3+} sites in hydrogenated calcium and strontium fluoride crystals

Host Xtal	Site	Temp °K	g	b_2^0	b_4^0	b_6^0	b_4^4	b_6^4	b_2^1	b_2^2	Fit cm^{-1}	Fit Gauss	No. of Lines
CaF_2	R3(H^-)	77	1.990(2)	.1665(2)	.0022(2)	.00002(10)	-.0147(5)	.0008(5)	.030(10)	.0011(10)	.0019	16.7	29
CaF_2	R3(D^-)	77	1.990(2)	.1665(2)	.0022(2)	.00002(10)	-.0147(5)	.0008(5)	.029(10)	.0023(10)	.0020	17.0	29
SrF_2	R1(H^-)	295	1.993(2)	.1612(2)	.0019(2)	.00009(10)	-.0094(7)	.0009(5)	-	.015(10)	3.5×10^{-4}	3.7	11
SrF_2	R1(D^-)	295	1.991(2)	.1637(2)	.0021(2)	.00006(10)	-.0108(7)	.0012(5)	-	.031(10)	3.7×10^{-4}	3.9	
SrF_2	R2(H^-)	295	1.992(2)	.1693(2)	.0021(2)	.0001(2)	-	-	-	-	-	-	-
SrF_2	R2(D^-)	295	1.993(2)	.1710(2)	.0021(2)	.0000(2)	-	-	-	-	-	-	-
SrF_2	R3	295	1.993(2)	.1250(2)	.0019(2)	.0001(2)	-.0128(5)	+.0002(2)	-	-	4.3×10^{-4}	4.5	8
SrF_2	R2X(H^-)	295	1.993(2)	.1706(2)	.0020(2)	.0000(2)	-	-	-	-	-	-	-
SrF_2	R2X(D^-)	295	1.993(2)	.1726(2)	.0022(2)	.0001(2)	-	-	-	-	-	-	-
SrF_2	R1X(H^-)	295	1.991(2)	.1594(2)	.0022(2)	.0002(2)	-	-	-	-	-	-	-
SrF_2	R1X(D^-)	295	1.992(2)	.1601(2)	.0022(2)	.0001(2)	-	-	-	-	-	-	-

model is incorrect.

An interstitial fluoride ion at the (001) position is almost certainly involved in the R3 site. The near tetragonal symmetry of the site indicates the presence of a charge compensating anion at this position, and the proximity of b_2^0(R3) to b_2^0 (tetragonal Gd^{3+}-F_I^-) and the zero isotope shift for H//001 shows that this anion is a fluoride ion rather than a hydride ion. Since the R3 site does show an isotope shift for H//(111) a hydride ion must also be involved and this must lie somewhere in the $\bar{1}10$ plane to satisfy the spectral symmetry. It seems unlikely that the hydride ion would occupy an interstitial site because this would result in the defect centre having an overall negative charge. In addition the R3 infrared line at 768 cm^{-1} is far removed from the lines of other interstitial sites; c.f. cubic ω = 1310 cm^{-1}, tetragonal ω_x = 1017 cm^{-1}, ω_z = 1104 cm^{-1}; so the hydride ion most probably occupies a substitutional site. Figure 16 illustrates two sites involving an interstitial fluoride ion and a substitutional hydride ion which are consistent with the experimental evidence, and which can be generated by displacement of ions in the tetragonal Gd^{3+}-H_I^- site.

The first site (Fig. 16(a)) can be generated when one of the four fluoride ions which are mutual neighbours of the Gd^{3+} and H_I^- ions in the tetragonal site is displaced to one of two adjacent unoccupied interstitial sites. The hydride ion then moves into the vacancy left by the displaced fluoride ion. It is difficult to find an equally plausible mechanism for the formation of the second site. It could be generated by one of the four fluoride ions which are n.n. neighbours of the

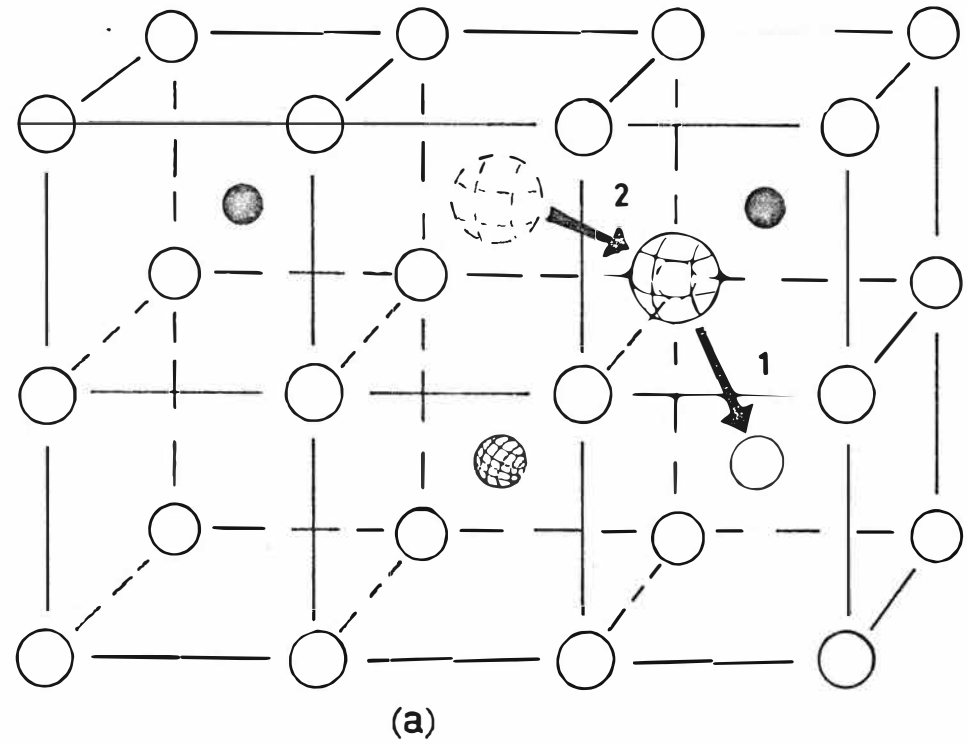

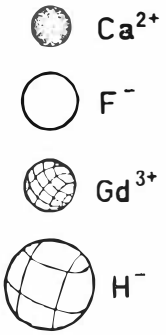

N.B. spheres drawn with dashed lines indicate the original or transitory positions of ions.

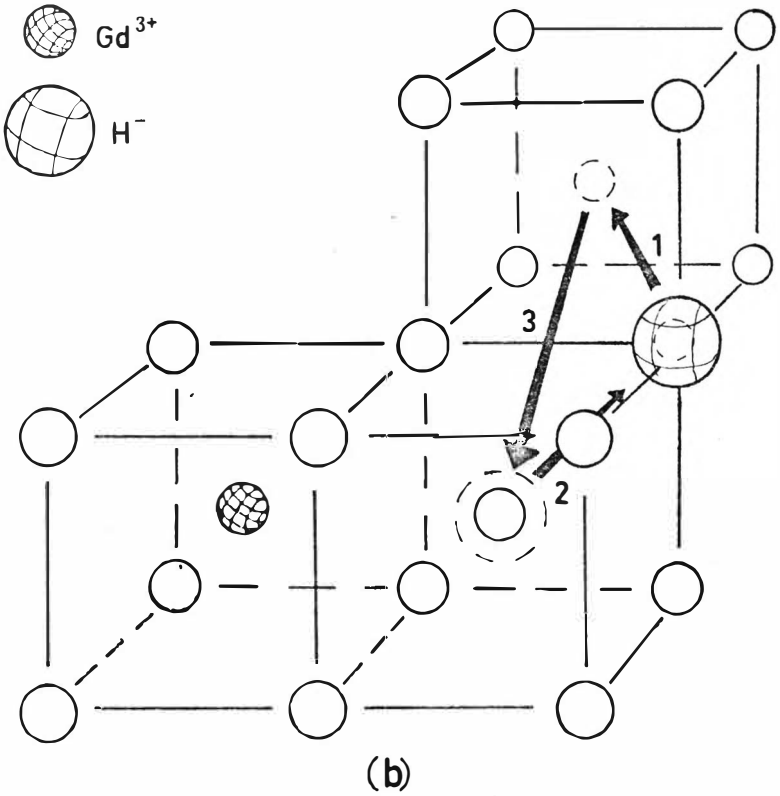

Fig 16: Two models for the new Gd^{3+} site produced by U.V. irradiation of hydrogenated crystals of calcium fluoride doped with Gadolinium Fluoride. In both cases the H_I^- ion in the original Gd^{3+}-H_I^- site dislodges a lattice F^- ion to an interstitial site (1) and takes its place (2) (an interstitialcy motion). In the model of Fig 16(b) a further jump (3) of the F^- ion to the (010) position is required.

hydride ion but not of the Gd^{3+} ion being displaced to an interstitial site along a (111) type direction. The hydride ion could then move into the vacancy so formed and the fluoride ion could hop back into the vacated interstitial position of the hydride ion. Both of these mechanisms are indicated on Figure 16.

The crystal field at the Gd^{3+} site for the two models discussed above will be predominantly determined by the interstitial fluorine anion, since this represents an extra unit charge inserted in the lattice. The substitutional hydride ion will give a smaller contribution since it replaces a regular lattice ion of similar charge. Thus for both models the overall crystal field will comprise a dominant tetragonal component and a weak rhombic perturbation. Which site arrangement occurs cannot yet be resolved.

Some information can, however, be derived from the presence of an isotope shift for H//111. Newman[56] has developed the superposition theory of crystal fields which assumes that the total crystal field is a linear combination of the fields produced by each ligand alone. In addition Newman and Urban[57] have noted that a linear relationship can be expected between the crystal field parameters A_n^m and the spin Hamiltonian parameters b_n^m for n = 2. Let the "intrinsic spin Hamiltonian parameters" defined by Newman[57] be denoted $\bar{b}_2^0(H)$ and $\bar{b}_2^0(F)$ for the hydride and fluoride ions respectively. Within the assumptions of the superposition model the spin Hamiltonians for the two models for terms up to n = 2 are:

Model 1

$$z//(001) \quad \mathcal{H} = g\beta H_z S_z + \bar{b}_2^0(F)O_2^0 + 2\sqrt{2}\bar{b}_2^0(H)O_2^1 + \bar{b}_2^0(H)O_2^2$$

$$z//(111) \quad \mathcal{H} = g\beta H_z S_z + \bar{b}_2^0(H)O_2^0 + 2\sqrt{2}\bar{b}_2^0(F)O_2^1 + \bar{b}_2^0(F)O_2^2$$

Model 2

$$z//(001) \quad \mathcal{H} = g\beta H_z S_z + (\bar{b}_2^0(F) + \frac{8}{11}\bar{b}_2^0(H))O_2^0 + \frac{\bar{b}_2^0}{11}(H)\ (18\sqrt{2}O_2^1 + 3O_2^2)$$

$$z//(111) \quad \mathcal{H} = g\beta H_z S_z + (\bar{b}_2^0(F) + \frac{7}{11}\bar{b}_2^0(H))O_2^0 + \frac{\bar{b}_2^0}{11}(H)\ (20\sqrt{2}O_2^1 + 4O_2^2).$$

It should be noted that S_z and O_2^0 have only diagonal matrix elements and O_2^1, O_2^2 only off-diagonal elements. In the light of previous discussion the magnitudes of the various terms in the spin Hamiltonian may be expected to follow the order:

$$\text{Zeeman} > \bar{b}_2^0(F) > \bar{b}_2^0(H),$$

and $\bar{b}_2^0(H)$ should be isotope dependent. Thus for model (1) $\bar{b}_2^0(H)$ affects the spin Hamiltonian eigenvalues in second order of perturbation for H//001, but in first order for H//111. An isotope shift may therefore be observable for H//111, in accordance with experiment, but not necessarily for H//001. For model (2) $\bar{b}_2^0(H)$ affects the eigenvalues in first order for both field orientations. The superposition theory thus favours model (1) as being the correct one, although it is recognised that the assumptions in the theory make this

identification tentative rather than conclusive. In particular, the induced dipole moment of the hydride ion will be influenced by the charge of the fluorine interstitial, and thus the two ligand crystal fields cannot be considered as being completely independent.

For both models the hydride ion is situated in a strongly anisotropic potential well of rhombic symmetry. Three different local mode frequencies would therefore be expected, but only two infrared absorption lines are observed; thus neither model is in full accord with the infrared spectra. In view of the fact that the site is unstable it is possible that the potential well has a very low barrier in one direction and that the first excited state for vibration in that direction is unbound.

The preceding discussion has shown that the first model for the R3 site (Fig. 16(a)) is consistent with most of the experimental evidence. ENDOR measurements would be useful to check on this tentative site identification.

III. EPR SPECTRA OF HYDROGENATED CRYSTALS OF STRONTIUM FLUORIDE CONTAINING GADOLINIUM IONS

Crystals of strontium fluoride containing .05% gadolinium fluoride which have been hydrogenated show EPR spectra characteristic of the tetragonal Gd^{3+}-F_I^- site and the trigonal (T4) Gd^{3+}-F_I^- site observed in the parent crystal. In addition, many new sets of lines appear which are one-twentieth or less of the intensity of the parent crystal lines. By examining the EPR spectra of some twenty crystals it was found that there are four main hydrogenic sites, whose relative intensities depend on the hydrogenation treatment and

subsequent thermal history of the crystals. Several sets of weaker lines were also observed but these were too difficult to examine in any detail.

The four main sites consist of one tetragonal and three rhombic sites, hereafter labelled R1, R2, R3. Crystals which were hydrogenated at temperatures in excess of 900^{o}C contained all four sites in similar concentrations. However, when samples were hydrogenated at 800^{o}C and subsequently quenched into liquid nitrogen only the tetragonal and R3 sites were observed. After such a crystal was left at room temperature for 24 hours the R1 site appeared and grew exponentially to its maximum intensity in a few weeks. Crystals which had been stored for a few weeks at room temperature showed an R2 spectrum which grew more intense in subsequent months. After periods of six months the EPR spectra of these crystals were indistinguishable from those hydrogenated at high temperature.

The weak intensity, low symmetry, and high site degeneracies of the various hydrogenic sites in SrF_2:Gd^{3+} results in the complex spectrum of many overlapping lines shown in Figure 17. Consequently only those lines in the 'wings' of the spectrum remote from the central g = 2 region could be unambiguously identified. For this reason the lines of the three rhombic spectra have been fitted to spin Hamiltonians truncated to include only spin operator terms expected to be dominant.

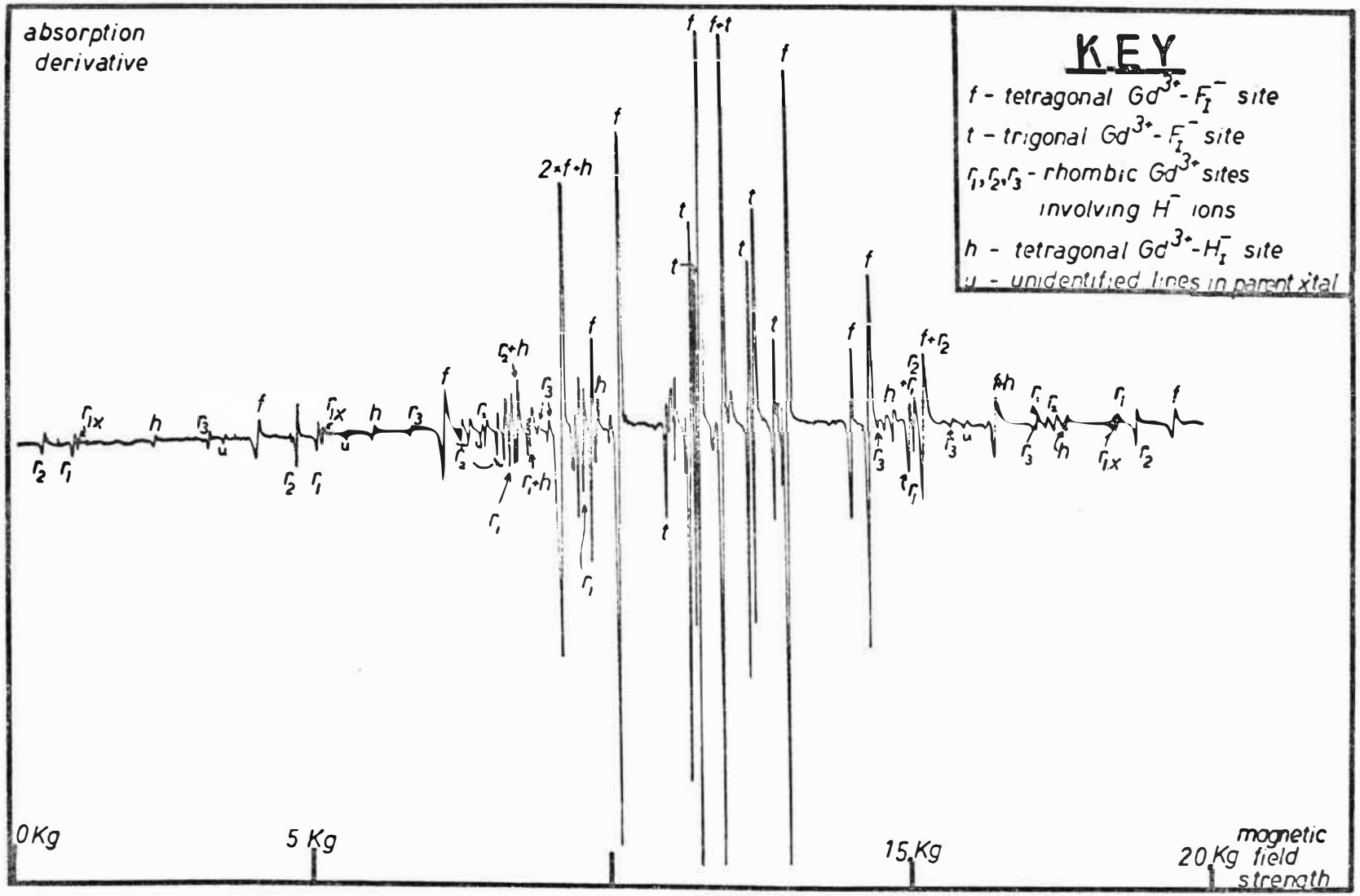

Fig 17. The Q-Band (34.5 GHz) E.P.R. spectrum of hydrogenated strontium fluoride doped with .05% GdF_3, for H // to the 001 axis.

(1) The Tetragonal Gd^{3+}-H_I^- Site

The tetragonal site could be readily identified by the simple angular variation of its spectrum around the (001) direction. Sufficient absorption lines were identified for this site from the H//z and H//x field orientations to enable all the parameters in the spin Hamiltonian to be evaluated as shown in Table 7. It is interesting to note that the isotope shift (refer to Table 8) is larger for SrF_2 than CaF_2 although the magnitude of the axial crystal field is smaller, and that a simple scaling factor appears to relate the spectra of tetragonal sites in the two crystals. The ratio of b_2^0 in SrF_2 to that in CaF_2 is evaluated in Table 10 and is close to 0.76 for both the tetragonal hydrogen and fluorine sites.

Proctor[58] and Freeth[59] have observed absorption lines at 919.8 cm^{-1} and 937.7 cm^{-1} in the 77°K infrared spectrum of SrF_2:Gd^{3+} which they assign to the tetragonal hydride ion site.

(2) The Rhombic R1 and R3 sites

The angular variation of the EPR spectra about the (001) field orientation and the line degeneracies for the R1 and R3 sites indicate that they possess the same symmetry as the irradiation-induced R3 site in calcium fluoride. The splitting patterns of the spectra reach a maximum at tilt angles of 2.5° and 3° (±.5°) for the R1 and R3 sites respectively. It was not possible to measure the spectra of these sites with the magnetic field in the (111) direction because of the difficulty in distinguishing their absorption lines from the multitude of lines due to other sites. The parameters which provide the best least squares fit to the

TABLE 10

The Ratio $b_2^0(CaF_2)/b_2^0(SrF_2)$ for some Gd^{3+} sites in strontium and calcium fluoride crystals

Site	$\frac{b_2^0(CaF_2)}{b_2^0(SrF_2)}$
Gd^{3+}-F_I^-	.757
Gd^{3+}-H_I^-	.759
R3 Site*	.761

* Corrected to equalise temperature of measurement for CaF_2 and SrF_2.

R1 and R3 ESR spectra of appropriately truncated spin Hamiltonians are displayed in Table 9. The y axis has been chosen to lie along the $\bar{1}10$ direction, and the x,z axes in the $\bar{1}10$ plane rotated by the tilt angle from the 110, 001 axes respectively.

The R3 site does not display an isotope shift for H//100, although it only appears in crystals which have been hydrogenated. It is similar in this respect to the CaF_2:R3 site. In addition the ratio of the b_2^0 parameters for the R3 sites in CaF_2 and SrF_2 is very close to that of the two tetragonal sites, as shown in Table 10, and the two tilt angles are almost equal. It therefore seems plausible that the same charge compensation mechanism is responsible for both sites and they have accordingly been given the same label. In SrF_2 the R3 site is stable at room temperature and u.v. irradiation for two hours at $77^{o}K$ did not cause any increase in the intensity of its EPR spectrum.

In contrast, the R1 site shows an isotope shift for H//(001) comparable to that of the tetragonal site. A possible model for this site involves a H_i^- and H_s^- at the positions shown in Figure 18. The R1 site could then be formed from the tetragonal C_{4v} site by the addition of a migratory hydride ion. This model was tested by treating a crystal in a mixed hydrogen/deuterium atmosphere, in which case four distinct R1 spectra from Gd^{3+} ions associated with H_i^--H_s^-, H_i^--D_s^-, H_s^--D_i^- or D_s^--D_i^- pairs should be observed. In fact only two spectra were recorded for H//001. However this test is inconclusive since it was shown for the R3 site

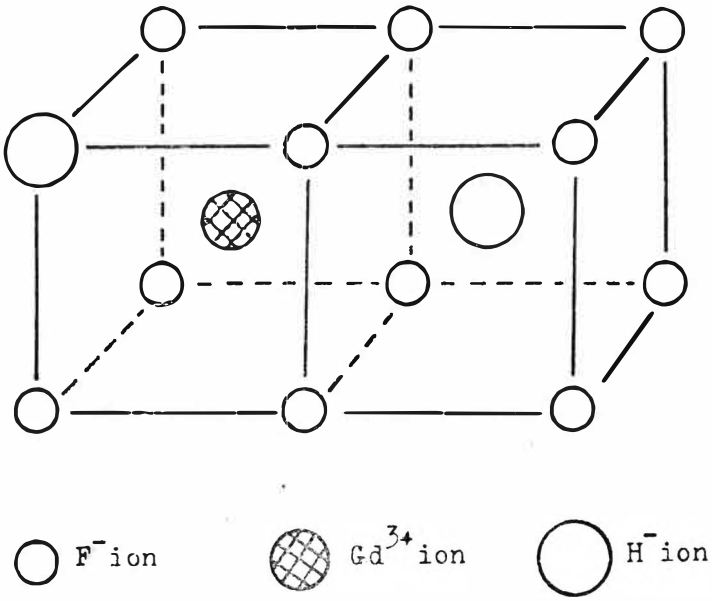

Fig 18: A possible model for the R1 site in hydrogenated strontium fluoride containing gadolinium ions.

that the substitutional hydride or deuteride ion contributes to an isotope shift for H//001 in second order of perturbation only.

A joint experiment was conducted with Mr C.A. Freeth[37] to observe the growth of the R1 site by means of both infrared and EPR spectroscopy. He has found that there are three IR absorption lines at 720.7, 784.1 and 969.1 cm^{-1} whose growth correlates to within experimental error with that of the R1 EPR spectrum. In both cases the intensity was calculated relative to the tetragonal site to eliminate the problem of making absolute intensity measurements. A total of six infrared lines would be expected for the proposed model of the new site. It is possible that the three remaining lines may be due to the interstitial hydride ion and are not sufficiently resolved from the strong tetragonal site absorption. It would be interesting to observe the IR spectrum of mixed hydrogen/deuterium crystals to check on the presence of combination lines.

(3) The R2 Site

The experimental observations on the R2 site are more difficult to analyse than those of the R1 and R3 sites. The EPR spectra of the latter consist of a set of seven degenerate quadruplets. This pattern is almost reproduced for the R2 site except that the outermost ($\pm 7/2 \rightarrow \pm 5/2$) lines for H//001 are resolved into two four-fold degenerate lines separated by 24 gauss at 35.6 GHz. An isotope shift and tilt angle similar to that of the R1 site is observed. The extra structure on the outermost lines is the same for both hydrogenated and deuterated crystals and so cannot be classed as hyperfine

structure since the nuclear spins of $_1H^1$ and $_1H^2$ differ. It is therefore probable that what has been labelled the "R2 site" consists of two slightly different perturbations of the same basic charge compensating mechanism. The isotope shift indicates that this basic mechanism is probably an interstitial hydride ion at the 001 position.

(4) Perturbations of the R2 and R1 Sites

In some crystals satellite lines were visible close to the EPR lines of the R1 and R2 sites. These are presumably due to the presence of an extra lattice defect in the vicinity of the rare earth ion in addition to those involved in the R1 and R2 sites. The approximate spin Hamiltonian parameters of these perturbed sites (denoted R1X and R2X) are listed in table 9.

IV. EPR SPECTRA OF HYDROGENATED CRYSTALS OF BARIUM FLUORIDE CONTAINING GADOLINIUM IONS

An intensive search of the EPR spectra of several $BaF_2:Gd^{3+}$ (.05%) crystals which had been hydrogenated failed to reveal the presence of a tetragonal Gd^{3+}-H_I^- centre analogous to that observed in calcium and strontium fluoride crystals. (The presence of hydrogen in the crystals was confirmed by the appearance in their infrared spectra of a strong absorption line at 798 cm^{-1} characteristic of the isolated substitutional (T_d) H^- site.) The absence of any tetragonal Gd^{3+}-H_I^- sites in barium fluoride is not unexpected in view of the absence of the analogous tetragonal Gd^{3+}-F_I^- centres.

No positive identification of any other Gd^{3+}-H_I^- centre could be made from the EPR measurements. However, the spectrum of the parent crystal contains many weak lines about one fiftieth the intensity of the trigonal (T4) F^- site) between the extreme up-field and extreme down-field lines of the (T4) F^- spectrum, which prevents the identification of any new lines in this interval. Thus the possibility that a Gd^{3+}-H_I^- site exists which produces a crystal field at the Gd^{3+} ion of predominantly cubic character cannot be excluded. It might be expected that hydrogenation would produce the hydride ion analogue of the trigonal (T4) F^- site, with the H^- ion at the (111) interstitial position. Due to the larger ionic radius of the H^- ion this hypothetical Gd^{3+}-H^- centre should produce a larger trigonal distortion on the predominantly cubic crystal field at the Gd^{3+} ion site. In consequence, the EPR spectrum of such a site should have a larger overall splitting than the corresponding (T3) F^- site, and at least two of the absorption lines should appear outside the confused central region. No such new lines were observed.

However, in a study of the infrared spectra of hydrogenated and rare earth doped BaF_2, C.A. Freeth[37] has observed a single rare earth dependent absorption line which shifts systematically from 736 cm^{-1} for lanthanum to 711 cm^{-1} for lutetium. The low frequency of this line suggests that it originates from a substitutional, rather than interstitial, hydride ion site. The EPR results suggest that the hydride ion must be relatively remote from the Gd^{3+} ion and so the site is probably a modification of the cubic or trigonal (T4) sites.

V. SUMMARY

Tetragonal Gd^{3+}-$H_I^-/D_I^-/T_I^-$ sites have been positively identified and measured in calcium and strontium fluorides, but no sites of this type were observed in barium fluoride. Ultraviolet irradiation destroys the tetragonal Gd^{3+}-H_I^- site in calcium fluoride but does not simultaneously create the tetragonal Gd^{3+}-H^0 site previously postulated; instead a new rhombic Gd^{3+} site appears which probably involves an interstitial fluoride ion and a substitutional hydride ion in the arrangement shown in Figure 16(a). Unirradiated crystals of SrF_2:Gd^{3+} which have been hydrogenated contain at least three rhombic Gd^{3+} sites involving hydride ions in addition to the tetragonal site. These sites appear to involve an interstitial fluoride or hydride ion, together with one or more substitutional hydride ion.

CHAPTER VI

THEORETICAL ANALYSIS OF THE GADOLINIUM ION SITES OF TETRAGONAL SYMMETRY IN HYDROGENATED CALCIUM AND STRONTIUM FLUORIDE CRYSTALS

It has been shown in the previous chapter that several different charge compensation mechanisms involving rare earth ions and hydride ions are found in calcium and strontium fluorides. The tetragonal (C_{4v}) site is the most suitable of these for the purposes of a theoretical investigation because of the simple ionic arrangement and the large amount of spectroscopic data known for this site. This chapter will collate the data with the object of explaining two features of interest in the EPR spectra of the tetragonal Gd^{3+} sites:

Firstly, the ground state splitting of the tetragonal Gd^{3+}-H_I^- site is larger than that of the corresponding Gd^{3+}-F_I^- site by 24% in both calcium and strontium fluoride. On a simple fixed point charge model the crystal fields produced at the neighbouring rare earth ion site by an interstitial fluoride or hydride ion should be identical. Secondly, an appreciable isotope shift is experimentally observed in the EPR spectrum of tetragonal Gd^{3+}-H_I^-, Gd^{3+}-D_I^- and Gd^{3+}-T_I^- sites. Since the hydride, deuteride and tritide ions are electronically identical, this isotope shift also cannot be explained by a simple fixed point charge model.

I. PARAMETERISATION OF THE CRYSTAL FIELD

The crystal field at the rare earth ion site may be expanded in a series in the Racah spherical tensors C_m^{ℓ} (defined in equations 2-3, 2-4) appropriate to C_{4v} symmetry:

$$V_c = B_0^2 C_0^2 + B_0^4 C_0^4 + B_0^6 C_0^6 + B_4^4 (C_4^4 + C_{-4}^4) + B_4^6 (C_4^6 + C_{-4}^6), \qquad (6\text{-}1)$$

where terms with ℓ odd or ℓ greater than 6 have been omitted because they have zero matrix elements within the $4f^7$ configuration[14]. The $4f^7$ electrons of the Gd^{3+} ion form a half filled shell, and so the crystal field produces no splittings in pure LS coupled states. However, spin orbit coupling mixes the Russell Saunders states and so a small splitting is obtained with intermediate coupling wavefunctions.

The parameters B_m^{ℓ} have been estimated[63,65] for the Gd^{3+}-F_I^- site in calcium and strontium fluorides by adjusting the parameter values until a minimum mean square is obtained between the eigenvalues of the crystal field Hamiltonian and the observed optical levels of the Gd^{3+} ion. This least squares fitting technique only yields a unique set of the B_m^{ℓ} when the number of such parameters is less than the number of observed levels. For the Gd^{3+}-H_I^- sites only the four levels of the $^6P_{7/2}$ multiplet have been measured and so this method cannot be used. The following section will develop an alternative first order technique based on the observed splitting patterns of the $^6P_{7/2}$ and $^8S_{7/2}$ multiplets for the tetragonal Gd^{3+} sites.

The optical spectra corresponding to the transitions between the $^6P_{7/2}$ excited state and the $^8S_{7/2}$ ground state have been measured for the Gd^{3+}-F_I^- site in calcium and strontium fluoride[60], and for the Gd^{3+}-H_I^-/D_I^- sites in calcium fluoride[6]. Since the crystal field splitting of the $^6P_{7/2}$ state is much smaller than the separations between the J multiplets of the $4f^7$ configuration, the $^6P_{7/2}$ splitting can be conveniently described by a spin Hamiltonian in the same way as the ground state. The spacings of the eigenstates in this multiplet are roughly in a 3:2:1 ratio for all the tetragonal sites listed above, which shows that the $\frac{1}{3}b_2^0O_2^0$ term is dominant. The diagonal parameters b_n^0, which are listed in Table 11, have therefore been estimated to first order by neglecting off-diagonal b_n^m ($m \neq 0$) terms. The crystal field parameter B_0^2 can be readily obtained from its spin Hamiltonian counterpart by equating the expectation values of the spin and crystal field Hamiltonians:

$$B_0^2 \langle \underline{^6P_{7/2}\ M} | C_0^2 | \underline{^6P_{7/2}\ M} \rangle = \frac{1}{3} b_2^0 (3M^2 - J(J+1)). \qquad (6\text{-}2)$$

Here the notation $|\underline{^6P_{7/2}\ M}\rangle$ indicates the intermediate coupled wavefunction of magnetic quantum number M whose major component is the pure LS state $|^6P_{7/2}\ M\rangle$. A similar formula may be written for the $^8S_{7/2}$ ground state, and hence two estimates of B_0^2 can be obtained for each site. However, the expectation values of C_0^2 in equation 6-2 must first be calculated before any comparison is possible.

TABLE 11

Spin Hamiltonian parameters for the $^6P_{7/2}$ state of the Gd^{3+} ion at various tetragonal sites in calcium and strontium fluoride

Site	b_2^0 (cm^{-1})	b_4^0 (cm^{-1})	b_6^0 (cm^{-1})	Ref.
CaF_2 Gd^{3+}-F^-	-10.81	-.58	-1.21	6
CaF_2 Gd^{3+}-H^-	-17.48	+.08	- .43	6
SrF_2 Gd^{3+}-F^-	- 6.88	-.28	-1.45	60

The electrostatic parameters for the $4f^7$ configuration of Gd^{3+} ions in calcium fluoride have been determined from the absorption spectrum down to 1350Å by Crosswhite et al.[61]. These authors have provided the intermediate coupled eigenvectors of the 50 x 50 matrix of J = 7/2 LS states calculated from these parameters. The expectation value of C_0^2 may now be calculated within these wavefunctions by using the relation[14]:

$$\langle f^7 \alpha SLJJ_z | C_0^2 | f^7 \alpha' SL'J'J_z \rangle = (-1)^{2J-J_z+S+L'+2} \begin{pmatrix} J & 2 & J' \\ -J_z & 0 & J_z' \end{pmatrix}$$

$$\begin{Bmatrix} J & J' & 2 \\ L' & L & S \end{Bmatrix} (f \| C^2 \| f)([J,J'])^{\frac{1}{2}} (f^7 \alpha SL \| U^2 \| f^7 \alpha' SL') \qquad (6\text{-}3)$$

The doubly reduced matrix elements of the unit tensor operator U^2 are tabulated by Nielson and Koster[62]. These values may be

used as the input to a computer program which calculates the expectation value of C_0^2 within the 50 component $^8S_{7/2}$ and $^6P_{7/2}$ intermediate coupling wavefunctions. The 3J and 6J symbols required can be evaluated by subroutines so as to eliminate transcription errors. The results are:

$$\langle {}^6P_{7/2}\ \tfrac{1}{2}|C_0^2|{}^6P_{7/2}\ \tfrac{1}{2}\rangle = .082841,$$

$$\langle {}^8S_{7/2}\ \tfrac{1}{2}|C_0^2|{}^8S_{7/2}\ \tfrac{1}{2}\rangle = .00049678 \qquad (6\text{-}4)$$

The crystal field parameters B_0^2 calculated using equations 6-2 and 6-4 applied to both the ground and the first excited states are presented in Table 12.

(1) Comparison of B_0^2 Parameters with Least Squares Values Reported in the Literature

Ivoilova and Leushkin[63] have performed least squares fittings of the parameters B_m^n to the Stark sub-levels of the $^8S_{7/2}$, $^6P_{7/2}$, $^6P_{5/2}$, $^6I_{7/2}$ multiplets for Gd^{3+}-F_I^- sites in both calcium and strontium fluoride; their values of B_0^2 are also shown in Table 12. It can be seen that there is good agreement with the values derived from the technique described above when applied to the $^6P_{7/2}$ state only. The value of B_0^2 ($^6P_{7/2}$) for the Gd^{3+}-F_I^- site in calcium fluoride is also in close agreement with the figure of 657 cm^{-1} calculated by Scheslinger and Nerenberg[64]. Thus the first order technique applied to the $^6P_{7/2}$ state yields reliable values of B_0^2 for the Gd^{3+}-F_I^- sites and so should be equally satisfactory for the Gd^{3+}-H_I^- sites being investigated, for which a complete crystal field analysis is not feasible. (It

TABLE 12

Crystal field parameters B_0^2 for various tetragonal sites in calcium and strontium fluorides estimated by different techniques

Site	Technique	B_0^2 (cm^{-1})	Spectral data ref.
$CaF_2:Gd^{3+}-F_I^-$	Least Squares	677.4	63,60
"	$^6P_{7/2}$ 1st Order	653	6
"	$^8S_{7/2}$ Hutchison Mechanism Only	1497	This work
"	$^8S_{7/2}$ Hutchison and relativistic mechanisms	650	This work
$SrF_2:Gd^{3+}-F_I^-$	Least Squares	409.4	63,60
"	$^6P_{7/2}$ 1st Order	415	6
"	$^8S_{7/2}$ Hutchison Mechanism Only	1134	This work
"	$^8S_{7/2}$ Hutchison and relativistic mechanisms	492	This work
$CaF_2:Gd^{3+}-H_I^-$	$^6P_{7/2}$ 1st Order	1055	6
	$^8S_{7/2}$ Hutchison Mechanism Only	1853	This work
	$^8S_{7/2}$ Hutchison and relativistic mechanisms	804	This work
$SrF_2:Gd^{3+}-H_I^-$	$^6P_{7/2}$ 1st Order	-	-
	$^8S_{7/2}$ Hutchison Mechanism Only	1408	This work
	$^8S_{7/2}$ Hutchison and relativistic mechanism	611	This work

should be noted, however, that O'Hare[65] has performed a least squares fit for Gd^{3+}-F_I^- sites in strontium fluoride which gave $B_0^2 = 206\ cm^{-1}$, almost exactly one half the value quoted by Ivoilova and Leushkin. This is possibly due to an error in the normalisation of C_0^2. The latter authors have recently defended their published parameters with the results of Zeeman measurements[129].)

The ground state ($^8S_{7/2}$) splittings yield values of B_0^2 which are at least a factor of two greater than those derived from the ($^6P_{7/2}$) first excited state. Since the latter values are in good agreement with the least squares values it appears that the simple first order technique fails for the ground state. This is not altogether surprising in view of the great difficulty which has been experienced in obtaining a satisfactory explanation of the ground state splitting of Gd^{3+} in many host crystals. The discrepancies between the values of $B_0^2(^8S_{7/2})$ and $B_0^2(^6P_{7/2})$ will be discussed and resolved in the following section.

(2) Contributions to the Ground State Splitting of Gd^{3+}

Wybourne[66] has estimated the contribution of eight distinct mechanisms for the $^8S_{7/2}$ splitting of Gd^{3+} in the gadolinium ethyl sulphate lattice for an ionic model of the crystal field, and has obtained an overall splitting which is twice the magnitude and of opposite sign to that experimentally observed. Buckmaster et al.[67] have shown that two of these mechanisms give rise to 90% of the overall splitting. The first is the fourth-order mechanism, proposed by Hutchison, which involves the interaction of the crystal field in first order with the spin orbit coupling in third order, and which

may be written schematically as:

$$\langle {}^8S_{7/2}|\Lambda|{}^6P_{7/2}\rangle\langle {}^6P_{7/2}|\Lambda|{}^6D_{7/2}\rangle\langle {}^6D_{7/2}|V_c|{}^6P_{7/2}\rangle\langle {}^6P_{7/2}|\Lambda|{}^8S_{7/2}\rangle,$$

where Λ represents the spin orbit coupling. This is the mechanism which has been effectively calculated in the ${}^8S_{7/2}$ version of equation (6-2).

The second mechanism is of negligible importance for the excited states where the Stark splittings are relatively large, but represents a significant contribution to the weak ground state splitting. In non-relativistic theory the crystal field matrix elements between LS states of different spin are identically zero, but when relativistic effects are included these matrix elements no longer necessarily vanish. In particular, the matrix element $\langle {}^6P_{7/2}|V_c|{}^8S_{7/2}\rangle$ has a finite value and is responsible for a further contribution to the ground state splitting. Wybourne[66] has shown that this second order mechanism gives a contribution E(M) to the ground state wavefunction $|M\rangle$ where,

$$E(M) = \frac{4B_0{}^2\zeta_{4f}(-5R_{++}^2 + 3R_{+-}^2 + 2R_{--}^2)M^2}{245(E_{{}^8S} - E_{{}^6P})} \qquad (6\text{-}5)$$

ζ_{4f} is the spin orbit coupling constant and the R's are radial integrals.

The total splitting, expressed in spin Hamiltonian form, may be calculated by inserting numerical values in equations (6-2) and (6-5) to give

$$b_2{}^0 = -(.99 + 1.3) \times 10^{-4} B_0{}^2 \qquad (6\text{-}6)$$

where the contributions are those of the Hutchison and relativistic mechanisms respectively. The values of $B_0^2(^8S_{7/2})$ deduced from equation (6-6) are displayed in Table 12; it can be seen that these recalculated values are in quite reasonable agreement with the corresponding $B_0^2(^6P_{7/2})$ figures. The remaining discrepancy is acceptable in view of the omission of the remaining mechanisms, discussed by Wybourne, and the neglect of crystal field mixing of other intermediate coupled multiplets. Thus it appears that the ionic theory satisfactorily explains the ground state splitting of Gd^{3+} in tetragonal sites in alkaline earth fluoride lattices, but fails for the ethyl sulphate type lattice.

Wybourne[66] has suggested that the failure of the theory in the latter case is due to the neglect of covalency contributions. This is feasible since the axial crystal field in the ethyl sulphate lattice is mainly produced by nearest neighbour ligand ions. However, for tetragonal sites in alkaline earth fluoride lattices it would be expected that the axial crystal field would be dominated by the next nearest neighbour interstitial anion. Thus covalency effects in this case should be less important, and the ionic theory of Wybourne is therefore more realistic.

The importance of this discussion lines in the fact that both the ground and the excited states of the Gd^{3+} sites of interest in this thesis can be consistently and satisfactorily described by a single empirical value of the dominant parameter B_0^2. A theoretical estimation of B_0^2 can now be attempted.

II. THEORETICAL CALCULATION OF B_0^2 FOR TETRAGONAL GD^{3+} SITES

A detailed calculation of the crystal field at the Gd^{3+} site, including overlap and covalency contributions, is a formidable task. It has been recognised in the literature[56] that simple electrostatic models of the crystal field are wholly inadequate for the high order B_m^4 and B_m^6 parameters, but yield reasonable results for the second order B_m^2 values. In the following section an electrostatic calculation of B_0^2 for tetragonal Gd^{3+}-F_I^-/H_I^- sites in calcium fluoride will be discussed.

(1) The Effect of Induced Dipole Moments

The electric field at lattice sites surrounding the Gd^{3+} ion is non-zero due to the extra charge of the ion itself and that of the F^- or H^- interstitial. The simple point charge model of the crystal field can be improved by including the point dipoles induced on neighbouring ions by these extra charges. The free ion dipole polarisabilities of the fluoride and hydride ions have been experimentally determined to be $.99\text{Å}^3$ and 30.2Å^3 respectively[17]. These figures show that a marked difference may be expected between the crystal fields generated by H^- and F^- interstitials due to the much larger polarisability of the former ion. However, the polarisabilities of anions in solids are expected to be smaller than in the case of a free ion, and must be estimated before any crystal field calculation can proceed.

Rufta[68] has calculated values of the dipole polarisability α_D for some ions in the alkali halide crystals and his tables show the expected decrease; Rufta's value of $\alpha_D = .81\text{Å}^3$ for F^- ions has been used in the following calculation.

The electronic structure of the hydride ion (U-centre) at substitutional sites in both the alkali halides and the alkaline earth fluorides has been the subject of several calculations; values of α_D (H^-) may be obtained from the resulting wavefunctions. Ashkin[69] has used a three parameter wavefunction to calculate the energy of a U centre substituted for a lattice F^- ion in CaF_2 when it is subject to an electric field; he obtained $\alpha_D(H^-) = 11.6\text{Å}^3$. Singh et al.[70] have calculated wavefunctions, energies and oscillator strengths for the ($1s^2$) ground state and 1s2p excited stateof the same system in the absence of an electric field. The value of α_D may be obtained from their results by

$$\alpha_D = \sum_n \frac{e^2}{4\pi^2 m} \frac{f_{n1}}{\nu_{n1}^2} \quad , \tag{6-7}$$

where f_{n1} is the oscillator strength between the ground state and the n^{th} excited state, and ν is the corresponding transition frequency. If the summation is restricted to the first excited state the formula yields $\alpha_D = 4.23\text{Å}^3$. This is a lower bound only, but since $f_{21} = 1.8$ and $\sum_n f_{n1} = 2$, the correct value should not be much larger. The calculations of Singh et al.[70] employed four variational parameters rather than the three of Ashkin and so may yield a more reliable value of α_D.

Jacobs et al.[11] have estimated the dipole moment of the H^- ion in the tetragonal Gd^{3+}-H_I^- site as p = 1.1e Bohr Radii, which corresponds to a polarisability of 3.7Å. However, it should be noted that this value was derived from an electrostatic model of the potential well in which the hydride

ion is located. This model has several deficiencies which are discussed later in this chapter.

Finally, Fieschi et al.[71] have used a value $\alpha_D(H^-) = 1.9\text{Å}^3$ in their work on U centres in the alkali halide crystals. This figure was obtained from an experimental study of lithium hydride by Calder et al.[72].

The wide range of values for $\alpha_D(H^-)$ quoted above implies that any value chosen for this work must have a large uncertainty. The theoretical estimates are valid only in the weak field approximation, and relate to a substitutional hydride ion site rather than an interstitial one. A 'mean' dipole polarisability for the hydride ion, based on the aforementioned values excluding that of Ashkin, and rounded to one significant figure accuracy ($\alpha_D = 3\text{Å}^3$) will be used in the following calculations.

(2) Estimation of B_0^2 on a Simple Point Charge - Point Dipole Model

Kiro and Low[73] have estimated the positions of the nearest neighbour (n.n.) and next nearest neighbour (n.n.n.) fluorine ions relative to the Ce^{3+} ion for Ce^{3+}-F_I^-/H_I^- tetragonal sites in calcium fluoride from their ENDOR measurements. A value of B_0^2 may be calculated from an ionic model of the lattice by using their plot of lattice distortions, assuming these are similar for equivalent Ce^{3+} and Gd^{3+} sites.

The following contributions to B_0^2 have been estimated, that of (1) the point charge $-|e|$ of the interstitial anion; (2) the 8 nn F^- ions at their shifted lattice sites; (3) the

24 n.n.n. F^- ions at their shifted lattice sites; (4) the dipole induced on the interstitial anion by the charge $+|e|$ of the Gd^{3+} ion; (5) the dipoles induced on the 8 n.n. F^- ions induced by the point charges of the anion interstitial and the Gd^{3+} ion; and (6) the similarly induced dipole moment on the 4 n.n.n. F^- ions which are also n.n. of the interstitial. Dipole-dipole interactions have been omitted. The various contributions for Gd^{3+}-H_I^-/F_I^- sites in calcium fluoride are listed in Table 13. It can be seen that the large point charge contribution of the interstitial anion is strongly reduced by the distortions of the lattice and the induced dipole moments. The crystal field which affects the 4f electron is modified by the screening effects of the outer 5s, 5p shells which reduce it to[56],

$$B_0^2 = (1-\sigma_2)B_0^2(\text{unscreened}) \qquad (6\text{-}8)$$

in the linear shielding approximation. The shielding parameter σ_2 has been theoretically estimated to be in the vicinity of .5 to .6 for trivalent Gadolinium[74,75] and experimental values are 0.58[79] and .61[80]. Thus the ionic model predicts values for B_0^2 of 320-400 cm^{-1} (c.f. 650 cm^{-1} by experiment) for the Gd^{3+}-F_I^- site, and 460-570 cm^{-1} (c.f. 1050 cm^{-1} by experiment) for the Gd^{3+}-H_I^- site. The net calculated B_0^2 values are only about one half of those observed, but since they are the sum of several contributions of opposite sign they are quite sensitive to the details of the lattice distortions etc. This point, and the unknown covalency contribution may account for the discrepancies.

Table 13

Contributions to B_0^2 for the tetragonal Gd^{3+}-F_I^- and Gd^{3+}-H_I^- sites calculated on an ionic model

F^-	H^-	Origin
1530	1580	1) Anion Interstitial
-460	-780	2) Nearest Neighbour F^- Ions
-70	-100	3) NN Neighbour F^- Ions
+220	+880	4) Interstitial Dipole Moment
-370	-400	5) Nearest Neighbour Dipole Moments
-50	-40	6) NN Neighbour Dipole Moments
+800	+1140	Total

N.B. Units are cm^{-1}.

Although the agreement with experiment is only fair the calculations are still useful because they give physical insight into the magnitudes of the various contributions, and they also qualitatively explain the origin of the larger ground state splitting of the Gd^{3+}-H_I^- site.

III. ISOTOPE SHIFTS OF ZERO FIELD SPLITTING FOR GD^{3+}:$H_I^-/D_I^-/T_I^-$ SITES

(1) Vibronic Wavefunctions and Energies

The isotope shifts in the zero field splitting of Gd^{3+}-X_I^- (X = H,D,T) ion pairs in MeF_2 crystals are a consequence of the different amplitudes of vibration of the different X^- isotopes, and the electron-phonon interaction discussed in Chapter II. This interaction arises from the modulation of the crystal field at the Gd^{3+} site by the vibrational motion of the crystal lattice. It has been shown in Chapter II that for the purposes of isotope shift calculations, the contribution of the regular lattice modes may be ignored and only that of the localised X^- mode considered; in this case the electron-phonon interaction Hamiltonian V_{ep} takes on the particularly simple form of equation 2-7. A theoretical calculation of these isotope shifts using this form of V_{ep} will be presented in the following section, and the results compared with the experimental observations recorded in Chapter V.

The unperturbed (zero order) Hamiltonian of the Gd^{3+}-X_I^- system can be taken as:

$$H_o = H_e + H_v, \qquad (6\text{-}9)$$

where H_e is the Hamiltonian of the $4f^7$ electrons of the Gd^{3+} ion (equation 2-2), and H_v is the axial harmonic oscillator Hamiltonian of the X^- anion in its static potential well,

$$H_v = (P_x^2+P_y^2+P_z^2)/2m + \tfrac{1}{2}m\omega_x^2(X^2+Y^2) + \tfrac{1}{2}m\omega_z^2Z^2. \qquad (6\text{-}10)$$

The anharmonic potential terms have been temporarily omitted from equation (6-10) since H_v has the simple and convenient eigenvectors $|N_xN_yN_z>$ of a harmonic oscillator of axial symmetry. The eigenvectors ϕ_v of H_o are the direct product "vibronic" wavefunctions,

$$\phi_v = \phi_e|N_xN_yN_z>,$$

where ϕ_e is an eigenfunction of H_e, and the eigenvalues of H_o are

$$E = (N_x+N_y+1)\hbar\omega_x + (N_z+\tfrac{1}{2})\hbar\omega_z + <\phi_e|H_e|\phi_e>.$$

The perturbation Hamiltonian V_p consists of V_{ep} plus the anharmonic terms omitted from equation (6-10), and may thus be explicitly written as:

$$V_p = cZ^3 + dZ(X^2+Y^2) + f_xX + f_yY + f_zZ + g_{xx}X^2 + g_{yy}Y^2 + g_{zz}Z^2 + g_{xy}XY + g_{xz}XZ + g_{yz}YZ. \qquad (6\text{-}11)$$

The modifications which V_p produces in the vibronic energy levels may now be calculated by standard perturbation theory, with due regard to the following points;

1) The EPR results only refer to the ground vibronic states denoted by $||^8S_{7/2}\ M>|000>>$ whose unperturbed energy is E_M.

2) Equation 2-3 is basically a Taylor's expansion of V_{ep} and

so the "g" terms, which are quadratic in the displacement coordinates, are expected to be smaller than the linear "f" terms and need be included only to first order, while the f terms are taken to second order.

The resulting expression for the modifications in E_M may be written as

$$\Delta E_M = -\frac{\beta_z^2}{\hbar\omega_z}|\langle M|f_z|M\rangle|^2 - \sum_{M'\neq M}\frac{\beta_x^2}{\hbar\omega_x}(1 + E_{M'}/\hbar\omega_x)^{-1}$$
$$\times\left[|\langle M|f_x|M'\rangle|^2 + |\langle M|f_y|M'\rangle|^2\right] - \frac{11\beta_z^6c^2}{\hbar\omega_z} - \frac{4\beta_z^2\beta_x^4d^2}{\hbar\omega_z}$$
$$- \frac{4\beta_z^2\beta_x^4d^2}{\hbar\omega_z} - \frac{(6\beta_z^4c + 4\beta_z^2\beta_x^2d)}{\hbar\omega_z}\langle M|f_z|M\rangle$$
$$+ \beta_z^2\langle M|g_{zz}|M\rangle + \beta_x^2\langle M|g_{xx}+g_{yy}|M\rangle, \qquad (6\text{-}12)$$

where $\beta_i^2 = \hbar/(2m\omega_i)$. Those terms in equation (6-12) which are independent of M affect all the $^8S_{7/2}$ levels equally and thus do not contribute to the overall $^8S_{7/2}$ zero field splitting. The first term does not contribute to the isotope shift because $\beta_i^2/\hbar\omega_i$ is just the reciprocal of the force constant, which is independent of mass. The contribution of the second term to an isotope shift is negligible since $E_{M'} < 2\ cm^{-1}$ and $\hbar\omega \approx 1100\ cm^{-1}$; the premultiplier of the electronic term is thus very nearly the force constant reciprocal again. The remaining terms, which are all mass dependent, may be conveniently regrouped into the form:

$$\Delta E'_M = \beta_z^2\left(\langle M|g_{zz}|M\rangle - \frac{3c}{m\omega_z^2}\langle M|f_z|M\rangle\right)$$
$$+ \beta_x^2\left(\langle M|g_{xx}+g_{yy}|M\rangle - \frac{2d}{m\omega_z^2}\langle M|f_z|M\rangle\right) \qquad (6\text{-}13)$$

The zero field splitting isotope shift (ZFSIS) is given by the difference in $|\Delta E'_{\pm 7/2} - \Delta E'_{\pm 1/2}|$ between Gd^{3+}-H_I^- and Gd^{3+}-D_I^- or Gd^{3+}-T_I^-. A numerical evaluation of the ZFSIS requires a quantitative model for the electron-phonon interaction, but equation (6-13) can be used to assess the ratio of the hydrogen-deuterium to hydrogen-tritium isotope shifts. The isotope dependence of $\Delta E'_m$ in equation (6-13) lies entirely in the coefficients $\beta_z^2 = h/(2m\omega_z)$ and $\beta_x^2 = h/(2m\omega_x)$, and so if we assume $\omega_z \approx \omega_x$ it follows that,

$$\frac{ZFSIS(H-T)}{ZFSIS(H-D)} = \frac{1 - M_H\omega_H/M_T\omega_T}{1 - M_H\omega_H/M_D\omega_D} \qquad (6\text{-}14)$$

Using the experimental values of ω_H and ω_D, and estimating that of ω_T, the theoretical value of equation (6-14) is 1.44. For comparison the experimentally observed ratios are 1.45 (± .02) for CaF_2:Gd^{3+}, and 1.49 (± .02) for SrF_2:Gd^{3+}. The close agreement between the theoretical and experimental ratios is encouraging and justifies more detailed verification of the electron-phonon interaction theory. However, the numerical values of the anharmonic parameters c and d must first be estimated as a prerequisite of further calculation.

(2) Evaluation of the Hydride Ion Potential Well Parameters

The hydride ion moves in a potential well which may be conveniently expanded in a power series (equation 2-1) in terms of its displacement from the equilibrium position. Jacobs et al.[11] have estimated the coefficients in this series by a simple electrostatic model in which the potential is

assumed to be the superposition of the cubic potential of an isolated H^- interstitial site, together with the axial potential of the hydride ion in the electrostatic field generated by the rare earth ion. However, the expression which Jacobs et al. developed for the parameters a,b,c and d do not include terms arising from the shift in the equilibrium position of the hydride ion away from the centre of its surrounding cube of F^- ions, or those arising from the high order interaction of the induced dipole moment of the hydride ion with the cubic potential. Within the approximations of their electrostatic model the extended expressions for the parameters a,b,...,k are:

$$a = A - \frac{q_1 q_2}{2D^3} + \frac{pq_1}{D^4} + \frac{2Ap}{q_2 D} + \left(\frac{Ap\alpha}{q_2 D^2} - \frac{2Cp\alpha}{q_2}\right)$$

$$b = A + \frac{q_1 q_2}{D^3} - \frac{3pq_1}{D^4} - \left(\frac{12Bp\alpha}{q_2}\right)$$

$$c = -\frac{q_1 q_2}{D^4} + \frac{4pq_1}{D^5} + \left(\frac{4Bp}{q_2} - 4B\alpha\right) \qquad (6\text{-}16)$$

$$d = \frac{3q_1 q_2}{2D^4} - \frac{4pq_1}{D^5} - \frac{3Ap}{q_2 D^2} - \left(2C\alpha - \frac{2Ap\alpha}{q_2 D^3} - \frac{4Cp\alpha}{q_2 D} + \frac{2Cp}{q_2}\right)$$

$$f = \left(B + \frac{3q_1 q_2}{8D^5} - \frac{pq_1}{D^6} + \frac{4Bp}{q_2 D} - \frac{Ap}{q_2 D^3} - \frac{3Ap\alpha}{q_2 D^4} + \frac{Cp\alpha}{q_2 D^2}\right)$$

$$g = \left(B + \frac{q_1 q_2}{D^5} - \frac{5pq_1}{D^6}\right)$$

$$h = \left(C - \frac{3q_1 q_2}{D^5} + \frac{10pq_1}{D^6} + \frac{4Ap}{q_2 D^3} + \frac{2Cp}{q_2 D} + \frac{4Cp\alpha}{q_2 D^2} + \frac{3Ap\alpha}{q_2 D^4} + \frac{6Bp\alpha}{q_2 D^2}\right)$$

$$k = \left(C + \frac{3q_1q_2}{4D^5} - \frac{2pq_1}{D^6} + \frac{4Cp}{q_2D} - \frac{2Ap}{q_2D^3} + \frac{2Cp\alpha}{q_2D^2} - \frac{3Ap\alpha}{2q_2D^4} \right),$$

and for equilibrium,

$$\frac{q_1q_2}{D^2} - \frac{2pq_1}{D^3} + 2A\alpha - \frac{2Ap}{q_2} = 0,$$

where the meaning of the symbols is indicated in Fig. 19, and the extra terms have been bracketed. The parameters A, B and C are those which occur in the power series expansion of the cubic potential of an isolated interstitial site:

$$V_c = A(X^2+Y^2+Z^2) + B(X^4+Y^4+Z^4) + C(X^2Y^2+Y^2Z^2+X^2Z^2) \quad (6\text{-}17)$$

The values of the parameters B, C and α are not known but an order of magnitude estimate of $|B| = |C| = 1 \times 10^{19}$ ergs/cm^4 and $\alpha = 0.1$Å shows that the extra terms in equations (6-16) may be neglected for the parameters a and b, but are comparable with Jacobs et al.'s terms for c and d. Since the latter parameters are of major importance in the isotope shift calculations an alternative estimation procedure was adopted.

Jones et al.[6] have measured two first harmonic and three second harmonic infrared transition frequencies for hydride ion localised modes of tetragonal Yb^{3+}, Gd^{3+} and Tb^{3+}-H_I^- ion pairs in calcium fluoride. Maradudin and Peretti[76] have calculated analytical formulae for those energy levels of an oscillator in a potential of tetragonal symmetry which are derived from the N = 0, 1 and 2 levels of a simple harmonic oscillator (refer to Fig. 2). These formulae, with corrections noted by C.A. Freeth[59], have been used to perform a least

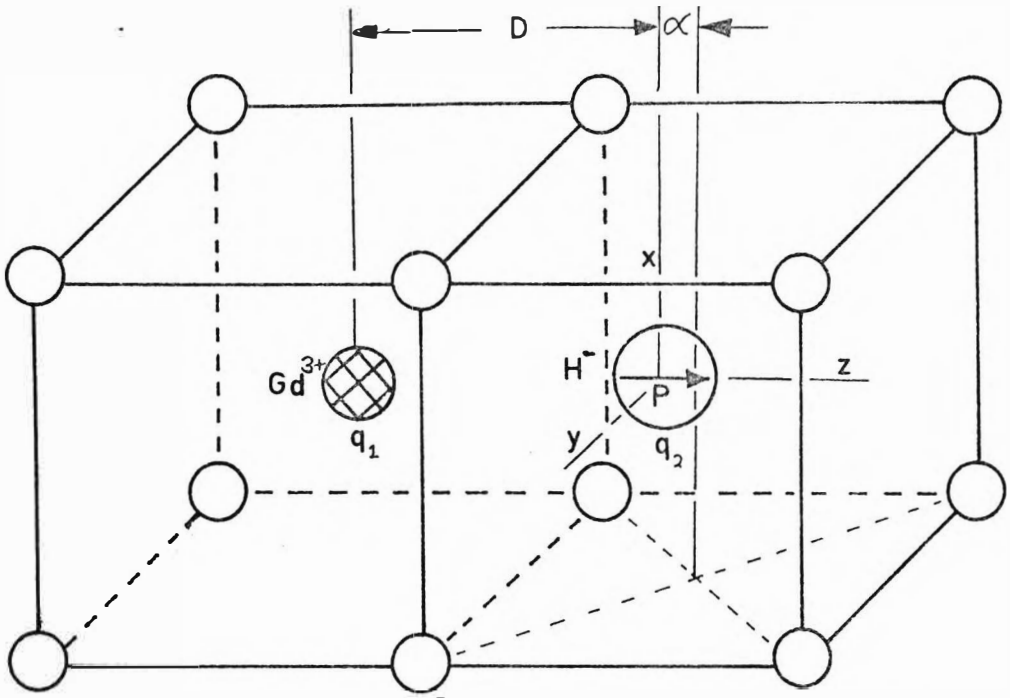

Fig 19: The tetragonal Gd^{3+}-H^- site in calcium fluoride, showing the meaning of the symbols used in the text. The Gd^{3+} and H^- ions have charges q_1, q_2 respectively, and the H^- ion has a dipole moment p.

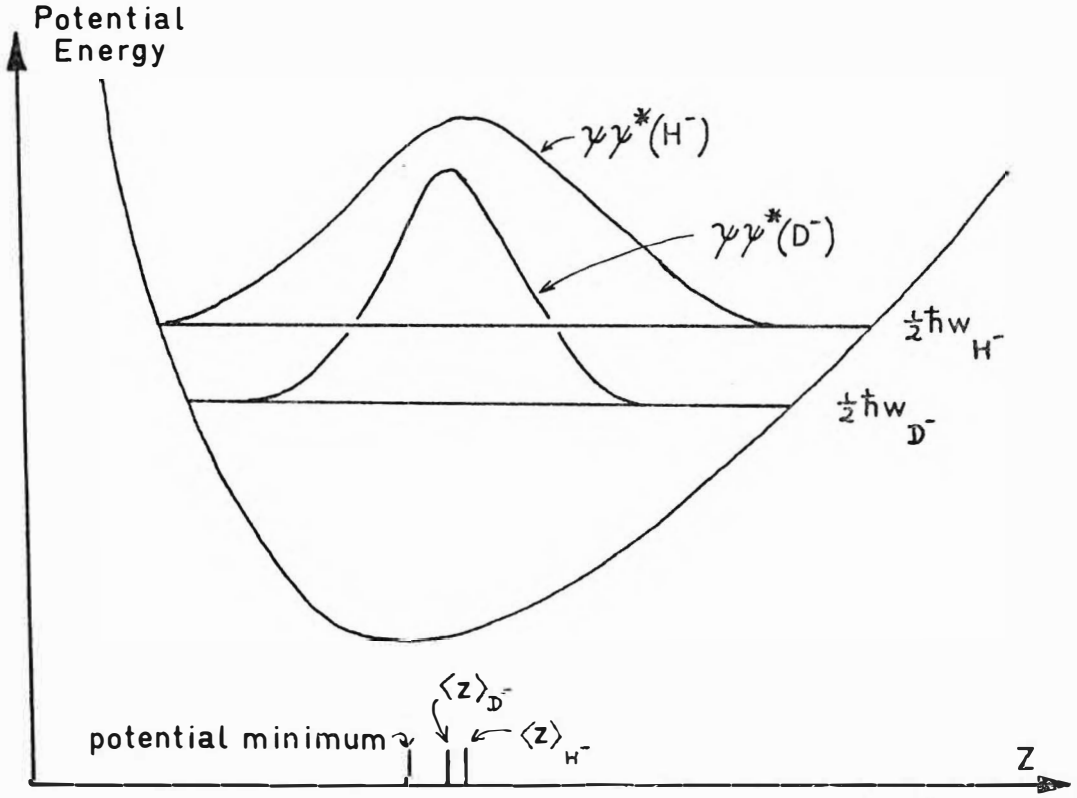

Fig 20: The ground state energies and wavefunctions of H^- and D^- ions in the asymmetric potential well of the Gd^{3+}-H^-/D^- site. The mean positions z differ for H^- and D^-, giving rise to the anharmonic isotope shift.

squares fitting of the parameters a,b,...,h and (6f+k) in equation (2-1) to the observations of Jones et al. There are seven parameters to fit to only five observations for each RE^{3+}-H_I^- pair, so the assumption was made that the three ion pairs could be characterised by common values of g, h and 6f+k. This assumption is physically reasonable since the equations (6-16) show that the quartic terms contain appreciable contributions from the cubic parameters B and C so they should be relatively insensitive to the particular rare earth ion in the RE^{3+}-H_I^- site. The parameter values which are obtained by this procedure are shown in Table 14. The parameter values which result when it is assumed that the quartic terms are all identically zero are also shown.

The relative signs of the odd parity terms c and d are fixed by the least squares fitting procedure but their absolute sign is uncertain since the inversion related Hamiltonians H(z) and H(-z) have identical eigenvalues. The only experimental observations which have been made that are sensitive to the overall sign of c and d are the isotope shift measurements in the EPR and optical spectra. The sign has therefore been chosen in accordance with these measurements, and the values

$$c = -2.00 \times 10^{12} \text{ ergs/cm}^2$$

$$d = -3.23 \times 10^{12} \text{ ergs/cm}^2$$

have been used throughout this work.

TABLE 14

Hydride ion potential well parameters for Gd^{3+}-H_I^- Sites in Calcium Fluoride crystals

ω_x sec^{-1}	ω_z sec^{-1}	$\|c\|$ $ergs/cm^3$	$\|d\|$ $ergs/cm^3$	g $ergs/cm^4$	h $ergs/cm^4$	6f+k $ergs/cm^4$	Standard Deviation cm^{-1}
1.931×10^{14}	2.138×10^{14}	2.13×10^{12}	2.15×10^{12}	-	-	-	.79 cm^{-1}
1.952×10^{14}	2.141×10^{14}	2.00×10^{12}	3.23×10^{12}	-1.8×10^{19}	9.8×10^{19}	-2.6×10^{20}	.14 cm^{-1}

(3) An Ionic Model for the Zero Field Splitting Isotope Shifts

The simple electrostatic model of the interaction between the $4f^7$ electron of the Gd^{3+} ion and the surrounding ligands which was discussed in part I of this chapter may also be used to calculate the magnitude of the electron-phonon interaction, and hence of the zero field splitting isotope shifts. In review, the major assumptions of this model are: (1) the ligands are represented by a point dipole and a point charge at the shifted lattice sites postulated by Kiro and Low[19], and (2) only the two dominant mechanisms are used to calculate the ground state splitting from the (screened) crystal field produced by the ligands. The reasonable success of this model in predicting the static crystal field parameter B_0^2 encourages its application to isotope shift calculations; in fact it should be more appropriate since the effect of a single ligand only (the H^- ion) need be considered.

It was shown in Chapter II that the electronic functions f_i and g_{ij} which occur in the electron-phonon interaction may be expanded in a series of the Spherical Tensors C_m^l. The expansion coefficients in these series have been evaluated by Zdansky[11] for the point charge and point dipole models, and are reproduced in Appendix I. For the point charge model we have that,

$$\langle M|f_z|M\rangle = \frac{-3e^2\langle r^2\rangle}{D^4}\langle M|C_0^2|M\rangle \qquad (6\text{-}18)$$

$$\langle M|g_{zz}|M\rangle = -\langle M|g_{xx}+g_{yy}|M\rangle = \frac{6e^2\langle r^2\rangle}{D^5}\langle M|C_0^2|M\rangle,$$

and for the point dipole model,

$$\langle M|f_z|M\rangle = \frac{12ep\langle r^2\rangle}{D^5}\langle M|C_0^2|M\rangle$$

$$\langle M|g_{zz}|M\rangle = \frac{-30ep\langle r^2\rangle}{D^6}\langle M|C_0^2|M\rangle \qquad (6\text{-}19)$$

$$\langle M|g_{xx}+g_{yy}|M\rangle = \frac{21ep\langle r^2\rangle}{D^6}\langle M|C_0^2|M\rangle,$$

$$\text{where} \quad p = \frac{\alpha_D(H^-)|e|}{D^2} .$$

Another important contribution to the electron phonon interaction arises from the dipoles which are induced on the other ligand ions by the point charge of the hydride ion. Since the polarisation of the ligand wavefunctions is a purely electronic effect, the induced dipoles can follow the nuclear motion of the hydride ion. The crystal field which the dipoles produce at the Gd^{3+} ion site is therefore modulated at the vibrational frequency of the hydride ion in the same way as for the direct point charge and point dipole mechanisms. The forms of f_i and g_{ij} for this dynamic F^- dipole mechanism calculated in reference (11) are in error and are corrected in Appendix I. The contributions of the four F^- ions which are common neighbours of the H_I^- and Gd^{3+} ion to the relevant matrix elements are given by,

$$\langle M|f_z|M\rangle = \frac{4e^2\alpha_D(F^-)}{R^4S^3}\left\{\frac{-3wv}{S^2}P_3^{\,1}(\frac{U}{R}) + 3(1-\frac{3v^2}{S^2})P_3^{\,0}(\frac{U}{R})\right\}$$

$$\times \langle r^2\rangle\langle M|C_0^2|M\rangle$$

$$\langle M|g_{zz}|M\rangle = -\frac{6e^2\alpha_D(F^-)}{R^4S^5}\left\{w(\frac{5v^2}{S^2}-1)P_3^{\,1}(\frac{U}{R}) + 3v(\frac{5v^2}{S^2}-3)P_3^{\,0}(\frac{U}{R})\right\}$$

$$\times \langle r^2\rangle\langle M|C_0^2|M\rangle \qquad (6\text{-}20)$$

$$\langle M|g_{xx}+g_{yy}|M\rangle = \frac{12e^2\alpha_D(F^-)}{R^4S^5}\left[w(3-\frac{5w^2}{2S^2})P_3^1(\frac{U}{R}) + 3v(1-\frac{5w^2}{2S^2})P_3^0(\frac{U}{R})\right]$$

$$\times \langle r^2\rangle\langle M|C_0^2|M\rangle,$$

where the meaning of the symbols is indicated in Figure A-1. The same formulae may be used to estimate the contribution of the remaining four F^- ions which are nearest neighbours of the Gd^{3+} ions.

It should be noted that in equations 6-18, 6-19 and 6-20 the higher order terms in C_0^4 and C_0^6 have been omitted because their coefficients are much smaller than that of C_0^2. If these terms were important they would produce an isotope shift in the spin Hamiltonian parameters b_4^0, b_6^0 since the matrix elements of O_4^0, O_6^0 have the same M-dependence as C_0^4, C_0^6; such a shift is not observed. Some care is needed in evaluating the matrix elements $\langle M|C_o^2|M\rangle$ since both the Hutchison and Wybourne (relativistic) mechanisms must be included.

The total zero field splitting isotope shift for $CaF_2:Gd^{3+}:H^-/D^-$ may be written as,

$$ZFSIS(H^--D^-) = |\Delta E_{\pm 7/2}(H^-) - \Delta E_{\pm 1/2}(H^-)| - |\Delta E_{\pm 7/2}(D^-) - \Delta E_{\pm 1/2}(D^-)| \qquad (6\text{-}21)$$

where ΔE_M denotes the isotope-dependent part of the electron phonon correction to the vibronic ground state energy E_M. This correction, which was previously evaluated in equation 6-13, may be logically divided into an "anharmonic" and "harmonic" part. The former consists of second order terms involving the anharmonic potential well parameters c and d,

whilst the harmonic part comprises the quadratic electron-phonon interaction terms g_{zz}, g_{xx} and g_{yy} acting in first order of perturbation. The physical origin of these two contributions may be readily visualised. Since the potential well of the X^- ion is asymmetric, the mean position of the X^- ion in the vibrational ground state does not coincide with the bottom of the potential well, as shown in Fig. 20. A straightforward calculation shows that,

$$\langle 000' | z | 000' \rangle = - \frac{6c\beta_z^4}{\hbar\omega_z} - \frac{4d\beta_z^2\beta_x^2}{\hbar\omega_z} \qquad (6\text{-}22)$$

and inserting numerical values we obtain shifts of .023, .016 and .013Å for H^-, D^- and T^- respectively. The anharmonic terms in the isotope shift expression (6-13) represent the differences in the crystal fields generated by the X^- anion for these three mean positions. The harmonic terms arise because the ground state wavefunction has a gaussian shape whose width is largest for the H^- ion, and smallest for T^-, reflecting the larger amplitude of vibration of the former ion. Since the crystal field produced by the X^- ion is a non-linear function of the Gd^{3+}-X^- separation, the charge of the X^- ion cannot be regarded as being wholly concentrated at the mean position. The correction for this smearing out of the charge differs for H^-, D^- and T^- because of their different amplitudes of vibration, and the harmonic terms in 6-13 represent the isotope dependence of this correction. The harmonic and anharmonic contributions to the ZFSIS of $CaF_2:Gd^{3+}:H^-/D^-$ have been calculated for the point charge, point dipole, and induced dipole models by inserting the

previously evaluated matrix elements of f_{zz}, g_{zz} and $g_{xx}+g_{yy}$ into equations 6-13 and 6-21. A shielding factor of $\sigma_2 = 0.6$[79,80] was used. Table 15 shows the results of this calculation.

It is evident from that table that the anharmonic contributions are generally much larger than the harmonic ones; this is to be expected since for the point charge model $-g_{zz} = g_{xx}+g_{yy}$, and only the anisotropy in ω prevents the harmonic contribution from vanishing. As in the static crystal field calculation, the point charge and point dipole of the H^- ion give the dominant contributions to the total calculated isotope shift. The effect of the induced F^- ion dipoles is relatively small, but it should be pointed out that it is very sensitive to lattice distortions. The factor $(1-3v^2/S^2)$ that occurs in equation 6-20 vanishes for the four F^- ions which are mutual neighbours of the Gd^{3+} and H_I^- ions if no lattice distortions are present. The sum of all the contributions in Table 15 is -.029 cm^{-1}, which is in very good agreement with the experimental result of -.028(±.02) cm^{-1} given in Chapter V. Considering the approximation involved in the model this degree of agreement is probably fortuitous.

The theory may also be applied, with very little modification, to calculate the isotope shift in the $^6P_{7/2}$ excited state which has been experimentally determined by Jones et al.[1] to be -2.4 (±.5) cm^{-1}. The calculated value is -2.2 which is again in excellent agreement with experiment.

Similar calculations to those described above have not been attempted for $SrF_2:Gd^{3+}:H^-/D^-$ because of the lack of information on second harmonic infrared frequencies from which

TABLE 15

Contributions to the ground state zero field splitting isotope shift for $CaF_2:Gd^{3+}:H^-/D^-$ calculated on a point charge/point dipole model

Origin	Anharmonic* Contribution	Harmonic* Contribution
Point Charge of H_I^-	-153	- 7
Point Dipole of H_I^-	-114	+15
Induced dipoles on $4F^-$ ions which are mutual neighbours of Gd^{3+} and H_I^-	- 4	-13
Induced dipoles on remaining $4F^-$ ions which are n.n. of Gd^{3+}	- 24	+10
TOTALS	-295	+ 5

* Units are 10^{-4} cm^{-1}

the cubic anharmonic parameters c and d are calculated. The experimental isotope shift for this system is larger than that for $CaF_2:Gd^{3+}:H^-/D^-$ by approximately 20%. The model discussed in this section predicts a 10% increase in the isotope shift due to the smaller values of ω_x and ω_z for SrF_2, but a 20% decrease due to the larger unit cell size for this lattice, assuming that the H_I^- ion remains at the centre of the cube of F^- ions. Larger values of the anharmonic parameters c and d could explain the larger isotope shifts which are observed in SrF_2, but detailed calculations must await the determination of these parameters.

CHAPTER VII

EPR SPECTRA OF TRIVALENT ERBIUM IN UNTREATED AND HYDROGENATED CALCIUM FLUORIDE

I. EPR SPECTRA OF ERBIUM IN CALCIUM FLUORIDE

Calcium fluoride crystals containing .05% ErF_3 were examined with the 35 GHz EPR Spectrometer over the temperature range of $3^{o}K$ to $20^{o}K$. The EPR spectra showed several sets of strong absorption lines, each of which was surrounded by eight subsidiary satellite lines. The main lines are due to the isotopes of erbium which have zero nuclear spin, and the eight satellite lines originate in the $_{68}Er^{167}$ isotope which has a nuclear spin of 7/2 and a natural abundance of 23%. It was anticipated that the hyperfine structure would be a source of difficulty when searching for the weak absorption lines expected for an Er^{3+}-H_I^- site in hydrogenated crystals. Consequently a small quantity of isotopically enriched erbium oxide was obtained from the Oak Ridge National Laboratory (Oak Ridge, Tennessee, U.S.A.) which contained 96% of the zero nuclear spin isotope $_{68}Er^{166}$ and only 3% of $_{68}Er^{167}$. The oxide was converted to erbium fluoride by heating it with ammonium bifluoride in a platinum crucible at $300^{o}C$, in accordance with the chemical process described by Spedding and Dane[81]. Most of the measurements reported here refer to crystals of CaF_2:Er^{166} (.05%); no measurements of hyperfine splittings were undertaken. The Q band EPR spectrum of CaF_2:Er^{166} for the magnetic field parallel to the (001) direction is shown in Figure 21.

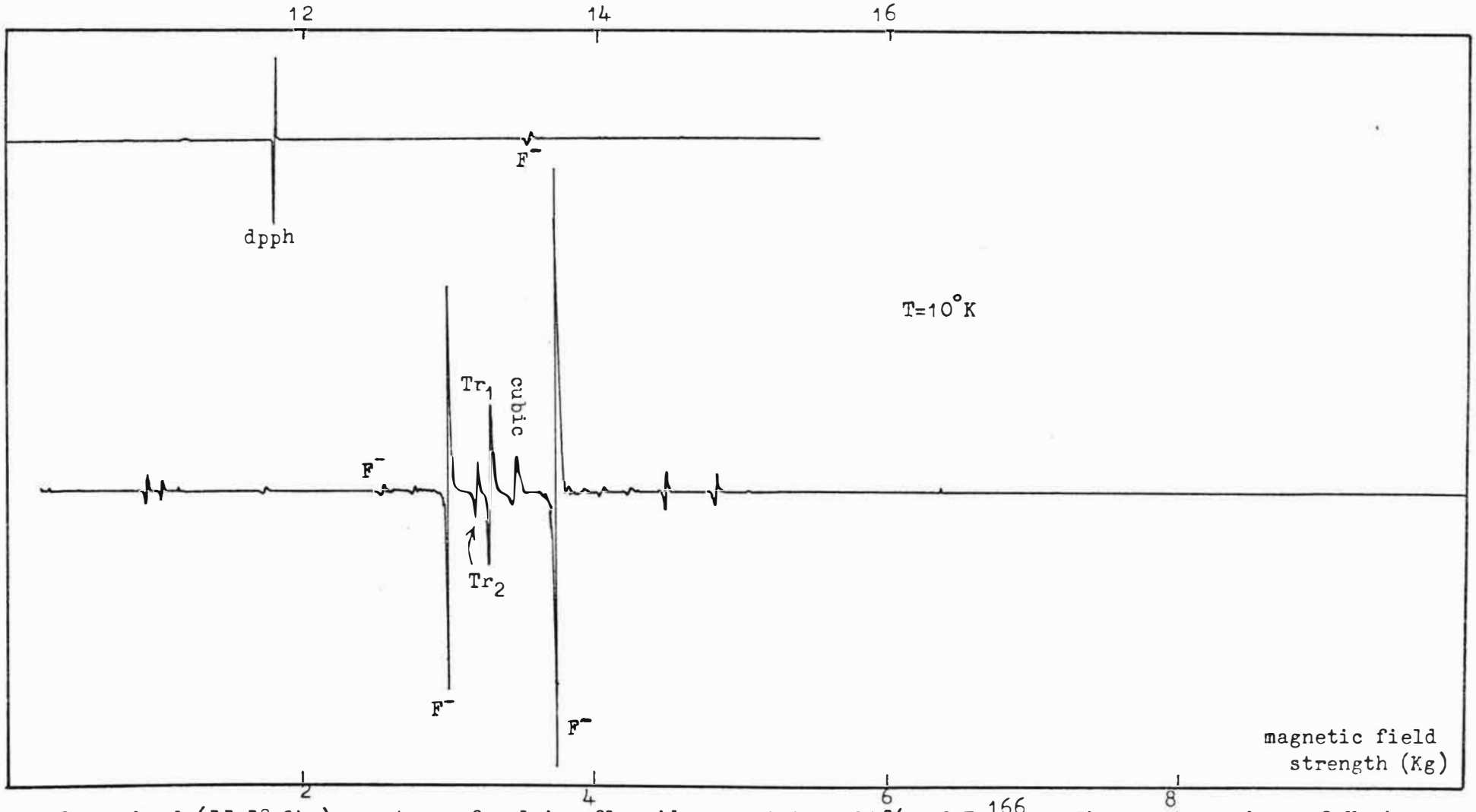

Fig.21: Q band (33.38 Ghz) spectrum of calcium fluoride containing .05% of $Er^{166}F_3$. The spectrum above 10 Kg is reproduced at the top left of the figure, and the lines marked F^- arise from the Er^{3+}-F_I^- site.

The angular dependence of the EPR spectra and the measured g values showed that the main absorption lines arose from a tetragonal Er^{3+}-F_I^- site, two trigonal Er^{3+} sites, and an Er^{3+} site of cubic symmetry, all of which have been reported in the literature[82-85]. The g values measured in this work are compared with those previously obtained in Table 16. The structure of the two trigonal sites has not yet been determined, but the site denoted Tr_2 in table 16 definitely involves oxygen ions because the Tr_2 spectrum was the only one observed in crystals doped with Er_2O_3 rather than ErF_3. The Tr_1 site occurred in all of the crystals doped with ErF_3, including some samples which showed only a very weak Tr_2 spectrum. Tentative identifications of the two sites are indicated in table 16.

The EPR spectrum of the first excited state of the tetragonal Er^{3+}-F_I^- site has been a source of confusion because whilst the origin of the spectrum was correctly identified by Baker et al.[84], their published value of $g_\perp$ is in error, being given as 6.76 instead of 1.746. Ranon and Low[83] reported the correct g values in a later work but these authors ascribed the spectrum to a different centre. The g values found in this work agree with those of Ranon and Low, and the identification of the spectra by Baker et al. was verified by measuring the temperature dependence of the spectrum. If E_u and E_ℓ are the energies of the upper and lower states involved in the EPR transition then the intensity of the transition is given by,

TABLE 16

G-values for various Er^{3+} sites in calcium fluoride.

Site	$T^{o}K$	Symmetry	$g_{//}$	$g_{\perp}$	Reference
Er^{3+}	20	Cubic	6.785 ± .002	-	Dvir & Low[82]
"	20	"	6.78 ± .01	-	Ranon & Low[83] Baker et al.[84]
"	5	"	6.774 ± .005	-	This work
$Er^{3+}-F_I^-$	20	Tetragonal	7.76 ± .02	6.253 ± .006	Baker et al.[84]
$Er^{3+}-F_I^-$	20	Tetragonal	7.78 ± .02	6.254 ± .005	Ranon & Low[83]
"	5	"	7.761 ± .007	6.252 ± .005	This work
"	20	"	1.746 ± .002	9.16 ± .01	Ranon & Low[83]
"	20	"	6.76 ± .02*	9.11 ± .01	Baker et al.[84]
"	5	"	1.746 ± .002	9.12 ± .01	This work
$Er^{3+}-F_I^-$?	20	Trigonal Tr_1	3.30 ± .01	8.54 ± .02	Ranon & Low[83]
"	5	"	3.275 ± .004	8.38 ± .02	This work
$Er^{3+}-F_7^--O^{2-}$?	4.2	Trigonal Tr_2	2.1853 ± .001	8.828 ± .003	Vorobko et al.[85]
"	20	"	2.206 ± .007	8.843 ± .010	Ranon & Low[83]
"	5	"	2.190 ± .002	8.823 ± .01	This work

* This value must be in error

$$I = K \sinh(\hbar\omega/2kT) \exp(-E/kT) \qquad (7\text{-}1)$$

where $E = (E_u+E_\ell)/2$,

and ω is the microwave frequency. A least squares fitting of the observed intensity to equation 7-1 showed that the best fit value for E was 20 cm^{-1}, in excellent agreement with the optically determined position (21 cm^{-1}) of the first excited state for the tetragonal Er^{3+}-F_I^- site[132].

The angular dependence of the EPR spectra of this excited state was interesting because it appeared at first that, for certain orientations of the magnetic field, the crystal was emitting rather than absorbing microwave power. As the magnetic field orientation approached the direction of the four-fold symmetry axis the intensity of the EPR line rapidly diminished. A few degrees past the axis the line vanished, and beyond this point the line reemerged with the opposite phase to that observed previously. This reversal of phase can be interpreted as a change from an absorption lineshape to an emission lineshape and it is important to establish whether emission is actually occurring. After further examination it was found that the effect was partly instrumental in origin and partly due to the large anisotropy of the g values for the tetragonal Er^{3+}-F_I^- excited state. The standard reference works on EPR do not mention this effect and it seems to have been hitherto unknown. It therefore is desirable to give a generalised discussion of this effect since it can occur when the magnetic resonance of any paramagnetic species which has sufficiently anisotropic g values is examined in a standard EPR spectrometer.

(1) The Orientation Modulation Effect

Suppose that the main magnetic field H is being rotated in the xy plane of some laboratory coordinate system (xyz) and makes an angle θ with the x axis as shown in Fig. 22. Suppose also that the modulation field $H_m \cos \omega t$ is fixed along the x axis, and that we are examining a paramagnetic species of axial symmetry with the $g_{//}$ axis in the xy plane making an angle ϕ with the x axis.

The important point to note is that the field H is modulated not only in amplitude by $H_m \cos \theta \cos \omega t$ gauss, but also in orientation by $\frac{-H_m}{H} \sin \theta \cos \omega t$ radians. This latter orientation modulation has hitherto been ignored but is important for anisotropic spectra since it results in the EPR line oscillating around the field value H and hence producing a second kind of signal at the detector. Suppose that the overall signal produced at the detector is V, that the EPR line is centred about the value $H_o(\theta)$, and that the modulation amplitude is very small compared to the linewidth. Then we have that for small changes in H and H_o,

$$\begin{aligned} \Delta V &= \frac{\partial V}{\partial H} \Delta H + \frac{\partial V}{\partial H_o} \Delta H_o \\ &= \frac{\partial V}{\partial H} \Delta H - \frac{\partial V}{\partial H} \Delta H_o \\ &= \frac{\partial V}{\partial H} \left(\Delta H - \frac{\partial H_o}{\partial \theta} \Delta\theta\right). \end{aligned} \tag{7-2}$$

Using the usual effective g-value expression,

$$g^2 = g_{//}^2 \cos^2(\theta-\phi) + g_{\perp}^2 \sin^2(\theta-\phi), \tag{7-3}$$

and the values of ΔH and $\Delta\theta$ evaluated above, equation 7-2 becomes

$$\Delta V = \frac{\partial V}{\partial H} H_m \cos \omega t \left[\cos \theta + \frac{\sin \theta \sin 2(\theta-\phi)(g_{//}^2 - g_{\perp}^2)}{2g^2}\right] \quad (7-4)$$

The first term in the bracket in equation (7-4) is the usual amplitude modulation term, and the second term is the new orientation modulation expression. The latter can become significant if $g_{//}$ and $g_{\perp}$ are markedly different, and can exceed the amplitude modulation for strongly anisotropic spectra.

In the case of Er^{3+}-F_I^- in CaF_2 $g_{//} = 1.746$, $g_{\perp} = 9.12$, $\phi = 48^{o}$. The expression in square brackets in equation (7-4) has been evaluated for this case and is plotted in Figure 23 along with the experimentally observed (normalised) EPR amplitudes. The experimental points in Fig. 23 have been corrected for off-axis line broadening. This effect was measured using pole-piece modulation coils. Deviations from the predicted curve may be due to an inhomogeneous modulation field (the sample size was one half of the radius of the modulation coils), or to an error in measuring ϕ.

This phase reversal effect has also been observed for other spectra of Er^{3+} where the g anisotropy is sufficiently large. In each case equation (7-4) correctly predicts the phase reversal effect and the angle at which it occurs (usually a few degrees past the $g_{//}$ axis).

In conclusion, it appears that the observed phase reversals are adequately explained by orientation modulation and that microwave emission does not occur.

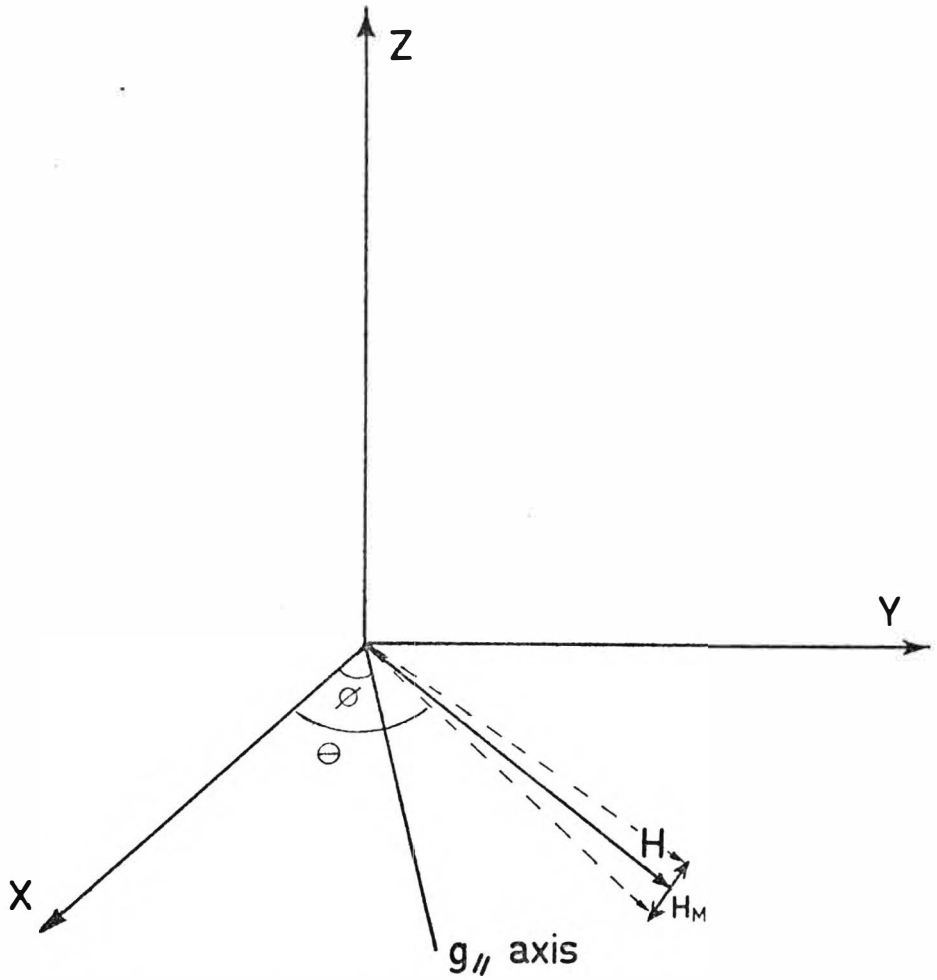

Fig 22: The geometry of the EPR experiment referred to in the text.

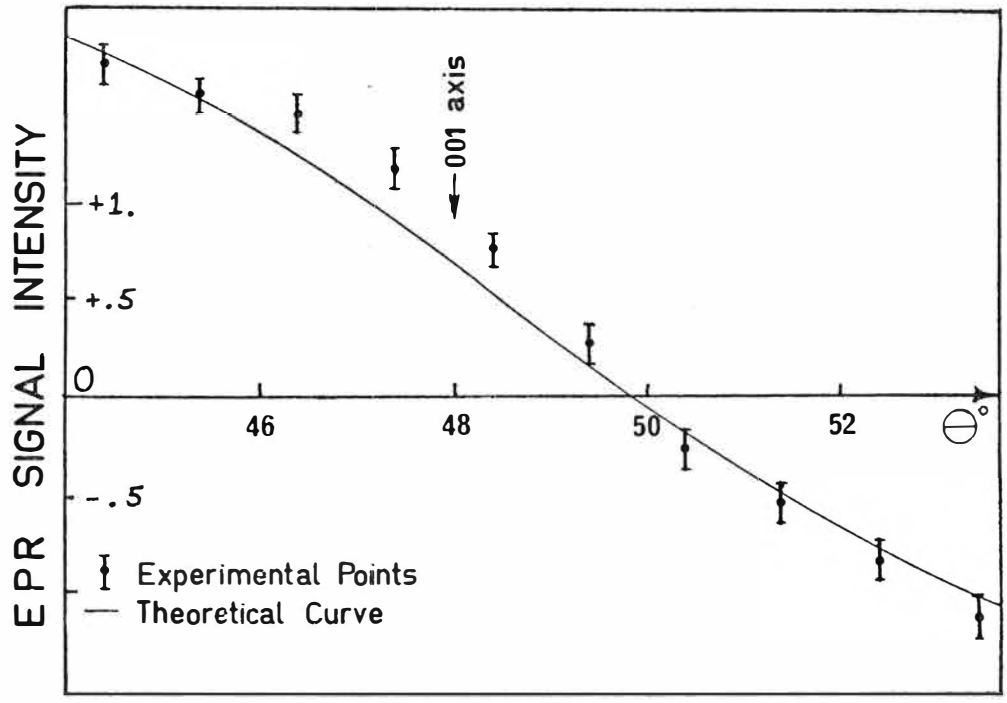

Fig 23: Comparison of the experimental and theoretical EPR line intensities about the $g_{//}$ axis.

(2) Minor Features of the $CaF_2:Er^{3+}$ EPR Spectrum

Several weak EPR lines were also observed which were less than one twentieth as intense as the lines of the main sites. Although the angular dependence of these lines was not investigated in detail, their effective g values were measured for H//001 at a frequency of 33.38 GHz with the results that g = 24.0, 21.6, 13.14, 5.56, 5.24 and 4.88. The first two values are interesting because they exceed the largest g value which has been observed for any rare earth ion in calcium fluoride, which is g = 17.8 for a Tb^{3+} site[86]. The observed lines do not show the characteristic I = 3/2 hyperfine splitting of Tb^{3+} and so cannot be due to this ion. A possible explanation of the anomalously large effective g value is that the transition is between the levels of two different Kramers doublets which have a separation of about 1 cm^{-1}. This was confirmed by measuring the field strengths of the lines for various frequencies in the Q band; this showed that the difference in the slopes of the energy levels for the g = 24.0 line did not correspond to a Kramers doublet with $g = 24$, but rather to a Δg of $8.5 \pm .5$. If it is assumed that the energy levels are linear functions of the field then the separation of the two Kramers doublets is .7 cm^{-1}.

II. THEORETICAL INTERPRETATION OF THE G VALUES FOR THE TETRAGONAL Er^{3+}-F_I^- SITE

Smirnov[87] and Presland[10] have obtained sets of crystal field parameters B_m^n for the tetragonal Er^{3+}-F_I^- site by fitting the optical and EPR data for this site to the crystal field Hamiltonian 6-1. Smirnov did not attempt a full least-squares fitting to the known energy level scheme, but used an argument based on the form of the wavefunction for the lowest $^4I_{15/2}$ level (Z_1). The parameters which he derived satisfactorily predict the positions of the first three $^4I_{15/2}$ levels (Z_1-Z_3), and the g values of the Z_1 and Z_2 levels, but the predicted positions of the higher $^4I_{15/2}$ shifts (Z_4-Z_8) and the Stark splittings of the excited state multiplets are in poor agreement with experiment. Presland[10] has derived a different set of parameters by a least squares fitting technique applied to the known energy levels of the $^4I_{15/2}$ multiplet (Z_1-Z_8) and the g values of the Z_1 and Z_2 states. These parameters accurately predict the known data for that multiplet, and also satisfactorily predict the Stark splittings of the excited state multiplets. Although the g values of the Z_1 and Z_2 states have thus been satisfactorily explained by the full crystal field analysis of Presland, the following section will consider a more limited approach which does, however, give some physical insight into the origin of the g values and the possible combinations of $g_{/\!/}$ and $g_\perp$ which may occur.

The total crystal field is considered to consist predominantly of the cubic potential of a site of O_h symmetry together with a tetragonal perturbation due to the

interstitial F^- ion. Lea, Leask and Wolf[88] have numerically calculated the eigenvalues and eigenvectors of several J multiplets for a cubic crystal field. Their eigenvalue diagram for J = 15/2 is reproduced in Figure 24; the ordinate X is a parameter defined by Lea, Leask and Wolf which is determined by the relative magnitudes of the crystal field parameters B_4 and B_6.

The appropriate value of X in the present case may be deduced by comparing the theoretical g values of 6.8 and 6.0 for the Γ_7 and Γ_6 doublets in Figure 24 with the experimentally measured ground state g values of 6.77 for the cubic Er^{3+} site[83], and 5.91 for the cubic site of the isoelectronic Ho^{2+} ion. This shows that the ground state of the Er^{3+} ion is Γ_7, whilst for Ho^{2+} it is Γ_6 and thus the value of X for these two ions must be close to -0.45 where the Γ_6 and Γ_7 levels cross. The value for Er^{3+} must be greater than this to make the ground state Γ_7 and it is convenient to choose X = -0.4 since Lea, Leask and Wolf[88] have tabulated the wavefunction for this value.

In a tetragonal crystal field the three Γ_8 quartets each split in a γ_6 and γ_7 doublet, and the single Γ_6 and Γ_7 doublets become γ_6 and γ_7 doublets respectively. (Here the γ are labels for the irreducible representations of the C_{4v} group.) The g values of the $|\Gamma_6\gamma_6>$ and $|\Gamma_7\gamma_7>$ doublets are no longer isotropic as in the cubic case because the tetragonal crystal field mixes the Γ_6 and Γ_7 with the Γ_8 states. From Figure 22 it is evident that the two upper Γ_8 quartets are widely separated from the Γ_6, Γ_7 and $\Gamma_8{}^1$ states at X = -0.4, and so their admixture into the Γ_7 and Γ_6 states should be

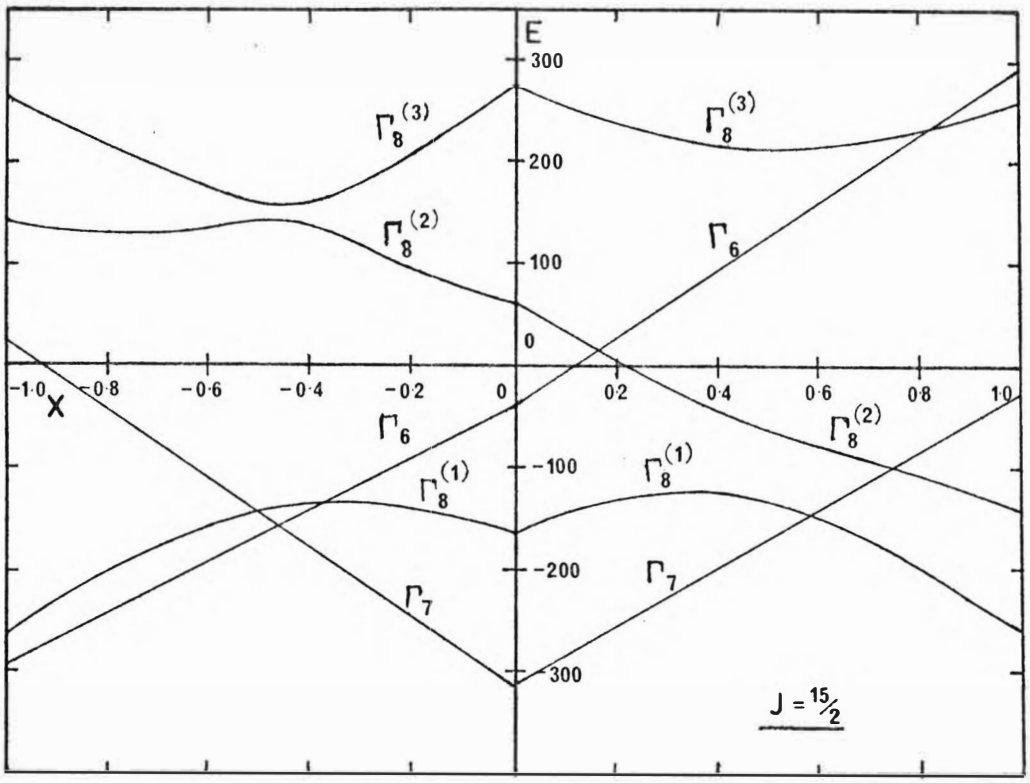

Fig. 24: Energy level diagram for a J=15/2 multiplet in a cubic crystal field, reproduced from Lea, Leask, and Wolf[88].

The ordinate X is defined by,

$$\frac{B_4}{B_6} = \frac{X}{1 - |X|} \frac{F(6)}{F(4)} ,$$

where F(4) and F(6) are Stevens' multiplying factors.

$B_4/B_6=0$ for X=0, and $B_4/B_6=\pm\infty$ for $X=\pm 1$.

negligible for small tetragonal perturbations. The wavefunctions for the $|\Gamma_6\gamma_6>$ and $|\Gamma_7\gamma_7>$ states may therefore be taken as

$$|\Gamma_6\gamma_6> = \text{Cos } \theta|\Gamma_6> + \text{Sin } \theta|\Gamma_8{}^1\gamma_6>,$$

$$|\Gamma_7\gamma_7> = \text{Cos } \theta|\Gamma_7> + \text{Sin } \theta|\Gamma_8{}^1\gamma_7>, \qquad (7\text{-}5)$$

where $|\Gamma_8{}^1\gamma_6>$, $|\Gamma_8{}^1\gamma_7>$ are the components of the $\Gamma_8{}^1$ quartet which form bases for the γ_6, γ_7 representations of the C_{4v} group respectively. The g values of these two wavefunctions have been calculated for $-\pi/2 \leqslant \theta \leqslant \pi/2$ and are plotted in Figures 25(a) and 25(b). The g values of the Er^{3+}-F_I^- site may be fitted by the following angles

$$\theta(\gamma_7) = 3^o50' \quad g_{/\!/} = 7.82(7.78) \quad g_\perp = 6.22(6.25),$$

$$\theta(\gamma_6) = -38^o \quad g_{/\!/} = 1.76(1.75) \quad g_\perp = 9.12(9.12),$$

where the associated g values are also given and the experimental g values are listed in brackets. A value of $\theta \simeq 59^o$ also fits the γ_7 ground state but it is physically unreasonable because the $\Gamma_8{}^1$-Γ_7 energy separation is much greater than the $\Gamma_8{}^1$-Γ_6 spacing and so the admixture for the γ_7 levels should be less than for the γ_6.

Thus the experimental g values of the tetragonal Er^{3+}-F_I^- can be closely fitted by the theoretical g values of wavefunctions which are admixtures of the Γ_6 and $\Gamma_8{}^1$ states, or of the Γ_7 and $\Gamma_8{}^1$ states. It may be anticipated that the g value plots in Figures 25(a) and 25(b) will be a useful guide in interpreting the EPR spectra of the Er^{3+}-H_I^- site. One particular point of interest is that both $g_{/\!/}$ and $g_\perp$ are

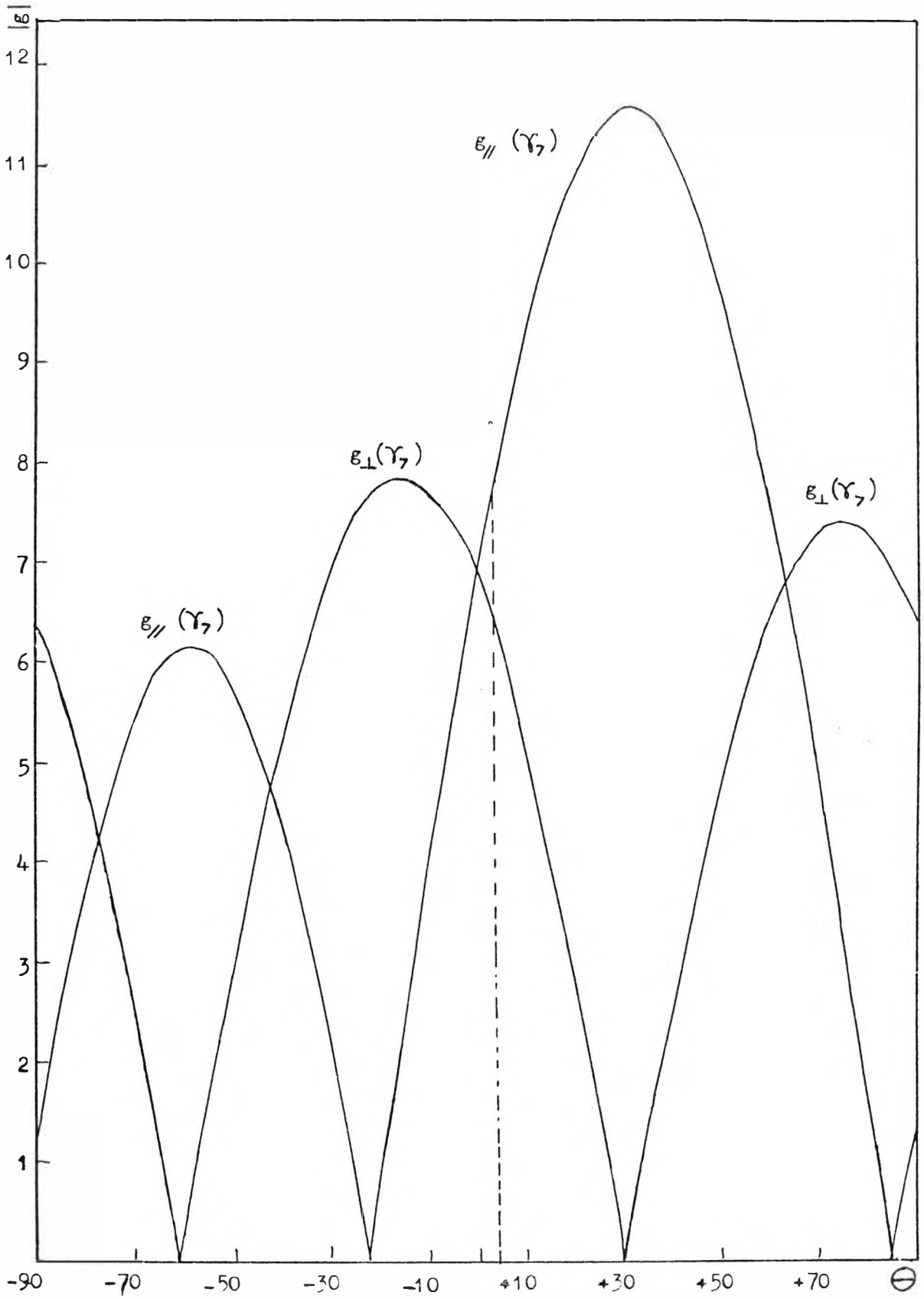

Fig.25(a): Values of $g_{//}$ and $g_{\perp}$ for wavefunctions which are admixtures of cubic crystal field eigenfunctions. The appropiate values of Θ for the Er^{3+}- F_I^- sites are indicated by dashed lines. Results for the γ_6 state are plotted overleaf.

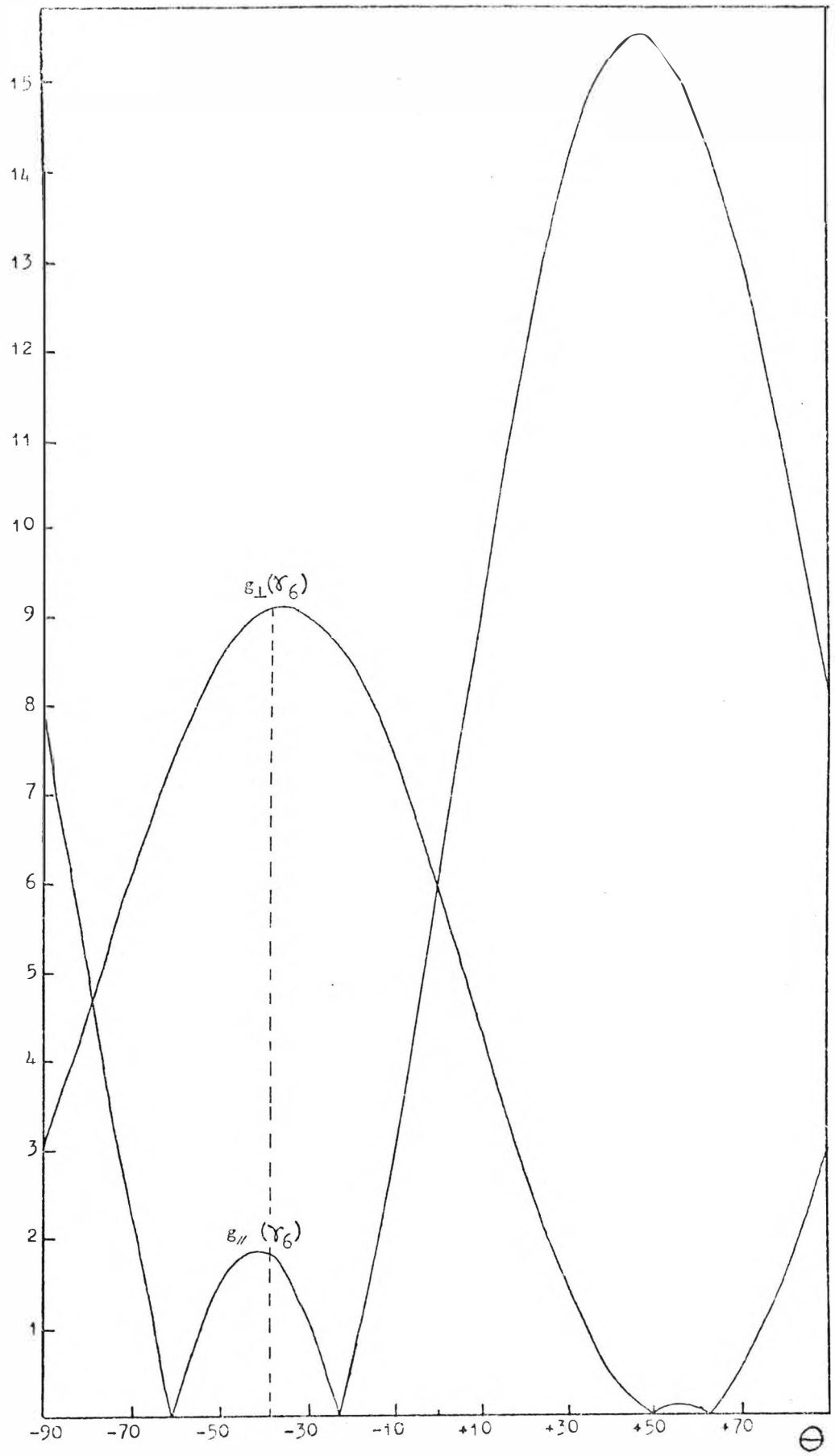

Fig.25(b): Values of $g_{//}$ and $g_\perp$ (continued).

near turning points for the γ_6 state of Er^{3+}-F_I^- and so any small change in the admixture coefficients will not affect these g values greatly.

III. THE EPR SPECTRA OF HYDROGENATED CRYSTALS OF ERBIUM-DOPED CALCIUM FLUORIDE

(1) Introduction

The optical spectra of hydrogenated CaF_2:Er^{3+} crystals has been investigated in this laboratory by M. Presland[10], with the following results: Two new sets of absorption lines appeared after hydrogenation, and one of these showed an isotope shift when deuterium was substituted for hydrogen and was also correlated in intensity with the I.R. spectrum observed by Jones et al.[6]. The corresponding Er^{3+} site was therefore identified as having the tetragonal RE^{3+}-H_I^- structure discussed earlier in this work; the site responsible for the other set of lines was not identified. By comparing transitions between different multiplets a partial energy level scheme for the Er^{3+}-H_I^- site was deduced, with the important result for this work that the lowest states of the ground $^4I_{15/2}$ multiplet are closely spaced, as shown in figure 28b. The EPR spectrum of the site is therefore expected to be complicated, because both the Z_1 and Z_2 Kramers doublets will be populated at temperatures above about 4^oK, and also because of magnetic field mixing of the Z_1 and Z_2 eigenstates for off-axis field directions.

(2) The EPR Spectra of Hydrogenated Crystals

Crystals of calcium fluoride containing .05% ErF_3 which had been hydrogenated for twelve hours at 850°C showed a complicated EPR spectrum for H//001, indicating the formation of several new Er^{3+} sites. When the magnetic field was rotated away from the 001 axis in the 010 plane some of the new lines split into four components, a characteristic of sites of rhombic symmetry. The large number of magnetically inequivalent sites for these rhombic sites and the large number of Er^{3+} centres in the crystals made detailed examination difficult. However, the g_x and g_y axes of one rhombic site were located in the $\bar{1}10$ plane; g_x = 9.69(±.01) and the axis is tilted by 23.3° from the 001 direction, and g_y = 3.238(±.005). A site with trigonal symmetry about the (111) axis was also identified and the values g = 3.672 (±.005) and g = 8.27(±.02) were measured. The g values of the latter site are the same, to within experimental uncertainty, for deuterated crystals. The room temperature infrared spectrum of these crystals is also complex, in addition to the two absorption lines of the tetragonal Er^{3+}-H_I^- site observed by Jones et al.[6], there are also strong lines at 1056, 1139, 1261, 1303 and 1374 cm^{-1}. The lines at 1056 and 1139 cm^{-1} are correlated from crystal to crystal and increase in intensity when a crystal is stored at room temperature for a few months.

The large number of different Er^{3+} sites observed in these samples precluded the identification of the EPR lines of the tetragonal Er^{3+}-H_I^- centre. Consequently a second batch of crystals was prepared by hydrogenating at 700°C for six hours. The infrared spectrum of these crystals only showed

the lines of the Er^{3+}-H_I^- site, and the EPR spectrum (figure 26) was also much simpler than for the more strongly hydrogenated samples. However, the maximum intensity of any of the new EPR lines was only about one thirtieth that of the lines which were also present in the untreated crystals.

(3) Interpretation of the EPR Spectra

The new absorption lines which appear after hydrogenation are labelled R_1, R_2, Tg_1...Tg_3 in figure 27. The lines R_1 and R_2 are due to the rhombic site which was discussed in the previous section. It is tempting to equate this site with that observed optically by Presland because of the simultaneous occurrence and the absence of isotope shifts for the two spectra; however, the excited Z_2 state at 8 cm^{-1} reported by Presland[10] was not observed in this work.

The proposed interpretation of the three Tg lines is as follows: The three lines are due to the tetragonal Er^{3+}-H_I^- site; specifically the Tg_1 and Tg_2 lines are transitions within an excited γ_6 (Z_2) Kramers doublet for field directions perpendicular and parallel to the four fold axis respectively, and the Tg3 line is a transition within the ground $\gamma_7(Z_1)$ doublet for the parallel field orientation. The EPR line for the ground doublet in the perpendicular field orientation is obscured by the equivalent line for the Er^{3+}-F_I^- site. This interpretation is based on the following observations:

(a) Angular Dependence of the Spectra. All of the Tg lines were either at maximum or minimum field strengths when the field was parallel with the (001) crystalline axis. The g values for other field directions in the (100) plane are indicated in figure 27 in the form of a plot of g^2 versus $\cos^2\theta$, where θ is the angle between the field direction and

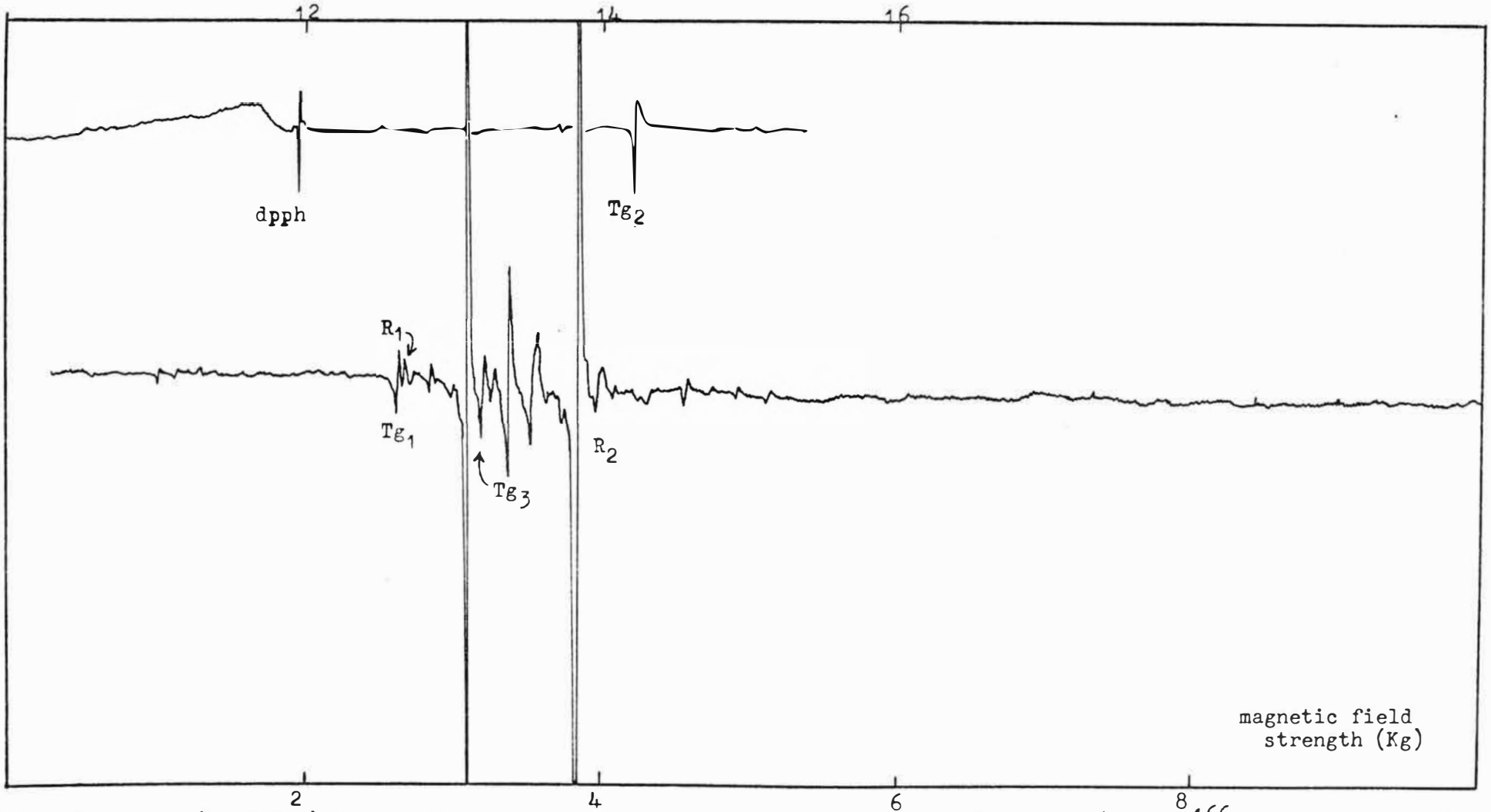

Fig.26: Q band (33.5 Ghz) EPR spectrum of hydrogenated calcium fluoride containing .05 % of $Er^{166}F_3$, recorded at 5^oK. The spectrum above 10 Kg is reproduced at the top left of the figure, and the line labels are explained in the text.

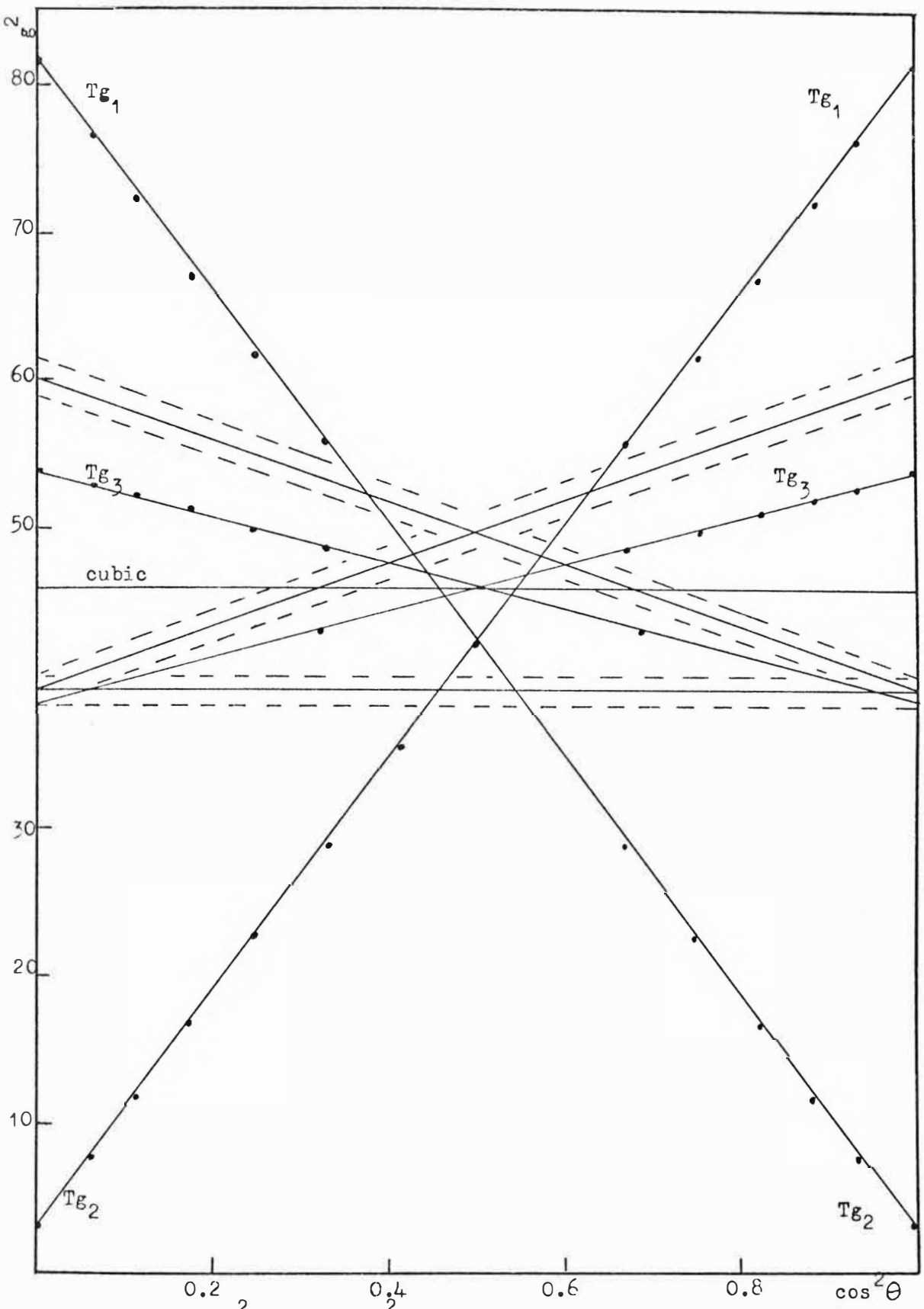

Fig.27: Plot of g^2 versus $\cos^2\theta$ for deuterated calcium fluoride doped with .05% $Er^{166}F_3$ when the magnetic field is rotated in the (100) plane and makes an angle θ with the (001) axis. The unlabelled lines are for the $Er^{3+}F^-_I$ site, and the dashed lines indicate their linewidths. Solid dots represent the experimental measurements.

the (001) axis. This form of plot is useful in EPR analysis because a straight line should result for an isolated Kramers doublet. Values of g^2 and the linewidths of the Er^{3+}-F_I^- ground state are also given in figure 27 so as to indicate the regions of the spectrum for which weak lines are obscured.

It is evident from the diagram that the points for the Tg_1 and Tg_2 lines can be interpolated with a straight line, indicating that these transitions occur within the same Kramers doublet. In the interpretation given here the Tg_1 line for H//001 should strictly be a degenerate doublet which splits into two distinct component lines for other field orientations. Only a single line is observed. However a transition probability calculation[131] for the relative orientations of the crystal, static magnetic field and RF field used here shows that the intensity of the second component should be only $g_{//}^2/g_{\perp}^2 = 1/33$ that of the observed component; hence the apparent absence of the second component line is satisfactorily explained.

The results for the Tg_3 line may also be fitted with a straight line. By extrapolating to $\theta = 90^o$ it is possible to predict a value of $g_{\perp}$ of approximately 6.1, which is sufficiently close to $g_{\perp}$ (6.25) for the Er^{3+}-F_I^- site for the corresponding EPR line to be obscured.

(b) G Values and Isotope Shifts. The measured g values for the three lines for both hydrogenated and deuterated crystals are given in table 17. There is a well resolved isotope shift in $g_{//}$ for the ground state, but the shifts observed for the γ_6 excited state are within the estimated experimental uncertainties. However, for $g_{//}$ the results given are the average of four measurements on different

crystals and the standard deviation was less than .002. The difference in the g values is, therefore, significant. Furthermore the Tg_2 line displays an unusual asymmetric lineshape which differs reproducibly between hydrogenated and deuterated crystals. (A possible cause of this asymmetry will be discussed later.) The g values and very small isotope shifts for the Tg_1 and Tg_2 lines are consistent with the insensitivity of the g values for a $|\Gamma_6\gamma_6>$ state near $\theta = -38^{\circ}$, as shown in Fig. 25(b). The Tg_1 and Tg_2 lines are therefore assigned to a Kramers doublet of this symmetry designation.

(c) Temperature Dependence. The Tg_3 line increased in intensity monotonically as the temperature was reduced from $15^{\circ}K$ to $3^{\circ}K$, in accordance with the normal $\exp(-\hbar\omega/kT)$ dependence for a Kramers doublet ground state. In contrast the Tg_2 line attains a maximum intensity at about $7.5^{\circ}K$ for H^- and $6^{\circ}K$ for D^-, and diminishes in amplitude above and below these temperatures. By fitting the observed line intensities between $3^{\circ}K$ and $15^{\circ}K$ to the expression (7-1) it was found that the Tg_2 line corresponds to a transition between two excited states whose mean energy is 7 cm^{-1} (H^-) or 5 cm^{-1} (D^-) above the ground state at a field of 14 Kg. If the proposed value of $g_{//}$ for the ground state is accepted then at zero field the excited doublet lies at 4 $cm^{-1} \pm 1$ cm^{-1} (H^-) or 2 $cm^{-1} \pm 1$ cm^{-1} (D^-) above the ground state, in good agreement with the optical measurements.

(4) The Form of the Spin Hamiltonian

The form of the spin Hamiltonian which is appropriate in the present case can be deduced from the results given in Appendix II. For S = 3/2 the non-zero terms are:

$$SH = b_2^0 T_2^0(S) + \beta\Big({}^1g_{/\!/} H_z S_z + {}^1g_{\perp}(H_x S_x + H_y S_y) + {}^2g_{/\!/} H_z T_3^0(S)$$
$$+ {}^2g_{\perp}(H_x(T_{31}(S) + T_{3-1}(S)) - iH_y(T_{31}(S) + T_{3-1}(S)))$$
$$+ {}^3g_{\perp}(H_x(T_{33}(S) - T_{3-3}(S) - iH_y(T_{33}(S) + T_{3-3}(S)))\Big). \quad (7\text{-}6)$$

This expression contains six unknown parameters, whereas only three transitions were observed, and so it is not possible to determine their values. The parameter b_2^0 is particularly significant because this determines the γ_6-γ_7 separation in zero field. Figure 28a shows the energy level diagram for the parallel field orientation when the optical data is used to evaluate the γ_6-γ_7 spacing. The latter could be directly determined by EPR if the transition shown in the figure between the $|\gamma_6\gamma_6'\rangle$ and $|\gamma_7\gamma_8'\rangle$ states could be observed. (Here the γ_n' are irreducible representations of the C_4 group, which is the site symmetry with H//z.) However, the corresponding EPR line is expected to be very broad and of low amplitude because the γ_6-γ_7 spacing is sensitive to strain induced variation in the crystal field. In contrast the observed lines, which are transitions within Kramers doublets, are insensitive to strain to first order.

Second order effects provide a possible explanation of the asymmetry of the Tg_2 line. This asymmetry is most unusual because it is the reverse of that which is frequently observed for paramagnetic ions in, for example, solutions or crystals

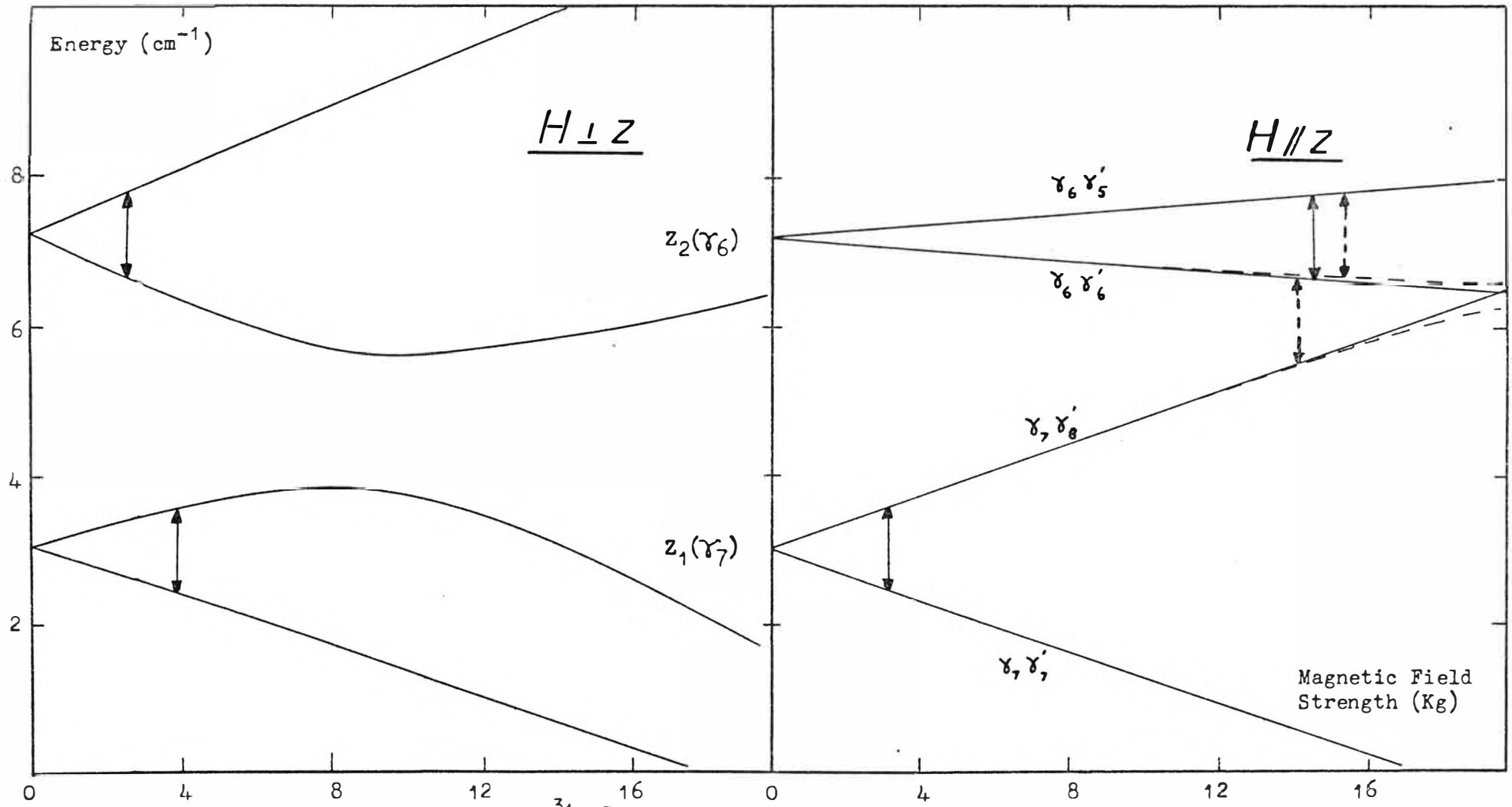

Fig. 28(a) Energy level diagram for the Er^{3+} - H_1^- site as calculated from the estimated crystal field parameters. Observed and possible transitions are denoted by solid and broken double arrows respectively. The effect of a crystal field perturbation of rhombic symmetry for the H//z case is indicated by dashed lines.

with a mosaic structure. The cause of the asymmetry in these cases is the distribution of principal axis directions within the sample, and the nett effect for axial spectra is that the $g_{//}$ line is broadened on the side closest to the $g_{\perp}$ line, and vice versa. However, the Tg_2 line is broadened on the high field side for both hydrogenated and deuterated crystals; the asymmetry being much more pronounced in the latter case. The effect is not instrumental in origin because the equivalent $g = 1.746$ line for the Er^{3+}-F_I^- site, which could be observed at higher temperatures, was recorded with a symmetrical lineshape.

A possible explanation is that impurity-induced random strains within the crystal produce a small crystal field component of rhombic (C_1) symmetry, which varies randomly from site to site, superimposed on the dominant C_{4v} component. In this case the levels which were labelled $|\gamma_6\gamma_6'\rangle$ and $|\gamma_7\gamma_8'\rangle$ for pure C_4 symmetry can no longer intersect and are repelled from each other, as shown schematically in figure 28a. The deviations from the behaviour expected for C_4 symmetry will only be significant when the levels are near degenerate, which occurs for Er^{3+}-H_I^- at about 21 kg and for Er^{3+}-D^- at about 14 kg. Suppose that the rhombic crystal field component $V(C_1)$ follows some symmetrical distribution function which has a maximum at $V(C_1) = 0$. The corresponding distribution function of resonant field strengths for the Tg_2 line will rise sharply to a peak at the field corresponding to the case of $V(C_1) = 0$, but then will gradually diminish for higher field values, in accordance with the observed lineshape.

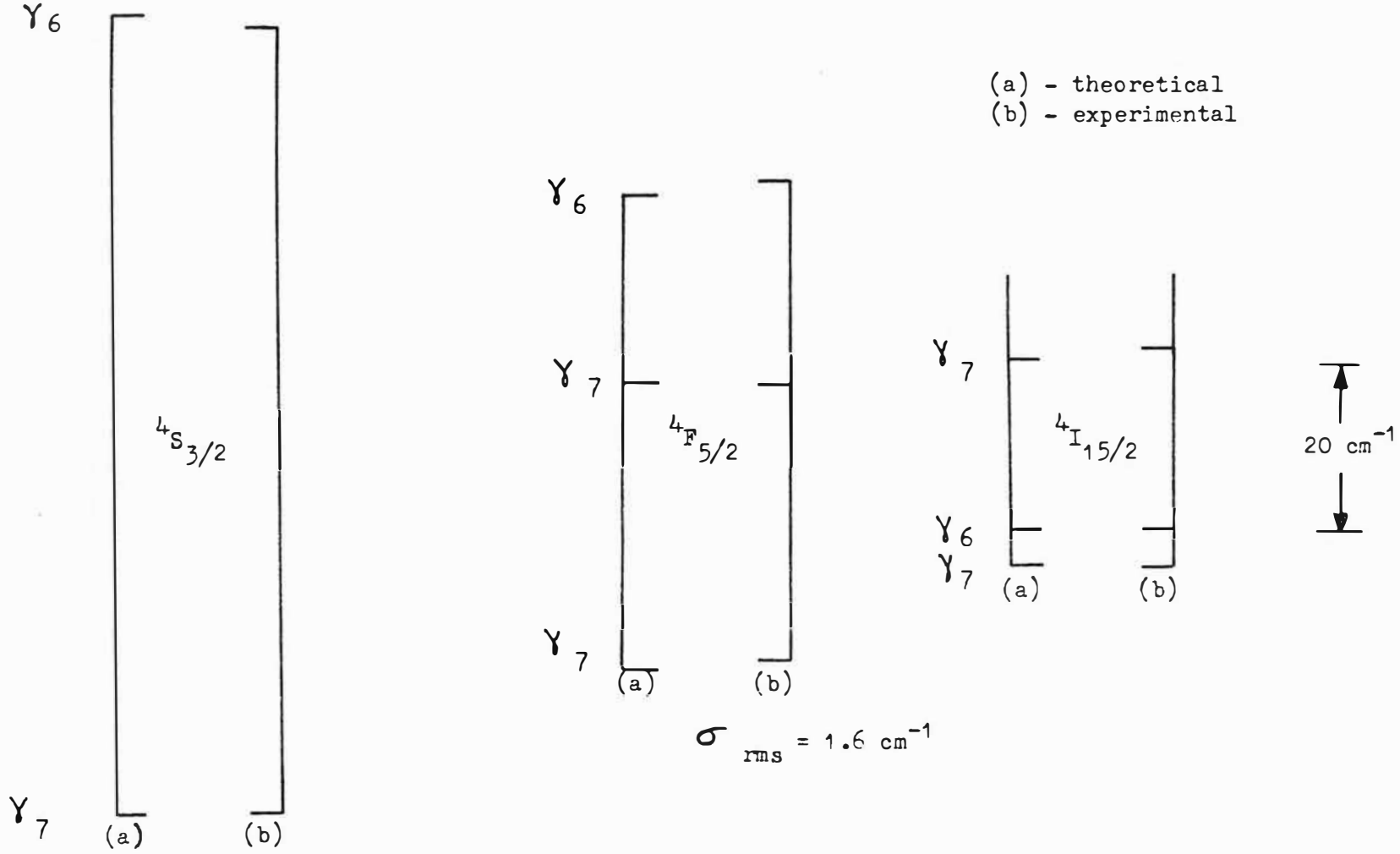

Fig.28(b) Comparison of experimental energy levels for the Er^{3+}-H^- site, taken from table 4 of reference 10, with those calculated using the crystal field parameters derived in this section.

This model also predicts the increased asymmetry for the Er^{3+}-D_I^- Tg_2 line because the energy levels for this site are more closely spaced at the field of 14 Kg where the Tg_2 line is observed. Furthermore, the model is also in agreement with the observation[122] that the asymmetry is much reduced at X band as compared with Q band.

(5) Parameterisation of the Crystal Field

Although there is insufficient data to evaluate the spin Hamiltonian parameters, it is possible to determine the crystal field parameters directly by combining the EPR data reported here with the optical measurements of Presland[10]. The crystal field parameters of the Er^{3+}-H_I^- site have been previously evaluated by a least squares fitting to the measured energy separations of certain Stark levels. However, the predicted values of $g_{//}$ = 12.34 and $g_{\perp}$ = 2.69 for the Z_1 ground state are not substantiated in this work, although the corresponding values for the Z_2 state are in satisfactory agreement. The discrepancy is not unexpected in view of the sensitivity of the Z_1 g values to the crystal field parameters, and since five parameters were fitted to five experimental observations the confidence level in the values obtained cannot be as high as in the case of the Er^{3+}-F_I^- site. A reevaluation was therefore undertaken

The experimental data chosen for the fitting comprised the splittings of the $^4S_{3/2}$ and $^4F_{5/2}$ multiplets plus the Z_1-Z_2, Z_2-Z_3 splittings of the $^4I_{15/2}$ multiplet, together with the values of $g_{//}(Z_1)$, $g_{//}(Z_2)$ and $g_{\perp}(Z_2)$ which were measured here. These eight observations were weighted in the fitting

routine in accordance with the experimental uncertainties, and the necessary matrix elements and operator equivalents were taken from the previous work[10]. The resulting best fit parameters, which are not greatly different from those derived by Presland, are given in Table 18, and the predicted energy levels are confronted with the experimental measurements in figure 28b. The predicted g values for the Z_1 and Z_2 states together with the experimental observations in parentheses are given below:

$$Z_1 \quad g_{//} = 7.48 \ (7.465), \qquad g_{\perp} = 6.23 \ (6.1)$$

$$Z_2 \quad g_{//} = 1.61 \ (1.683), \qquad g_{\perp} = 9.20 \ (9.09).$$

Values of $g_{\perp}$ were calculated from the relation

$$g_{\perp} = (E_1 - E_2)/\beta H_{\perp}, \tag{7-9}$$

where $H_{\perp}$ is the field at which the corresponding transition is observed. The effects of magnetic field mixing shown in Figure 28a make these effective g values slightly smaller than the true low field g values, but they have the advantage that they are directly comparable with the experimental results.

The good fit which was obtained to both energy levels and g values encourages confidence in the derived parameters. It is especially significant that the experimental value for $g_{\perp}(Z_1)$ which was estimated by extrapolating the angular dependence results, but which was not used in the fitting routine, is in good agreement with the predicted value. The value of B_0^2 is consistent with that estimated in Chapter VI for the Gd^{3+}-H_I^- site (800-1050 cm^{-1}), and furthermore the 26%

TABLE 17

G values for tetragonal Er^{3+} sites in calcium fluoride

Site	$g_{//}(z_1)$	$g_{//}(z_2)$	$g_{\perp}(z_2)$
$Er^{3+}-H_I^-$	7.465 ± .01	1.683 ± .001	9.09 ± .05
$Er^{3+}-D_I^-$	7.330 ± .01	1.680 ± .002	9.03 ± .05

TABLE 18

Crystal field parameters (in cm^{-1}) for tetragonal Er^{3+} sites in calcium fluoride

Site	B_0^2	B_0^4	B_0^6	B_4^4	B_4^6	Reference
$Er^{3+}-F_I^-$*	613.8	-761.2	908.58	-1083.4	-842.30	Presland[10]
$Er^{3+}-H^-$ *	729.2	-120.0	1023.2	- 787.9	-571.1	Presland[10]
$Er^{3+}-H^-$	796.8	- 55.2	880.5	- 645.9	-562.8	This Work

* These values have been converted from the Stevens normalisation with the aid of Table 8 in reference 127.

increase in this parameter from the Er^{3+}-F_I^- site to the Er^{3+}-H_I^- site is very close to the corresponding figure (24%) for Gd^{3+}.

The parameter values in table 18 have therefore been used in the following calculation of g value isotope shifts.

(6) Isotope Shifts

The theory of isotope shifts developed in Chapter VI can be applied to the present case with very few modifications. To recapitulate, the electron phonon interaction between the RE^{3+} ion and the H^- ion is responsible for corrections to the electronic energy levels which are given by equation 6-12. These corrections differ for hydride and deuteride ions, giving rise to an isotope shift. The isotope shifts obtained from off-diagonal contributions of the type $\langle\phi_i|f_x|\phi_j\rangle$ are small for the ground states and can be ignored. The remaining terms have the form given in equation (6-13) which is reproduced here for convenience:

$$\Delta E_{\phi_i} = \beta_z^2\left(\langle\phi_i|g_{zz}|\phi_i\rangle - \frac{3c}{m\omega_z^2}\langle\phi_i|f_z|\phi_i\rangle\right) + \beta_x^2\left(\langle\phi_i|g_{xx}+g_{yy}|\phi_i\rangle - \frac{2d}{m\omega_z^2}\langle\phi_i|f_z|\phi_i\rangle\right) \quad (7\text{-}7)$$

The electronic operators f_z, g_z and $g_{xx}+g_{yy}$ can be represented as linear combinations of the tensor operators C_0^{ℓ}, as given by equation 2-8, and so the energy level corrections can be considered as being due to an effective perturbation Hamiltonian of the form;

$$V_{ep} = \Delta B_0^{\,2} C_0^{\,2} + \Delta B_0^{\,4} C_0^{\,4} + \Delta B_0^{\,6} C_0^{\,6}, \qquad (7\text{-}8)$$

where the $\Delta B_0^{\,\ell}$ coefficients incorporate the vibrational quantities in (7-7), and also the α, β, γ coefficients of (2-8). It can be readily established that the hydrogen to deuterium isotope shift in the $\Delta B_0^{\,\ell}$ is given by,

$$\Delta B_0^{\,\ell}(H\text{-}D) = \Delta B_0^{\,\ell}(H) - \Delta B_0^{\,\ell}(D)$$

$$= (1 - \tfrac{1}{\sqrt{2}})\ \Delta B_0^{\,\ell}(H), \qquad (7\text{-}10)$$

since the isotope dependence is contained entirely in the factors $\beta_z^{\,2}$ and $\beta_x^{\,2}$ in equation (7-7). To proceed further with the calculation the values of the vibrational parameters ω_x, ω_z, c and d appropriate to the Er^{3+}-H_I^- site must be determined. By interpolating the results obtained in the previous chapter for Gd^{3+}-H_I^- and Tm^{3+}-H_I^- sites, the following values are found to be appropriate for the ionic radius of Er^{3+},

$$\omega_x = 1.997 \times 10^{14}\ \text{Hz}, \quad \omega_z = 2.125 \times 10^{14}\ \text{Hz},$$
$$c = 2.18 \times 10^{12}\ \text{ergs/cm}^3$$
$$d = 3.35 \times 10^{12}\ \text{ergs/cm}^3.$$

The point charge-point dipole model may now be used to calculate the parameter increments (7-10), assuming the same lattice distortions as found for Ce^{3+}-H_I^- sites by ENDOR[73]. The results are,

$$\Delta B_0^{\,2}(H\text{-}D) = -21.7\ \text{cm}^{-1} \qquad \Delta B_0^{\,4}(H\text{-}D) = -4.6\ \text{cm}^{-1},$$
$$\Delta B_0^{\,6}(H\text{-}D) = -.9\ \text{cm}^{-1}.$$

No allowance has geen made for electrostatic shielding effects, which are expected to be large for $B_0^{\,2}$, but less

important for B_0^4 and B_0^6. For the Er^{3+} ion the quadrupolar shielding factor σ_2 has been experimentally estimated[80] at 0.6, and by comparison with calculated values for other rare earth ions it is reasonable to take $\sigma_4 = .1$ and $\sigma_6 = .1$. With these shielding factors the revised parameter increments are

$$\Delta B_0^2(H\text{-}D) = -8.7\ cm^{-1}, \quad \Delta B_0^4(H\text{-}D) = -4.1\ cm^{-1}$$

$$\Delta B_0^6 = -.8\ cm^{-1}.$$

The relationship between these parameter increments and the corresponding g value isotope shifts can be found numerically by calculating the expectation values of the C_0^ℓ operators for the eigenfunctions of the Hamiltonian which contains both crystal and magnetic field terms. Using the crystal field parameters determined in the previous section the g value dependences are,

$$\begin{aligned}
\Delta g_{/\!/}(Z_1) &= -.0277\Delta B_0^2 + .0080\Delta B_0^4 + .0270\Delta B_0^6 \\
\Delta g_{/\!/}(Z_2) &= -.0002\Delta B_0^2 + .0003\Delta B_0^4 - .0006\Delta B_0^6 \qquad (7\text{-}11) \\
\Delta g_{\perp}(Z_2) &= -.0017\Delta B_0^2 + .0010\Delta B_0^4 + .0003\Delta B_0^6.
\end{aligned}$$

On substituting the parameter increments into these equations the predicted hydrogen to deuterium g value isotope shifts can be found and are given below, together with the experimental values in parentheses:

$$\begin{aligned}
\Delta g_{/\!/}(Z_1) &= +.19 \qquad (+.13 \pm .02) \\
\Delta g_{/\!/}(Z_2) &= +.001 \qquad (+.003 \pm .003) \\
\Delta g_{\perp}(Z_2) &= +.01 \qquad (0, \pm .1).
\end{aligned}$$

The experimental uncertainties in the Z_2 g value shifts are comparable with the shifts themselves and so a comparison with the predicted values does not provide a good quantitative test of the theory. However theory and experiment are at least consistent in that only very small shifts are involved. In contrast the experimental isotope shift for $g_{//}$ of the Z_1 level is much larger than its uncertainty, and a comparison shows that the experimental and predicted isotope shifts are of the same sign and nearly the same magnitude.

Thus the point charge-point dipole model for the electron phonon interaction is in satisfactory agreement with the isotope shifts observed for both Gd^{3+}-H^-/D^- sites and Er^{3+}-H^-/D^- sites in calcium fluoride. The relative success of this model will be further discussed in the conclusion (Chapter 9).

CHAPTER VIII

THE REORIENTATION OF GD^{3+}-F_I^- AND GD^{3+}-H_I^- ELECTRIC DIPOLES IN CALCIUM FLUORIDE CRYSTALS

Introduction

Rare earth doped calcium fluoride has become an important material for studying the reorientation of dipolar defects subject to an applied stress or electric field. The rare earth ion is charge compensated by a nearby defect of effective unit negative charge which can migrate between several equivalent positions. This thermally activated hopping motion is equivalent to the reorientation of the electric dipole formed by the RE^{3+} and defect ions, and can be observed and measured by Dielectric Loss and Ionic Thermocurrent (I.T.C.) techniques. In particular, calcium fluoride doped with the rare earth fluoride has been extensively investigated because of the simplicity and well established character of the tetragonal RE^{3+}-F_I^- site discussed in earlier chapters of this thesis. The F^- interstitial can occupy any one of the six interstices located at $(0,0,\pm a)$, $(0,\pm a,0)$ or $(\pm a,0,0)$, where a is 2.7Å, one half the length of the unit cell for calcium fluoride. The reorientation mechanism has been assumed hitherto in the literature to be a simple jump of the F_I^- between two adjacent interstitial positions.

An EPR experiment with the magnetic field along the (001) axis distinguishes between the two RE^{3+}-F_I^- sites which have their symmetry axes parallel to the field, and the four which

have their axes perpendicular to the field. Distinct spectra from the two kinds of site are observed. The hopping motion of the interstitial between these two types of site results in lifetime broadening of the electronic energy levels of the rare earth ion because of the Heisenberg uncertainty relation. This can be observed as a corresponding lifetime broadening of the RE^{3+} EPR lines and a measurement of the linewidth can, in principle, yield information complementary to that obtained by the Dielectric Loss and I.T.C. techniques. Although this EPR method yields relaxation frequencies over a relatively narrow range (approximately 10^7-10^8 Hz), the measurements are valuable because the relaxing ionic species is directly identified.

Franklin and Marzullo[90] have recently measured the relaxation times of Gd^{3+}-F_I^- dipoles in CaF_2 by the EPR line broadening technique, and also by Dielectric Loss measurements. In this chapter the results of similar measurements on Gd^{3+}-H_I^-, Gd^{3+}-D_I^- and Gd^{3+}-F_I^- dipoles will be presented. Frnaklin and Marzullo's observations for the latter species have been extended by higher frequency dielectric loss data and by improved linewidth analysis techniques. The new results for the Gd^{3+}-H_I^- and Gd^{3+}-D_I^- dipolar species are qualitatively different from the case of Gd^{3+}-F_I^- dipoles; consequently the latter part of this chapter will be concerned with comparing and contrasting the expected and observed reorientation behaviour of these three dipolar systems.

I. EPR LINEWIDTH MEASUREMENTS

(1) Experimental Techniques

Preliminary experiments indicated that a great deal of care was necessary to record a true, undistorted lineshape. The major difficulty arises at high temperatures where the EPR lines are strongly broadened and, consequently, greatly diminished in amplitude. In order to obtain a sufficiently intense spectrum the spectrometer sensitivity must be boosted by increasing the microwave power, the modulation amplitude, and the detector time constant. There is an upper limit to all of these factors at which the lineshape becomes distorted by microwave power saturation, modulation broadening etc. In the final measurement runs the optimum pre-distortion power level was determined empirically and the modulation amplitude and time constant set by the empirical criteria proposed in Poole's book[91].

Two additional factors are important in the recorded low temperature lineshape: sample temperature fluctuations, and temperature induced sample orientation changes. The first effect is due to the temperature dependence of the zero field splitting which produces a shift in the measured line positions of approximately 1.5 gauss/^{o}K. Thus if the sample temperature shifts by one degree during the scan of an EPR line the recorded linewidth will be significantly different from the true linewidth of approximately 15 gauss. This effect was minimised by allowing the sample ten minutes to reach thermal equilibrium after a ten degree temperature resetting, and by using the smallest scan time compatible with

the detector time constant. The sample orientation can also be changed by temperature fluctuations due to differential thermal contraction in the sample glue. Since the residual EPR linewidth is orientation dependent these orientation fluctuations can produce changes in the recorded linewidth. This effect is minimal for the (001) field orientation at which the spectra were recorded because the EPR lines are at a turning point in this direction; the needle-shaped sample was also a tight fit inside the hollow quartz tube which greatly limited any possible shift of the sample.

The particular EPR lines whose widths were measured in these experiments corresponded to the $M = -\frac{1}{2} \rightarrow -\frac{3}{2}$ (F^-) or $M = -\frac{3}{2} \rightarrow -\frac{5}{2}$ (H^-,D^-) transitions. These lines were considered the best for measurement since they did not overlap neighbouring lines at high temperatures. The linewidth measurements were performed for Gd^{3+}-F_I^-, Gd^{3+}-H_I^- and Gd^{3+}-D_I^- dipoles in calcium fluoride but Gd^{3+}-T_I^- dipoles were not studied because of the low concentration of Gd^{3+}-T_I^- sites, and also because of the problem of overlap with Gd^{3+}-H_I^- contaminant.

The recorded linewidth should differ from the true linewidth by no more than ±1% since the methods discussed above were used to prevent instrumental broadening of the EPR lines. The residual low temperature linewidth is approached asymptotically and so the estimated uncertainty in this value is somewhat larger at ±2%.

(2) Theoretical Analysis of the Linewidth

An inhomogeneously broadened EPR line may be thought of as an assembly of individual resonance lines, or "spin packets" which all have slightly different resonant field strengths. The distribution in resonant field strengths may be due to such mechanisms as an inhomogeneous magnetic field, spin-nucleus interactions, or crystalline mosaic structure. The overall lineshape (Fig. 29) is then the convolution of the spin-packet lineshape with the distribution function of resonant field strengths.

For the RE^{3+}-anion systems discussed in this chapter, the width of the spin packets is determined not only by the usual spin-lattice relaxation time, but also by the relaxation time associated with the anion hopping motion. If these two mechanisms are independent the total spin-packet linewidth ΔH_T is given by,

$$\Delta H_T = \Delta H_{SL} + \Delta H_{AH}, \qquad (8\text{-}1)$$

where ΔH_{SL}, ΔH_{AH} are the linewidths which would result if each mechanism acted alone.

The relative magnitudes of the two terms in equation (8-1) depends critically on the particular rare earth ion and temperature region under consideration. For most of the trivalent rare earth ions the spin lattice contribution increases rapidly with increasing temperature and overwhelmingly dominates that of the anion hopping motion. However, gadolinium is an exception becuase its $^8S_{7/2}$ electronic ground state is only weakly coupled to the surrounding crystal lattice; consequently the spin lattice contribution increases relatively slowly with increasing

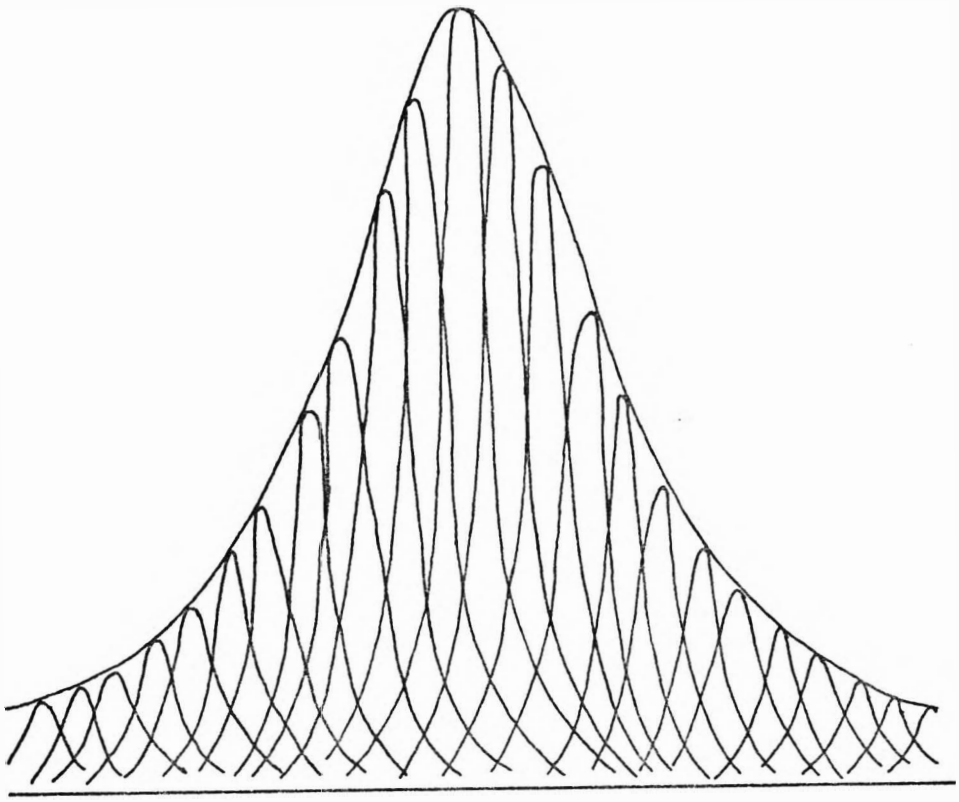

Fig. 29: Schematic diagram of an inhomogenously broadened EPR line.

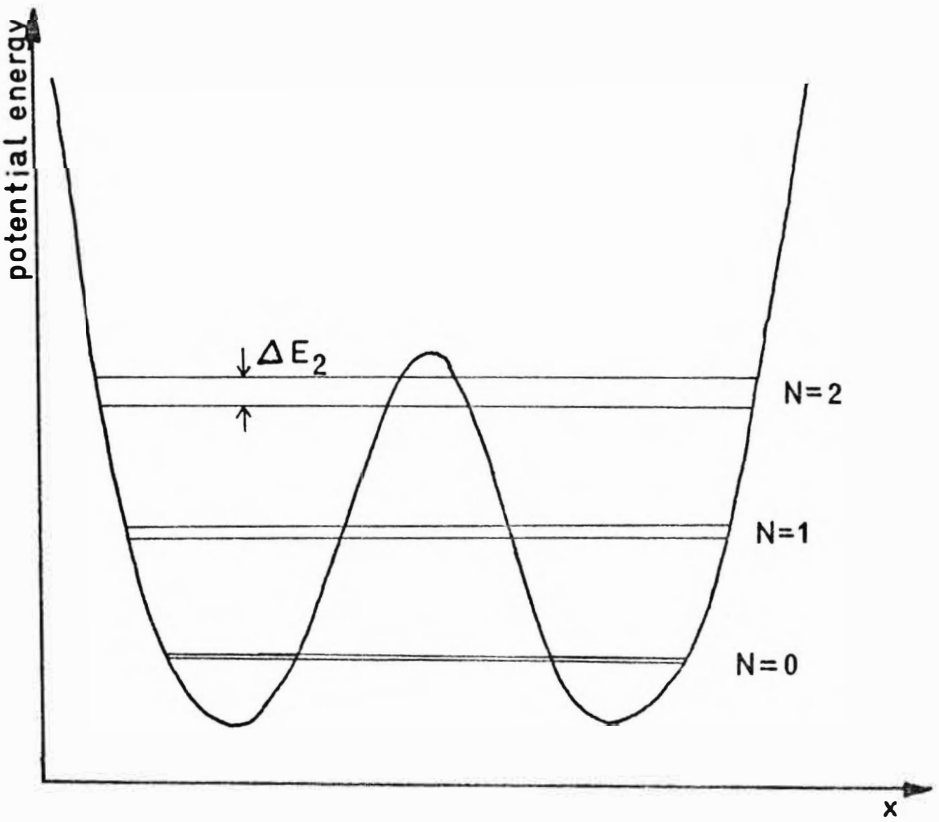

Fig.30:Energy levels for a simple double well system.

temperature and so may ultimately dominate the observed spin packet linewidth. Thus Gd^{3+} is uniquely suited amongst the rare earths for defect reorientation measurements using the linewidth technique discussed here.

The spin packet linewidth at very low temperatures is small relative to the total observed linewidth and so the low temperature EPR lineshape may be identified with the distribution of spin packet resonant field strengths, as discussed previously. Thus the overall lineshape at higher temperatures is the convolution of a Lorentzian spin packet, whose linewidth increases with temperature, and a temperature independent distribution function. If the latter is Lorentzian in shape, the total peak to peak linewidth ΔT is given by

$$\Delta_T = \Delta_{L_1} + \Delta_{L_2} \tag{8-2}$$

where ΔL_1, ΔL_2 are the peak to peak linewidths of the spin packet and the distribution function. The more usual case of a Gaussian distribution function has been investigated numerically by Stoneham[92], who found that the total linewidth is given to within 1% uncertainty by,

$$\Delta_T = \frac{.4621\Delta_L^2 + .9085\Delta_{G\,L} + \Delta_G^2}{\Delta_G + .4621\Delta_L} \tag{8-3}$$

where Δ_G is the peak to peak width of the distribution function, and Δ_L is that of the spin packet. Thus it is important to ascertain the exact shape of the low temperature linewidth because the formulae (8-2) or (8-3) will yield

different results for the spin packet linewidth. The analysis of the linewidths for the Gd^{3+}-F_I^- site by Franklin and Marzullo[90] is unsatisfactory in this respect because they inherently assumed equation (8-2) was valid although they observed a Gaussian lineshape at low temperatures

The shapes of the low temperature first derivative EPR lines for Gd^{3+}-F_I^-, Gd^{3+}-D_I^-, and Gd^{3+}-H_I^- sites was carefully recorded in this work, and compared with the theoretical curves for Gaussian and Lorentzian first derivatives tabulated in Poole's book[91]. In all three cases the lineshape was intermediate between the two, that for Gd^{3+}-H_I^- dipoles being most closely Lorentzian, and that for Gd^{3+}-D_I^- dipoles being most closely Gaussian. Neither formula (8-2) nor (8-3) is therefore directly applicable. The three derivative lineshapes were then integrated by means of a mechanical planimeter to give true absorption curves, and compared with other established lineshapes. They most closely matched the Voigt lineshape[91], which is a convolution of Lorentzian and Gaussian functions of arbitrary relative widths. The Voigt lineshape can take on any shape intermediate between Lorentzian and Gaussian depending upon the ratio b of its Lorentzian and Gaussian component widths. A value of the ratio b for each curve was estimated by comparing the observed lineshapes with Posener's[93] tabulations of the Voigt lineshape; the actual values of the component linewidths were then obtained from equation 8-3.

The overall high temperature lineshape observed in this work for the three Gd^{3+}-anion sites thus consists of the convolution of a temperature independent Voigt lineshape,

which is itself the convolution of Gaussian and Lorentzian components, with a temperature dependent Lorentzian spin packet. The linewidth of the latter component was extracted from the total linewidth by applying equation (8-3), assuming that the linewidths of two Lorentzian components were simply additive in the sense of equation (8-2).

This analysis procedure has been discussed in detail because it represents a significant improvement over that adopted in the previous work by Franklin and Marzullo[91]. The accuracy of the extracted spin packet linewidths should be especially improved in the region of weak line broadening since these results are particularly sensitive to the assumed low temperature lineshape.

(3) The Linewidth-Lifetime Relationship

The Lorentzian spin packets have a shape which is given by:

$$g(\omega) = \left(\frac{2\tau}{1+\omega^2\tau^2}\right) \qquad (8\text{-}5)$$

where τ is a parameter associated with the linewidth. Watkins[95], in a study of a Mn^{2+}-vacancy system in NaCl similar to that under present discussion, has shown that the relaxation time associated with the vacancy hopping motion is just the τ appearing in equation (8-5). It may be readily established from the magnetic resonance condition and equation (8-5) that

$$\tau = \left(h/\left(\sqrt{3}\pi g \beta \Delta H_L\right)\right) \qquad (8\text{-}6)$$

where ΔH_L is the peak to peak width of the derivative of the spin packet. Inserting numerical values for Gd^{3+}, (8-6)

becomes:

$$\tau = 6.59 \times 10^{-8}/\Delta H_L \qquad (8\text{-}7)$$

or $\nu = 1/2\pi\tau = 2.41 \times 10^{6}\ \Delta H_L$

Thus by utilising equations (8-2), (8-3) and (8-7) the relaxation frequencies (or lifetimes) for Gd^{3+}-anion dipole reorientation may be readily obtained from the observed variation of EPR linewidth versus temperature.

(4) Results

The measured relaxation frequencies for all three dipolar species are plotted against reciprocal temperature in figure 31. It is evident that the results for Gd^{3+}-F_I^- and Gd^{3+}-D_I^- dipoles are just those expected for a classical relaxation system which has a relaxation frequency ν given by:

$$\nu = \nu_0 \exp(-E/kT), \qquad (8\text{-}6)$$

where E is the height of the energy barrier which the interstitial anion must surmount in order for the dipole to reorientate. The pre-exponential factor ν_0 may be approximately interpreted as the frequency of vibration of the interstitial in its potential well. The parameters ν_0 and E were determined for both dipolar species by performing a least squares fit of equation 8-6 to the experimental relaxation frequencies, which were weighted in accordance with the uncertainties indicated in Figure 31. Table 19 lists the resulting best-fit parameters. Both species have similar activation energies, but the pre-exponential factor for Gd^{3+}-D_I^- is several times higher than for Gd^{3+}-F_I^-.

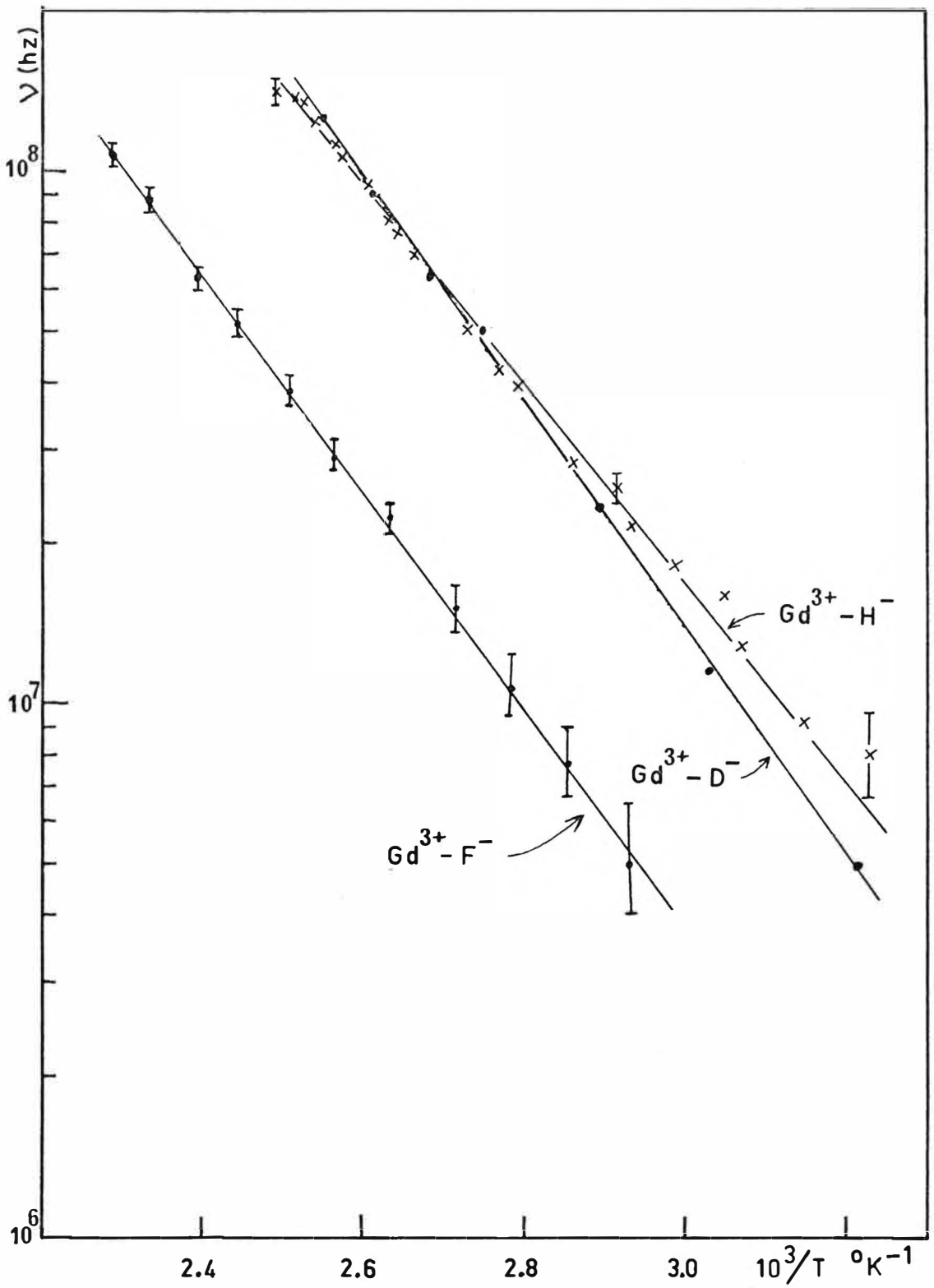

Fig. 31: Relaxation frequencies for three tetragonal Gd^{3+} sites in calcium fluoride, determined by EPR linebroadening.

TABLE 19

Relaxation parameters for several Gd^{3+} sites in calcium fluoride determined by various techniques.

Site	Technique	E(eV)	ν_0(Hz)	Reference
Gd^{3+}-F_I^-	EPR	.396	3.9×10^{12}	This Work
"	D Loss	.404	6.9×10^{12}	"
"	EPR & D Loss	.390	3.3×10^{12}	"
"	EPR & D Loss	.38	1.9×10^{12}	Franklin & Marzullo[90]
"	ITC	.395	1.3×10^{12}	Stott & Crawford[107,108]
"	ITC	.42	64×10^{12}	Kitts[78]
Gd^{3+}-H_I^-	EPR	.375	7.5×10^{12}	This Work
Gd^{3+}-H_I^-	EPR, T>350°K	.383	9.6×10^{12}	"
Gd^{3+}-D_I^-	EPR	.425	3.6×10^{13}	"
Gd^{3+}-F_I^-(nnn)	ITC	.69	1.6×10^{13}	Kitts[78]
Unidentified	ITC	.167	7.9×10^{11}	Stott & Crawford[107,108]

This is in accordance with the light deuteride ion vibrating in its potential well at a higher frequency than the fluoride ion.

The Gd^{3+}-H_I^- dipolar system is anomalous in that equation 8-6 gives a relatively poor fit to the relaxation frequency data for this species. At temperatures above 350°K the relaxation frequencies are consistent with those of the Gd^{3+}-D_I^- system, but at lower temperatures they are faster than for the latter species. These results suggest that quantum mechanical tunneling may be important for the Gd^{3+}-H_I^- system. In this interpretation the high temperature relaxation frequency is dominated by the classical contribution of equation (8-6), but at lower temperatures the relaxation frequency is significantly enhanced by the finite probability that the H_I^- ion can tunnel through the barrier between adjacent potential wells. Since the tunneling probability depends exponentially on the (negative) mass of the particle it would be expected that tunneling should become significant for Gd^{3+}-D_I^- sites at a lower temperature than for the Gd^{3+}-H_I^- sites. These predictions are in qualitative agreement with the experimental data in Figure 31, and so the possibility of tunneling will now be quantitatively examined.

(5) Discussion of the Tunneling Model for Gd^{3+}-H_I^- Reorientation

Jones et al.[6] originally suggested that the H_I^- ion tunnels between the six equivalent H_I^- positions for the Gd^{3+}-H_I^- site to explain the disappearance of the Gd^{3+} fluorescence at 220°K. However, M. Presland[10] has observed

the absorption spectrum for this site up to 350°K and so the disappearance of the fluorescence lines at 220°K is probably due to the onset of radiation loss transitions and not to tunneling, The possibility of tunneling at higher temperatures may be quantitatively examined by means of a simple semi-classical theory applied to the one-dimensional double-well potential shown in Figure 30 (page 159). If ν_n is the tunneling frequency for a particle in a state of energy E_n then the total jump frequency is given by[95],

$$\nu = \sum_{N=0}^{M} \nu_N \exp(-E_N/kT) + \nu_0^c \exp(-E_b/kT), \qquad (8\text{-}7)$$

where there are M levels below the barrier height E_b. In this equation the tunneling terms are assumed to be given by the product of the tunneling frequency for a particular level weighted by the appropriate Boltzmann thermal excitation factor, and the last term represents the classical Arrhenius form for the barrier climbing contribution. A possible interpretation of the present results is that the relaxation frequencies below 350°K contain a significant tunneling contribution from the first bound state below the barrier, but that above 350°K the classical barrier climbing contribution is dominant.

The general features of the quantum mechanics of one-dimensional double wells are well known. If ψ_1^n, ψ_2^n are the wavefunctions of a particle in either of two wells labelled 1 and 2 which are at infinite separation and divided by a potential barrier of infinite height, then the approximate wavefunctions for finite separations and barrier heights are given by,

$$\psi_s^n = \psi_1^n + \psi_2^n,$$
$$\psi_a^n = \psi_1^n - \psi_2^n. \qquad (8\text{-}8)$$

The symmetric wavefunction ψ_s^n and the antisymmetric wavefunction ψ_a^n are split by the exchange energy $\Delta E_n = E_a^n - E_s^n$, and the theory shows that a particle initially located in a particular potential well will oscillate between the two with a tunneling frequency given by $\nu_n = \Delta E_n/h$. The problem of finding the tunneling frequencies for the various levels reduces to finding the energy eigenvalues and thus the exchange splittings for a double well system. In this work the eigenvalues were found by numerically integrating the Schrodinger equation using the technique described by Chow[96]. This method has the advantage that it is applicable to any shape of the potential curve.

The technique was tested before being applied to the present case, with a harmonic oscillator potential, for which it predicted the first five eigenvalues correct to seven significant figures. In a second test the exchange splitting of the ground states in the two double well systems investigated analytically by Sussman[97], and by Dennison and Uhlenbeck[98] was computed. In both cases the numerical result of Chow's technique agreed with the predictions of the analytical formula to within 0.6%.

Before the computation for the present case can proceed the shape of the potential well must first be estimated from the available experimental data. The separation of the wells in the undistorted lattice is 3.85Å. The infrared measurements of Jones et al.[6] show that the potential well for

the H_I^- in the Gd^{3+}-H_I^- site is closely harmonic up to the N = 2 level; thus it may be assumed that the curvature of the well corresponds to that of a Simple Harmonic Oscillator of frequency $\omega = (2\omega_x+\omega_z)/3 = 1060\ cm^{-1}$, and that $E_b > 2650\ cm^{-1}$. At sufficiently high temperatures the classical mechanism will dominate the hopping frequency and so the actual value of E_b may be taken as the observed high temperature activation energy plus the zero point energy, i.e. $3000+530 \simeq 3{,}500\ cm^{-1}$. The shape of the barrier above the N = 2 level is indeterminate and so two different shapes were examined. In the first case, the two potential wells were assumed to be exactly parabolic and to be connected by a flat topped barrier. In the second case the potential was assumed to be of the form

$$V = ax^2 + bx^4 + cx^6 + dx^8, \qquad (8\text{-}9)$$

and the values of a, b, c and d were chosen to fit the well separation, the barrier height, and the curvature at the bottom of the well.

The tunneling interpretation of the observed low temperature relaxation frequencies requires that the tunneling frequency for the first level below the barrier (which is the N = 3 state) should be of the order of 3×10^6 MHz, to explain the experimental results. In contrast the calculations show that a tunneling frequency of 60 MHz may be expected for this level for the power series potential of equation 8-9, and a frequency of less than 1 MHz for the flat-topped barrier shape. Thus it does not appear that a simple tunneling model is capable of explaining the magnitude of the

the observed deviations from the high temperature Arrhenius behaviour. The major factor which limits the theoretical tunneling frequency in the present model is the relatively large spacing of the potential wells (3.85 Å). For comparison, the well spacings in some hydrogenic systems for which tunneling has been shown to be important are 0.76Å for the NH_3 molecule[98], and 0.76Å and 1.65Å for ion states and orientational defects in ice[95]. A more advanced tunneling theory which includes the possibility of jumps caused by interaction with lattice phonons has been discussed by Flynn and Stoneham[99]. They found that this phonon assisted tunneling process was important below a temperature of about one third to one fifth the Debye temperature, but that above this value the jump frequencies obeyed the classical Arrhenius behaviour. In the present case the transition temperature is at about 150°K. It may be concluded from this theoretical discussion that tunneling is not important for the reorientation of Gd^{3+}-H_I^- dipoles in CaF_2 over the region of 300-350°K.

This conclusion is supported by the results of the dielectric loss experiments which are reported later in this chapter. Crystals of CaF_2:Gd^{3+}:H^- should show two dielectric loss peaks corresponding to the reorientation of Gd^{3+}-F_I^- dipoles and Gd^{3+}-H_I^- dipoles. If the tunneling interpretation of the Gd^{3+}-H_I^- results was correct it would be expected (from the EPR linewidth measurements) that the two peaks should be closely spaced at about 350°K, but that as the temperature is lowered the separation between the peaks should rapidly increase as the H_I^- tunneling becomes significant. In fact the two peaks are unresolved at 300°K and remain unresolved down to 200°K.

The tunneling interpretation is therefore inconsistent with both experimental observation and with theoretical predictions. The observed deviations from the high temperature Arrhenius behaviour may be due to either experimental error, or to a linebroadening mechanism which is not connected with the reorientation motion. The points in Fig. 31 have therefore been interpolated with a single straight line. Table 19 gives the best fit relaxation parameters for all the Gd^{3+}-H_I^- results, and also those for the data recorded above $350^{O}K$ only.

(6) The Measurement of Relaxation Times by the EPR-Stress Technique

The reorientation of Gd^{3+}-anion dipoles may be measured by another EPR technique which was first used by Watkins and Corbett[100] in a study of irradiated silicon. The application of a static uniaxial stress to the crystals renders the six potential wells inequivalent and consequently the populations of Gd^{3+}-H_I^- dipoles are different for the six different directions of the dipole axis. This population redistribution can in principle be observed by the change in the relative EPR intensities of the Gd^{3+} ion for the different dipole axis directions, and the relaxation time of the system can be found by observing the decay of the EPR signals back to the equilibrium intensities when the stress is removed.

A suitable resonant cavity similar to that described by Watkins was constructed and stresses of up to 12,500 psi were applied to a crystal of CaF_2:Gd^{3+}:H^- along the (100) direction whilst the EPR spectrum was monitored with the magnetic field in the (001) direction. No measurable population redistribution was observed and so it appears that the defect-stress

coupling is too small in this case for the technique to be successful.

II. DIELECTRIC LOSS MEASUREMENTS

Dielectric loss measurements were performed on crystals of $CaF_2:Gd^{3+}:F_I^-/H_I^-/D_I^-$ in an attempt to confirm and extend the results of the EPR linewidth experiments described previously; in particular it seemed desirable to check the anomalous behaviour of the Gd^{3+}-H_I^- dipole system. However, crystals of $CaF_2:Gd^{3+}:H_I^-/D_I^-$ displayed a complicated dielectric loss spectrum and so some preliminary work on CaF_2, $CaF_2:H^-$ and $CaF_2:Gd^{3+}$ crystals was necessary.

(1) Dielectric Loss in Crystals of Pure CaF_2

The dielectric loss factor ε'' for pure CaF_2 over the frequency range ω = 10 radians/sec to 1 M radians/sec is plotted in Figure 32. It is apparent from the figure that the loss factor is the sum of very small frequency-independent contribution of $\Delta\varepsilon'' = .0006$, together with a weak low frequency tail which varies as the reciprocal of the frequency. The latter feature is indicative of a conduction mechanism in the sample since it is well known that if a crystal has a DC conductivity σ, then there is a corresponding contribution to the AC loss factor given by[101],

$$\Delta\varepsilon'' = \frac{\sigma}{\omega\varepsilon_0} . \qquad (8\text{-}10)$$

The results of Bollman and Henninger (1972)[102] show that the DC conductivity of nominally pure CaF_2 at room temperature is in fact due to impurity-induced populations of F^-.

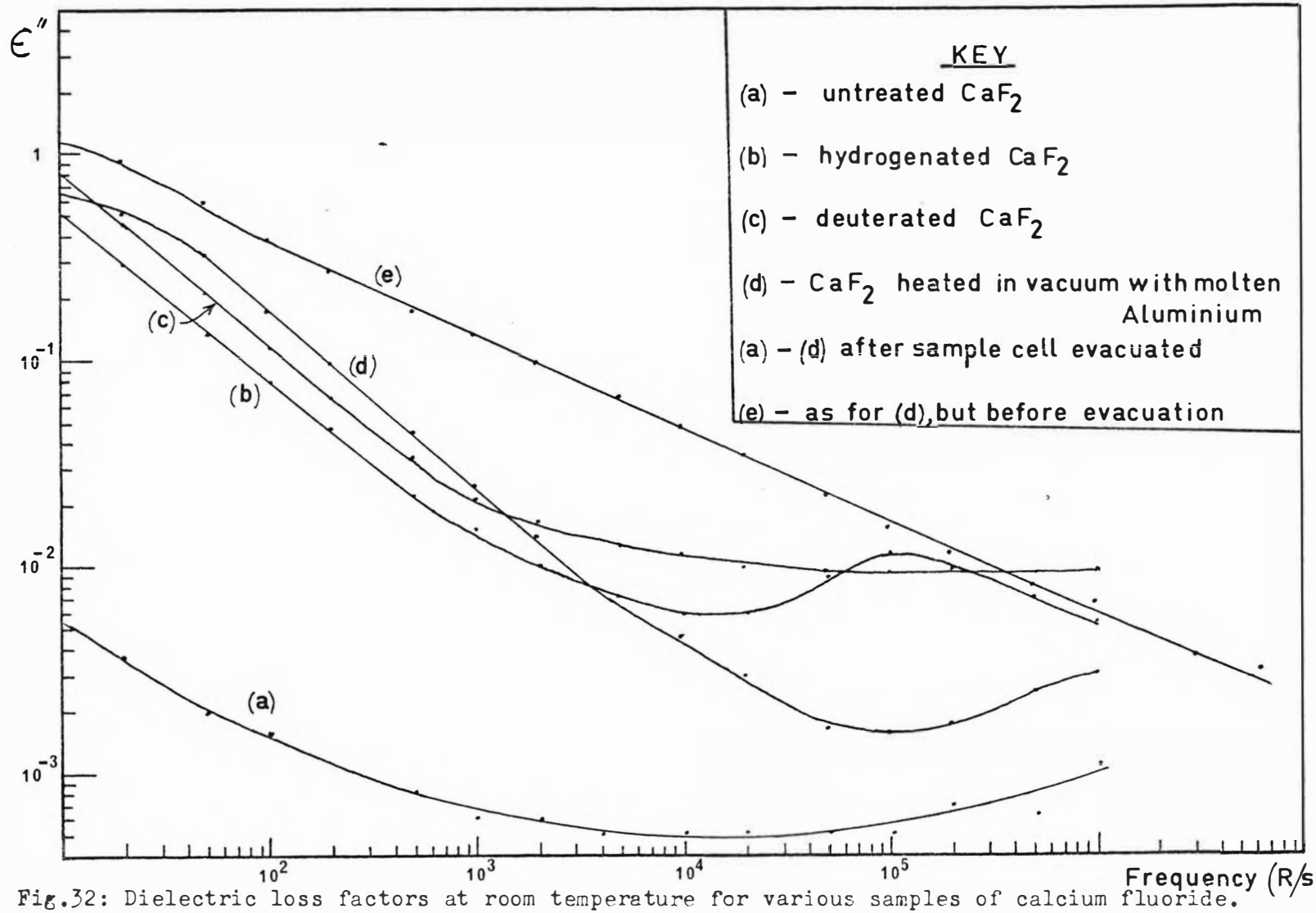

Fig.32: Dielectric loss factors at room temperature for various samples of calcium fluoride.

interstitials or F^- vacancies. Their published values of σ for several different samples correspond to values of ε'' (for ω = 10 radians/sec) in the range from .004 to .0004, in good agreement with the observed value of .004.

(2) Dielectric Loss in Crystals of $CaF_2:H^-/D^-$

Crystals of calcium fluoride which had been hydrogenated or deuterated by the method discussed in Chapter III showed a dielectric loss spectrum at room temperature and atmospheric pressure which varied markedly from sample to sample. Some crystals displayed loss factors which were very similar to pure CaF_2, whilst others showed a strong low frequency tail two or three orders of magnitude larger than in the pure material. The frequency dependence of this loss tail was typically $\omega^{-0.4}$, in contrast to the ω^{-1} dependence for a well-behaved conduction mechanism. It is important to discover the origin of this low frequency tail since it was also present in several hydrogenated samples of $CaF_2:Gd^{3+}$.

The pertinent experimental observations are:

1) The loss tail was present in approximately half of the hydrogenated and deuterated crystals which were examined. It was also found in some crystals which had been subject to the thermal treatment involved in the hydrogenation procedure, but in a vacuum rather than hydrogen. Two samples of $CaF_2:Gd^{3+}:H^-$ provided by the author were examined by Kitts and Crawford[103] using the ITC technique, with the result that one of them showed an abnormally large background current. These authors speculated that the effect may be due to conduction by hydride ions tunneling through the crystal.

2) Evacuating the sample cell for periods of up to an hour reduced the dielectric loss by a factor of two or three at the lowest frequencies, and by an order of magnitude or more at 10^4 radians/sec. After two hours of evacuation the loss factor stabilised at a constant value. It was later found that baking a sample at 110°C for two hours had the same effect. After evacuation the loss factor varied with frequency as $f^{-0.9}$, as shown in Figure 32. There are deviations from this dependence at very low frequencies for some crystals, but these can be attributed to an effective series capacitance resulting from imperfect electrode-sample contact.

The presence of a loss tail in crystals which had been heated in a vacuum suggests that Kitts and Crawford's[103] speculations concerning hydride ion tunneling may be incorrect since such crystals have no hydrogen content. Rather it appears that there are two contributing effects, the first being some surface layer which is removed by evacuation or baking, and the second being an ionic conduction mechanism within the crystal.

The origins of the surface layer evidently lie in some volatile impurity. A search of the literature after the completion of these experiments revealed that CaF_2 is soluble in acidified $AlCl_3$ to form the complex $(CaF_2)_3AlCl_3 6H_2O$[104]. The reactants are exactly those that are formed when the aluminium which adheres to hydrogenated crystals is removed by aqueous hydrochloric acid. Thus it seems very probable that either the complex, or H_2O, or HCl is adsorbed on the surface of the crystal; such a layer may be expected to give rise to a

broad loss peak whose frequency extent is determined by the properties of the adsorbed layer. Certainly the unusual pre-evacuation frequency dependence of $f^{-0.4}$ is consistent with a distribution of Debye peaks originating in an assembly of Maxwell-Wagner dielectric layers, but without any detailed knowledge of the layer properties or structure it is impossible to calculate the position of such peaks. It is of interest to note that a loss peak has been observed at the low frequency of 1 radian/sec in CaF_2 by Chatain, Gautier and Lacabanne (1970)[105], but these authors do not comment on the origin of this peak or their crystal treatment.

The frequency dependence of the loss factor for all of the crystals after evacuation was very nearly ω^{-1}, which shows that the second effect must be due to conduction. The conductivities are as much as two orders of magnitude larger than for pure calcium fluoride, so there must be some new impurity in the crystal introduced during the hydrogenation procedure. The most probable contaminants are water vapour and oxygen since CaF_2 may react with both of these substances in the hydrogenation furnace:

$$\begin{aligned} CaF_2 + H_2O &\xrightarrow{800^oC} CaO + HF\uparrow, \\ 2CaF_2 + 2H_2 + O_2 &\xrightarrow{800^oC} 2CaO + 4HF\uparrow. \end{aligned} \qquad (8\text{-}11)$$

It is known that the ground glass joints in the hydrogenation furnace glassware are occasionally prone to small leakage over long periods of assembly, as indicated by the characteristic flower pattern in the vacuum grease. Also the hydrogen gas may still retain traces of water vapour despite the use of a liquid nitrogen cold trap. Thus the irregular

inclusion of small quantities of air or water vapour in the hydrogenation furnace is quite plausible. In addition, Bontwick[104] has shown that oxygen-contaminated CaF_2 crystals have a characteristic UV absorption band at 200 nm. This band was also present in some of the hydrogenated crystals, but not in pure calcium fluoride, thus conclusively demonstrating that sporadic oxygen-contamination was occurring in the hydrogenation procedure.

The importance of the above discussion lies in the fact that the DC conductivity of calcium fluoride has been observed to increase by two orders of magnitude after heating in oxygen[106], or water vapour. The divalent oxygen anion substitutes for a regular lattice fluoride ion and is charge compensated by a neighbouring F^- vacancy. The observed increase in the conductivity is due to the large population of relatively mobile F^- vacancies which have dissociated from the oxygen-vacancy defect pairs. Thus it appears almost certain that the residual post-evacuation low frequency tail in the dielectric loss spectrum is due to conduction by oxygen-induced F^- vacancies.

It may be concluded that the unusual low frequency tail observed in the dielectric loss spectrum of $CaF_2:H^-$, and, more importantly, $CaF_2:Gd^{3+}:H^-$ crystals, can be satisfactorily ascribed to various impurities accidentally introduced during the hydrogenation treatment, and that it is not due to tunneling of unassociated hydride ions, as suggested by Kitts and Crawford.

(3) Dielectric Loss in Crystals of Calcium Fluoride Doped with Gadolinium

The dielectric loss spectra of three crystals of CaF_2 doped with .05%, .10% and .25% molar Gd^{3+} were measured at room temperature and in a vacuum. The loss factor ε'' is plotted against logarithmic frequency in Figure 33 for each of the samples. Also shown are the loss factors for the two lowest concentration crystals after they were annealed at $800^{o}C$ for 12 hours in a vacuum.

Prior to annealing, the three crystals showed similar room temperature dielectric loss spectra consisting of a weak low frequency tail, a small loss peak at 25 Hz, and a larger asymmetric loss peak at 800 kHz. When the .25% doping crystal was cooled to $210^{o}K$, the origin of the asymmetry became evident; the 800 kHz peak shifted to 1.5 kHz and a new loss peak at 200 kHz was resolved. The relative amplitudes of the 1.5 kHz and 200 kHz peaks in this crystal were in the approximate ratio of 2:1. The loss factor of the .05% doping crystal did not change appreciably after the annealing treatment, but the amplitude of the 800 kHz peak in the .1% doping crystal increased by a factor of two and the peak became symmetrical in shape.

The low frequency tail may be due to the previously discussed effects of oxygen contamination during the growth process, or alternatively to conduction by the F^- interstitials which are produced by Gd^{3+}-F_I^- disassociation. This is plausible since it has been shown in Chapter IV that an appreciable population of isolated Gd^{3+} sites of cubic symmetry exist in CaF_2:Gd^{3+}.

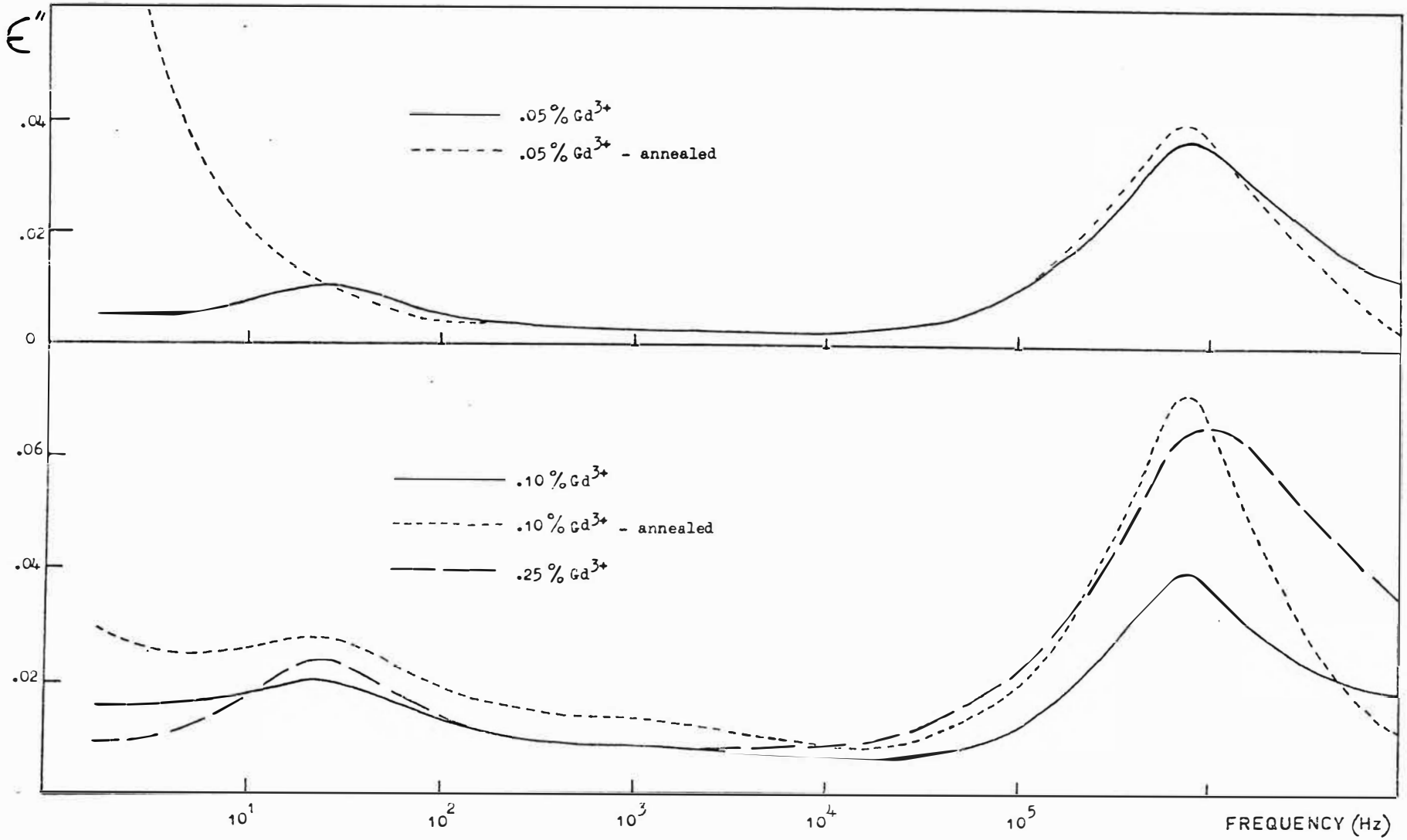

Fig. 33:- Room temperature dielectric loss spectra for several samples of calcium fluoride doped with gadolinium ions, before and after annealing.

Variable temperature experiments permitted the determination of the activation energies and pre-exponential factors, as defined in equation 8-6, for the three peaks. A limited set of measurements showed that the 25 Hz peak was characterised by an activation energy of .7 eV ± .05 eV, and that the very high frequency peak present in the samples before annealing corresponded to the rather low activation energy of 0.2 eV ± 0.1 eV. The short period available for the measurements precluded more intensive investigation of these two loss peaks. However, the 800 kHz peak was studied over a wide temperature range. The relaxation frequency of this peak is plotted against reciprocal temperature in figure 34; it can be seen that the relaxation frequencies for this peak and those determined by EPR linewidth measurements for the tetragonal Gd^{3+}-F_I^- site can be fitted by a single straight line. The present results confirm and extend those of Franklin and Marzullo[90], who first demonstrated that the 800 kHz peak was due to the reorientation of this dipolar species. A least squares fitting to the combined EPR and dielectric loss results resulted in the relaxation parameters shown in Table 19; these are expected to be more accurate than those obtained previously due to the more extensive dielectric loss data and the improved EPR linewidth analysis.

The interpretation of the remaining two loss peaks is facilitated by the previous work on CaF_2:Gd^{3+} crystals performed by Stott and Crawford[107,108], and Kitts[78] using the ITC technique. They observed one large peak and two subsidiary peaks in the ITC spectra of CaF_2:Gd^{3+} (.1%), and have determined the relaxation parameters which give the best

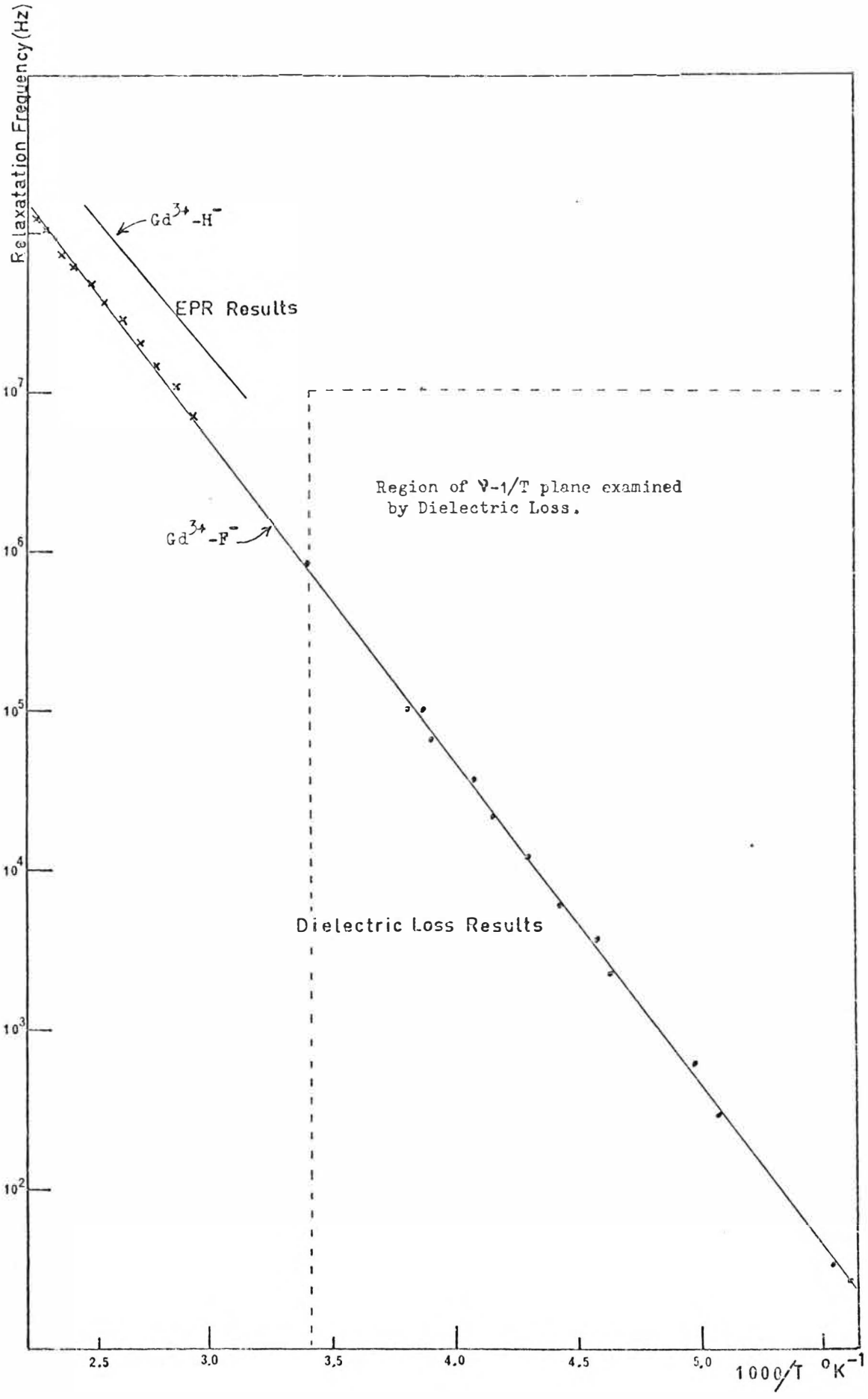

Fig.34: Relaxation frequency as a function of reciprocal temperature for the tetragonal $Gd^{3+}-F_I^-$ site in calcium fluoride.

fit to the three peaks. These values are listed in Table 19. They identified the largest peak with the reorientation of tetragonal Gd^{3+}-F_I^- dipoles and this interpretation is supported by the close agreement between the parameters for this peak and those determined for the tetragonal Gd^{3+}-F_I^- dipoles by EPR and dielectric loss measurements.

One of the subsidiary peaks ITC peaks was characterised by an activation energy of .69 eV, in good agreement with the value of .7 eV determined for the low frequency dielectric loss peak. Furthermore a calculation using Kitts[78] parameters for the ITC peak predicts a relaxation frequency of 37 Hz at $295^{o}K$, which is very close to the observed room temperature dielectric loss peak frequency of 25 Hz. Evidently the two techniques are monitoring the same dipolar species. Kitts[78] has identified the ITC peak as originating from a Gd^{3+}-F_I^- site with trigonal symmetry with F_I^- at the (111) next nearest neighbour position by comparing it with similar ITC peaks in SrF_2:Gd^{3+} and BaF_2:Gd^{3+} where this type of site is dominant. Kitts, Ikeya and Crawford[109] have recently observed a weak trigonal EPR spectrum in CaF_2:Gd^{3+} with $b_2^0 = 256 \times 10^{-4}$ cm^{-1} which they tentatively associate with this site, and they have estimated the ratio of tetragonal to trigonal sites as 10:1. If this concentration ratio is correct it is surprising that the trigonal site was not observed in the EPR measurements reported in Chapter IV. A detailed examination of the Q band spectrum of the CaF_2:Gd^{3+} crystals used in this work revealed a complex pattern of weak lines in the region from 10 to 14 Kg, whose general position is thus consistent with the reported site, but the relative intensity of the lines was

much less than the given ratio. No positive confirmation of the new site could be made.

Although Kitts'[78,109] comparitive study of $MeF_2:Gd^{3+}$ crystals indicates that trigonal $Gd^{3+}-F_I^-$ (nnn) centres are definitely involved there are some difficulties with the theory. Franklin and Crissman[110] have pointed out that there is no simple way by which these centres can reorientate because the F_I^- ions are not located in adjacent F_S^- cubes, but are separated by a cube containing a Ca^{2+} ion. Rather it seems that a jump of the form $Gd^{3+}-F_I^-(nnn) \rightarrow Gd^{3+}-F_I^-(nn)$ is responsible for the observed relaxation, in which case a full relaxation mode analysis of the $Gd^{3+}-F^-$ system must be used to calculate the ITC peak amplitudes. Also the loss peaks due to $Gd^{3+}-F_I^-(nn)$ and $Gd^{3+}-F^-(nnn)$ sites should be in a constant ratio as determined by the Boltzmann factor for the difference in their potential energies, whereas Fig. 33 shows that a constant ratio is not observed. However, Sierro[43] has found that various thermal treatments change the population ratio of the trigonal and tetragonal sites in $SrF_2:Gd^{3+}$, so it may be that the mean potential energy difference is sensitive to strain fields within the crystal.

Stott and Crawford[107,108] observed another subsidiary ITC peak in the ITC spectrum which was characterised by an activation energy of .167 eV, in reasonable agreement with the .2 eV ± .1 eV found here for the high frequency dielectric loss peak. However, Welsh[111] has recently made more extensive measurements on this loss peak which show that the activation energy is accurately given by 0.076 eV, and that the

reorientation process is not of simple Debye character. At low temperatures the amplitude of the loss peak diminishes as exp(-.02 eV/kT), which is the expected behaviour for a dipole which reorientates between two inequivalent potential wells whose depths differ by 0.02 eV. Furthermore the relaxation parameters determined by Stott and Crawford[108] predict a loss peak at 70 MHz at 210^{o}K, in contrast to the value of 200 kHz observed here. (It is interesting to note that after an earlier publication Stott and Crawford discovered an error in their heating rate of only 5% which caused them to revise the estimate of the activation energy by 12%, but the pre-exponential factor was changed by two orders of magnitude.) Thus it is difficult to decide whether the dielectric loss and ITC measurements are monitoring the same dipolar species because of the undetermined effect of inequivalent potential wells on the shape of the ITC curve, from which the ITC relaxation parameters are derived.

From the asymmetry in the 800 kHz loss peak shown in Fig. 33, it is evident that the higher frequency loss peak increases rapidly in amplitude with increasing Gd^{3+} concentration, but disappears after annealing, with an accompanying increase in the amplitude of the Gd^{3+}-F_I^- peak. These experimental observations suggest that the high frequency peak may be due to a cluster site of the form $(Gd^{3+}\text{-}F_I^-)_2$, in which the Gd^{3+} ion substitute for two nearest neighbour Ca^{2+} ions. Analogous $(Y^{3+}\text{-}F_I^-)_2$ clusters have been observed experimentally by Cheetham et al.[112,113] using neutron diffraction, and investigated theoretically by Catlow[114], and $(Nd^{3+}\text{-}F_I^-)$ clusters have been observed by Kask

and Kornienko[115] using EPR. The population of these cluster sites is observed to increase rapidly with increasing RE^{3+} concentration[116], and they may dissociate at high temperatures to form two separate RE^{3+}-F_I^- sites. The electric dipole of a cluster site depends upon the relative orientation of the two component RE^{3+}-F_I^- dipoles, and is zero if they are anti-parallel. Any F_I^- jump must be to an inequivalent site since the relative orientation of the dipoles is changed, and the associated dielectric loss would have an exponential temperature dependence, as observed.

One objection to this theory is that the EPR spectrum of a Gd^{3+} cluster site has not been reported. However, the exchange and dipolar coupling effects between the two Gd^{3+} ions would result in the spins of the ions being coupled to form states of total spin S where S = 7,6,...,0. Experimentally this would mean that 56 EPR lines should be observed for each of the six possible orientations of the Gd^{3+}-Gd^{3+} axis, and a complex EPR spectrum of many weak lines would ensue. Although this is consistent with the large number of weak lines observed in the 10-14 Kg region of the Q band EPR spectrum for the two highest concentration crystals, the identification of the high frequency loss peak with a cluster site must remain tentative until an EPR-dielectric loss correlation is attempted. Because of the complexity of the Gd^{3+} cluster site EPR spectrum this would best be performed for CaF_2:Nd^{3+} crystals for which the cluster site EPR spectrum is simpler (S = 1,0), and already known.

To summarize, the dielectric loss spectra of CaF_2:Gd^{3+} crystals is consistent with the usual model for MeF_2:RE^{3+} in which RE^{3+} ions are charge compensated by interstitial F^- ions

at nn, nnn or more remote positions for low RE^{3+} concentrations, but at higher dopant concentrations cluster sites involving two or more RE^{3+} ions can form. The observed activation energies for the reorientation of the various defect species are substantially in agreement with measurements made by other techniques.

(4) Dielectric Loss in Hydrogenated and Deuterated Crystals of $CaF_2:Gd^{3+}$

The room temperature dielectric loss spectra of three hydrogenated samples of calcium fluoride containing .05%, .10% and .25% GdF_3 are shown in Figure 35. These samples were cut from the same boules as the parent crystals discussed in the previous section, and so it is interesting to compare the loss spectra before and after hydrogenation. All three samples showed an increased loss tail at low frequencies due to the oxygen contamination discussed previously. The 25 Hz peak disappeared in the .05% doping crystal, and was reduced in amplitude on the higher concentration crystals. This can be interpreted as the decay of the trigonal Gd^{3+}-F_I^- site to the more stable tetragonal site. The hydrogenated samples also showed a weak loss peak in the region between 300 Hz and 30 kHz but this was very broad and did not have the same peak frequency in all three samples. It is therefore unlikely to be due to an isolated dipole species. The dominant 800 kHz peak due to tetragonal Gd^{3+}-F_I^- dipoles was slightly smaller in the .05% doping crystal but increased in amplitude in the two higher concentration crystals. In all three samples the peak was nearly symmetrical in shape, indicating that the 5 MHz peak observed in the parent crystals had disappeared.

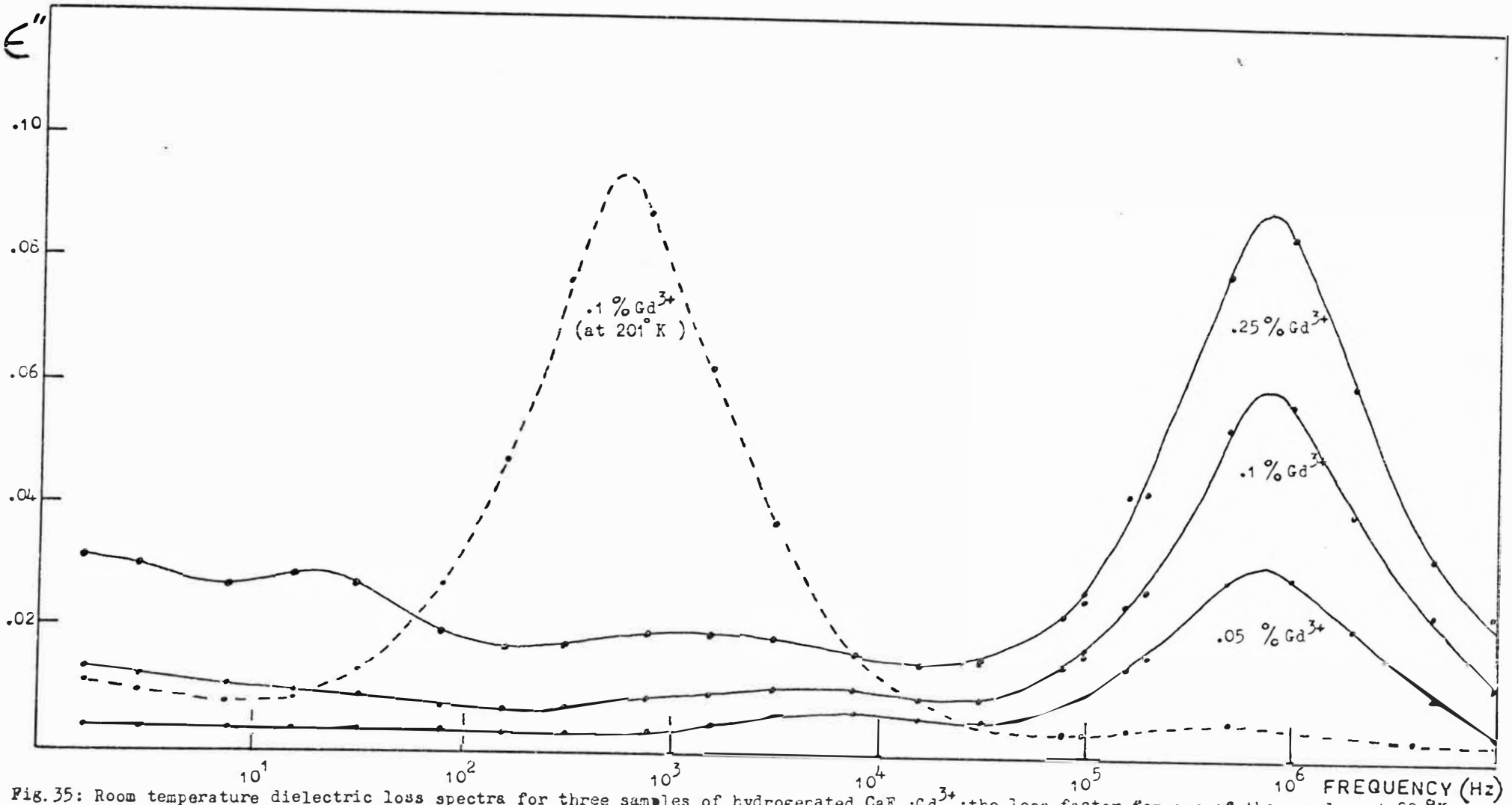

Fig. 35: Room temperature dielectric loss spectra for three samples of hydrogenated $CaF_2:Gd^{3+}$; the loss factor for one of the samples at 201°K is also shown (dotted line). In each case the experimental points (solid dots) have been interpolated with a smooth curve.

The search for a new dielectric loss peak due to tetragonal Gd^{3+}-H_I^- dipoles was guided by the EPR linewidth results previously obtained, which suggest that the peak frequency for this species should be higher than that for Gd^{3+}-F_I^- dipoles by a factor of three or more. Since this frequency was on the very edge of the range of measurement at room temperature, the hydrogenated CaF_2:Gd^{3+} (.1%) sample was cooled in steps of approximately 40^oK from room temperature to 100^oK and the dielectric loss measured from 1.5 Hz to 10 MHz at each temperature. The surprising result of this set of measurements was that no new loss peak was observed. A similar set of measurements on a deuterated crystal produced the same null result.

(5) Interpretation of Dielectric Loss Measurements on Hydrogenated CaF_2:Gd^{3+} Crystals

There are several plausible explanations for the apparent absence of a Gd^{3+}-H_I^- dielectric loss peak, but the following section will show that some of these can be eliminated after detailed consideration. The various possibilities are that:

1) The crystals may not have contained a sufficiently high concentration of Gd^{3+}-H_I^- dipoles to be observable in the dielectric loss spectra. This was tested by performing EPR assays of the various crystals. The concentration N of a particular Gd^{3+} site may be estimated from the shape and size of one of its EPR lines by the formula,

$$N = KM(AI\Delta H^2), \qquad (8\text{-}12)$$

where ΔH is the peak to peak derivative linewidth, I the amplitude of the line, M the transition probability, K an unknown constant depending on the spectrometer sensitivity, and the constant A has the value 3.6276 for Lorentzian lines and 1.0332 for Gaussian lines[92]. The three dominant sites observed in the EPR spectra were the cubic, tetragonal Gd^{3+}-F_I^-, and tetragonal Gd^{3+}-H_I^- sites. The formula (8-12) was used to calculate the relative proportions of these sites in the three parent crystals, the two annealed parent crystals, and the three hydrogenated crystals; the results are shown in figure 36.

These results should be treated with some caution since the EPR assay technique has never been rigorously tested; in particular the proportion of cubic sites may be subject to error because of the presence of unresolved hyperfine structure which slightly distorts the lineshape. However, it is thought that the ratio of the two tetragonal sites should be reliable because of the similar crystal fields and common symmetry for those sites.

It may be seen from the figure that the ratio of tetragonal Gd^{3+}-F_I^- sites to tetragonal Gd^{3+}-H_I^- sites in the .1% doping crystal is almost 2:1. Thus, since the dipole moments of the two species should be similar, the loss peak due to the Gd^{3+}-H_I^- dipoles should be nearly half that of the Gd^{3+}-F_I^- dipoles.

2) It is possible that the Gd^{3+}-H_I^- loss peak may have a relaxation frequency which falls outside the frequency and temperature ranges used in this work. The area searched with the dielectric loss technique is illustrated in Figure 34. The EPR linewidth results are also plotted in this figure and it

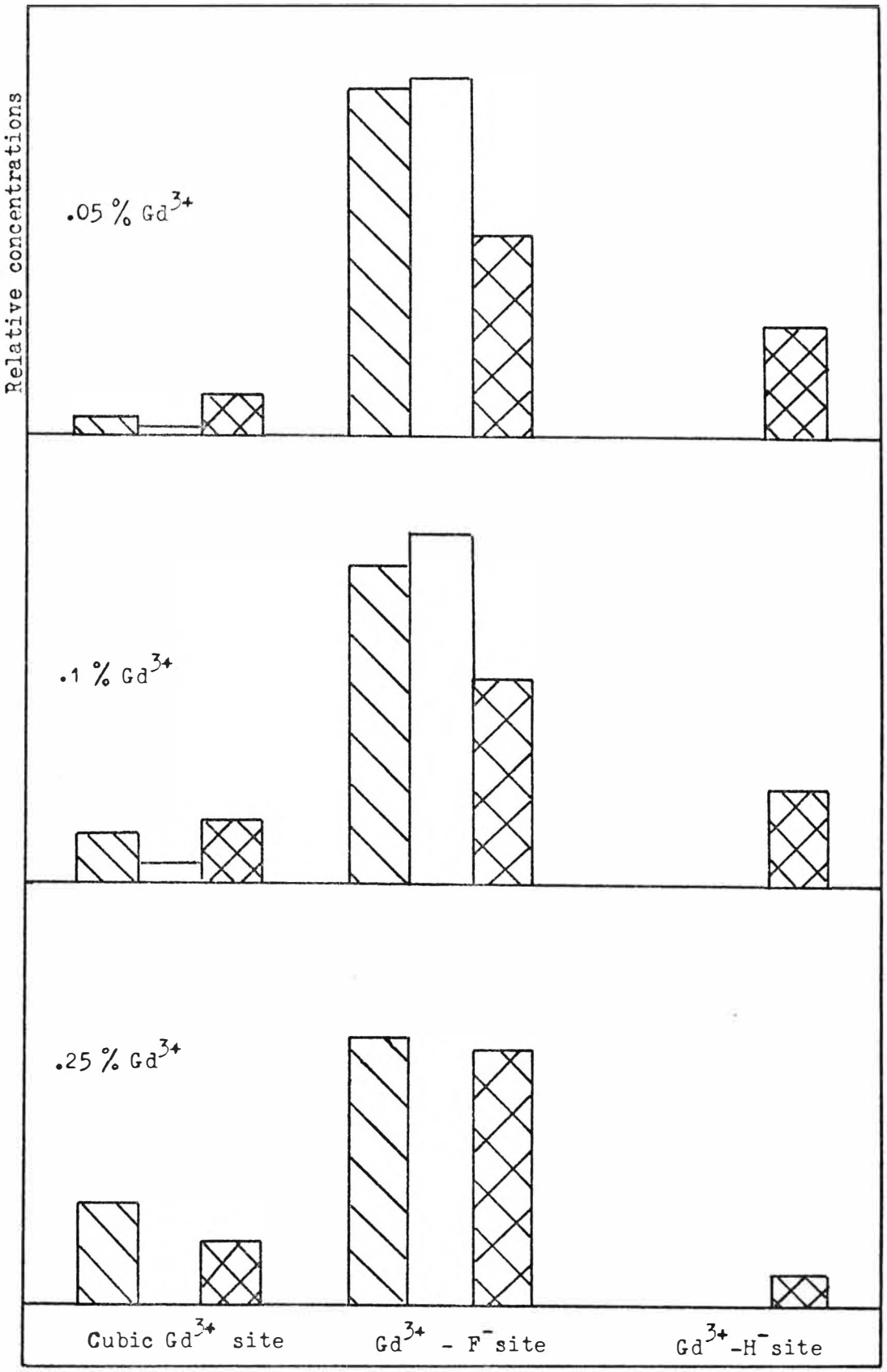

Fig. 36: Historogram showing the relative populations of different Gd^{3+} sites determined by EPR in as grown(diagonal stripes), annealed (unshaded), and hydrogenated(cross hatching) crystals of CaF_2: Gd^{3+}.

can be seen by extrapolation that it is most unlikely that the relaxation frequency lies outside the investigated ranges.

3) There may not be any measurable dielectric loss associated with the Gd^{3+}-H_I^- dipoles. It is known that a dipole which reorientates between two potential wells of different depth shows only a very weak loss factor, although there is no reason to assume that the six potential wells for the Gd^{3+}-H_I^- site are of different depths. The reorientation motion may occur via an intermediate configuration of different depth but it will be shown in part III that the loss factor is not appreciably altered in this case. This explanation may therefore be reasonably discounted.

4) The fourth possibility is that the centre frequencies of the loss peaks for the Gd^{3+}-H_I^- and Gd^{3+}-F_I^- dipoles are so close that the two peaks are not resolved. This was tested by calculating the value of the function,

$$Y = \frac{2X}{1+X^2} + \frac{2\alpha(X/\beta)}{1+(X/\beta)^2}$$

which represents the sum of two Debye-shaped loss peaks, one centred at a value X = 1 and of unity amplitude, and the other centred at X = β and of amplitude α. This function is plotted in Figure 37 for several different values of α and β. Also shown are the experimental points for the main loss peak of hydrogenated CaF_2:Gd^{3+} (.1%) taken at two different temperatures. In each case the background loss was measured at a frequency well removed from the centre of the peak, and subtracted from the recorded loss factors. The set of curves in Fig. 37 have been matched on the low frequency side since

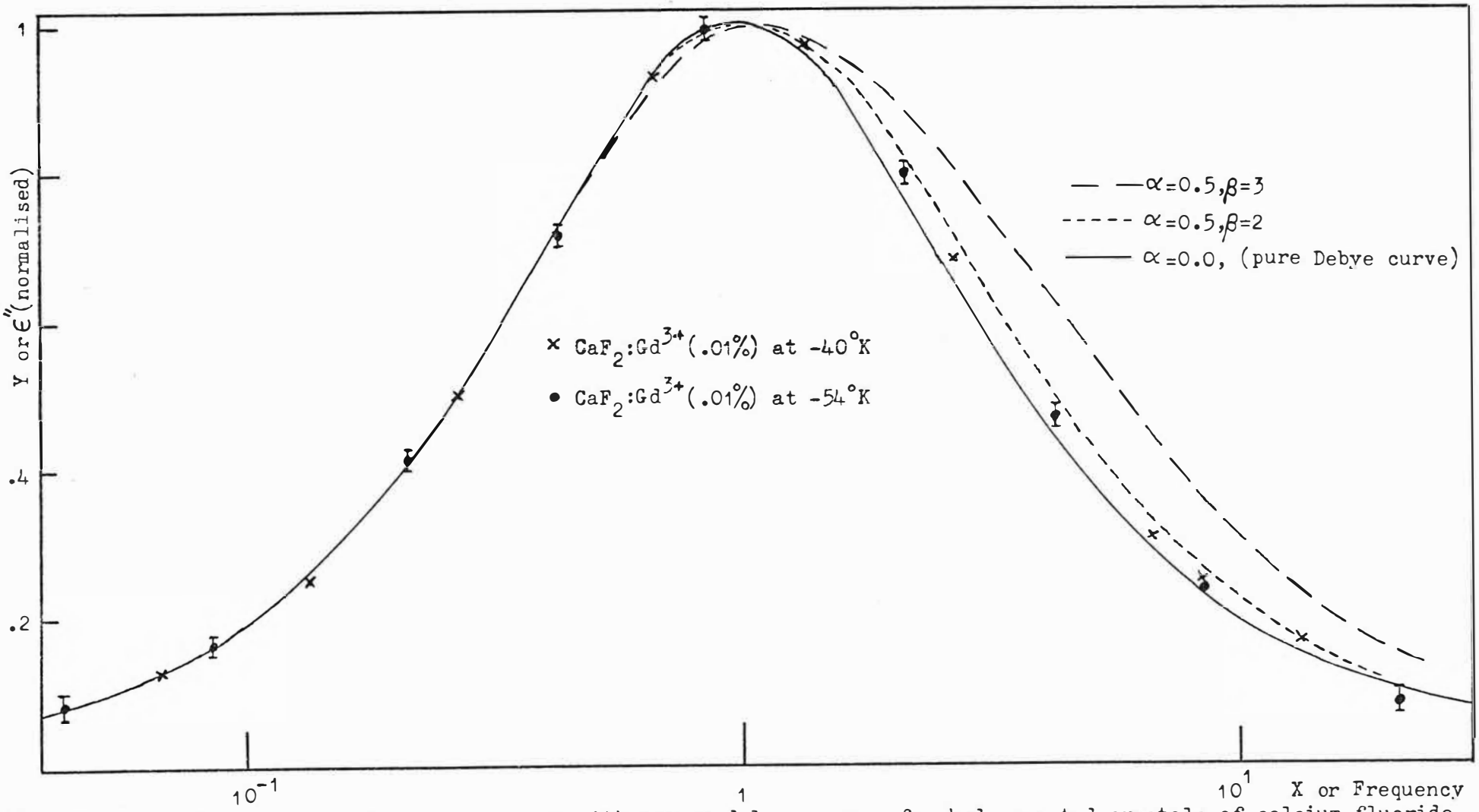

Fig. 37: Comparison of composite Debye curves with measured loss curves for hydrogenated crystals of calcium fluoride containing gadolinium.

it is expected that any asymmetry due to unresolved peaks should be most pronounced on the high frequency side.

The EPR linewidth measurements and the EPR assay results suggest that appropriate values of α and β are 0.5 and 3 respectively for the crystal of interest. It can be seen from the Figure that the curve based on these parameters does not fit the experimental points as well as a simple Debye curve. However, as β is progressively reduced, the lineshape rapidly approaches that of a Debye curve. If the value of $\alpha = .5$ is accepted then any value of β which is less than 1.5 is compatible with the experimental results.

To summarise this discussion: The most plausible interpretation of the dielectric loss results for hydrogenated and deuterated $CaF_2:Gd^{3+}$ is that the loss peak for $Gd^{3+}:H_I^-$ or Gd^{3+}-D_I^- dipoles cannot be resolved from that due to Gd^{3+}-F_I^- dipoles. If this is true then the dielectric relaxation occurs at a lower frequency than that predicted by the extrapolated EPR linewidth results.

(6) Correlation of EPR Assay and Dielectric Loss Results for Hydrogenated $CaF_2:Gd^{3+}$

It is evident from the composite loss curves in Fig. 37 that it is very difficult to differentiate between the two cases of (a) a single loss peak, and (b) a composite curve consisting of a dominant and a subsidiary peak whose peak frequencies are closely spaced. The basic problem is that a normal Debye loss curve has a relatively large linewidth; such a curve reaches its half amplitude points at approximately three times and one third the peak frequency.

Neither the resultant shape nor the peak frequency is sensitive to a subsidiary component whose peak frequency lies within the halfwidth.

An alternative approach is to examine the resultant peak amplitude, for if the component peak separation is less than the halfwidth of the dominant component the amplitudes are approximately additive. The incentive for this approach is the observation that the amplitudes of the 800 kHz loss peaks in the hydrogenated crystals are very similar to those in the annealed crystals. On the usual model of the hydrogenation process some Gd^{3+}-F_I^- centres are replaced by their hydride ion analogues; thus the 800 kHz peak would be expected to decrease markedly in strongly hydrogenated crystals. However, if the 800 kHz peak in hydrogenated crystals contains component peaks from both Gd^{3+}-H_I^- and Gd^{3+}-F_I^- dipoles then the amplitudes of this peak in annealed and hydrogenated crystals should be approximately the same if the total number of tetragonal sites is conserved during the hydrogenation. Thus it is of crucial importance to determine how the populations of the various Gd^{3+} species, particularly Gd^{3+}-F_I^- sites, change during hydrogenation, and to attempt to correlate these results with the changes in the 800 kHz loss peak.

The EPR assay results shown in Figure 36 suggest that the concentration of Gd^{3+}-F_I^- dipoles increases after annealing and decreases after hydrogenation. However, these results must be treated with caution because they only indicate the relative populations of the three dominant EPR sites, not the absolute populations. The latter may be simply calculated if it is assumed that the total gadolinium content of a crystal

is distributed between these sites only, but this assumption is questionable. A previous section showed that the subsidiary dielectric loss peaks observed in the $CaF_2:Gd^{3+}$ crystals were probably due to trigonal $Gd^{3+}-F_I^-$ sites or cluster sites.

An EPR experiment was therefore devised which was capable of measuring the changes in the absolute $Gd^{3+}-F_I^-$ site concentration after annealing or hydrogenation. Several samples were cut from a boule of $CaF_2:Gd^{3+}$ (.05%) in the shape of rectangular blocks of dimension 1 mm x 1 mm x 2 mm, with the (001) axis parallel to the block length. These blocks were a tight fit inside a Teflon sample holder, as shown in Fig. 38, so that the samples could be accurately relocated at the same position in the cavity after the treatment. A sealed sample of DPPH was fixed to a second sample holder at the other end of the cavity. With this arrangement any change in the absolute concentration of a site may be readily measured by comparing the EPR line intensities to the DPPH standard before and after the treatment. This procedure nullifies the effect of varying microwave powers, Q factors etc. between each experiment. The measurements were found to be reproducible to within 5%.

The changes in the populations of the cubic Gd^{3+}, tetragonal $Gd^{3+}-F_I^-$ site and the tetragonal $Gd^{3+}-H_I^-$ site after annealing at 800°C and after hydrogenation at 800°C are shown in Figure 39. The concentration of the tetragonal $Gd^{3+}-F_I^-$ species increases after annealing, probably due to the decay of cluster sites and/or $Gd^{3+}-F_I^-$ sites of other symmetries. Evidently the as grown crystals do not contain the

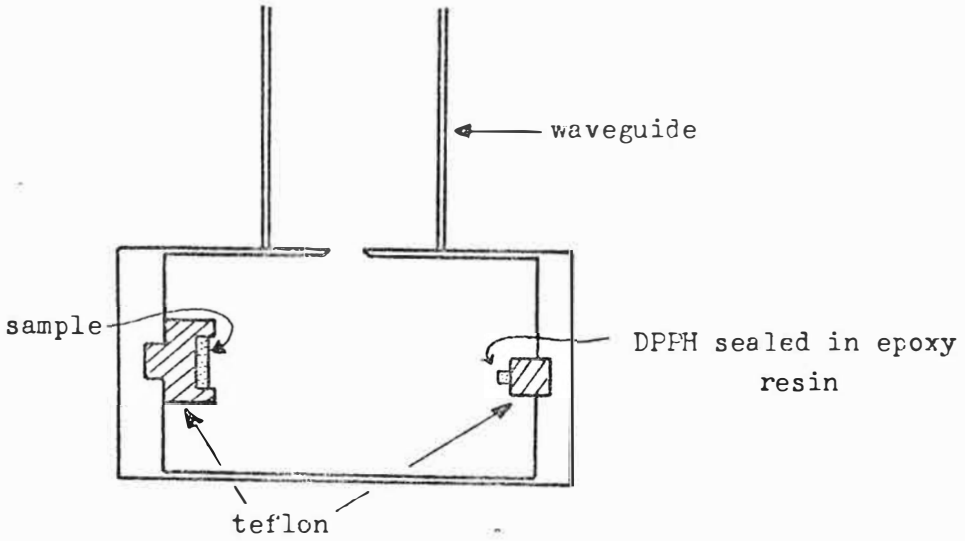

Fig. 38: The resonant cavity used to measure changes in the concentration of Gd^{3+} sites in crystals of $CaF_2:Gd^{3+}$.

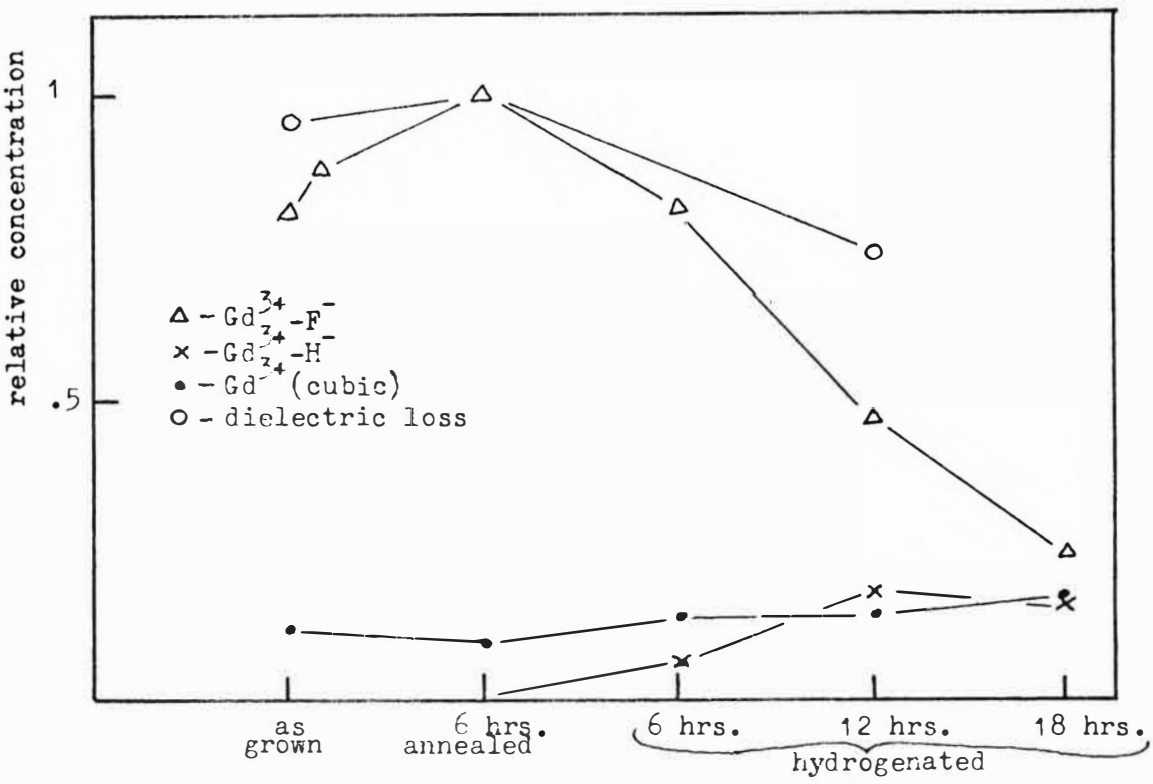

Fig. 39: The relative concentrations of different Gd^{3+} sites in calcium fluoride after various crystal treatments.

population of tetragonal Gd^{3+}-F_I^- dipoles characteristic of the equilibrium situation at 800°C. It is preferable to compare the EPR and dielectric loss results for the hydrogenated crystals with the annealed crystals rather than the as grown crystals, for two reasons. First, the amplitude of the 800 kHz peak in the as grown crystals is larger than the true amplitude of the Gd^{3+}-F_I^- loss peak because of the overlap with the unresolved high frequency peak. Second, the initial reactant concentration of the Gd^{3+}-F_I^- dipoles in the hydrogenation reaction should be closest to that in the annealed crystals since the samples are first baked in a vacuum at 600°C to remove any volatile impurities.

The Dielectric Loss Results for the 800 kHz peak have also been plotted in Figure 39 for the purposes of comparison. The increase in the 800 kHz peak after annealing is not as large as that observed by EPR because of the overlap with the high frequency peak in the as grown crystals. After the usual 12 hour period of hydrogenation the concentration of Gd^{3+}-F_I^- dipoles determined by EPR falls to less than 50% of the 800°C equilibrium concentration. In contrast the dielectric loss results for the .05% doping crystal show that the 800 kHz peak is reduced to only 74% of the peak height in the annealed crystals.

The dipole moments of the Gd^{3+}-H_I^-, Gd^{3+}-F_I^- sites may be estimated from the plots of lattice distortions for the analogous Ce^{3+}-H_I^-, Ce^{3+}-F_I^- sites compiled by Kiro and Low[73]. The resulting values are $\mu = 2.17$ ea for Gd^{3+}-F_I^-, and $\mu = 2.35$ ea for Gd^{3+}-H_I^-, where e is the electronic charge and a is one quarter the lattice parameter. On the overlapping peak

model the resultant peak height should be proportional to the sum of the Gd^{3+}-F_I^- and Gd^{3+}-H_I^- concentration weighted by their respective dipole moments. Using the concentrations determined by EPR the resultant loss peak should be about 67% of that in the annealed crystals, which may be compared with the observed value of 74%. These measurements therefore indicate that the loss peak observed in hydrogenated crystals is too large to be due to Gd^{3+}-F_I^- dipoles only, and hence that some secondary component must be present. It cannot be definitely established that it is due to Gd^{3+}-H^- dipoles but this is physically reasonable and consistent with the observations.

An interesting problem posed by the EPR results of Fig. 39 is the explanation of the overall decrease in the concentration of the three main Gd^{3+} sites during hydrogenation. At least part of the decrease is associated with the growth of the T2 oxygen compensated site, but it is difficult to measure the concentration of this species relative to the others because of the different symmetry axes. It is also possible that Gd^{3+}-H^- clusters form with increasing hydrogen concentration in the crystals.

III. THE INTERSTITIALCY MODEL OF DIPOLE REORIENTATION

It has been tacitly assumed in the literature that the tetragonal RE^{3+}-F^- dipole reorientates by a simple jump of the F_I^- along a 110 direction to an adjacent interstitial site. On a simple hard sphere model the volume of the F_I^- is greater than the space available at an interstice and so the eight surrounding F^- ions are pushed radially outwards. For a simple 110 jump the F_I^- would have to push through an edge of the already strained cube of F^- ions and so it would be expected that this motion would be associated with a high activation energy.

An alternative to the simple jump is the interstitialcy mechanism wherein the interstitial F^- ion displaces a nearest neighbour lattice F^- ion to an adjacent interstitial site, and takes its place. This mechanism is illustrated in Figure 40. Both the direct jump and the interstitialcy mechanism result in a reorientation of the RE^{3+}-F_I^- dipole and there is no way of distinguishing between them by techniques such as Dielectric Loss or ITC. However, Catlow and Norgett[117] have performed calculations of the activation energies for F_I^- migration by the two types of motion in <u>pure</u> CaF_2 which suggest that interstialcy is the operative mechanism for RE^{3+}-F_I^- dipoles. They found that the direct jump and interstitialcy motions were characterised by activation energies of 3.3 eV and 0.7 eV respectively, compared with the observed activation energy for Gd^{3+}-F_I^- dipoles of 0.4 eV.

The interstitialcy mechanism has more interesting consequences for the Gd^{3+}-H_I^- site. The interstitialcy motion creates a completely new kind of site involving a F^-

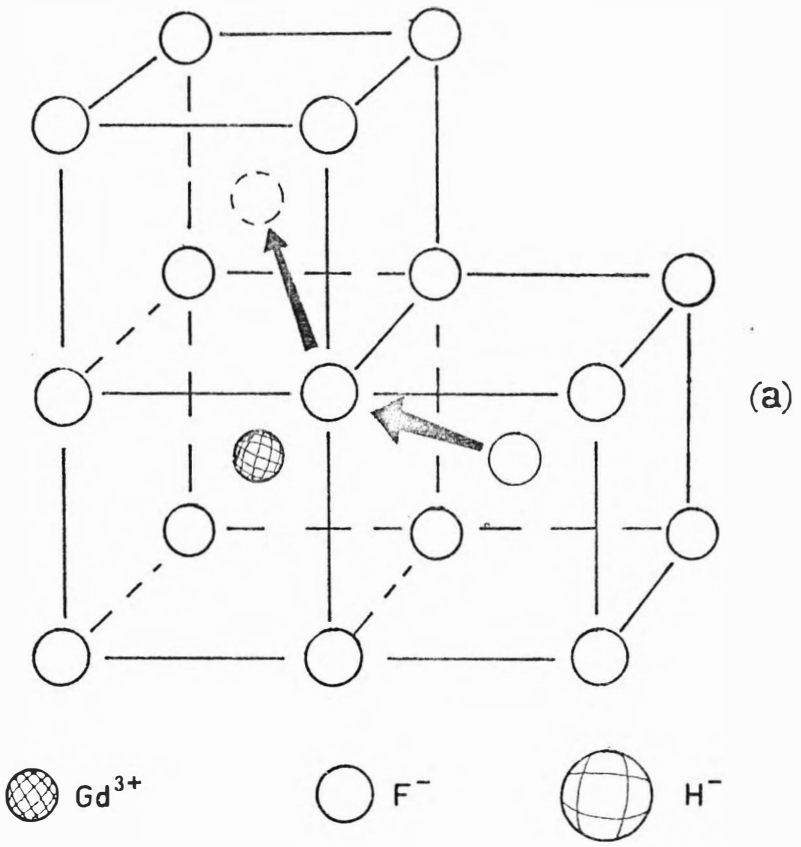

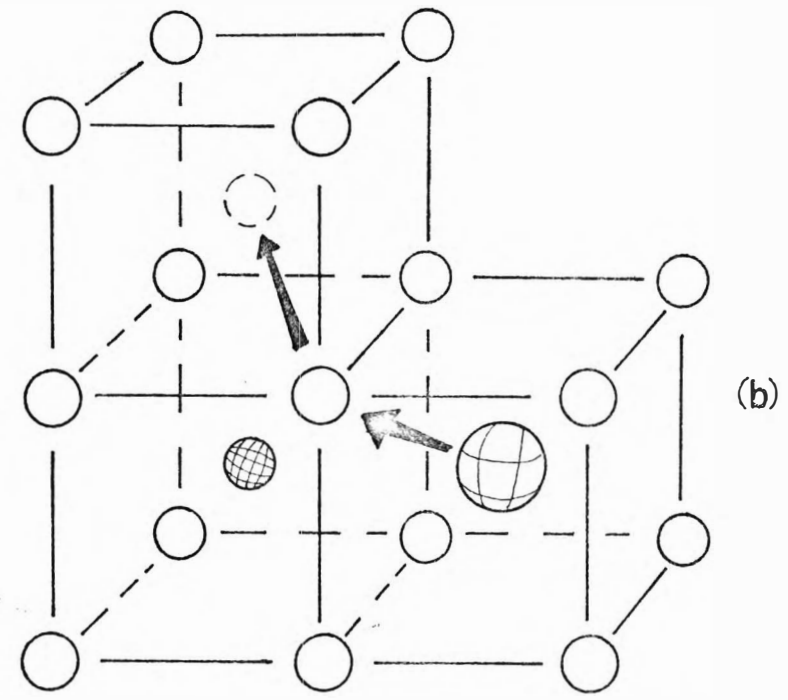

Fig.40: The interstitialcy reorientation mechanism for (a) Gd^{3+}-F^- and (b) Gd^{3+}-H^- dipoles in calcium fluoride crystals.

interstitial and a substitutional H^- ion, as shown in Figure 40. It may be recalled that just this type of site was invoked in Chapter V to explain the new rhombic EPR spectra observed after irradiation of the Gd^{3+}-H_I^- site with UV light. The new UV-induced site was thermally unstable, and degenerated back to the Gd^{3+}-H_I^- site at 90^oK. These EPR results show that there is an important difference between the mechanisms of a simple H_I^- jump and an interstitialcy motion for the reorientation of Gd^{3+}-H_I^- dipoles in CaF_2. The dipoles before and after a simple jump are identical and have the same energy, whereas an interstitialcy motion creates a new dipole of higher energy. Thus whilst interstitialcy and direct jumps cannot be experimentally distinguished for the case of Gd^{3+}-F_I^- dipoles it is possible that the operative mechanism can be identified for Gd^{3+}-H_I^- dipoles. The following section will compare the expected dielectric loss factor for the reorientation of Gd^{3+}-H^- dipoles based on the direct jump model with that expected from the interstitialcy model.

(1) Theoretical Models for the Dielectric Loss of RE^{3+}-X^- Dipoles in CaF_2

(a) The Direct Interstitial Jump. This case has already been considered in detail by Franklin et al.[178] in connection with the dielectric loss for the unmatched point defect pair in the NaCl structure. He has shown that if ω_0 is the jump frequency of the X^- ion between two adjacent interstitial sites, then the associated dielectric loss peak occurs at a frequency $4\omega_0$ if only jumps within the nearest neighbour shell of F_I^- ions are considered. The factor of four is a direct consequence of each potential well having four neighbouring wells. The magnitude of the loss peak is given by[101],

$$\Delta\varepsilon = 2\pi N\alpha, \qquad (8\text{-}12)$$

where N is the concentration of the dipoles, and α is the polarisability given by

$$\alpha = \mu^2/3kT, \qquad (8\text{-}13)$$

where μ is the electric dipole moment of the site.

(b) The Interstitialcy Mechanism. The case of Gd^{3+}-F_I^- reorientation via the interstitialcy mechanism is described by a simple modification of the theory appropriate to direct interstitial jumps. A dipole aligned along the 100 direction can switch to the 010 direction by one of two interstitialcy motions, involving either the F^- lattice ion at the $(\frac{1}{2},\frac{1}{2},\frac{1}{2})$ position, or that at $(\frac{1}{2},\frac{1}{2},-\frac{1}{2})$. Thus if the jump frequency for the motion is ω_I then the dielectric loss peak occurs at $8\omega_I$. The magnitude of the peak is the same as for the direct jump process.

The case of Gd^{3+}-H_I^- reorientation via the interstitialcy mechanism is more complicated, and is best approached by means of the rate-equation theory proposed by Hoffman and Pfeiffer[119]. This theory will be briefly reviewed before being applied to the case of interest; the papers of Hoffman and Pfeiffer[119], Hoffman[120] and Wachtmann[121] should be consulted for further details.

Suppose that there are a set of Ω possible sites which the dipoles can occupy, and that the instantaneous population of any particular type of site labelled i is N_i. Then the usual rate theory shows that the population vector $\underline{N} = (N_1, N_2, \ldots, N_\Omega)$ obeys the relation

$$\frac{d\underline{N}}{dt} = \underline{\underline{W}}\,\underline{N} \tag{8-14}$$

where $\underline{\underline{W}}$ is a matrix whose elements w_{ij} correspond to the jump frequency between site i and site j. The general solution of this equation is of the form

$$\underline{N} = \sum_{\beta} a_{\beta}\,\underline{C}_{\beta}\,\exp(-\omega_{\beta}t), \tag{8-15}$$

where ω_{β} is an eigenvalue of the matrix $\underline{\underline{W}}$, $\underline{C}_{\beta}$ is the corresponding eigenvector, and a_{β} is an expansion coefficient determined by the initial conditions. One of the eigenvalues, labelled $\beta = 1$, is always zero and corresponds to the equilibrium condition. It follows from (8-14) and (8-15) that

$$\sum_{i} a_{\beta}\,C_{i\beta} = N\delta(\beta,1) \tag{8-16}$$

where N is the total population of dipoles. Equation (8-15) shows that the decay of an initially non-equilibrium distribution to the equilibrium one can be described by a set of distribution modes, each with its own distinct decay constant. If the initial distribution is due to an applied electric field then the induced dipole moment is

$$\underline{P} = \sum_{\beta=1}^{\Omega} a_{\beta}\underline{P}_{\beta} \tag{8-17}$$

where $\underline{P}_{\beta}$ is the dipole moment of the distribution mode β. The polarisability α_{β} associated with each mode is given by

$$\alpha_{\beta} = a_{\beta}P_{\beta}/FN \tag{8-18}$$

where F is the applied field strength. In a sinusoidal electric field each mode gives rise to a dielectric loss peak at a frequency $\omega = \omega_\beta$ whose amplitude is proportional to the polarisability of the mode. Thus the main problem in the present application is to determine the spectrum of relaxation mode frequencies and the polarisability associated with each.

The six possible Gd^{3+}-H_I^- sites will be labelled according to the position of the H_I^- as (100), $(0\bar{1}0)$, etc. and the 24 possible Gd^{3+}-F_I^--H_S^- sites will be denoted by the location of the F_I^- and H_S^- ions, for example $(\frac{1}{2},\frac{1}{2},\frac{1}{2})(001)$. The latter notation can be conveniently abbreviated to the form $(\frac{1}{2},\frac{1}{2},\frac{3}{2})$ since there is a one to one relationship between the F_S^- at this type of position and the Gd^{3+}-F_I^--H_S^- sites. Figure 41 shows in a schematic way the energy diagram for the system. The jump frequency ω_A corresponds to a (100) → $(\frac{1}{2},\frac{1}{2},\frac{3}{2})$ jump and ω_B corresponds to the reverse jump.

Two assumptions are necessary to limit the order of the relaxation matrix to manageable proportions. The interstitial ion, F^- or H^-, is assumed to be always in the nearest neighbour shell of interstitial sites. This is reasonable since trigonal Gd^{3+}-F_I^- or Gd^{3+}-H_I^- sites with the interstitial ion of the nnn (111) position were not observed in this work. Secondly, it will be assumed that a Gd^{3+}-F_I^--H_S^- site wherein the F_I^- and H_S^- ion occupy the $(\bar{1}00)$ and $(\frac{1}{2}\frac{1}{2}\frac{1}{2})$ positions respectively is less stable than that discussed here, i.e. $(100)(\frac{1}{2}\frac{1}{2}\frac{1}{2})$. This is equivalent to assuming that in the schematic motion,

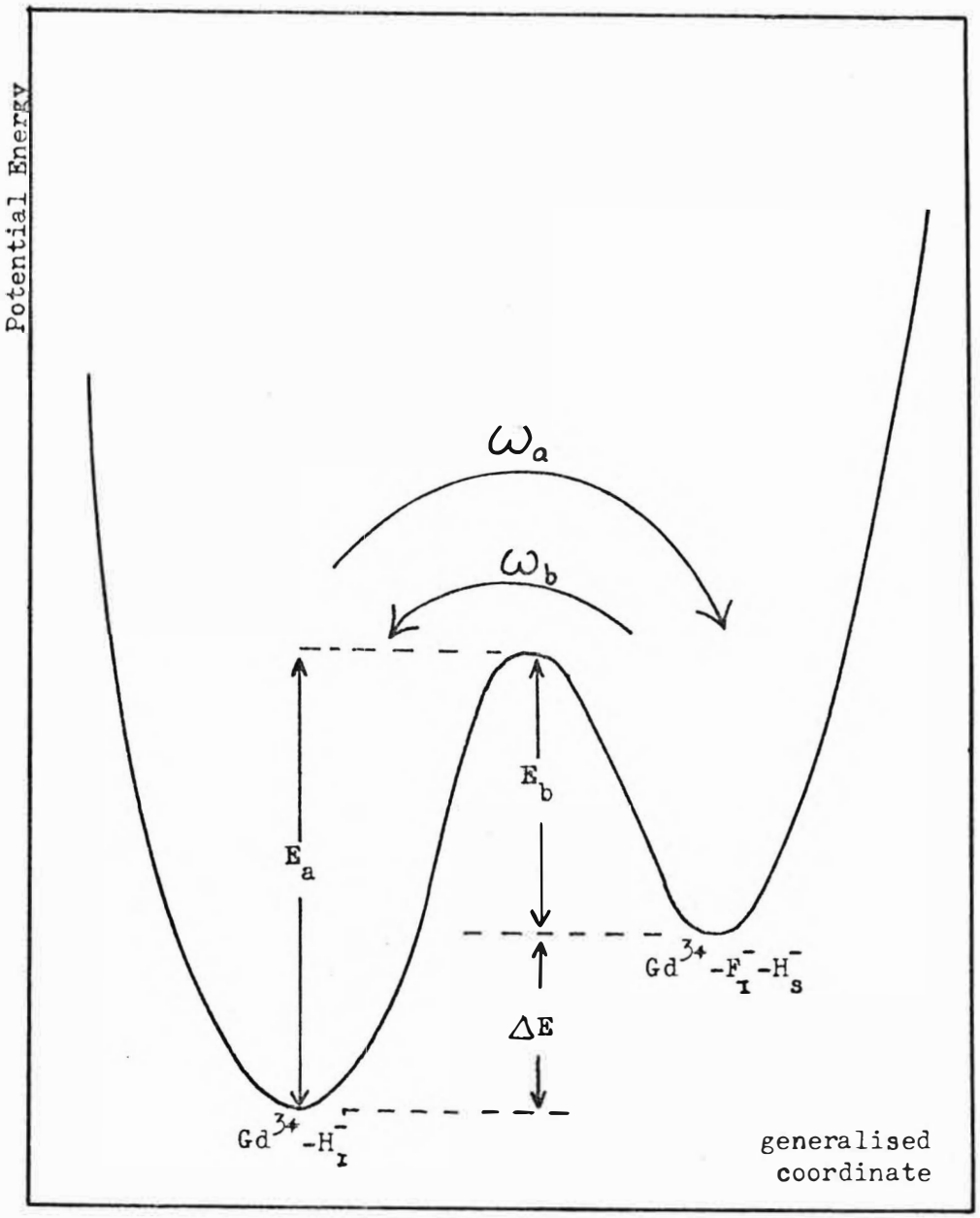

Fig.41:Schematic diagram of the potential energy of a $Gd^{3+}-H^-$ site during an interstitialcy motion, showing the meaning of the symbols used in the text.

$$(1\underset{H}{\bullet}0) \underset{\omega_B}{\overset{\omega_A}{\rightleftharpoons}} (0\underset{F}{1}0)(\tfrac{1}{2}\underset{H}{\tfrac{1}{2}}\tfrac{1}{2}) \underset{\omega_D}{\overset{\omega_C}{\rightleftharpoons}} (\bar{1}\underset{F}{0}0)(\tfrac{1}{2}\underset{H}{\tfrac{1}{2}}\tfrac{1}{2}), \qquad (8\text{-}19)$$

the jump frequencies ω_B, ω_C, ω_D are such that $\omega_D, \omega_B >> \omega_C$. Only one new spectrum was observed in UV irradiated $CaF_2:Gd^{3+}:H^-$ and this degenerated back to the original Gd^{3+}-F_I^- site on warming, so this approximation is justified. This second assumption has the important effect that the formulae which will be developed for Gd^{3+}-H_I^- interstitialcy do not reduce to those for Gd^{3+}-F_I^- interstitialcy when $\omega_A = \omega_B$, for in that case we also have $\omega_A = \omega_B = \omega_C = \omega_D$.

Under the assumptions outlined above the relaxation matrix has the form,

$$\underline{\underline{W}} = \begin{array}{c} \\ 6 \\ 24 \end{array} \begin{array}{c} \begin{array}{cc} 6 & 24 \end{array} \\ \left[\begin{array}{c|c} -8\omega_a \underline{\underline{I}} & \omega_B \underline{\underline{A}} \\ \hline \omega_B \underline{\underline{A}}^T & -2\omega_B \underline{\underline{I}} \end{array}\right] \end{array}, \qquad (8\text{-}20)$$

where $\underline{\underline{I}}$ is the identity matrix, $\underline{\underline{A}}$ is the 24x6 matrix given in Table 20 and the figures give the dimensions of the partitions. An analytical solution of the eigenvalue problem for large relaxation matrices is usually obtained by a lengthy application of group theory, but in the present case an algebraic approach is simpler. Suppose that $(\underline{X},\underline{Y})$ is an eigenvector of $\underline{\underline{W}}$ with corresponding eigenvalue E, and that $\underline{X}$ is of order 6 and $\underline{Y}$ of order 24. Then from the form of the relaxation matrix (8-20) we have that,

$$\begin{aligned} \omega_B \underline{\underline{A}}\, \underline{Y} &= (E + 8\omega_a)\underline{X}, \\ \omega_a \underline{\underline{A}}^T \underline{X} &= (E + 2\omega_B)\underline{Y}, \end{aligned} \qquad (8\text{-}21)$$

	($\bar{1}$ ½ ½)	(½ ½ 1)	(½ $\bar{1}$ ½)	($\bar{1}$ ½ ½)	(½ 1 ½)	(½ ½ 1)	(½ 1 ½)	(1 ½ ½)	(½ ½ 1)	(½ $\bar{1}$ ½)	(1 ½ ½)	(½ ½ 1)	(½ $\bar{1}$ $\bar{1}$)	(½ ½ $\bar{1}$)	($\bar{1}$ ½ ½)	(½ 1 ½)	(½ ½ $\bar{1}$)	(½ 1 ½)	(1 ½ ½)	(½ ½ 1)	(½ $\bar{1}$ ½)	(½ ½ $\bar{1}$)	(½ $\bar{1}$ ½)
($\bar{1}$ 0 0)		1	1		1	1							1	1			1	1						
(0 0 1)	1		1	1	1		1	1		1	1													
(1 0 0)							1		1	1		1								1	1		1	1
(0 0 $\bar{1}$)													1		1	1		1	1		1	1		1
(0 $\bar{1}$ 0)	1	1									1	1		1	1							1	1	
(0 1 0)				1		1		1	1							1	1		1	1				

TABLE 20: The form of the relaxation submatrix $\underline{\underline{A}}$

Footnotes : (a) A blank entry represents a zero

(b) The notation (½ ½ 1) refers to a Gd^{3+}-H_S^--F_I^- site which has an H_S^- at the (½ ½ ½) position and a F_I^- at the (0 0 1) position.

which may be combined to give a new eigenvalue problem,

$$\underline{\underline{A}}\ \underline{\underline{A}}^T\ \underline{X} = \frac{(E+8\omega_a)(E+2\omega_B)}{\omega_a\omega_b}\ \underline{X} \qquad (8\text{-}22)$$

One set of eigenvectors of $\underline{\underline{W}}$ is generated by the trivial solution $\underline{X} = \underline{0}$ of (8-22). From (8-21) it follows that,

$$\underline{X} = \underline{0} \rightarrow \underline{\underline{A}}\ \underline{Y} = \underline{0} \quad \text{and} \quad E = -2\omega_B. \qquad (8\text{-}23)$$

There are 18 non-trivial, linearly independent solutions of the equation $\underline{\underline{A}}\ \underline{Y} = \underline{0}$ and hence there are 18 degenerate eigenvectors of $\underline{\underline{W}}$ of the form $(\underline{0},\underline{Y})$ with common eigenvalue $E = -2\omega_b$. These eigenvectors are listed in Table 21. 12 of the eigenvectors have an associated dipole moment; the remainder are dielectrically inactive.

The other 12 eigenvectors of $\underline{\underline{W}}$ correspond to the non-trivial solutions of (8-22). If the eigenvalues of $\underline{\underline{A}}\ \underline{\underline{A}}^T$ are denoted by λ, then equation (8-22) shows that,

$$\lambda = \frac{(E+8\omega_a)(E+2\omega_B)}{\omega_A\omega_B}\ , \qquad (8\text{-}23)$$

which may be solved for E to give,

$$E = -(4\omega_A+\omega_B) \pm \sqrt{(4\omega_A+\omega_B)^2 - (16-\lambda)\omega_A\omega_B} \qquad (8\text{-}24)$$

Thus there are two eigenvalues of $\underline{\omega}$ for each eigenvalue of $\underline{\underline{A}}\ \underline{\underline{A}}^T$. The eigenvalues of the 6x6 matrix $\underline{\underline{A}}\ \underline{\underline{A}}^T$ are easily found to be 16, 8 and 4 with degeneracies of 1, 3 and 2 respectively. The solutions of equation (8-22) are therefore,

	1	2	3	4	5	6	7	8	9	10	11	13	14	15	16	17	18	12
$\bar{1}\,0\,0$																		
$0\,0\,1$																		
$1\,0\,0$																		
$0\,0\,\bar{1}$																		
$0\,\bar{1}\,0$																		
$0\,1\,0$																		
$\bar{1}\,\bar{\frac{1}{2}}\,\frac{1}{2}$	1											1						
$\bar{\frac{1}{2}}\,\bar{\frac{1}{2}}\,1$		1														1		
$\bar{\frac{1}{2}}\,\bar{1}\,\frac{1}{2}$			1											-1				
$\bar{1}\,\frac{1}{2}\,\frac{1}{2}$				1								-1						
$\bar{\frac{1}{2}}\,1\,\frac{1}{2}$			-1												-1			
$\bar{\frac{1}{2}}\,\frac{1}{2}\,1$					1											-1		
$\frac{1}{2}\,1\,\frac{1}{2}$						1									1			
$1\,\frac{1}{2}\,\frac{1}{2}$				-1									1					
$\frac{1}{2}\,\frac{1}{2}\,1$							1									1		
$\frac{1}{2}\,\bar{1}\,\frac{1}{2}$						-1								1				
$1\,\bar{\frac{1}{2}}\,\frac{1}{2}$	-1												-1					
$\frac{1}{2}\,\frac{1}{2}\,1$								1								-1		
$\bar{\frac{1}{2}}\,\bar{1}\,\bar{\frac{1}{2}}$									1					1				
$\bar{\frac{1}{2}}\,\bar{\frac{1}{2}}\,\bar{1}$		-1															1	
$\bar{1}\,\bar{\frac{1}{2}}\,\bar{\frac{1}{2}}$										1		-1						
$\bar{1}\,\frac{1}{2}\,\bar{\frac{1}{2}}$											1	+1						
$\bar{\frac{1}{2}}\,\frac{1}{2}\,\bar{1}$					-1												-1	
$\bar{\frac{1}{2}}\,1\,\bar{\frac{1}{2}}$									-1						1			
$1\,\frac{1}{2}\,\bar{\frac{1}{2}}$											-1		-1					
$\frac{1}{2}\,\frac{1}{2}\,\bar{1}$							-1										1	
$\frac{1}{2}\,1\,\bar{\frac{1}{2}}$															-1			1
$1\,\bar{\frac{1}{2}}\,\bar{\frac{1}{2}}$										-1			1					
$\frac{1}{2}\,\bar{\frac{1}{2}}\,\bar{1}$								-1									-1	
$\frac{1}{2}\,\bar{1}\,\bar{\frac{1}{2}}$														-1				-1
e/value																		

19	20	21	22	23	24	25	26	27	28	29	30
α	-8	α	α					α	α	α	α
α	-8					α	α	-α	-α		
α	-8	-α	-α					α	α	α	α
α	-8					-α	-α	-α	-α		
α	-8			α	α					-α	-α
α	-8			-α	-α					-α	-α
1	1			1	1	1	1	-1	-1	-1	-1
1	1	1	1	1	1	1	1	1	1		
1	1	1	1							1	1
1	1			-1	-1	1	1	-1	-1		
1	1	1	1			1	1			1	1
1	1	1	1	-1	-1			1	1		
1	1	-1	-1			1	1			1	1
1	1			-1	-1	1	1	-1	-1	-1	-1
1	1	-1	-1	-1	-1			1	1		
1	1	-1	-1			-1	-1			1	1
1	1			1	1			-1	-1	-1	-1
1	1	-1	-1	1	1	-1	-1	1	1	-1	-1
1	1	1	1			-1	-1			1	1
1	1	1	1	1	1			1	1		
1	1			1	1	-1	-1	-1	-1	-1	-1
1	1			-1	-1	-1	-1	-1	-1	-1	-1
1	1	1	1	-1	-1			1	1		
1	1	1	1			-1	-1			1	1
1	1			-1	-1	-1	-1	-1	-1	-1	-1
1	1	-1	-1	-1	-1			1	1		
1	1	-1	-1			-1	-1			1	1
1	1			1	1	-1	-1	-1	-1	-1	-1
1	1	-1	-1	1	1			1	1		
1	1	-1	-1			-1	-1			1	1
α e/value	0	E_2	E_3	E_4	E_3	E_4	E_3	E_4	E_5	E_6	E_5	E_6
$\frac{\omega_b}{\omega_a}$		$\frac{E_3+2\omega_b}{\omega_a}$	$\frac{E_4+2\omega_b}{\omega_a}$	$\frac{E_3+2\omega_b}{\omega_a}$	$\frac{E_4+2\omega_b}{\omega_a}$	$\frac{E_3+2\omega_b}{\omega_a}$	$\frac{E_4+2\omega_b}{\omega_a}$	$\frac{E_5+2\omega_b}{\omega_a}$	$\frac{E_6+2\omega_b}{\omega_a}$	$\frac{E_5+2\omega_b}{\omega_a}$	$\frac{E_6+2\omega_b}{\omega_a}$

TABLE 21 (Continued)

Footnotes: (a) A blank entry represents a zero

(b) The notation ($\frac{1}{2}\frac{1}{2}$1) refers to a Gd^{3+}-H_S^--F_I^- site which has an H_S^- at the ($\frac{1}{2}\frac{1}{2}\frac{1}{2}$) position and a F_I^- at the (0 0 1) position.

$$
\begin{array}{lll}
 & E_1 = 0 & 1 \text{ fold} \\
\lambda = 16 & & \\
 & E_2 = -(8\omega_A + 2\omega_B) & 1 \text{ fold} \\
 & & \\
 & E_3 = -(4\omega_A + \omega_B) + \sqrt{16\omega_A^2 + \omega_B^2} & 3 \text{ fold} \\
\lambda = 8 & & \\
 & E_4 = -(4\omega_A + \omega_B) - \sqrt{16\omega_A^2 + \omega_B^2} & 3 \text{ fold} \\
 & & \\
 & E_5 = -(4\omega_A + \omega_B) + \sqrt{16\omega_A^2 - 4\omega_A\omega_B + \omega_B^2} & 2 \text{ fold} \\
\lambda = 16 & & \\
 & E_6 = -(4\omega_A + \omega_B) - \sqrt{16\omega_A^2 - 4\omega_A\omega_B + \omega_B^2} & 2 \text{ fold}
\end{array}
\qquad (8\text{-}25)
$$

where the origin and degeneracies of each solution are also given. The corresponding eigenvectors may be simply calculated from those of $\underline{\underline{A}}\,\underline{\underline{A}}^T$ by equation (8-22). A check of the 30 eigenvalue solutions is provided by their sum of $-48(\omega_A+\omega_B)$, which is identical with the sum of the diagonal matrix elements of $\underline{\underline{W}}$.

Thus the frequency of each of the relaxation modes has been calculated and it remains to find the polarisability associated with each mode. This can be done by calculating the population distribution vector under the effect of a static electric field by the usual Boltzmann distribution law, and expressing it as a linear combination of the relaxation mode eigenvectors. The net polarisation and individual mode polarisabilities may then be calculated by equations (8-16) and (8-18). This procedure is straightforward but tedious, and so only the results will be given here. The polarisabilities of the three dielectrically active modes, and the corresponding relaxation frequencies are:

$$\alpha_1 = \frac{N_a^0}{N}\left(1 - \frac{(4\omega_a - \omega_B)}{\sqrt{16\omega_a^2+\omega_b^2}}\right)\left(\frac{\mu_a^2}{kT}\right)$$

$$\omega_1 = 4\omega_a + \omega_b - \sqrt{16\omega_a^2+\omega_B^2}$$

$$\alpha_2 = \frac{N_a^0}{N}\left(1 + \frac{4\omega_a - \omega_b}{\sqrt{16\omega_a^2+\omega_B^2}}\right)\left(\frac{\mu_a^2}{kT}\right) \qquad (8\text{-}26)$$

$$\omega_2 = 4\omega_a + \omega_b + \sqrt{16\omega_a^2+\omega_b^2}$$

$$\alpha_3 = \frac{8N_b^0}{N}\left(\frac{\mu_b^2}{kT}\right), \qquad \omega_3 = 2\omega_b$$

where N_a^0, N_b^0 are the equilibrium populations of a Gd^{3+}-H_I^- site and a Gd^{3+}-F_I^--H_S^- site, and μ_a,μ_b are the corresponding dipole moments. It is interesting to note that,

$$\alpha_1+\alpha_2+\alpha_3 = \frac{\mu^2}{3kT}, \qquad (8\text{-}27)$$

which is the orientational polarisability of a dipole which is free to rotate.

The relative magnitudes of ω_A,ω_B and N_a^0,N_b^0 may be determined from the results of the EPR experiments on UV-irradiated CaF_2:Gd^{3+}:H^- described in Chapter V. The temperature dependence of the jump frequencies is assumed to be of the usual Arrhenius form,

$$\omega = \omega_0 \exp -E/kT, \qquad (8\text{-}28)$$

where E is the activation energy for the motion, and the proportional factor ω_0 is typically 10^{13} for atomic systems. The thermal degeneration of the Gd^{3+}-F_I^--H_S^- site proceeds with a time constant of approximately one second at $90^{o}K$,

which leads to an estimate of E_b of 0.2 eV, and the EPR linewidth results indicate that E_a = .4 eV. Thus the jump frequencies and equilibrium populations satisfy the inequalities

$$\omega_b >> \omega_a \qquad \text{and} \qquad N_a^0 >> N_b^0$$

over the temperature range of the dielectric loss measurements, and the formulae for the relaxation mode frequencies and polarisabilities may therefore by simplified to,

$$\begin{aligned} \alpha_1 &\simeq \frac{\mu_a^2}{3kT} & \omega_1 &\simeq 4\omega_a \\ \alpha_2 &\simeq 0 & \omega_2 &\simeq 2\omega_B \\ \alpha_3 &\simeq 0 & \omega_3 &\simeq 2\omega_B. \end{aligned} \qquad (8\text{-}29)$$

The important difference between the expected Dielectric Loss spectra for Gd^{3+}-F_I^- and Gd^{3+}-H_I^- dipoles which reorientate by an interstitialcy motion is now evident. Both systems are associated with single dielectric loss peaks whose amplitudes are in the ratio of the square of their respective dipole moments, but the peak frequency for Gd^{3+}-H_I^- dipoles is $4\omega_a$, whereas that for Gd^{3+}-F_I^- dipoles is $8\omega_a$. Physically, the reason for this difference lies in the restriction on the routes by which a Gd^{3+}-H_I^- site can reorientate under the assumptions of the interstitialcy model discussed previously. The two possible routes may be summarised in the schematic notation:

$$(100)_{H^-} \underset{\omega_B}{\overset{\omega_A}{\rightleftharpoons}} (010)_{F^-}\,(\tfrac{1}{2}\tfrac{1}{2}\tfrac{1}{2})_{H^-} \xrightarrow{\omega_B} (001)_{H^-} \qquad (8\text{-}30)$$

Thus there is a probability of one half that a Gd^{3+}-H_I^- dipole which undergoes an interstitialcy motion will return to its original configuration, with no net dipole reorientation. Therefore the dielectric relaxation frequency, taken over one cycle of the two stage relaxation process, is approximately $8\omega_A/2 = 4\omega_A$. For Gd^{3+}-F_I^- dipoles there is no restriction of the form (8-30) and the relaxation frequency is just $8\omega_A$.

The EPR linewidth experiments measure the relaxation frequency corresponding to the lifetime of the F_I^- or H_I^- at an interstitial site. This is identical to the frequency of the dominant relaxation mode for Gd^{3+}-X_I^- (X = H,F) reorientation by the direct jump mechanism, or for Gd^{3+}-F_I^- reorientation by the interstitialcy mechanism. However, the frequency measured by the linewidth measurements for the Gd^{3+}-H_I^- site on an interstitialcy model will be $8\omega_a$, whereas the calculation shows that the dielectric relaxation occurs at $4\omega_a$. On this basis the expected dielectric loss peak for the Gd^{3+}-H_I^- dipoles would be at a frequency which is one half that derived by an extrapolation of the EPR linewidth results. This would put the peak at 1.5 times the frequency of the Gd^{3+}-F_I^- peak, and this is consistent with the experimental observations. It may be concluded that the interstitialcy hypothesis supports the interpretation of the dielectric loss spectra which has the Gd^{3+}-F_I^- and Gd^{3+}-H_I^- loss peaks unresolved, but not that in which there is no dielectric loss associated with Gd^{3+}-H_I^- dipoles.

Some independent support for the overlapping peak interpretation proposed in this thesis is provided by Kitts' ITC measurements[22] on two samples of $CaF_2:Gd^{3+}:H^-$ supplied by the author. No new ITC peak which could be ascribed to Gd^{3+}-H_I^- dipoles was observed, and the only difference between the ITC spectra of $CaF_2:Gd^{3+}$ and $CaF_2:Gd^{3+}:H^-$ was that the Gd^{3+}-F_I^- peak in the latter crystals was slightly broader than in the untreated samples. These observations are entirely consistent with the dielectric loss measurements reported here, and may be explained by the same arguments.

VI. SUMMARY

The previous measurements of the reorientation of Gd^{3+}-F_I^- dipoles have been confirmed and extended, and it seems likely in view of the work of Catlow and Norgett[117] that this dipolar species reorientates by the interstitialcy mechanism. The EPR linewidth measurements for Gd^{3+}-H_I^- and Gd^{3+}-D_I^- sites show that the activation energy for these species is very similar to that for Gd^{3+}-F_I^- dipoles, but the pre-exponential frequency factor is several times larger in accordance with expectations. It is unlikely that direct tunneling of the H_I^- ion makes an appreciable contribution to the relaxation rate above 200^oK. The dielectric loss spectra for hydrogenated or deuterated crystals of $CaF_2:Gd^{3+}$ are difficult to interpret, but a consistent though not conclusive theory is that the Gd^{3+}-H_I^- system reorientates by the interstitialcy mechanism, which results in the loss peak for Gd^{3+}-H_I^- dipoles being swamped by and not resolvable from that for the Gd^{3+}-F_I^-

dipoles. This interpretation is supported by the observation of a Gd^{3+}-F_I^--H_S^- site in UV irradiation CaF_2:Gd^{3+}:H^-, and by a theoretical calculation of the dielectric relaxation frequencies of Gd^{3+}-H_I^- dipoles on an interstitialcy model.

CHAPTER IX

CONCLUSIONS AND SUGGESTIONS FOR FURTHER WORK

The major emphasis in this work has been on the tetragonal RE^{3+}-F_I^-/H_I^- sites, but much useful information has also been collected on other rare earth ion sites. For the non-hydrogenated crystals the Gd^{3+}-$F_7^-O^{2-}$ site has been observed in calcium, strontium and barium fluorides, and accurate spin Hamiltonian parameters determined. This ionic structure may provide an interesting test of the superposition model proposed by Newman[56] if the exact position of the ligand ions can be established (for example by ENDOR), because the values of b_2^0 determined do not vary systematically with the unit cell size. The situation should be tractable since only two kinds of ligand ion are involved, and in the absence of distortions the six off-axis ions do not contribute to b_2^0. Thus the major contributions will arise from only two ions, the on-axis F^- and O^{2-} ions.

It is unlikely that further attempts to produce RE^{3+}-Li^+ sites with the aim of studying the electron phonon interaction will be profitable. In view of the results reported here for RE^{3+}-H_I^-/D_I^- sites, the isotope shift between the EPR spectra of RE^{3+}-$(Li^6)^+$ and RE^{3+}-$(Li^7)^+$ sites is probably too small for measurement because of the smaller relative mass increment and the larger separation of ions. On the other hand the Gd^{3+} sites of rhombic symmetry found in hydrogenated strontium fluoride show large isotope shifts, but the location of the ions is not known although plausible models have been proposed here. Samples have been forwarded to Professor Hutchison at

the University of Chicago to examine the feasibility of ENDOR measurements on these sites.

The calculation of the static crystal field parameter B_0^2 for the tetragonal Gd^{3+}-F_I^-/H_I^- sites as a point charge/point dipole model yields a value which is only about one half of that estimated from the EPR and optical data. This discrepancy may be due to either the inadequacy of the electrostatic model itself, or the approximations made in its present application. The first point is discussed in the review by Newman[56] which contains a detailed summary of the magnitudes of the various contributions to the crystal field parameters B_0^2, B_0^4, B_0^6 and B_6^6 for the case of praesodymium trichloride. Electrostatic contributions (point charge, point dipoles etc.) are almost self cancelling for the B_4^m and B_6^m parameters, and their resultants are only about 10% of the total theoretical values with the remainder arising from covalency and overlap contributions. However the equivalent figure for B_0^2 is at least 50%, and so although a purely electrostatic calculation is largely irrelevant for B_m^4 and B_m^6, it is a reasonable approach for B_0^2. The actual application of the electrostatic model for calculating B_0^2 in the present case is simplified by the cubic symmetry of the fluorite lattice since the contribution of distant ions is zero. A major approximation is the use of the lattice distortion determined for Ce^{3+}-F_I^-/H_I^- sites by ENDOR, because the ionic radii of the Ce^{3+} and Gd^{3+} ions differ. The effective charges and polarisabilities of the neighbouring ions may also differ from the values assumed here. It is therefore uncertain whether the discrepancy between calculated and experimental B_0^2 values is due mainly

to the omission of overlap and covalency contributions, or to the approximations made in the application of the electrostatic model. An ab initio calculation of the covalency and overlap contributions would resolve the situation, but this is a very challenging problem[123].

The isotope shift calculations for both Gd^{3+}-H_I^- and Er^{3+}-H_I^- sites are in good agreement with the experimental measurements. It is expected that the electrostatic model should be more accurate in application in this case because the only significant contribution comes from a single ion (the interstitial hydride/deuteride ion), and so uncertainties in the position of the next nearest neighbour F^- ligands are not as important as for the static crystal field calculation. An ambiguity in the theory lies in the ad hoc assumption that the anharmonic vibrational parameters c and d are negative. However, this is reasonable in the circumstances since the isotope shift experiments are the only ones which have been performed that are sensitive to the signs and not just the magnitudes of the parameters. It is difficult to devise an independent experiment which is sensitive to the signs because for every RE^{3+}-H_I^- site with the H^- along the (001) direction there is an equivalent site with the H^- along the $(00\bar{1})$ direction. An electric field applied along the (001) axis renders these two sites inequivalent, but the task of interpreting the field induced shifts in the EPR spectra so as to identify the sign of c and d would not be straightforward.

The EPR spectrum of the excited Z_3 state of the Er^{3+}-H_I^- site was not observed in this work due to insufficient spectrometer sensitivity, and it would be interesting to see if the g value isotope shifts are in accordance with the

calculations. Using the crystal field parameters for the Er^{3+}-H_I^- site it is possible to predict g values and hydrogen to deuterium shifts of $g_{//} = 1.478$, $\Delta g_{//} = -.14$, $g_{\perp} = 5.94$, $\Delta g_{\perp} = +.06$. The expected isotope shift for $g_{//}$ is large and should be accurately measurable. With this object a conversion of the Q band spectrometer to 110 kHz modulation has been initiated in an attempt to boost the sensitivity.

The reorientation rate experiments for Gd^{3+}-H_I^- sites have necessarily been interpreted by rather indirect evidence, and, although the overlap arguments are fairly convincing, it is desirable that a distinct dielectric loss peak for Gd^{3+}-H_I^- dipoles be observed. It is unlikely that this can be achieved by further direct measurements on hydrogenated crystals because it has been found by experience that it is impossible to produce a crystal which contains more Gd^{3+}-H_I^- sites than Gd^{3+}-F_I^- sites. It has been reported[124] that X-ray irradiation of CaF_2:Gd^{3+} crystals at room temperature depletes the Gd^{3+}-F_I^- site and creates a new site of trigonal symmetry. Heating the sample at 200°C for a few minutes completely reversed the reaction, which indicates that the process involves migration of the F_I^- ion. Presumably X-rays have a similar effect on the Gd^{3+}-H_I^- site, and so both of the tetragonal sites in hydrogenated CaF_2:Gd^{3+} would be completely depleted by a sufficiently long irradiation period. However, when the irradiation is terminated the Gd^{3+}-H_I^- site should be repopulated first because of the greater mobility of the H^- ion. Depending on the time constants involved it may thus be possible to obtain crystals containing only the required Gd^{3+}-H_I^- sites, although other irradiation induced and

dielectrically active sites may pose problems. An alternative approach which achieves the opposite result to that described above is to irradiate a sample with UV light at 77^{o}K, but this would require a specially designed electrode cell.

The most important points to emerge from the reorientation rate measurements are that hydride ion tunneling for the Gd^{3+}-H_I^- sites is insignificant, at least above 200^{o}K, and that the reorientation mechanism is probably an interstitialcy motion rather than a direct jump. As far as is known the only technique which can unambiguously distinguish between these two mechanisms is the rotating frame NMR method discussed by Ailion and his coworkers[125,126]. Such measurements would be helpful in proving the conclusions made here.

REFERENCES

1. M.J. Weber and R.W. Bierig, Phys. Rev. 134, 1492 (1964).
2. J.H. Van Vleck, J. Chem. Phys. 7, 61 (1939).
3. J.L. Hall and R.T. Schumacher, Phys. Rev. 127, 1892 (1962).
4. R.C. Newman, Advances in Physics 18, 545 (1969).
5. R.J. Elliott, W. Hayes, G.D. Jones, H.F. McDonald, C.T. Senett, Proc. Roy. Soc. 289, 1 (1965).
6. G.D. Jones, S. Peled, S. Rosenwaks, S. Yatsiv, Phys. Rev. 183, 353 (1969).
7. E.Kh. Ivoilova and A.M. Leushkin, Sov. Phys. Sol. State 13, 1914 (1972).
8. J.M. O'Hare, Phys. Rev. B3, 3603 (1971).
9. D.J. Newman, J. Phys. C. 6, L271 (1973).
10. M.R. Presland, Ph.D. Thesis, University of Canterbury (1974).
11. I.T. Jacobs, G.D. Jones, K. Zdansky and R.A. Satten, Phys. Rev. B 3, 2888 (1971).
12. I.J. Ashburner, R.C. Newman, S.D. McLaughlan, Phys. Letts 27A, 212 (1968).
13. A.A. Maradudin, E.W. Montroll, G.H. Weiss, "Theory of Lattice Dynamics in the Harmonic Approximations", Solid State Physics Supplement 3, Academic Press (1963).
14. B.G. Wybourne, "Spectroscopic Properties of the Rare Earths", Interscience, New York (1965).
15. G.D. Jones and R.A. Satten, Phys. Rev. 147, 566 (1966).
16. M. Tinkham, "Group Theory and Quantum Mechanics", McGraw Hill, New York (1964), page 329.

17. S. Fraga and G. Malli, "Many Electron Systems: Properties and Interactions", Saunders, Philadelphia (1968), page 89.

18. M.H.L. Pryce, Proc. Phys. Soc. London, A63, 25 (1950).

19. A. Abragam and M.H.L. Pryce, Proc. Roy. Soc. A205, 135 (1951).

20. H. Statz and G.F. Koster, Phys. Rev. 115, 1568 (1959).

21. Huang Wu Han, Lin Fu-Cheng and Zhu Ji-Keng, Proc. Phys. Soc. 84, 661 (1964).

22. Tuhina Ray, Proc. Roy. Soc. 277A, 76 (1964).

23. J.S. Griffith, Mol. Phys. 3, 79 (1960).

24. W.J.C. Grant and M.W.P. Strandberg, J. Phys. Chem. Solids 25, 635 (1964).

25. J.S.M. Harvey and H. Kiefte, J. Phys. B. 3, 1326 (1970).

26. H.A. Buckmaster, R. Chatterjee and Y.H. Shing, J. Phys. C 4, L130 (1971).

27. R. McWeeny, J. Chem. Phys. 42, 1717 (1965).

28. A.D. Rae, J. Chem. Phys. 50, 2672 (1969).

29. H.A. Buckmaster, R. Chatterjee, Y.H. Shing, Phys. Stat. Sol. 13, 9 (1972).

30. D.R. Hutton and T.J. Seed, J. Sci. Inst. 43, 949 (1966).

31. N.G. Harlick and D.R. Hutton, J. Sci. Inst. 44, 299 (1967).

32. K.G. Weir and J.S. Dryden, J. Sci. Inst. 40, 318 (1963).

33. A.M. Thompson, Proc. Instn. Elect. Engrs B 103, 704 (1956).

34. J.M. Baker, B. Bleaney, W. Hayes, Proc. Roy. Soc. A 247, 141 (1958).

35. J.M. Baker, E.R. Davies, J.P. Hurrell, Phys. Letts 26A, 352 (1968).

36. T.Rs. Reddy, E.R. Davies, J.M. Baker, D.N. Chambers, R.C. Newman, B. Özbay, Phys. Lett. 36A, 231 (1971).

37. U. Ranon, A. Yariv, Phys. Letts 9, 17 (1964).

38. L.A. Boatner, R.W. Reynolds, M.M. Abraham, J. Chem. Phys. 52, 1248 (1970).

39. M.T. Hutchings, Solid State Physics, Vol. 16 (Academic Press 1964).

40. K.M. Beem, E.J. Hornyak, P.G. Rasmussen, Phys. Rev. B 4, 2124 (1971).

41. H.A. Buckmaster, R. Chatterjee, J.C. Dering, D.J.I. Fry, Y.H. Shing, J.D. Skirrow, B. Venkatesan, J. Magn. Res. 4, 113 (1971).

42. J. Sierro, Helv. Phys. Acta 36, 505 (1963).

43. J. Sierro, Phys. Letts 4, 178 (1963).

44. V.M. Vinokurov, M.M. Zaripov, Yu.E. Pol'skii, V.G. Stepanov, G.K. Chirkin, L.Ya. Shekun, Soviet Phys. - Sol. State 4, 1637 (1963).

45. Authors as above, Soviet Phys. - Sol. State 5, 436 (1963).

46. Authors as above, Soviet Phys. - Sol. State 5, 2126 (1963).

47. M.H. Weiler, D.W. Wylie, Proc. Phys. Soc. 85, 608 (1965).

48. H.A. Buckmaster, R. Chatterjee, Y.H. Shing, Phys. Stat. Sol. 13, 9 (1972).

49. A.D. Franklin, S. Marzullo, Proc. Br. Ceram. Soc. 19, 135 (1970).

50. F.Z. Gilfanov, L.D. Livanova, A.L. Stolov, Soviet Phys. - Solid State 8, 108 (1966).

51. C. Ryter, Helv. Phys. Acta 30, 353 (1957).

52. S.R.P. Smith and T. Cole, J. Chem. Phys. 52, 1286 (1970).

53. A.A. Antipin and I.N. Kurkin, Fiz. Tverd. Tela 6, 947 (1964).

54. R.H. Heist and F.K. Fong, Phys. Rev. B1, 2970 (1970).

55. I.J. Ashburner and R.C. Newman, J. Phys. C. 5, L283 (1972).

56. D.J. Newman, Advances in Physics 20, 197 (1971).

57. D.J. Newman and W. Urban, J. Phys. C. 5, 3101 (1972).

58. R. Proctor, this laboratory, personal communication.

59. C.A. Freeth, this laboratory, personal communication.

60. F.Z. Gilfanov, L.D. Livanova, A.L. Stolov, Yu.P. Khadyrev, Opt. Spektrosk. 23, 431 (1967).

61. H.M. Crosswhite, R.L. Schwiesow, W.T. Carnall, J. Chem. Phys. 50, 5032 (L) (1969).

62. C.W. Nielson and G.F. Koster, "Spectroscopic Coefficients for p^n, d^n and f^n Configurations", MIT Press, Cambridge, Mass. (1964).

63. E.Kh. Ivoilova, and A.M. Leushkin, Sov. Phys. Sol. State 13, 1914 (1972).

64. Z. Scheslinger and M. Nuremberg, Phys. Rev. 178, 568 (1969).

65. J.M. O'Hare, Phys. Rev. B 3, 3603 (1971).

66. B.G. Wybourne, Phys. Rev. 148, 317 (1966).

67. H.A. Buckmaster, R. Chatterjee and Y.H. Shing, Can. J. Phys. 50, 991 (1972).

68. A.R. Rufta, Phys. Rev. 130, 1412 (1963).

69. M. Ashkin, J. de Phys. 26, 709 (1965).

70. R.S. Singh, D.W. Galipeau, S.S. Mitra, J. Chem. Phys. 52, 2341 (1970).

71. R. Fieschi, G.F. Nardelli and N. Terzi, Phys..Rev. 138, A203 (1965).

72. R.S. Calder, W. Cochran, D. Griffiths and R.D. Lowde, Phys. Chem. Solids 23, 621 (1962).

73. D. Kiro and W. Low, Phys. Letters 29A, 537 (1969).

74. C.J. Lenander and E.Y. Yong, J. Chem. Phys. 38, 2750 (1963).

75. R.E. Watson and A.J. Freeman, Phys. Rev. 133, A1571 (1964).

76. A.A. Maradudin and J. Peretti, Phys. Rev. 161, 852 (1967).

77. S.D. McLaughlan and R.C. Newman, Phys. Letts 19, 552 (1965).

78. E.L. Kitts, Ph.D. Thesis, University of North Carolina (1973).

79. H.H. Wickman and I. Nowick, Phys. Rev. 142, 115 (1966).

80. J. Blok and D.A. Shirley, Phys. Rev. 143, 278 (1968).

81. F.H. Spedding and A.H. Daane, J. Metals 6, 504 (1954).

82. M. Dvir and W. Low, Proc. Phys. Soc. 75, 136 (1960).

83. U. Ranon and W. Low, Phys. Rev. 132, 1609 (1963).

84. J.M. Baker, W. Hayes and D.A. Jones, Proc. Phys. Soc. B73, 942 (1959).

85. Yu.K. Voron'ko, G.M. Zverev, B.B. Meshkov, A.I. Smirnov, Sov. Phys. Sol. State 6, 2225 (1965).

86. P.A. Forrester and S.D. McLaughlan, Phys. Rev. 138, A1682 (1965).

87. A.I. Smirnov, Sov. Phys. Sol. State 12, 590 (1970).

88. K.R. Lea, M.J.M. Leask and W.P. Wolf, Phys. Chem. Solids 23, 1381 (1962).

89. H.R. Lewis and E.S. Sabisky, Phys. Rev. 130, 1370 (1963).

90. A.D. Franklin and S. Marzullo, J. Phys. C 3, L171 (1970).

91. C.P. Poole, "Electron Spin Resonance", Interscience Publishers, New York (1967).

92. A.M. Stoneham, J. Phys. D. 5, 670 (1972).

93. D.W. Posener, Australian J. Phys. 12, 184 (1959).

94. G.D. Watkins, Phys. Rev. 113, 91 (1959).

95. N.H. Fletcher, "The Chemical Physics of Ice", Cambridge University Press, Cambridge (1970).

96. P.C. Chow, A.J.P. 40, 730 (1972).

97. J.A. Sussman, Phys. Kondens. Materie 2, 146 (1964).

98. D.M. Dennison and G.E. Uhlenbeck, Phys. Rev. 41, 313 (1932).

99. C.P. Flynn and A.M. Stoneham, Phys. Rev. B 1, 3966 (1970).

100. G.D. Watkins and J.W. Corbett, Phys. Rev. 121, 1001 (1961).

101. A.B. Lidiard, "Encyclopedia of Physics" 20, 246 (1957), Springer Verlag, Berlin.

102. W. Bollmann and H. Henniger, Phys. Stat. Sol. (a) 11, 367 (1972).

103. E.L. Kitts and J.H. Crawford, Bull. Am. Phys. Soc. 18, 250 (1972).

104. W. Bontinck, Physica 24, 650 (1958).

105. D. Chatain, P. Gautier, C. Lacabanne, C.R. Acad. Sci. Paris 270, 1694 (1970).

106. V.A. Arkhangel'skaya, T.I. Nikitinskaya, M.S. Tyutin, Sov. Phys. Sol. State 7, 2976 (1965).

107. J.P. Stott and J.H. Crawford, Phys. Rev. Letts 26, 384 (1971).

108. J.P. Stott and J.H. Crawford, Phys. Rev. B 4, 668 (1971).

109. E.L. Kitts, M. Ikeya and J.H. Crawford, Phys. Rev. B 8, 5840 (1973).

110. A.D. Franklin and J. Crissman, J. Phys. C 4, L239 (1971).

111. H.K. Welsh, personal communication (1974).

112. A.K. Chatham, B.E.F. Fender, M.J. Cooper, J. Phys. C. 4, 3107 (1971).

113. A.K. Cheetham et al., Solid State Commun. 8, 171 (1970).

114. C.R.A. Catlow, J. Phys. C. 6, L64 (1973).

115. N.E. Kask, L.S. Kornienko and M. Fakir, Sov. Phys. Sol. St. 6, 430 (1964).

116. Yu.K. Voron'ko, A.A. Kaminskii, V.V. Osiko, Sov. Phys. - JETP 22, 295 (1966).

117. C.R.A. Catlow and M.J. Norgett, J. Phys. C. 6, 1325 (1973).

118. A.D. Franklin, A. Sharb and J.B. Wachtman, J. Res. Nat. Bur. Stands 68A, 425 (1964).

119. J.D. Hoffman and H.G. Pfeiffer, J. Chem. Phys. 22, 132 (1954).

120. J.D. Hoffman, J. Chem. Phys. 23, 1331 (1955).

121. J.B. Wachtmann, Phys. Rev. 131, 517 (1963).

122. V.H. McCann, this laboratory, personal communication (1974).

123. J.M. Baker and W.B.J. Blake, Proc. Roy. Soc. Lond., A316 (1970).

124. A.J. Bevelo, Ph.D. Thesis, University of St Louis (1970).

125. D.C. Ailon and P. Ho, Phys. Rev. 168, 662 (1968).

126. G.L. Samuelson and D.C. Ailon, Phys. Rev. B 5, 2488 (1972).

127. G.H. Dieke, "Spectra and Energy Levels of Rare Earth Ions in Crystals", Interscience Publishers, New York (1968).

128. P.T. McMahon, this laboratory, personal communication (1974).

129. E.Kh. Ivoilova, B.N. Kazakov, A.M. Leushkin and A.L. Stolov, Sov. Phys. - Sol. State 15, 1426 (1974).

130. K. Zdansky and A. Edgar, Phys. Rev. B 3, 2133 (1971).

131. A. Abragam and B. Bleaney, "Electron Paramagnetic Resonance of Transition Ions", Clarendon Press, Oxford (1970), page 136.

132. C.W. Rector, B.C. Pandey and H.W. Moos, J. Chem. Phys., 45, 171 (1966).

APPENDIX I

The calculations discussed in Chapter VI extensively utilise the properties of the solid harmonics which were developed for the problem here by Zdansky[11,130]. These properties are incidental to the main theme of that chapter, and so are summarised here. Some of Zdansky's formulae appear to be in error and have been corrected. They are marked with an asterisk.

The potential of a point charge has been traditionally expanded as a series of terms involving the spherical harmonics Y_m^{ℓ}, or the related Racah spherical tensors C_m^{ℓ}. Zdansky has shown that for calculations of the electron phonon interaction, in which the Cartesian derivatives of the Coulomb potential are required, it is more convenient to use the solid harmonics $T_{\ell x}^{m}$, $T_{\ell y}^{m}$. These are defined for $0 \leqslant m \leqslant n$ as,

$$T_{n,x}^{m} = r^n P_n^m(\cos\theta) \cos m\phi,$$

$$T_{n,y}^{m} = r^n P_n^m(\cos\theta) \sin m\phi,$$

where r,θ and ϕ are the spherical coordinates, and the $P_n^m(x)$ are the Legendre polynomials defined by,

$$P_n^m(x) = (-1)^m \frac{(1-x^2)^{m/2}}{2^n n!} \frac{d^{n+m}}{dx^{n+m}} (x^2-1)^n .$$

The first few solid harmonics are,

$$T^0_{0x} = 1, \qquad T^0_{0y} = 0,$$

$$T^0_{1x} = z, \qquad T^0_{1y} = 0,$$

$$T^1_{1x} = -x, \qquad T^1_{1y} = -y,$$

$$T^0_{2x} = \tfrac{1}{2}(3z^2-r^2), \qquad T^0_{2y} = 0,$$

$$T^1_{2x} = -3zx, \qquad T^1_{2y} = -3zy,$$

$$T^2_{2x} = 3(x^2-y^2), \qquad T^2_{2y} = 6xy.$$

The solid harmonics are related to the Racah spherical tensors $C_m^{\ n}$ used in this thesis by,

$$C^{\ n}_{\pm m} = r^{-n}\left(\frac{(n-m)!}{(n+m)!}\right)^{\frac{1}{2}} (T^{\ m}_{n,x} \pm iT^{\ m}_{n,y}).$$

The derivatives of the solid harmonics with respect to $x = r \sin\theta \cos\phi$ and $y = r \sin\theta \sin\phi$ are given by,

$$2\frac{\partial}{\partial x} T^{\ m}_{n,x} = -(n+m)(n+m-1)T^{\ m-1}_{n-1,x} + T^{\ m+1}_{n-1,x},$$

$$2\frac{\partial}{\partial x} T^{\ m}_{n,y} = -(n+m)(n+m-1)\, T^{\ m-1}_{n-1,y} + T^{\ m+1}_{n-1,y},$$

$$2\frac{\partial}{\partial y} T^{\ m}_{n,x} = +(n+m)(n+m-1)\, T^{\ m-1}_{n-1,y} + T^{\ m+1}_{n-1,y},$$

$$2\frac{\partial}{\partial x} T^{\ m}_{n,y} = -(n+m)(n+m-1)\, T^{\ m-1}_{n-1,x} - T^{\ m+1}_{n-1,x},$$

for $m > 0$, and

$$\frac{\partial}{\partial x} T^0_{n,x} = T^1_{n-1,x}, \qquad \frac{\partial}{\partial y} T^0_{n,x} = T^1_{n-1,y},$$

for $m = 0$.

For differentiation with respect to $z = r\cos\theta$ we have that

$$\frac{\partial}{\partial z} T_{n,x}^{m} = (n+m)\, T_{n-1,x}^{m}, \qquad \frac{\partial}{\partial z} T_{n,y}^{m} = (n+m)\, T_{n-1,y}$$

The Coulomb potential at $\underline{r}$ of a unit point charge at $\underline{R}$ can be expanded in terms of the solid harmonics for $|r| < |R|$:

$$\frac{1}{|\underline{R}-\underline{r}|} = \Sigma\, M_n^m\, R^{-(2n+1)} \left(T_{n,x}^{m}(\underline{R}) T_{n,x}^{m}(\underline{r}) + T_{n,y}^{m}(\underline{R}) T_{n,y}^{m}(\underline{r}) \right)$$

where $M_n^m = \frac{2(n-m)!}{(n+m)!}$ for $m \neq 0$ and $M_n^0 = 1$ for $m = 0$.

Similarly the potential of a unit charge at $\underline{r}$ due to a point dipole at $\underline{R}$ can be expressed as

$$-\underline{p}.\nabla_{xyz} \frac{1}{|\underline{R}-\underline{r}|} = -p_x \frac{\partial}{\partial x} \frac{1}{|\underline{R}-\underline{r}|} - p_y \frac{\partial}{\partial y} \frac{1}{|\underline{R}-\underline{r}|} - p_z \frac{\partial}{\partial z} \frac{1}{|\underline{R}-\underline{r}|} .$$

The derivatives in this equation may be evaluated by using the recursion formulae given previously:

$$\frac{\partial}{\partial z} \frac{1}{|\underline{R}-\underline{r}|} = \sum_{n=0}^{\infty} (n+1) R^{-(2n+3)} T_{n+1,x}^{0}(\underline{R}) T_{n,x}^{0}(\underline{r})$$

$$+ \sum_{n=0}^{\infty} \sum_{m=1}^{n} \frac{2(n-m+1)!}{(n+m)!} R^{-(2n+3)}$$

$$\times \left[T_{n+1,x}^{m}(\underline{R}) T_{n,x}^{m}(\underline{r}) + T_{n+1,y}^{m}(\underline{R}) T_{n,y}^{m}(\underline{r}) \right]^{*}$$

$$\frac{\partial}{\partial x}\frac{1}{|\underline{R}-\underline{r}|} = -\sum_{n=0}^{\infty} R^{-(2n+3)} T_{n+1,x}^{1}(\underline{R}) T_{n,x}^{0}(\underline{r})$$

$$+ \sum_{n=0}^{\infty}\sum_{m=1}^{\infty} R^{-(2n+3)} \left\{ \frac{(n-m+2)!}{(n+m)!} \left(T_{n+1,x}^{m-1}(\underline{R}) T_{n,x}^{m}(\underline{r}) \right.\right.$$

$$\left. + T_{n+1,y}^{m-1}(\underline{R}) T_{n,y}^{m}(\underline{r}) \right)$$

$$\left. - \frac{(n-m)!}{(n+m)!} \left(T_{n+1,x}^{m+1}(\underline{R}) T_{n,x}^{m}(\underline{r}) + T_{n+1,y}^{m+1}(\underline{R}) T_{n,y}^{m}(\underline{r}) \right) \right\} *$$

$$\frac{\partial}{\partial y}\frac{1}{|\underline{R}-\underline{r}|} = -\sum_{n=0}^{\infty} R^{-(2n+3)} T_{n+1,y}^{1}(\underline{R}) T_{n,x}^{0}(\underline{r})$$

$$+ \sum_{n=0}^{\infty}\sum_{m=1}^{\infty} R^{-(2n+3)} \left\{ \frac{(n-m)!}{(n+m)!} \left[T_{n+1,x}^{m+1}(\underline{R}) T_{n,y}^{m}(\underline{r}) \right.\right.$$

$$\left. - T_{n+1,y}^{m+1}(\underline{R}) T_{n,x}^{m}(\underline{r}) \right]$$

$$\left. + \frac{(n-m+2)!}{(n+m)!} \left[T_{n+1,x}^{m-1}(\underline{R}) T_{n,y}^{m}(\underline{r}) - T_{n+1,y}^{m-1}(\underline{R}) T_{n,x}^{m}(\underline{r}) \right] \right\} *$$

The formulae developed thus far may now be applied to calculate the point charge, point dipole, and induced dipole contributions to the electron-phonon interaction discussed in Chapter II. It was shown there that the electronic functions f_i and g_{ij} may be expressed as a series of spherical tensors C_m^{ℓ} and that the possible values of ℓ and m were restricted by symmetry arguments. The equations (2-5) may be re-expressed in solid harmonic form:

$$f_z = a_{0n} T_n^0, \qquad g_{zz} = b_{0n} T_n^0, \qquad g_{yz} = b_{1n} T_{ny}^1,$$

$$f_x = a_{1n} T_{nx}^1, \qquad (g_{xx}+g_{yy}) = c_{0n} T_n^0, \qquad g_{xx}-g_{yy} = b_{2n} T_{nx}^2,$$

$$f_y = a_{1n} T_{ny}^1, \qquad g_{xz} = b_{1n} T_{nx}^1, \qquad g_{xy} = c_{2n} T_{ny}^2.$$

The values of the coefficients a_{ij}, b_{ij}, c_{ij} may be evaluated for the three models considered in the test by utilising the expressions for the Cartesian derivatives of the solid harmonics, and the forms of the point charge and point dipole potentials, in the expression (2-6) for the electron-phonon interaction. The results for the point charge model are:

$$a_{0n} = -(n+1)eQ\, D^{-(n+2)} \qquad b_{0n} = -C_{0n} = \tfrac{1}{2}(n+1)(n+2)\frac{eQ}{D^{n+3}}$$

$$a_{1n} = -\frac{eQ}{D^{n+2}} \qquad b_{1n} = \frac{(n+2)eQ}{D^{n+3}}$$

$$b_{2n} = C_{2n} = \frac{eQ}{2D^{n+3}} \quad *,$$

where Q is the hydride ion charge, e is the electron charge, and D is the RE^{3+}-H_I^- separation.

For the point dipole model, if p is the magnitude of the dipole, we have that:

$$a_{0n} = \frac{(n+1)(n+2)ep}{D^{n+3}} \qquad a_{1n} = \frac{(n+1)ep}{D^{n+3}} \quad *$$

$$b_{0n} = -\frac{(n+1)(n+2)(n+3)ep}{2D^{n+4}} \qquad C_{0n} = \frac{(n+1)\left[(n+1)(n+2)+2\right]ep}{2D^{n+4}}$$

Finally, for the induced dipole model, we have that

$$a_{02} = \frac{4eQ\alpha_D(F^-)}{R^4 S^3}\left(-\frac{3wv}{S^2} P_3^1\left(\frac{U}{R}\right) + 3\left(1 - \frac{3v^2}{S^2}\right) P_3^0\left(\frac{U}{R}\right)\right), \quad *$$

$$b_{02} = \frac{-6eQ\alpha_D(F^-)}{R^4S^5}\left\{w\left(\frac{5v^2}{S^2} - 1\right)P_3{}^1\left(\frac{U}{R}\right) + 3v\left(\frac{5v^2}{S^2} - 3\right)P_3{}^0\left(\frac{U}{R}\right)\right\},^*$$

$$c_{02} = \frac{12eQ\alpha_D(F^-)}{R^4S^5}\left\{w\left(3 - \frac{5w^2}{2S^2}\right)P_3{}^1\left(\frac{U}{R}\right) + 3v\left(1 - \frac{5w^2}{2S^2}\right)P_3{}^0\left(\frac{U}{R}\right)\right\},^*$$

where $\alpha_D(F^-)$ is the dipole polarisability of the F^- ion, and the remaining symbols are defined in Figure A1.

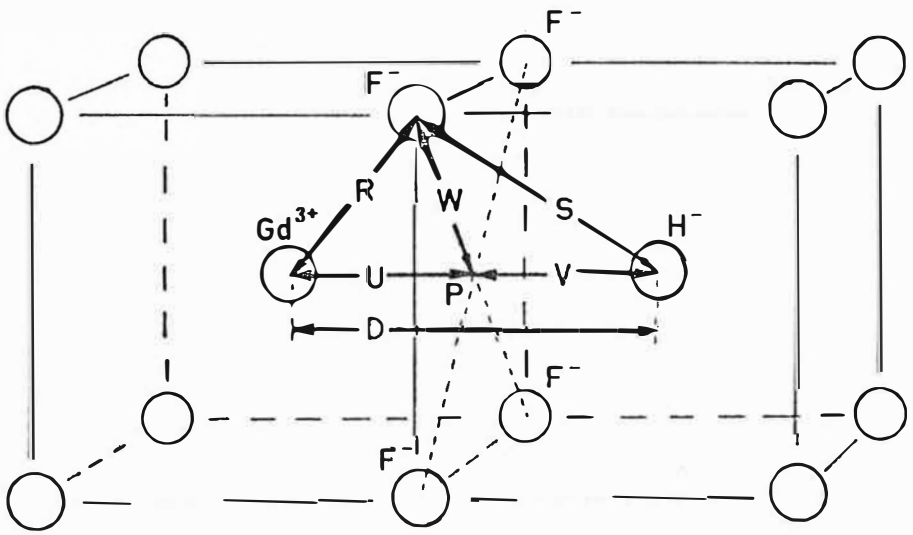

Fig.A1: The tetragonal Gd^{3+}-H^- site, showing the meaning of the symbols used in Appendix 1.

APPENDIX II

a) Decomposition of Spin-Field Tensors for Cubic Symmetry

$$T_4^{\,0}(S,H) \rightarrow T_4^{\,0}(S)$$

$$[T_4^{\,4}(S,H) + T_4^{-4}(S,H)] \rightarrow [T_4^{\,4}(S) + T_4^{-4}(S)]$$

$$T_6^{\,0}(S,H) \rightarrow T_6^{\,0}(S)$$

$$[T_6^{\,4}(S,H) + T_6^{-4}(S,H)] \rightarrow [T_6^{\,4}(S) + T_6^{-4}(S)]$$

$$T_0^{\,0}(S,H) \rightarrow \frac{1}{\sqrt{3}}[T_1^{\,1}(H)T_1^{-1}(S) + T_1^{-1}(H)T_1^{\,1}(S) - T_1^{\,0}(H)T_1^{\,0}(S)]$$

b) Bleaney-Koster Linear Field Terms for Tetragonal Symmetry

A total of nine such terms are possible:

$$\begin{aligned}
\Delta H_{BK} = {} & {}^{a}_{2}{}^{0}(T_3^{\,1}(S)T_1^{-1}(H) + T_3^{-1}(S)T_1^{\,1}(H) - T_3^{\,0}(S)T_1^{\,0}(H)) \\
& + {}^{1}_{a}{}^{0}_{4}(T_3^{\,1}(S)T_1^{-1}(H) + T_3^{-1}(S)T_1^{\,1}(H) + \frac{2\sqrt{2}}{3}T_3^{\,0}(S)T_1^{\,0}(H)) \\
& + {}^{2}_{a}{}^{0}_{4}(T_5^{\,1}(S)T_1^{-1}(H) + T_5^{-1}(S)T_1^{\,1}(H) - \sqrt{\frac{5}{3}}T_5^{\,0}(S)T_1^{\,0}(H)) \\
& + {}^{1}_{a}{}^{0}_{6}(T_5^{\,1}(S)T_1^{-1}(H) + T_5^{-1}(S)T_1^{\,1}(H) + \sqrt{\frac{12}{5}}T_5^{\,0}(S)T_1^{\,0}(H)) \\
& + {}^{2}_{a}{}^{0}_{6}(T_7^{\,1}(S)T_1^{-1}(H) + T_7^{-1}(S)T_1^{\,1}(H) - \sqrt{\frac{7}{2}}T_7^{\,0}(S)T_1^{\,0}(H)) \\
& + {}^{2}_{a}{}^{0}_{6}(T_7^{\,1}(S)T_1^{-1}(H) + T_7^{-1}(S)T_1^{\,1}(H) - \sqrt{\frac{7}{2}}T_7^{\,0}(S)T_1^{\,0}(H)) \\
& + {}^{1}_{a}{}^{4}_{4}(T_3^{\,3}(S)T_1^{\,1}(H) + T_3^{-3}(S)T_1^{-1}(H)) \\
& + {}^{2}_{a}{}^{4}_{4}([T_5^{\,3}(S)T_1^{\,1}(H) + T_5^{-3}(S)T_1^{-1}(H)] + 3\sqrt{5}[T_5^{\,5}(S)T_1^{-1}(H) \\
& \qquad + T_5^{-5}(S)T_1^{\,1}(H)] - 3[T_5^{\,4}(S)T_1^{\,0}(H) + T_5^{-4}(S)T_1^{\,0}(H)])
\end{aligned}$$

$$+ {}^{1}a_{6}^{4}\left([T_5^{3}(S)T_1^{1}(H) + T_5^{-3}(S)T_1^{-1}(H)] + \frac{1}{3\sqrt{5}}[T_5^{5}(S)T_1^{-1}(H) + T_5^{-5}(S)T_1^{1}(H)] + \frac{2}{3}[T_5^{4}(S)T_1^{0}(H) + T_5^{-4}(S)T_1^{0}(H)]\right)$$

$$+ {}^{2}a_{6}^{4}\left([T_7^{5}(S)T_1^{-1}(H) + T_7^{-5}(S)T_1^{1}(H)] + \frac{1}{\sqrt{11}}[T_7^{3}(S)T_1^{1}(H) + T_7^{-3}(S)T_1^{-1}(H)] - \frac{1}{\sqrt{2}}[T_7^{4}(S)T_1^{0}(H) + T_7^{-4}(S)T_1^{0}(H)]\right)$$

The above terms have been derived directly from the considerations discussed in Chapter II and may be regrouped into a shorter form for convenience by collecting terms which are common to several expressions. However, the number of independent parameters is unchanged.

APPENDIX III

An account of some of the work done on the tetragonal Gd^{3+}-H_I-/F_I^- sites in calcium fluoride has been published and is included overleaf. Improvements to some aspects of the theoretical treatment have been made since the date of publication and are incorporated in the main body of this thesis. In particular, the estimates of the anharmonic parameters c and d, and of the zero field splitting have been revised and allowance has been made for the effects of shielding. However, the arguments and general approach are unchanged.